

CONTINUOUS LIQUID INTERFACE PRODUCTION OF MEDICAL DEVICES FOR DRUG
DELIVERY AND CANCER THERAPY

Cameron James Bloomquist

A dissertation submitted to the faculty at the University of North Carolina at Chapel Hill in partial fulfillment of the requirements for the degree of Doctor of Philosophy in the Eshelman School of Pharmacy (Pharmacoengineering and Molecular Pharmaceutics).

Chapel Hill
2017

Approved by:

Joseph M. DeSimone

Samuel K. Lai

Joel E. Tepper

Andrew Z. Wang

Wei You

© 2017
Cameron James Bloomquist
ALL RIGHTS RESERVED

ABSTRACT

Cameron James Bloomquist: Continuous liquid interface production of medical devices for drug delivery and cancer therapy
(Under the direction of Joseph M. DeSimone)

With increasing interest in patient-specific dosage forms to tailor treatment and improve patient compliance, 3D printed drug formulations and medical devices have garnered much attention. The software-driven design and ability to fabricate a unique part with each print, makes 3D printing a versatile platform. This versatility affords personalization through anatomically-specific designs and the tuning a dosage form to each individual patient's clinical needs. The recent introduction of the 3D printing technique, Continuous Liquid Interface Production (CLIP), presents a platform capable of producing devices in a rapid manner with mechanical properties suitable to serve as a final product rather than just a prototype. The study described herein is the investigation of CLIP as a methodology to fabricate drug-loaded, biocompatible medical devices with controlled release properties.

We sought to characterize how parameters including crosslink density, polymer network composition, and the geometric complexity afforded by CLIP can be utilized to modify drug release from 3D printed dosage forms. Through systematic variation of the crosslink density and polymer composition of polycaprolactone and poly(ethylene glycol) based formulations, it was demonstrated that release kinetics of a small molecule drug surrogate, rhodamine B-base, can be modified through alterations in the resin formulation. Further, using a constant resin formulation, the RhB release was shown to be controllable through the geometric complexity built into the computer aided design (CAD) model.

The suitability of CLIP for production of drug-loaded devices was investigated by screening a panel of clinically-relevant small molecule therapeutics for stability towards potential stresses from the CLIP process, including UV irradiation and interactions with free radicals. Additionally, select formulations were chosen to produce model devices which were tested for biocompatibility, degradation and encapsulation of a chemotherapeutic, docetaxel, and a corticosteroid, dexamethasone-acetate. Devices indicated biocompatibility over the course of 175 days of *in vitro* degradation and mirrored the release kinetics observed for the RhB model drug.

Finally, these lessons learned were applied to the development and *in vivo* testing of two chemotherapeutic-loaded implantable devices: 1) an intraoperative implant for the prevention of lung cancer recurrence following resection and 2) brachytherapy spacers for the treatment of localized prostate cancer.

Dedicated to Isaac James Bloomquist

May your curiosities and passion to pursue them know no bounds

ACKNOWLEDGEMENTS

I want to express my sincere gratitude to the countless people that without whom the completion of this work would not have been possible. I would first like to thank my advisor Dr. Joseph DeSimone for the opportunity to be a part of your group, work with an amazingly diverse and talented team of students and scientist, and to contribute to exciting and meaningful projects. The lessons I have learned about entrepreneurship, communication, and collaboration within interdisciplinary teams have been integral to my development as a scientist and leader. I would also like to thank my co-advisor and collaborator Dr. Andrew Wang for the opportunity to be a part of your group, and for the guidance and direction you provided throughout my graduate studies. The clinical perspective I gained from working with you and your group will prove invaluable for my career. Thank you to Dr. Wei You, Dr. Joel Tepper, and Dr. Sam Lai for agreeing to be a part of my committee and for the helpful feedback and guidance along the way. I would also like to acknowledge the UNC core facilities and groups, especially Charlene Santos and the Animal Studies Core, Dr. Stephanie Montgomery from the Animal Histopathology and Lab Medicine Core, as well as Dr. Amar Kumbhar from CHANL.

To the amazing colleagues that I have had the pleasure of working alongside, learning from, and laughing with – I could not have asked for a better group and team to be a part of. Special thanks to the entire leadership team: Dr. Shaomin Tian, Dr. Jillian Perry, Dr. Sue Mecham, and Dr. Chris Luft. It is impossible to overstate how much I appreciate all the work you put in to develop students into scientists and researchers. Thanks to all the 3D printing team members past and present: Rima Januszewicz, Dr. Adam Quintanilla, Dr. Cassie Caudill, Dr. Ashley Johnson, Dr. Greg Robbins, Dr. Ali Nebipasagil, Dr. Bob Pinschmidt, Dr. Lihong Huang,

and Dr. Kseniya Gavrilov. Thanks to the rest of the current DeSimone team, Dr. Kevin Olson, Dr. Jason Coffman and Dr. Erin Wilson. This has been an awesome challenge and I am grateful to each and every one of you for the truly collaborative atmosphere that makes doing research fun!

I would also like to thank former DeSimone group members for making me feel like a valuable part of the team from day one: Dr. Cathy Froman for being my desk buddy and always telling me the honest truth about everything, and in the process giving me some of the best advice I have received throughout this experience – you are going to make an incredible mentor and teacher to those that will have the pleasure of working with you; Dr. Chintan Kapadia - your work ethic is inspirational, and your passion for life and persistent joy was contagious and made life in lab better every day; and Dr. Kevin Reuter for showing me the ropes during my rotation and always providing a laugh or two when needed. Special thanks to Dr. Tojan Rahhal – I am so glad we joined the DeSimone group at the same time. I never thought I would have developed as much as I have as a person and leader over the past 5 years. This would not have been the case if not for your willingness to talk about the important topics beyond science and your inclusion of me in the CCLD project. I will be forever grateful for the perspective you provided. Your hard work is already inspiring countless future leaders, engineers, and scientists; and I look forward to seeing how your efforts will positively impact the future of science.

To my family, thank you so much for always being a source of support and encouragement. Geoff, you set the precedent for academic success in our family and were always willing to offer support, encouragement and guidance throughout my education. Your ability to argue about any topic (as frustrating as it can be) shaped my scientific approach by pushing me to be sure that I was always capable of backing up any statement with evidence or facts. Eric, your genuine curiosity helped shape the way I approached and communicated my research. You were never satisfied with the simple explanations that I gave most laypersons and you always wanted to know more. That pushed me to think deeper about my research and

allowed me to look at my work from a different scientific perspective. That desire to know more will serve you well in your career. Mom and Dad, thank you nurturing my sense of wonder and curiosity, which is essential for success as a scientist, from an early age. From going to science expos at school to building 2-liter tornados, you always found time to develop our curiosity. A wise man once told me, “Life is positioning,” and you guys put me in a position to be successful. I do not take that for granted.

Lastly, and most importantly, I would like to thank my amazing wife, Ashley. You encouraged me to pursue my Ph.D. and supported me throughout the process. It is impossible to express how much I appreciate the sacrifices you made and the extra work you did for me during these years. I can say, without a doubt, that if not for you I would not have been able to do this. You played so many important roles for me: my motivation, my support, my therapist, my secretary, my accountant, my nutritionist, and my best friend. I love you so much.

TABLE OF CONTENTS

LIST OF FIGURES	xv
LIST OF TABLES	xix
LIST OF ABBREVIATIONS	xx
CHAPTER 1: INTRODUCTION TO DRUG DELIVERY AND 3D PRINTING	1
Chapter goals.....	1
1.1 Drug delivery and controlled release	1
1.2 3D printing and applications in drug delivery	7
1.2.1 Extrusion based 3D printing	13
1.2.1.1 Fused deposition modeling (FDM)	13
1.2.1.2 Semi-solid Extrusion (EXT)	15
1.2.2 Powder-bed fusion	16
1.2.2.1 Selective laser sintering (SLS)	17
1.2.2.2 Inkjet and polyjet binder deposition	18
1.2.3 Stereolithography (SLA).....	19
1.3 Continuous Liquid Interface Production (CLIP).....	22
1.4 3D printing biomaterials	24
1.4.1 3D printing in a clinical setting.....	24
1.4.2 Tissue engineering.....	25
References.....	29
CHAPTER 2: SYNTHESIS AND CHARACTERIZATION OF PHOTOPOLYMERS FOR BIOMEDICAL APPLICATIONS	38
Chapter goals.....	38

2.1 Introduction	38
2.1.1 Radical photopolymerization	38
2.1.2 Current state of biomaterials based on photopolymers	42
2.2 Materials and Methods.....	44
2.2.1 Materials.....	44
2.2.2 Synthesis of methacrylate-functionalized polycaprolactone.....	44
2.2.2.1 Synthesis of PCL ₁₁₀₀ -TMA	44
2.2.2.2 Synthesis of PCL ₇₀₀ - DMA	45
2.2.3 Photocalorimetry	46
2.2.4 Differential Scanning Calorimetry.....	47
2.2.5 Synthesis of HA-GMA	47
2.2.6 Photo-rheology of HA-GMA	48
2.2.7 Continuous Liquid Interface Production of a HA-GMA hydrogel	48
2.3 Results and Discussion.....	48
2.3.1 Synthesis of methacrylate-functionalized polycaprolactone.....	48
2.3.2 Characterization of methacrylate-functionalized polycaprolactone	51
2.3.2.1 Photokinetics	51
2.3.2.2 Thermal properties	54
2.3.3 Synthesis of HA-GMA	55
2.4 Conclusions	58
References.....	59
CHAPTER 3: CONTROLLING THE RELEASE OF A SMALL MOLECULE DRUG SURROGATE FROM DEVICES FABRICATED WITH CLIP	63
3.1 Introduction	63
3.2 Materials and Methods.....	68
3.2.1 Materials.....	68
3.2.2 Continuous Liquid Interface Production	68

3.2.3 CLIP fabrication of geometrically complex devices	69
3.2.3.1 Varying unit cell geometry with a constant unit cell size.....	69
3.2.3.2 Varying unit cell size with a constant unit cell geometry and print parameters.....	70
3.2.3.3 Constant unit cell geometry, theoretical volume, optimized print parameters.....	71
3.2.4 CLIP fabrication of devices with varying crosslink density	73
3.2.5 CLIP fabrication of devices with varying polymer network composition.....	75
3.2.6 Characterization of CLIP devices	77
3.2.6.1 Swelling and gel fractions	77
3.2.6.2 Scanning electron microscopy.....	78
3.2.6.3 Thermal analysis of printed parts	78
3.2.6.3 RhB extraction	78
3.2.6.3 In vitro RhB release	78
3.3 Results and Discussion.....	79
3.3.1 Effect of Geometry	79
3.3.1.1 Varying unit cell geometry with a constant unit cell size.....	81
3.3.1.2 Varying unit cell size while holding unit cell geometry and print parameters constant	86
3.3.1.3 Constant unit cell geometry, theoretical volume, optimized print parameters.....	89
3.3.2 Effect of crosslink density.....	94
3.3.3 Effect of polymer network composition	98
3.4. Conclusions	101
References.....	102
CHAPTER 4: PRE-CLINICAL EVALUATION OF CLIP FOR THE FABRICATION OF PHARMACEUTICAL AND MEDICAL DEVICES	105
4.1 Introduction	105
4.2 Materials and Methods.....	107

4.2.1 Materials.....	107
4.2.2 Drug screen for UV and radical stability.....	107
4.2.3 Formulation of docetaxel and dexamethasone-acetate resins.....	109
4.2.4 Polymerization kinetics of resins	110
4.2.5 Continuous Liquid Interface Production	111
4.2.6 Drug loading and <i>in vitro</i> release from DTXL- and DexAc-loaded devices	111
4.2.7 Coating devices with DTXL and DexAc	112
4.2.8 <i>In vitro</i> cytocompatibility	113
4.2.8.1 Cell culture.....	113
4.2.8.2 Cytotoxicity of monomers	113
4.2.8.3 Cytocompatibility of leachables and degradation products	114
4.3 Results and Discussion.....	115
4.3.1 Drug screen for UV and radical stability.....	115
4.3.2 Formulation and photokinetics of drug-loaded resins	119
4.3.3 Encapsulation, extraction and release of DTXL and DexAc from CLIP devices	121
4.3.4 Coating as a method for API incorporation	125
4.3.5 <i>In vitro</i> biocompatibility of CLIP materials	126
4.3.5.1 Cytotoxicity screen of CLIP monomers	127
4.3.5.2 Degradation and cytotoxicity of CLIP devices	129
4.4 Conclusion and Future Work	130
References.....	134
CHAPTER 5: PRECLINICAL EVALUATION OF CLIP MEDICAL DEVICES	136
Chapter goals.....	136
5.1 Introduction	136
5.1.1 Lung cancer recurrence following surgical resection	136
5.1.2 Brachytherapy background	138

5.2 Materials and Methods.....	140
5.2.1 Materials.....	140
5.2.2 Cell culture	141
5.2.3 Experimental Animals	142
5.2.4 Methods for Intraoperative needles to reduce cancer recurrence.....	142
5.2.4.1 Optimization of CLIP parameters for the fabrication of intraoperative devices	142
5.2.4.2 Fabrication of drug-loaded intraoperative devices.....	143
5.2.4.3 In vitro drug release studies	143
5.2.4.4 In vivo tumor recurrence model	144
5.2.4.5 Clinical chemistry and histopathological analysis.....	145
5.2.5 Methods for CLIP brachytherapy spacers.....	145
5.2.5.1 CLIP brachytherapy spacers for in vitro toxicity and in vivo efficacy	145
5.2.5.2 In vitro cytotoxicity of CLIP brachytherapy spacers.....	146
5.2.5.3 In vivo efficacy of CLIP brachytherapy spacers.....	146
5.2.5.4 Solvent uptake in brachytherapy spacers printed with different overall light exposures	147
5.2.5.5 DTXL release from brachytherapy spacers printed with different overall light exposures	148
5.2.5.6 Printing complex geometries on the scale of brachytherapy spacers	149
5.3 Results and Discussion.....	150
5.3.1 Intraoperative implants to reduce cancer recurrence.....	150
5.3.1.1 Optimization of CLIP parameters and processing for fabrication of intraoperative device.....	150
5.3.1.2 Fabrication and characterization of drug loaded intraoperative devices	153
5.3.1.3 Preliminary characterization of in vivo resection and recurrent tumor models	157
5.3.1.4 In vivo efficacy of intraoperative devices against tumor recurrence	159
5.3.1.5 Future directions for development of intraoperative implants.....	164

5.3.2 Brachytherapy spacers	165
5.3.2.1 In vitro cytotoxicity of CLIP brachytherapy spacers	165
5.3.2.2 In vivo efficacy of DTXL-loaded brachytherapy spacers	166
5.3.2.3 Photopolymerization kinetics as a method to control drug release	167
5.3.2.4 Complex geometries on the scale of brachytherapy spacers	169
5.4 Conclusions and future directions	171
References.....	173

LIST OF FIGURES

Figure 1.1 Controlled release systems compared to conventional administration	2
Figure 1.2 Osmotically-driven drug release devices. Elementary osmotic pump	4
Figure 1.3 General process of 3D printing	9
Figure 1.4 Potential system of patient-centered healthcare	10
Figure 1.5 Examples of different designs used to manufacture 3D printed tablets	12
Figure 1.6 Extrusion based 3D printing methods	15
Figure 1.7 Powder-bed fusion 3D printing techniques	17
Figure 1.8 Diagrams of stereolithography 3D printers.....	20
Figure 1.9 CLIP enables fast print speeds and layerless part construction	23
Figure 1.10 Typical process for fabrication of a tissue engineering scaffold to be seeded with cells following complete fabrication.....	27
Figure 2.1 Initiation and propagation steps in free radical photopolymerization of a monomethacrylate monomer.	40
Figure 2.2 Bimolecular termination of propagating methacrylate radicals.....	41
Figure 2.3 Synthesis of PCL ₁₁₀₀ -TMA.....	49
Figure 2.4 Synthesis of PCL ₇₀₀ -DMA.....	50
Figure 2.5 Quantitative ¹³ C NMR of PCL ₇₀₀ -DMA.....	51
Figure 2.6 Schematic of photo-DSC apparatus.....	52
Figure 2.7 Photocalorimetry thermograms	52
Figure 2.8 Effects of light intensity of the extent of polymerization of PCL ₁₁₀₀ -TMA.....	53
Figure 2.9 Thermal analysis of methacrylated PCL monomers	54
Figure 2.10 Synthesis of HA-GMA	55
Figure 2.11 Photo-rheology and CLIP of HA-GMA hydrogels.....	57
Figure 3.1 Potential approaches for producing drug-loaded devices	67
Figure 3.2 Geometrically complex CAD models of varying unit cells	70
Figure 3.3 Schematic of CAD generation for geometricly complex devices.....	71

Figure 3.4 Generation of CAD files for model devices containing various surface areas and a constant volume.....	72
Figure 3.5 Schematic of <i>MC</i> calculation for a network made up entirely of crosslinking monomers	74
Figure 3.6 Comparison of 3D printed and polymer foam scaffolds	80
Figure 3.7 Geometrically complex model devices made from three unique unit cell geometries with constant unit cell size	81
Figure 3.8 Solvent uptake and gel fraction of geometrically complex devices generated by arraying different unit cell geometries	83
Figure 3.9 Linear correlation between the theoretical surface area to volume ratio and gel fraction.	84
Figure 3.10 Mass and RhB loading in geometrically complex devices with constant unit cell size	84
Figure 3.11 <i>In vitro</i> RhB release from geometrically complex devices with uniform unit cell size	86
Figure 3.12 Effect of unit cell size on theoretical part volume and surface area	87
Figure 3.13 Visible light photograph of devices with constant print parameters, constant unit cell geometry, and various unit cell dimensions	88
Figure 3.14 <i>In vitro</i> RhB release and fabricated part mass	89
Figure 3.15 Optimization of print parameters to achieve similar device mass	91
Figure 3.16 Geometrically complex model devices loaded with RhB as a surrogate drug.....	92
Figure 3.17 Solvent swelling of geometrically complex devices generated by arraying node unit cells of 1, 2, and 3 mm fabricated with optimized parameters to control for part mass.	93
Figure 3.18 Characterization of geometrically complex model devices	94
Figure 3.19 Gel fractions of RhB-loaded disks with different crosslink densities	96
Figure 3.20 Characterization of RhB-loaded model devices with different crosslink densities.....	97
Figure 3.21 Dependence of the PBS uptake and T_g of model devices on diluent content in PCL ₇₀₀ -DMA.....	99
Figure 3.22 Effect of polymer network composition on <i>in vitro</i> RhB release from PCL ₇₀₀ -DMA based formulations.....	100

Figure 4.1 Representative HPLC chromatographs for drugs that are UV stable and UV labile	116
Figure 4.2 Stability of a panel of clinically-relevant drugs to UV exposure and radical presence	117
Figure 4.3 Stability testing in additional conditions.....	119
Figure 4.4 Photocalorimetry thermal traces of blank, DTXL- and DexAc-loaded resins	120
Figure 4.5 Characterization of DTXL- and DexAc-loaded model devices	122
Figure 4.6 Analysis of progress of drug extraction from release study samples	124
Figure 4.7 Drug loading of coated disks	125
Figure 4.8 Dissolution of DTXL and DexAc from drug-coated model disks.	126
Figure 4.9 Biocompatibility of monomers on 344SQ cells	128
Figure 4.10 Mass loss and cytotoxicity of model devices due to degradation and extraction of soluble content.....	130
Figure 4.11 Theoretical approaches to functionalize drug into network	133
Figure 5.1 Brachytherapy schematic.....	139
Figure 5.2 Modified Slide-a-lyzers™ MINI dialysis cassettes for <i>in vitro</i> release studies.....	149
Figure 5.3 Intraoperative implant model.....	150
Figure 5.4 Effect of UV absorber on resolution of needle arrowhead resolution	151
Figure 5.5 Optimization of parameters for the post-processing of intraoperative implants to ensure uniformity of fabricated devices.....	153
Figure 5.6 Visible light image of blank, PTX, CPP, and PTX/PPP intraoperative implants	154
Figure 5.7 SEM imaging of intraoperative devices	155
Figure 5.8 SEM micrographs of intraoperative devices (no drug) showing surface texture of implant backings	156
Figure 5.9 <i>In vitro</i> release of PTX and CPP from PEG ₅₅₀ -DMA/HEMA resins	157
Figure 5.10 Tumor volume curves for preliminary characterization of recurrent tumor models.....	157
Figure 5.11 Results of preliminary tolerability study	158

Figure 5.12 Tumor inhibition effects of PTX implants compared to I.V. PTX, blank implants, and resection only	160
Figure 5.13 Individual tumor volume curves for each treatment arm	161
Figure 5.14 Histopathology of tumor tissue	163
Figure 5.15 Results of complete blood count and serum biochemical analysis of hematological, hepatic, and renal toxicity.....	164
Figure 5.16 Janus-style intraoperative devices	165
Figure 5.17 <i>In vitro</i> cytotoxicity of brachytherapy spacers	166
Figure 5.18 <i>In vivo</i> efficacy of DTXL-loaded brachytherapy spacers	166
Figure 5.19 Characterization of CLIP brachytherapy spacers fabricated using different overall light exposures.....	168
Figure 5.20 <i>In vitro</i> DTXL release from spacers printed at different light intensities	169
Figure 5.21. Complex geometries printed on the scale of brachytherapy spacers	170

LIST OF TABLES

Table 2.1 Photokinetic parameters of PCL ₁₁₀₀ -TMA upon exposure with a range of light intensities for 15 minutes	53
Table 3.1 Formulations and M_C values for resins used in crosslink density experiment	73
Table 3.2 Formulations and M_C calculations for resins used in the experiments to test the effect polymer network composition.	76
Table 4.1 Details of HPLC methods used in UV and radical stability screen	109
Table 4.2 Formulations and M_C values for resins used to fabricate DTXL- and DexAc-loaded disks and disks used in degradation and cytotoxicity studies.....	110
Table 4.3 Photocalorimetry results of blank and drug-loaded resins.	121
Table 4.4 IC ₅₀ values for resin components in 344SQ cells	128

LIST OF ABBREVIATIONS

3D	Three dimensional
5FU	5-fluorouracil
AA	Acrylic acid
ALT	Alanine aminotransferase
API	Active pharmaceutical ingredient
AST	Aspartate aminotransferase
BLS 1326	2- <i>tert</i> -Butyl-6-(5-chloro-2 <i>H</i> -benzotriazol-2-yl)-4-methylphenol
BUN	Blood urea nitrogen
CAD	Computer aided design
CDDP	Cisplatin
CLIP	Continuous Liquid Interface Production
CPP	Cisplatin prodrug
DBC	Double bond conversion
DCM	Dichloromethane
DexAc	Dexamethasone-21-acetate
DMAEMA	2-(dimethylamino)ethyl methacrylate
DMF	Dimethylformamide
DMSO	Dimethyl sulfoxide
DSC	Differential Scanning Calorimetry
DTXL	Docetaxel
EGDMA	Ethylene glycol dimethacrylate
EOP	Elementary osmotic pumps
EXT	Semi-solid extrusion
FDA	Food and Drug Administration
FDM	Fused deposition modeling

GMA	Glycidyl methacrylate
HA	Hyaluronic acid
HA-GMA	Hyaluronic acid-glycidyl methacrylate
HEMA	2-hydroxyethyl methacrylate
HME	Hot melt extrusion
HPLC	High-performance liquid chromatography
LAP	Lithium phenyl(2,4,6-trimethyl benzoyl) phosphinate
LTPO	Ethyl (2,4,6-trimethylbenzoyl) phenylphosphinate
M_c	Theoretical molecular weight between crosslinks
MP ₂ MA	Di(ethylene glycol) methyl ether methacrylate
mPEG	PEG-dimethyl ether
mPEG-MA	Poly(ethylene glycol) methyl ether methacrylate
OROS	Osmotic controlled-release oral delivery systems
PBS	Phosphate buffered saline
PCa	Prostate cancer
PCL	Poly(caprolactone)
PCL-DMA	Poly(caprolactone) dimethacrylate
PCL-TMA	Poly(caprolactone) trimethacrylate
PEG	Poly(ethylene glycol)
PEG-DA	Poly(ethylene glycol) diacrylate
PEG-DMA	Poly(ethylene glycol) dimethacrylate
PEG-MA	Poly(ethylene glycol) methacrylate
PMA	n-Propyl methacrylate
PTX	Paclitaxel
RhB	Rhodamine B-base
R_p	Rate of polymerization

SA/V	Surface area to volume ratio
SEM	Scanning electron microscope
SLA	Stereolithography
SLS	Selective laser sintering
STL	Standard tessellation language file
TEA	Triethylamine
TEA•HCl	Triethylamine hydrochloride
T_g	Glass transition temperature
t_{\max}	Time at max rate of polymerization
TPO	Diphenyl(2,4,6-trimethylbenzoyl)phosphine oxide
UV	Ultraviolet

CHAPTER 1: INTRODUCTION TO DRUG DELIVERY AND 3D PRINTING

Chapter goals

The following chapter presents the relevant background materials and published literature to provide a context to the purpose of the work presented in this dissertation. Section 1.1 introduces the ideas and approaches implemented in the development and engineering of controlled drug release systems, including oral, systemic, and local administration routes. Also introduced are the various layer-by-layer approaches of traditional 3D printing, and a comparison to Continuous Liquid Interface Production (CLIP). The ways that 3D printing has been used in a clinical and preclinical setting to produce medical devices and tissue engineering applications is reviewed. And lastly, 3D printing techniques that are being implemented for production of drug products are introduced and a perspective on the benefits and potential concerns for each method is discussed.

1.1 Drug delivery and controlled release

Even the best drug compounds and bioactive agents are entirely useless if they cannot reach their intended target. Traditionally, bioactive drugs are administered via the oral or intravenous route. However, if the drug of interest is not stable to the acidic environment of the gastrointestinal tract or results in dose-limiting toxicities when delivered systemically, alternative drug delivery approaches are required for the drug candidate to be effective. As genomic screening technology continues to improve and drug targets become more specific, biologics have been increasingly utilized in drug development such as gene therapy, monoclonal antibodies, and recombinant proteins [1-5]. While these therapies provide benefits in their specificity and have the capability to treat diseases that were previously untreatable, the nature of their physicochemical properties typically does not afford simple oral and intravenous

delivery. Advanced drug delivery systems (DDS), such as nanoparticle formulations, implantable polymer systems, and alternative delivery routes have been used clinically and preclinically to improve the efficacy and clinical outcomes for many of these therapies [6-11].

In addition to physicochemical protection, the use of an advanced DDS affords the ability to prolong and control the release kinetics of a therapeutically active drug [6,12]. Due to the rapid release and subsequent clearance of a drug when using traditional methods of administration, repeated dosing is often required to maintain a drug concentration within a desired therapeutic window (Fig. 1.1). This pharmacokinetic profile and requisite repeated dosing can lead to reduced drug effectiveness, poor patient compliance, and decreased quality of life; especially in patients requiring prolonged treatment or with chronic disease. The use of controlled release technology, however, affords the potential to maintain a constant drug concentration in the body without the multiple doses required of traditional systems.

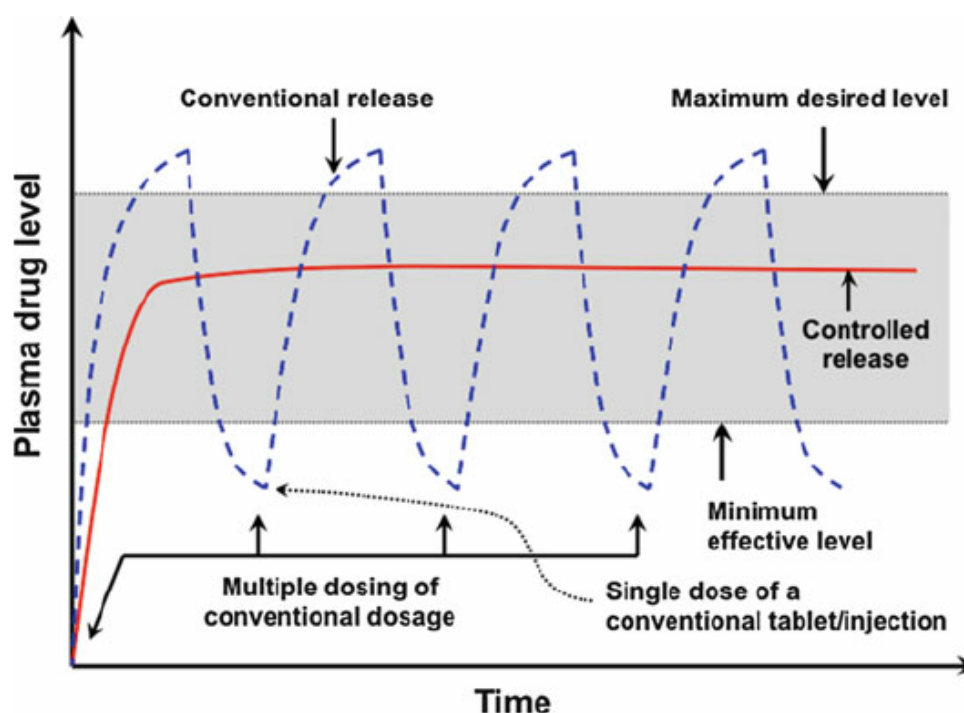


Figure 1.1 Controlled release systems compared to conventional administration. Reproduced with permission from [12].

Many different approaches have been used to develop controlled release platforms, including methods to control release from oral, inhaled, implantable, injectable, and transdermal dosage forms. The commonality among the controlled release dosage forms is their reliance on polymeric materials and polymer properties to achieve their desired release profile. Generally, controlled release systems rely on principles of diffusion, dissolution, and permeation to tune release of drugs from the formulation. The wide range and tunability of said properties in polymeric systems makes their use relatively ubiquitous for the engineering of DDS with controlled release characteristics. Although specific requirements will vary by route of administration, generally, controlled release DDS can be split into categories based on the mechanism controlling their release: dissolution-controlled, diffusion-controlled, osmotically controlled, complexation-controlled systems, and “smart” triggered systems.

In systems where dissolution controls the rate of drug release, the drug is typically directly encapsulated in a polymer with relatively low solubility or by applying polymer coatings with different thicknesses to drug granules to achieve various release rates. Similarly, systems can be designed to be controlled by diffusion through a polymer matrix or a membrane coating. In the case of the former, drug can be encapsulated like in dissolution-controlled systems. However, in the case of diffusion-controlled release, the release rate will be dictated by the rate at which the drug can propagate through the matrix material. Diffusion-controlled systems can also be achieved by coating drug granules with a membrane coating, creating a reservoir-like device. The drug granule serves as a reservoir of drug and the release of that drug is controlled by the rate at which the drug can diffuse through the membrane material. Thus, the material properties and coating thickness of the chosen polymer will control the release rate.

Osmotic pumps have also been used to modify release kinetics of drugs. In elementary osmotic pumps (EOP), first developed in the 1970s, a drug loaded core is coated with a semipermeable membrane with a laser-drilled orifice. Drug release is then controlled by the permeation of water across the membrane, driven by osmotic pressure, resulting in the

evacuation of the drug through the delivery orifice (Fig. 1.2 A). In EOP systems, drugs need to be highly water soluble because poorly water-soluble drugs cause insufficient osmotic pressure and incomplete release [13]. To address this drawback, the ALZA Corporation developed osmotic controlled-release oral delivery systems (OROS), which included the “Push-Pull” technology to facilitate improved and complete drug release for a wider range of drug molecules. OROS utilizes two layers in the osmotic core of the device, one containing the drug and a second hydrophilic polymeric layer (Fig. 1.2 B). This polymeric layer swells as water is transferred across the membrane, acting as a pump pushing the drug out of the drilled orifice (Fig. 1.2 C). OROS is capable of delivering drug at a zero order rate for up to 80 % of the drug load for 24 hours and has been successfully implemented in formulations to deliver verapamil HCl for the treatment of hypertension [14].

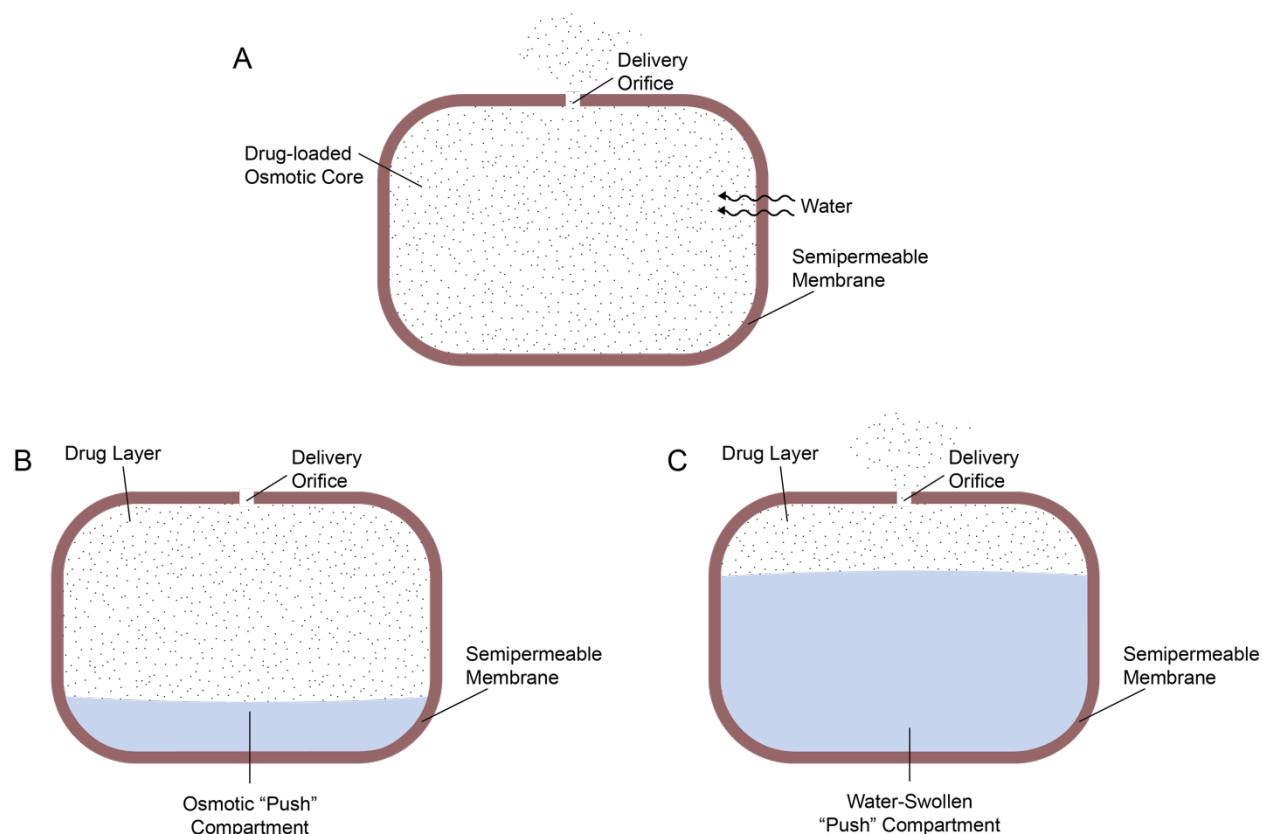


Figure 1.2 Osmotically-driven drug release devices. Elementary osmotic pump (A). “Push-Pull” osmotic pump system prior to swelling (B) and following the swelling of the “push” compartment (C).

EOP and OROS were developed for oral delivery of drugs, but implantable devices utilizing osmotic control have also been developed for implantable, longer-term delivery systems as well. For example, ALZA developed the ALZET pump for research use in laboratory animals to address difficulties in regular oral dosing of animals [15]. ALZA also developed the Duros implant, an osmotically driven drug delivery device that has been used in humans [16].

Another approach to achieve controlled release is through the complexation of drug to the polymer network directly, either through ionic or covalent bonds. One of the most widely implemented approaches for ionic complexation is the use of ionic exchange resins. Ion exchange resins, originally designed for analytical and protein chemistry purposes, are typically composed of water-insoluble polymers that have been functionalized to a high degree with ionizable groups. Resins can be formulated to be either anionic or cationic to be used to release either cationic or anionic drugs, respectively. Release of the active drug occurs upon ionic exchange with similarly charged ions in the release medium. This release can be controlled through modification of crosslink density of the resin, particulate size and surface area, ionic charge density of the resin and drug molecules, and ionic strength and pH of the release medium [12]. One example of successful implementation of ionic exchange resin for sustained drug release is in the smoking cessation aid, Nicorette[®] [17]. Nicorette is a sorbitol-based chewing gum loaded with a nicotine cation-exchange resin that slowly releases nicotine while chewing [18]. Another common approach used to complex a drug within a polymer network is through covalent bonds. Typically, drugs are linked to the polymer network through spacers that are labile to hydrolytic, enzymatic, stimuli-sensitive cleavage releasing the drug. With this approach, DDS can be tailored to release drug after a certain time based on hydrolysis kinetics or in a certain location based on specific location of a stimulus.

Similarly, DDS can be designed using “smart materials” so that drug is only released when triggered with an external stimulus like ultrasonic or magnetic irradiation. Further, smart DDS can be designed to serve as a closed loop system [19]. In this approach, the DDS would

act in a self-regulating manner in that the drug release would be adjusted according to the level of stimulation and constant feedback without the need for external intervention. This is to say that these systems would be able to modulate the flux of drug from the device as a function of physiological need, rather than a constant zero order release rate. For example, diabetes patients would not benefit from the constant elution of insulin from a device, but rather need insulin released in a fashion that is dependent on the glucose concentration. Release from self-regulated smart DDS can be controlled by several stimuli similar to the systems innate to healthy human systems. Examples include pH- [20], temperature- [21], inflammation-responsive systems [22]. Systems have also been designed to respond to antibody binding [23] and ion-exchange with chelators [24]

As important as the kinetics of the release and delivery are, it means nothing if the drug is not able to reach or remain at the target site of treatment. Thus, another key consideration in the design and engineering of DDS is the ability to localize the treatment to the site of action. By improving the localization of the therapeutic, drug efficacy will improve and resulting off target toxicities and complications will be reduced. Many approaches have been utilized to improve both the localization of the drug as well as its retention time at the site of action.

Localization in DDS delivered through traditional intravenous routes include the utilization of nanoparticle delivery systems. When utilized for the treatment of cancer, nanoparticles have been shown to preferentially localize in tumors through the enhanced permeability and retention effect. The specific size of nanoparticles allows for their permeation into the tumor through the leaky vasculature of the tumor environment. Once there, nanoparticles have increased retention due to the poor lymphatic drainage in tumor tissue, leading to a higher concentration of drug in the tumor compared to healthy tissue. Further, nanoparticles can be targeted to the target cells by decorating the outside of the DDS with moieties that will increase cell uptake in tumor cells compared to healthy cells. Smart materials,

as mentioned previously, can further improve the specificity and effectiveness of these therapies by only allowing for drug release following uptake by a specific cell type.

Drug localization can also be achieved through localized administration and engineering the material to increase site retention. Techniques and strategies include mucoadhesive materials for inhaled dosage forms [25], injectable dosage forms that undergo *in situ* gelation following administration [9], and direct implantation. One such example is the use of Gliadel Wafers for the delivery of carmustine following glioblastoma resection, which is often limited debulking rather than complete resection and thus requires adjuvant chemotherapy [26]. Though Gliadel Wafers only provide moderate improvement to an already dismal prognosis, and is not recommended for newly diagnosed patients. Another example of localized administration is drug eluting vascular stent, of which numerous approaches have been implemented for delivery of a range of drugs to prevent restenosis following angioplasty [27,28]. Drug eluting stents serve as one of the prime examples of success for a drug-device combination product.

While these methods are the most direct approach to localized treatment, these are not without hurdles. Drug delivery still depends on diffusion from the material and the ability to overcome biological barriers at the disease site. The factors affecting delivery to multiple tissue types and the mathematical models developed to describe the have been reviewed by Weiser and Saltzman [29].

1.2 3D printing and applications in drug delivery

Personalized medicine has long been a goal of the medical field and has recently started to become a reality. With the evolution and application of genomic screening and sequencing, many therapies benefit from the use of pharmacogenetics to identify and understand the populations that a drug will be most efficacious for [2]. As personalized medicine has advanced, so has the appeal of using 3D printing techniques to personalize dosage forms. Current mass production manufacturing processes limit pharmaceutical dosage forms to a finite number of

doses and dissolution profiles available. However, as we move towards the age of personalized healthcare, it will be advantageous to have more ability to tune the characteristics of a drug formulation to the current needs of an individual patient. 3D printing offers interesting approaches to achieve this.

3D printing, also known as rapid prototyping, solid freeform fabrication or additive manufacturing, was first reported in 1981 by Hideo Kodama [30,31]. 3D printing was originally developed to facilitate prototyping of designs in a relatively rapid manner and to avoid the resource intensive processes of molding or casting that require expensive tooling and long lead times. Industries such as aerospace, automotive, and other engineering fields quickly adopted 3D printing for prototyping. There are multiple technologies and methods that fall under the umbrella term 3D printing, but they all share the concept of converting a 3D computer aided design (CAD) file to a physical part. Typically, a 3D file is first generated using a CAD software (e.g. Solidworks, AutoCAD, Autodesk, Materialise). The file is subsequently converted to an STL (standard tessellation language or STereoLithography) file, which defines the surface of the CAD file as triangulated vertices stored as a text file. This file is then sliced along the Z-axis and fed to the 3D printer consecutively as 2D layers. The 3D printer, through a combination of software and hardware, then converts that information into a solid 3D part by fabricating each layer in succession (Fig. 1.3). There are various 3D printing techniques that use different methods of forming the solid object. The most widely used forms of 3D printing can be categorized generally according to the method by which they deposit material and form the solid layers, including extrusion, binding of a powder, and photopolymerization of a liquid resin.

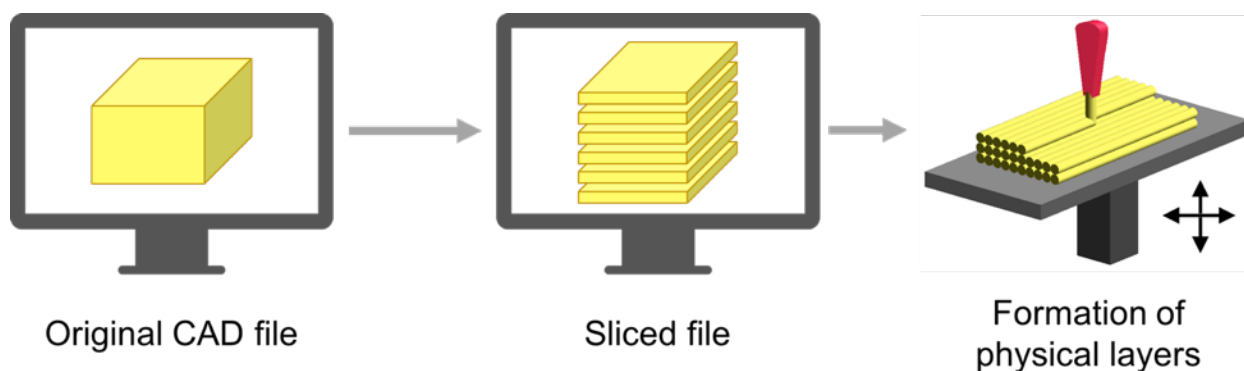


Figure 1.3 General process of 3D printing: Generation of CAD file and conversion to .STL, computational slicing, and formation of the 3D part layer-by-layer (in this case using, fused deposition modeling).

Unlike the mass production of traditional pharmaceutical manufacturing, 3D printing allows for production of a unique design and formulation with each print without additional tooling or lead time. The additional benefit of 3D printing being a small footprint, software-driven production platform could allow point of care manufacturing in pharmacies and hospitals. Further, small incremental changes can be made as the needs of the patient changes, as opposed to the limited selection of dose and formulations that traditional pills provide. With expected advancements in patient monitoring through implementation of wearable technology in the healthcare field, clinicians will be able to utilize constant feedback to understand a patient's current needs. Fine tuning of dose and delivery methods will potentially revolutionize the way that physicians treat patients (Fig. 1.4).

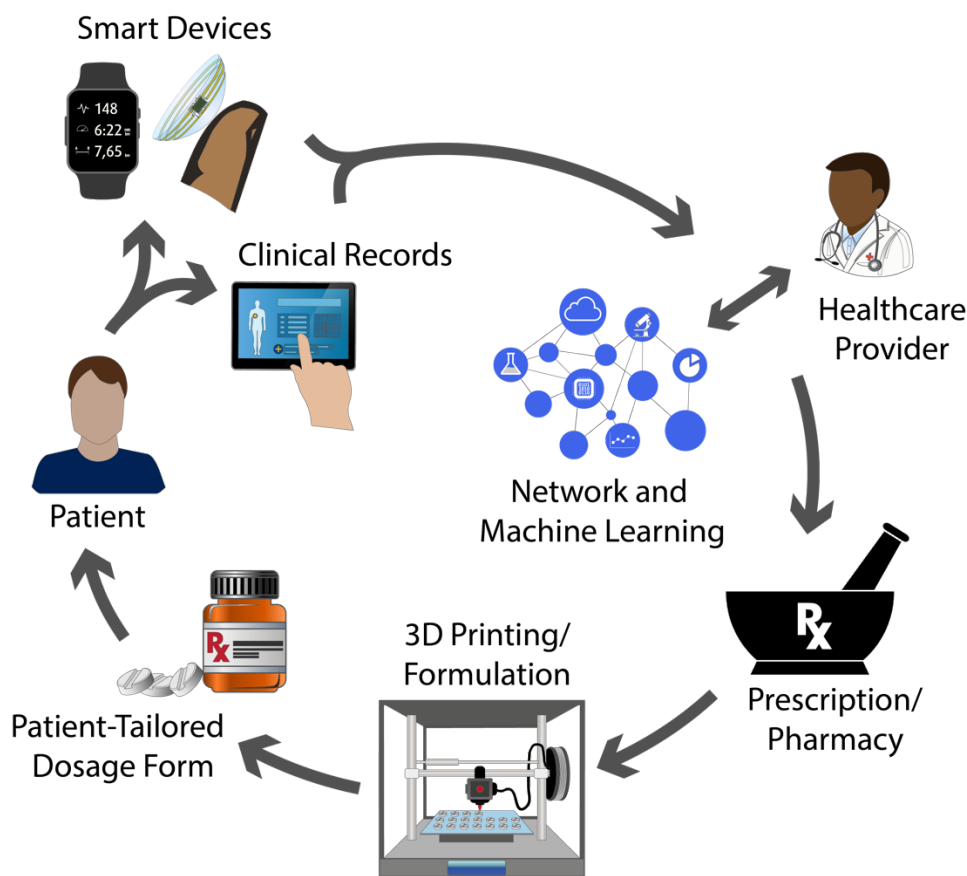


Figure 1.4 Potential system of patient-centered healthcare. Clinical data generated from wearable technology and physiological sensors in a patient's body can feed into a cloud-based network. Healthcare providers can then interface with machine learning to order a prescription based on the patient's current needs. The prescription can then be filled by remotely printing the individualized formulation at a location that is easily accessible to the patient. Figure modified from [32]

The benefits in personalization and production complexity that make 3D printing an attractive manufacturing method in many fields also apply to pharmaceuticals. The most straightforward improvement 3D printing of drug formulations will provide is the ability to print exact doses rather than depending on the large jumps in dosing required when using mass produced formulations. This is especially important when implementing drugs with a small therapeutic window, where small changes in dose can have significant impacts on the toxicity to the patient. Further personalization can be achieved by incorporating all of a patient's required medications into a single "poly-pill" (Fig. 1.5). For obvious reasons, it would not be possible to manufacture the vast number of drug combinations into single pills on a patient-by-patient bases

using traditional manufacturing methods. Printing of “Poly-pills” have been proposed as a way to improve patient compliance and reduce the burden of taking numerous pills, typically required in elderly patients.

Beyond personalization, the additional complexity afforded by 3D printing can also be harnessed to improve pharmaceutical dosage forms. For example, Aprecia’s anti-epileptic drug, Spritam, has accrued a great deal of attention for being the first 3D printed drug product approved by the FDA. Spritam does not use 3D printing to personalize the product to patients. In this case, Aprecia’s “ZipDose” technology relies on 3D printing to create a formulation that achieves rapid dissolution that would not be possible with traditional pill and tablet presses. 3D printing also offers the ability to control the spatial distribution of different materials in a part. This also provides a method to control release rates of a single or multiple drugs from a single pill and can potentially be customized to the needs of individual patients. Beyond dose and dissolution tailoring, 3D printing has also been proposed as a method to improve pediatric compliance by allowing a child to choose the shape of their medication (e.g. in the shape of a child’s favorite animal) [33].

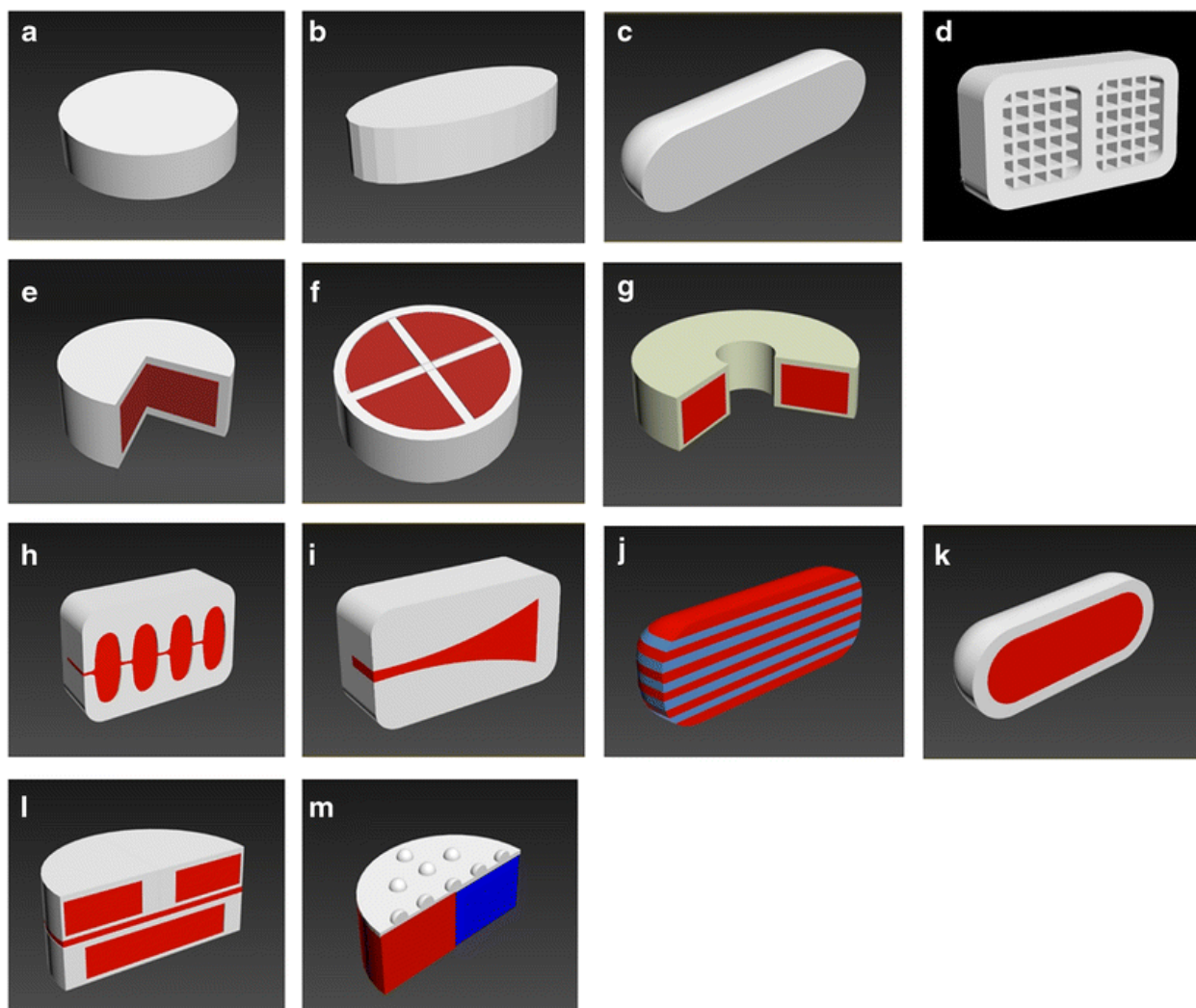


Figure 1.5 Examples of different designs used to manufacture 3D printed tablets. Simplistic design of disc has been initially employed (a) [34]. Oval shape (b) [35] and an easier to swallow caplet shape was possible to fabricate using FDM 3D printing (c) [36]. FDM 3D printing allowed fabrication of partially hollow tablets (d) [34]. PB 3D printing constructed shell-core structure by selective deposition of binder solution in the shell domains (e) [37] and by adding internal supporting walls, tablet's physical resistance can be improved (f) [38]. PB 3D printing was also utilized to build doughnut shape tablets with linear drug release (g) [39]. Pulsated drug release (h) and accelerating drug release (i) were achieved using casted gels in 3D printed containers [40]. Multi-layer (j) and core-shell (k) caplets allowed simultaneous and sub sequential release of two actives [41]. Polypills of 3 drugs (l) [42] or 5 different drugs (m) [43] with immediate and extended release patterns were EXT 3D printed. Figure and caption reused with permission from [32].

One of the most significant hurdles to surpass for 3D printing pharmaceutical devices and dosage forms will be the regulatory one. While the FDA is encouraging continued research into 3D printing of dosage forms, there are a lot of important questions that remain unanswered. The regulatory concerns and issues have been discussed in a number of reviews and opinions

and will not be discussed in detail here [32,44-46]. The focus of the following subsections will be to describe the benefits and limitations of each of the 3D printing methods that have been demonstrated as possible means to produce drug products. Previous publications have reviewed many of the advances in drug 3D printing [32,44,47-49]. Thus, the following subsections will not serve as a comprehensive survey of the literature, but rather present a selected representation to demonstrate the benefits and potential of each method.

1.2.1 Extrusion based 3D printing

1.2.1.1 Fused deposition modeling (FDM)

Fused deposition modeling (FDM) is one of the most well known versions of 3D printing. This is in large part thanks to the wide commercial availability and relatively low cost of FDM printers through manufacturers such as MakerBot. FDM operates through the patterning a two-dimensional layer onto a print bed by extruding a thermoplastic filament through a heated nozzle (Fig. 1.6 A). The nozzle traces the pattern of the 2D slice, depositing the semi-molten plastic, which can cool to form the solid layer. The print is then lowered and the next layer can be printed. This is repeated in a layer-by-layer manner until the entire model is fabricated.

FDM printers are easily accessible and meet much of the demand for early stage design and prototyping. However, FDM prints have limitations including slow build speeds, poor resolutions and accuracy, and a porous final product. FDM also typically results in parts that are anisotropic in the z-dimension. And while they can be isotropic in the x-y plane, this also is dependent on the infill and design parameters chosen [50].

The small footprint, benchtop platform and lack of post-processing requirements makes FDM an attractive method for the 3D printing of drug products in a pharmacy setting, such as compounding pharmacies. FDM can produce pharmaceutical products using techniques analogous to those currently used in pharmaceutical manufacturing, such as hot melt extrusion (HME), and injection molding. However, the reliance on thermal extrusion limits the materials

available to formulate the drug products to thermoplastics. Due to difficulties in producing usable filaments, most early studies using FDM were limited to impregnating the commercially available 3D printing filaments through solvent swelling. Researchers have since started to develop their own drug-loaded feedstocks based on pharmaceutical-grade materials previously used and accepted for large scale HME manufacturing. This has expanded the ability to modify the release through the employment of insoluble, readily soluble, and enteric materials [51,52]. As the range of stock materials expands, FDM printers equipped with multiple extrusion heads will be capable of fine tuning formulations to contain multiple release rates and drugs in a single formulation.

Due to the high temperatures often involved in the extrusion of the FDM process, there would be no concern for potential microbial contamination. However, the same heat will limit the drugs that are available to be formulated using FDM to those that are not heat labile [53]. Another concern for the fabrication of drug products outside of a plant setting is the variability between printers that require calibration of the print bed [49]. Improvements including self-calibrating machines and uniformity among printer features, such as nozzle diameter and print bed temperature could be among the many parameters that will be necessary to control prior to implementation of on-site printing.

While 3D printing has the potential to help improve patient compliance, acceptability of parts from 3D printers may prove problematic. Specifically, FDM results in a part with visible layers and texture. A different appearance in a medication can often make patients uncomfortable. Recent studies by Goyanes *et al.* looked at patient acceptability of 3D printed medicines [54]. In their single site, open label trial, different geometries of FDM-printed placebo pills were given to 50 adult participants to determine the effect the shape, size and color had on acceptability and ease of picking and swallowing. The results of this study showed that conventional shapes such as capsules and disks were observed to be easy to swallow and pick, highlighting the importance of familiarity in end-user acceptability. Additionally, the torus shape

also showed ease of picking and swallowing, as well as the highest overall acceptability scores, indicating possible improvements over traditional shapes. Further, they showed that certain shapes were perceived as larger or smaller depending on their geometry, which may be important information that can direct the design of pills that are required to contain a large amount of drug. Alternatively, this could provide strategies for making a pill that requires a small dose appear larger without wasting excipient and filler material. Further patient-focused human factors studies will be important as this technology nears implementation in the clinical setting.

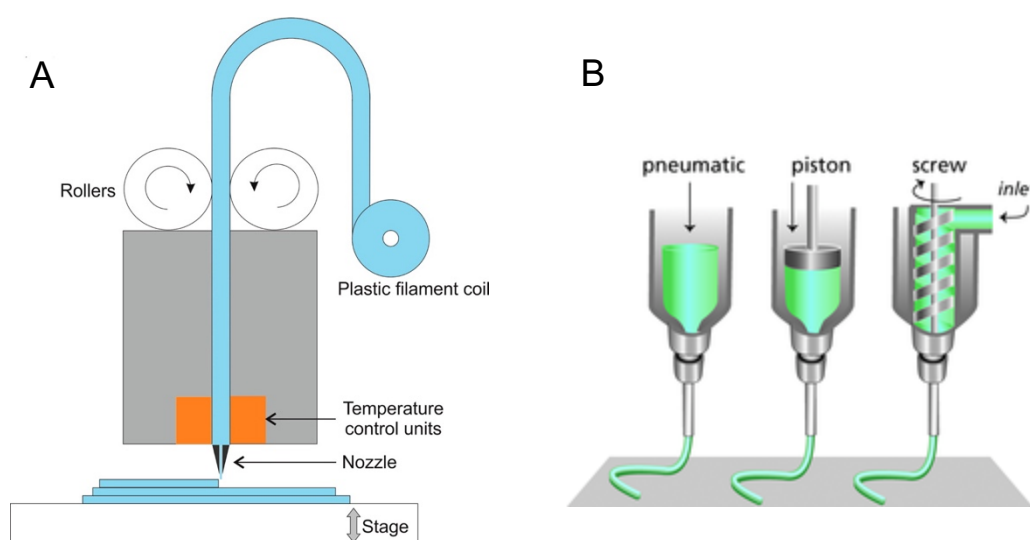


Figure 1.6 Extrusion based 3D printing methods A) Schematic drawing of FDM 3D printing. B) Schematic of various forms of semi-solid extrusion (EXT). Reused with permission from [55] and [56].

1.2.1.2 Semi-solid Extrusion (EXT)

Semi-solid extrusion (EXT) is like FDM, in that 3D objects are built by extrusion of material in 2D patterns in an iterative fashion. Rather than heating a filament for extrusion, EXT forms objects by extrusion of gels and pastes that are mixtures of polymers and solvent systems. Typically, material is deposited from syringes, in which the pressure can be modulated using pneumatic or mechanical means (Fig. 1.6 B). Following extrusion, the solvent is removed through evaporation, leaving a solid material. These systems have been used for a variety of applications from bioprinting with living cells [57] to the deposition of cheese for 3D printing of

food products [58]. The mechanical properties of the final material will depend on the combination and ratios of solids and solvents used. The resolution of EXT is limited by the nozzle from which the material is extruded, and is thus dependent on the bore size of the nozzle used.

The EXT process is delicate and requires minimal or no heating. For applications in printing drug formulations, this has obvious benefits regarding drug stability. While operating temperatures are low, many of these formulations rely on solvents, and incomplete solvent removal may lead to toxicities or unpredictable dissolution profiles. Further, drying time may be climate dependent, and thus will be an important issue to address prior to fabrication of drug products outside of a typical plant manufacturing setting.

With the ability to fabricate multi-material devices using benchtop instruments with multiple extrusion nozzles [42,43,59], EXT presents the possibility of producing “poly-pills” in a pharmacy using pre-formulated and regulated semi-solid inks. These potentially can be modified for the drugs they will contain as well as their release rates by manipulation of the excipients included in the inks. For implementation, however, the delicate nature of the resulting part and poor resolution requires improvement.

1.2.2 Powder-bed fusion

Another approach to 3D printing is through the spatially controlled binding of powder particles. This can be achieved through multiple methods but all have the commonality of the reliance on the joining of powder particles to form a solid 2D layer. Because of this, these methods share some benefits and some drawbacks. Specifically, powder-based 3D printing does not require the use of supports, which simplifies the planning and design process. The nature of powder binding also presents draw backs in regards to the final product being

characterized by a high level of porosity, which can affect the resulting mechanical properties [50].

1.2.2.1 Selective laser sintering (SLS)

Selective laser sintering (SLS), like FDM, forms solid 2D layers through a thermal phase transition using a laser to fuse a layer of plastic or metal through sintering or melting according to the digitally sliced file (Fig. 1.7 B). Once a layer of powder has been patterned, the piston of the fabrication stage lowers, and a powder delivery stage raises to allow a leveling roller to spread a new layer of material for the next layer. Characteristically long fabrication times and potential heterogeneity of the fusion process, caused by thermal carryover from hot spots of the previously sintered layer, limit the application of SLS.

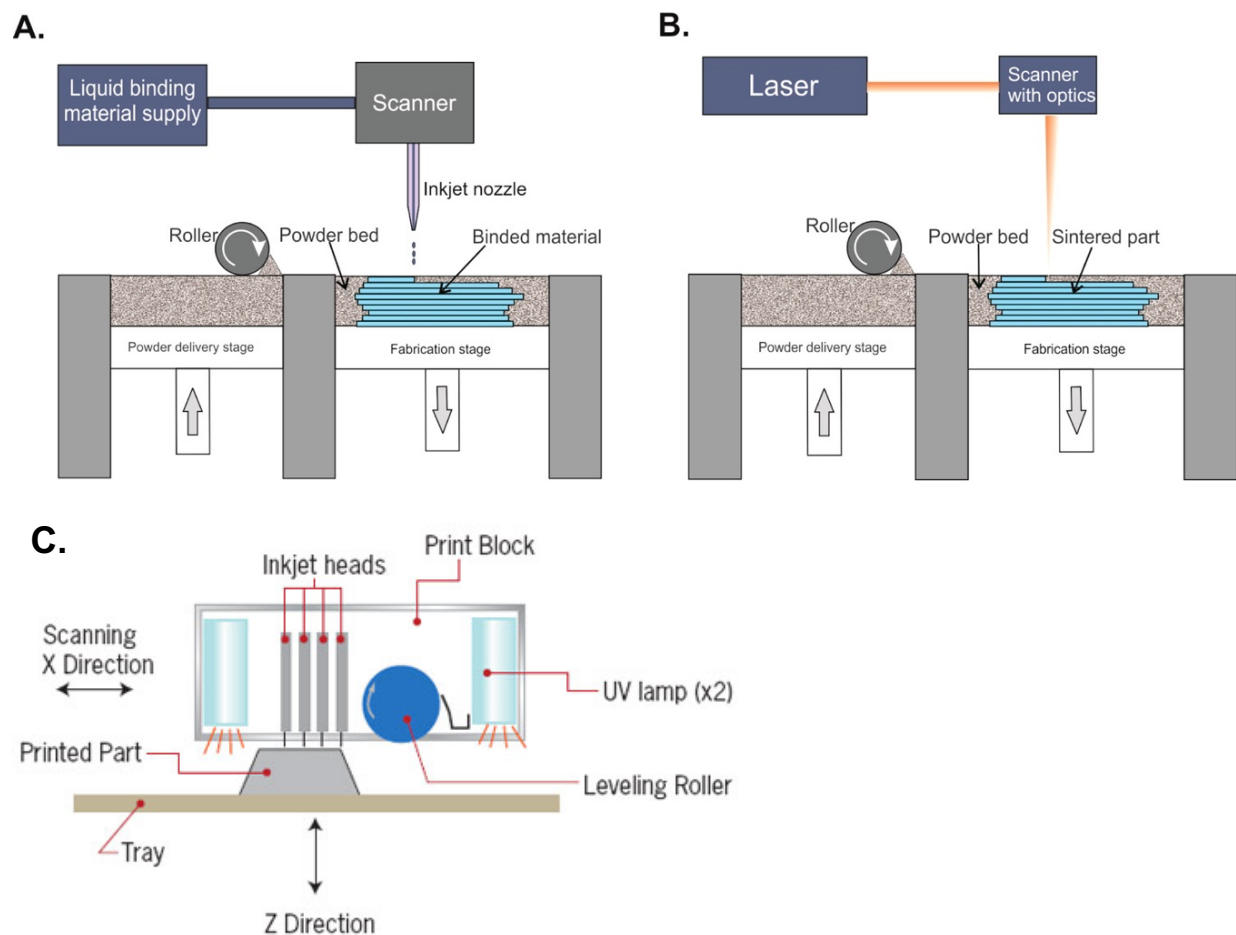


Figure 1.7 Powder-bed fusion 3D printing techniques. Schematic drawing of (A) inkjet printing and (B) selective laser sintering, and (C) polyjet 3D printing. Reused from [55] and [60].

1.2.2.2 Inkjet and polyjet binder deposition

Inkjet printing is similar to the SLS process in that it forms 2D layers through the binding of a powder layer that has been spread out using pistons and rollers (Fig. 1.7 A). In inkjet printing, however, powder particles are bound together using droplets of liquid binder on the powder layer in the x-y plane with respect to the design file.

Similarly, a technique known as polyjetting uses multiple jets to expel powder and binder simultaneously to form each layer (1.7 C). This technique relies on the photochemical crosslinking of the binder solution for solidification. By fixing UV lamps onto either side of the laterally scanning jet apparatus, the blend of binder and powder is solidified immediately of the binder solution by having UV lamps on either side of the jetting apparatus, so that when the jets pan back and forth the material is exposed immediately following deposition. Polyjetting is the technology behind many commercial 3D printers including those developed by Stratasys and HP.

The use of powders and binder solutions provides many advantages for 3D printing of pharmaceutical products. Most notably, binder solutions and powder formulations have been well established for use in the pharmaceutical field [49]. API can be incorporated both into the powder as well as into the binder liquid. If the drug is part of the binder solution, use of multiple binder jets can allow for spatial control over the location of the API within layers [61].

Powder-based 3D printing results in a high porosity part, which can be both a positive and a negative. The porosity of the part is advantageous when the application requires fast disintegration, which is easily achieved [38]. Alternatively, this porous product leads to challenges in tablet friability and stability. The porosity can also be controlled to provide for gradients in material properties and release rates [62].

Relative to other 3D printing platforms, powder-based printing subjects the API minimal physical stresses, being carried out at room temperature and does not require UV exposure. However, the process often requires the use of organic solvents to the binding solution. These

can potentially pose a toxicity issue as well as lead to extended processing times due to the required drying process. The process also can require large powder waste [32].

A process that is similar to poly-jetting that does not use powder is direct write inkjet printing. Inkjet printing uses similar instrumentation as 2D printers to dispense inks through thermal or piezo based jetting. This has been used to print personalized doses directly onto edible paper [63,64]. This has been used as a method to print drugs that require extremely accurate dosing, having shown standard deviation as low as 1.4 % when a 52 µg doses was printed of a model drug for printing [48,65]. Further, thermal inkjet printing has used to develop geometrically complex tablets beyond droplet printing in 2 dimensions. Kyobula *et al.* used thermal inkjet printing to fabricate honeycomb structures from an FDA approved material, beeswax [66]. Drug dissolution from these devices could be tuned by adjusting the size of the honeycomb cell and thus the surface area to volume ratio. Moving forward, this type of inkjet printing of 3D objects will be useful in reducing the amount of waste associated with powder-based processes, but will require further material development and optimization.

1.2.3 Stereolithography (SLA)

SLA was developed and commercialized by Chuck Hull and 3D Systems. In SLA, a liquid photopolymer resin is solidified upon exposure from a UV light source. Different SLA techniques can be broken into two categories depending on how the UV light is projected into the resin. In top down SLA, a stage is located just below the top of a liquid resin bath (Fig. 1.8 A). The resin on top of the stage is then exposed to UV light via direct laser writing, where a UV laser is rastered along the X- and Y-axes to cure the layer as dictated by the CAD file. At the completion of that layer, the platform lowers and a new layer of liquid resin is drawn on top using a blade. This process is then repeated until the 3D object is formed. In contrast to top down SLA, bottom up SLA uses a digital micromirror device to project the 2D slice in its entirety

through a transparent window beneath the resin (Fig. 1.8 B). This enables curing of the entire layer at once, eliminating the need for laser raster. In bottom up SLA, the stage will begin at the bottom of the reservoir a specific distance from the window, dictated by the slice thickness. UV light is then exposed in the pattern of the 2D layer, the resin between the build platform and window is completely cured. After exposure, the solidified part must be delaminated from the window, typically through a peeling mechanism or mechanical scraping. Following delamination, the build platform can move up to the height of the next slice, allowing uncured resin to fill the space between the part and window. This filling process can add significant time to the print for high viscosity resins, and stage pumping mechanisms are typically employed to accelerate this process. Once the resin renewal is complete, the following layer is exposed. This process is then iterated until the full 3D structure is formed.

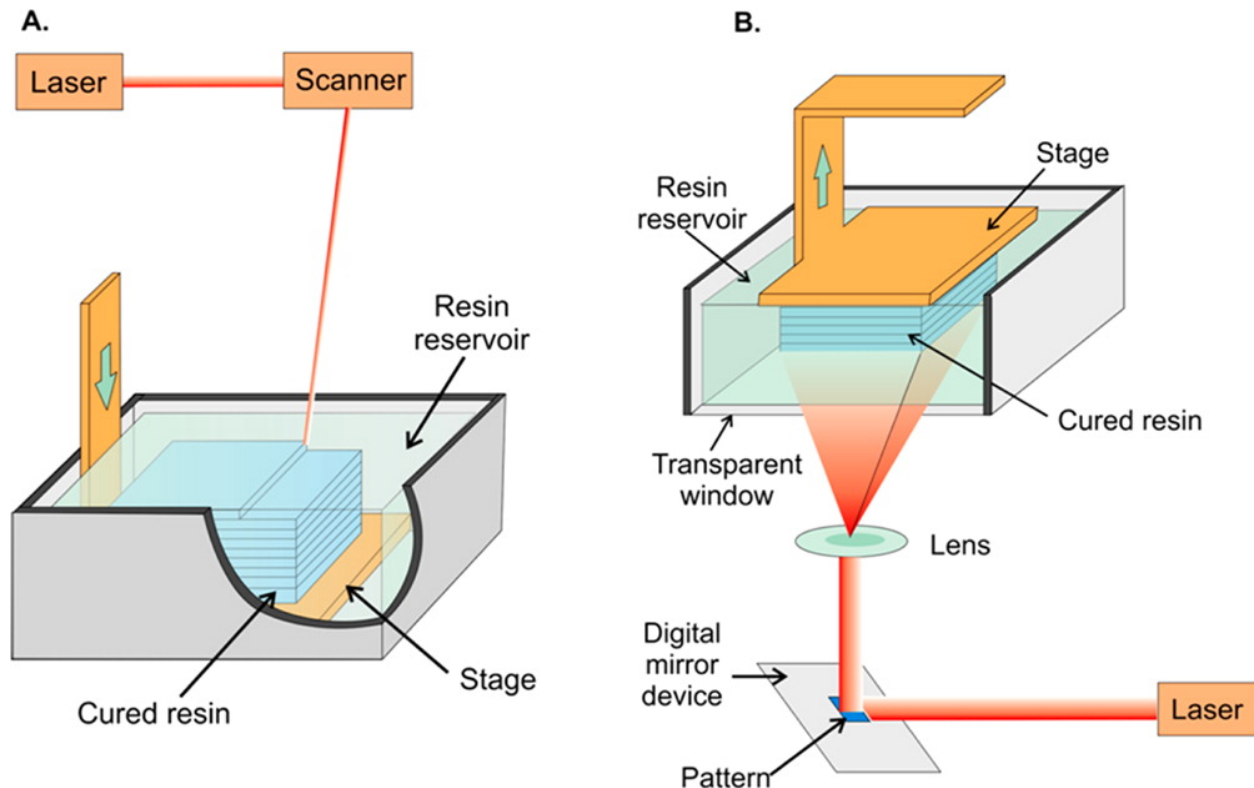


Figure 1.8 Diagrams of stereolithography 3D printers. (A) Top-down stereolithography apparatus. (B) Bottom-up DLP-based stereolithography apparatus. Figure reused with permission from [55]

SLA has many benefits to 3D printing for biomedical applications, most notably is the resolution. SLA has been shown to have a vertical resolution of 1 μm and horizontal resolution of 2 μm [67]. Further, two-photon polymerization (2PP) techniques are able to print with a nanometer resolution because polymerization only occurs at the focal point of two lasers [68]. This favorable resolution and accuracy of SLA has led to many applications towards tissue engineering and medical devices [69]. However, minimal research has been carried out in the form of drug products. This is likely due to the toxicity of many of the starting materials, such as methacrylates and acrylates, vinyl ethers, and epoxy-based resins.

Goyanes *et al.* used SLA to generate topical delivery devices based on the scanning of a nose [70]. Poly(ethylene glycol) (PEG) based devices containing salicylic acid for the treatment of acne were formulated with different ratios of PEG-diacrylate (PEGDA) to soluble PEG. Wang *et al.* used SLA to fabricate PEGDA-based formulations for oral delivery of model drugs, acetylsalicylic acid and acetaminophen [53]. The model drugs showed sustained release over a 10-hour period, independent of the pH differences in a simulated environment of the GI tract. Further, this is an example of the use of an alternative 3D printing formulation for a drug that is not stable (acetylsalicylic acid) to a different 3D printing method (FDM). Another study by Vehse *et al.* also used Acetylsalicylic acid incorporated in microstereolithography-produced scaffolds fabricated with PEGDA [71]. In this study, a decrease in compression strength was observed with the addition of 1 %, 2 %, and 3 % by weight and a burst release effect was observed. The difference between the Wang and Vehse study in addition to the complex kinetics of radical photopolymerization highlights the importance of characterizing all parameters that affect the drug release all the parameters prior to implementation of drug products fabricated using this technology outside of a well-controlled manufacturing setting.

1.3 Continuous Liquid Interface Production (CLIP)

A novel 3D printing approach was recently introduced called Continuous Liquid Interface Production (CLIP), which enables continuous fabrication of solid parts from a liquid resin bath [72]. Of the presented approaches, bottom up SLA is the most comparable, in that CLIP also forms the solid part from a photopolymerizable resin by projecting UV light from a DLP chip through a transparent window. However, due to permeability of the window to oxygen, a well-known inhibitor of photopolymerization [73], no polymerization occurs at the interface of the window and the liquid resin (Fig. 1.9 A). This liquid interface negates the steps in between fabrication of layers necessitated by the complete cure to the window in bottom-up SLA (Sect. 1.2.3). As a result, CLIP affords the ability to print in a continuous fashion, pulling the part out of the liquid resin bath while the DLP projects the slices in the form of a UV movie. The lack of steps between layer formation eliminates the tradeoff between print time and resolution in traditional layer-by-layer 3D printing approaches (Fig. 1.9 C).

Beyond benefits to print speed, the lack of a delamination step allows parts to be fabricated in a delicate manner using CLIP. This widens the scope of materials that can be applied to CLIP, allowing for fabrication using materials with low green strengths, such as hydrogels or elastomers, as well as delicate geometries that may not be possible using fabrication methods that apply more mechanical stress during the process [74,75]. Further, CLIP has been shown to not be affected by the anisotropy that limits many other additive manufacturing methods to prototyping techniques [76].

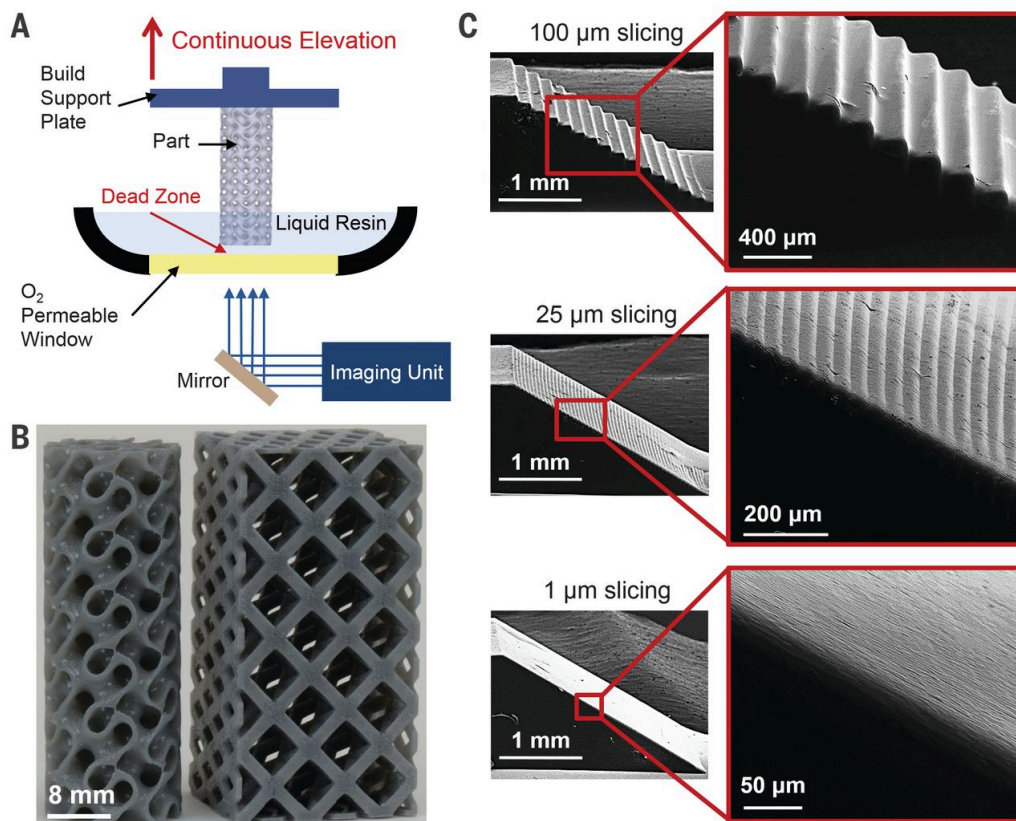


Figure 1.9 CLIP enables fast print speeds and layerless part construction. (A) Schematic of CLIP printer where the part (gyroid) is produced continuously by simultaneously elevating the build support plate while changing the 2D cross-sectional UV images from the imaging unit. The oxygen-permeable window creates a dead zone (persistent liquid interface) between the elevating part and the window. (B) Resulting parts via CLIP, a gyroid (left) and an argyle (right), were elevated at print speeds of 500 mm/hour (movies S1 and S2). (C) Ramp test patterns produced at the same print speed regardless of 3D model slicing thickness (100 μm , 25 μm , and 1 μm). Reproduced with permission from [72].

CLIP has been employed in the development of medical devices through use in prototyping multiple materials and design factors for the fabrication and optimization of microneedles [77]. Additionally, a custom-built microCLIP instrument was developed by van Lith *et. al.* to be used for printing high resolution stents with radical scavenging abilities [78]. This dissertation seeks to present the application of CLIP towards the development and fabrication of biomedical and drug-eluting devices.

1.4 3D printing biomaterials

1.4.1 3D printing in a clinical setting

Over the relatively short 30-year lifetime of 3D printing and rapid prototyping, a great deal of progress has been made towards clinical application of this technology. By nature, the personalized design and fabrication that 3D printing and additive manufacturing provide make traditional regulatory approaches difficult. However, as of 2015, 85 medical devices that are produced by 3D printing have been approved by the FDA. In 2016 the FDA released a technical guidance for the engineering and manufacturing of medical devices with additive manufacturing [79]. One area that 3D printing has been used to improve how clinicians are treating patients is in the manufacture and application of custom orthopedic implants. Traditionally, to perform bone grafts and reconstruction operations, surgeons were required to use drills and tools to modify the implants to fit the patient. With the use of 3D printing approaches like the implant developed by Oxford Performance Materials for skull reconstruction, which was approved by the FDA in 2013, implants can be precisely manufactured according to the patient's anatomy [80].

The implementation of 3D printing in the clinic has been driven and aided by the evolution of medical imaging technology, which has become more accurate and less invasive. High definition 3D imaging data can be captured through techniques such as multi-detector computed tomography (MDCT) and magnetic resonance imaging (MRI), though MDCT is more commonly used thanks to its less complex processing requirements [81]. The use of medical imaging has been used to guide the design of personalized medical implants. For example, a team of surgeons and biomedical engineers at the University of Michigan used image-based, 3D printed tracheal stents to treat infants with tracheobronchomalacia [82,83]. Other common uses of medical imaging include the production of bespoke devices to improve radiotherapy techniques [84]; the design of patient-specific surgical instruments and guides; and printing 3D

models of patients' anatomy to aid in surgical planning, patient education, and medical training [85-87].

1.4.2 Tissue engineering

Outside of the clinic, a great deal of research has focused on uses of 3D printing techniques for biomedical applications. Many of the recent developments towards biocompatible materials suitable for various 3D printing techniques have been thoroughly reviewed by others [55,57,69,88-94]. Some highlights will be presented here, with an emphasis on photopolymerization applications, due to the relevance to CLIP.

Tissue engineering has been a major focus for the application of 3D printing, with the goal to mimic the organization and complex nature of living tissues. Better recapitulation of functional tissue improves the ability to create more accurate research models for studying pharmacokinetic and drug metabolism *in vitro* [95], *in vitro* disease models [96,97], and potentially lead to development of fully functional tissue equivalents for regenerative medicine [98]. Often referred to as bioprinting or biofabrication, the use of 3D printing to selectively pattern a matrix of cells and/or synthetic or natural polymers provides many advantages over traditional methods of tissue engineering. For example, bioprinting allows for production of cell-laden scaffolds with control over the 3D organization of cells and matrix material rather than a random distribution of cell type and support material [56].. This is important for the development of tissue mimics that have a non-uniform distribution of mechanical environments or cell types. Typical methods for bioprinting employ semisolid extrusion techniques discussed in Sect. 1.2.1.2, as well as more advanced techniques that have been reviews more extensively elsewhere [56,99]. A main area of focus in the biofabrication field is the development of appropriate materials, both naturally-derived and synthetic to serve as the matrix for the cells, also known as bioink. Natural polymers used for biofabrication include hyaluronic acid (HA), collagen, alginate, gelatin, and fibrin, and provide chemical signals to guide cell growth and

mimic the innate extra cellular matrix. However, these natural polymers also present draw backs such as batch-to-batch variability in levels of signal. An alternative approach has been to use synthetic polymers such as poly(ethylene-glycol) (PEG), poly(lactic acid) (PLA), poly(lactic-co-glycolic acid) (PLGA) and poly(caprolactone) (PCL). These synthetic bioinks have been used as biologically inert materials, but do not provide the much-needed biological signals required for cell viability.

Regardless of the methodology, a major hurdle for the 3D printing of organ systems is the need for vascularization. Recent successes in incorporating vascular constructs into biofabricated parts have been achieved [100], and further strategies to encourage vascularization of scaffolds are being pursued. Alternatively, others have attempted to design artificial organs, like ears, that are cartilage-based and do not depend on vascularization. Organs like an ear do, however, require complex electrochemical systems to perform the requisite function. McAlpine *et al* have used bioprinting in addition to a silver nanoparticle-loaded conductive polymer to manufacture a bionic ear that was capable of processing radio frequency signals [101]. McAlpine's group has also developed the ability to 3D print tactile sensors directly onto freeform structures, like human fingers, which may have future impacts in the fields of artificial skin, wearable devices, and smart prosthetics [102].

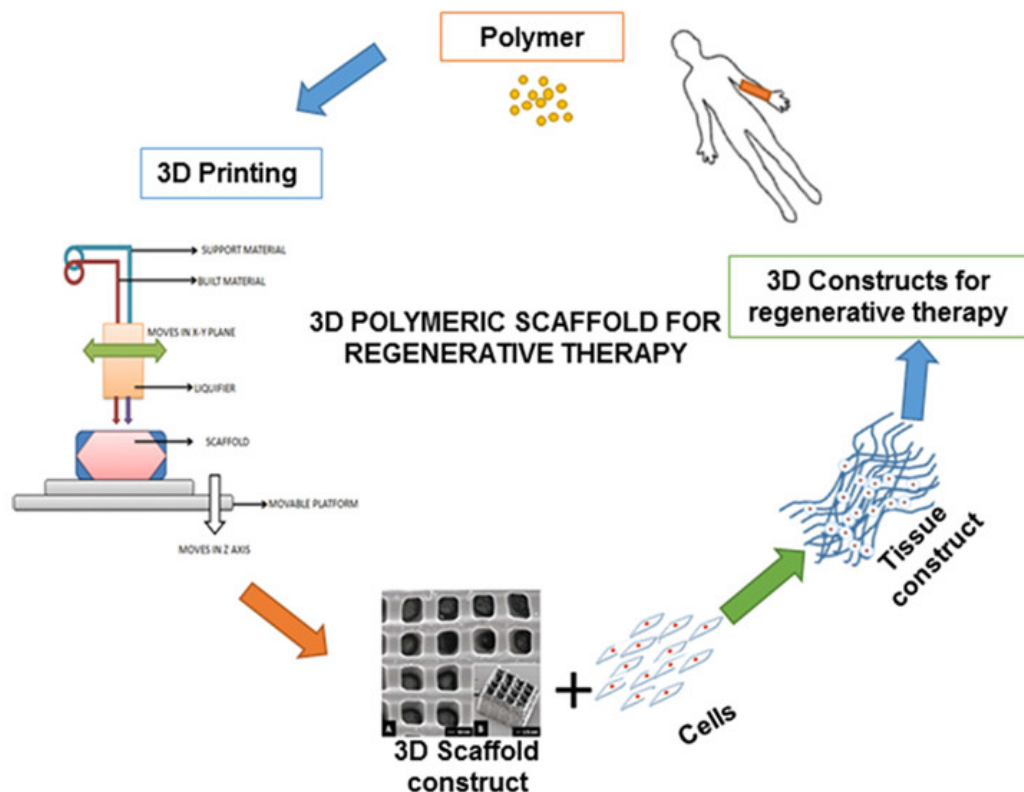


Figure 1.10 Typical process for fabrication of a tissue engineering scaffold to be seeded with cells following complete fabrication. Reproduced with permission from [103]

Due to the cytotoxic nature of the starting materials and intermediates associated with photopolymer and stereolithography resins, these technologies have been predominantly used for the fabrication of biocompatible scaffolds to be seeded with cells following complete post-processing (Fig. 1.10). There are examples of cell-containing resins being used during stereolithography [104,105]; however, most are only a few layers thick, which allows for short print times prior to introduction to cell medium and appropriate conditions for cell viability [69]. Stereolithography and other 3D printing techniques that do not allow cell viability during the fabrication process are often used in applications that require robust and specific mechanical properties. Precise control of mechanical properties, which may not be achievable within the limited printing materials that allow cell viability, is an important factor in directing the differentiation of mesenchymal stem cells [106]. Future directions for biofabrication and 3D

printing tissue engineering applications will include enhancement in the ability to induce vascularization in scaffolds printed from both acellular and cell-loaded bioinks. For acellular print materials, an understanding of the factors that are most important and creative ways to incorporate and control the release of biochemical growth signals will be important steps forward for development of tissue engineering scaffolds.

REFERENCES

- [1] L. Xu, T. Anchordoquy, CLINICAL TRIALS AND TRANSLATIONAL MEDICINE COMMENTARY: Drug Delivery Trends in Clinical Trials and Translational Medicine: Challenges and Opportunities in the Delivery of Nucleic Acid-Based Therapeutics, *J. Pharm. Sci.* 100 (2011) 38–52. doi:10.1002/jps.22243.
- [2] M.A. Hamburg, F.S. Collins, The path to personalized medicine, *N. Engl. J. Med.* 363 (2010) 301–304. doi:10.1056/NEJMp1006304.
- [3] A.L. Nelson, E. Dhimolea, J.M. Reichert, Development trends for human monoclonal antibody therapeutics, *Nat Rev Drug Discov.* 9 (2010) 1–9. doi:10.1038/nrd3229.
- [4] I. Khanna, Drug discovery in pharmaceutical industry: productivity challenges and trends, *Drug Discovery Today.* 17 (2012) 1088–1102. doi:10.1016/j.drudis.2012.05.007.
- [5] M. Rask-Andersen, M.S. Almén, H.B. Schiöth, Trends in the exploitation of novel drug targets, *Nat Rev Drug Discov.* 10 (2011) 1–13. doi:10.1038/nrd3478.
- [6] K.E. Uhrich, S.M. Cannizzaro, R.S. Langer, K.M. Shakesheff, Polymeric Systems for Controlled Drug Release, *Chem. Rev.* 99 (1999) 3181–3198. doi:10.1021/cr940351u.
- [7] Y. Zhang, H.F. Chan, K.W. Leong, Advanced materials and processing for drug delivery: The past and the future, *Advanced Drug Delivery Reviews.* 65 (2013) 104–120. doi:10.1016/j.addr.2012.10.003.
- [8] R.A. Jain, The manufacturing techniques of various drug loaded biodegradable poly(lactide-co-glycolide) (PLGA) devices, *Biomaterials.* 21 (2000) 2475–2490.
- [9] D. Chitkara, A. Shikanov, N. Kumar, A.J. Domb, Biodegradable injectable in situ depot-forming drug delivery systems, *Macromol Biosci.* 6 (2006) 977–990. doi:10.1002/mabi.200600129.
- [10] R.A. Petros, J.M. DeSimone, Strategies in the design of nanoparticles for therapeutic applications, *Nat Rev Drug Discov.* 9 (2010) 1–14. doi:10.1038/nrd2591.
- [11] D.A. Edwards, J. Hanes, G. Caponetti, J. Hrkach, A. Ben-Jebria, M.L. Eskew, et al., Large porous particles for pulmonary drug delivery, *Science.* 276 (1997) 1868–1871.
- [12] C.T. Huynh, D.S. Lee, Controlled Release, in: S. Kobayashi, K. Müllen (Eds.), *Encyclopedia of Polymeric Nanomaterials*, Springer Berlin Heidelberg, Berlin, Heidelberg, 2014: pp. 1–12. doi:10.1007/978-3-642-36199-9_314-1.
- [13] F. Theeuwes, Evolution and design of “rate controlled” osmotic forms, *Curr Med Res Opin.* 8 Suppl 2 (1983) 20–27. doi:10.1185/03007998309109820.
- [14] S. Venkatraman, N. Davar, A. Chester, An overview of controlled release systems, in: *Handbook of Pharmaceutical Controlled Release Technology*, CRC Press, 2000.

- [15] F. Theeuwes, S.I. Yum, Principles of the design and operation of generic osmotic pumps for the delivery of semisolid or liquid drug formulations, 4 (1976) 343–353. doi:10.1007/BF02584524.pdf.
- [16] C.L. Stevenson, F. Theeuwes, J.C. Wright, Osmotic implantable delivery systems, Handbook of ..., 2000.
- [17] Fazal-Ur-Rehman, S.N. Khan, Therapeutic Applications of Ion Exchange Resins, in: Ion Exchange Technology II, Springer Netherlands, Dordrecht, 2012: pp. 149–168. doi:10.1007/978-94-007-4026-6_7.
- [18] F. Ove, L. Stefan, L. Claes, L. Ab, Chewable smoking substitute composition, (1975).
- [19] J. Kost, S.A. Lapidot, Smart polymers for controlled drug delivery, in: Handbook of Pharmaceutical Controlled Release Technology, CRC Press, 2000.
- [20] P. Gupta, K. Vermani, S. Garg, Hydrogels: from controlled release to pH-responsive drug delivery, Drug Discovery Today. 7 (2002) 569–579.
- [21] D. Schmaljohann, Thermo-and pH-responsive polymers in drug delivery, Advanced Drug Delivery Reviews. 58 (2006) 1655–1670.
- [22] Y. Nobuhiko, O. Teruo, S. Yasuhisa, Inflammation responsive degradation of crosslinked hyaluronic acid gels, Journal of Controlled Release. 22 (1992) 105–116.
- [23] C.G. Pitt, Z.W. Gu, R.W. Hendren, J. Thompson, M.C. Wani, Triggered drug delivery systems, Journal of Controlled Release. 2 (1985) 363–374. doi:http://dx.doi.org/10.1016/0168-3659(85)90058-6.
- [24] C.G. Pitt, Y.T. Bao, Z.W. Gu, M.C. Wani, Z.H. Zhu, The self-regulated delivery of chelating agents, Pulsed and Self-Regulated Drug Delivery. (1990) 117.
- [25] H. Takeuchi, H. Yamamoto, Y. Kawashima, Mucoadhesive nanoparticulate systems for peptide drug delivery, Advanced Drug Delivery Reviews. 47 (2001) 39–54. doi:http://dx.doi.org/10.1016/S0169-409X(00)00120-4.
- [26] J.B. Wolinsky, Y.L. Colson, M.W. Grinstaff, Local drug delivery strategies for cancer treatment: Gels, nanoparticles, polymeric films, rods, and wafers, Journal of Controlled Release. 159 (2012) 14–26. doi:10.1016/j.jconrel.2011.11.031.
- [27] K. Vedantham, S. Chaterji, J. Kitsongsermthom, K. Park, Future outlook for drug eluting stents, in: Drug-Device Combination Products, Elsevier, 2010: pp. 117–153. doi:10.1533/9781845697488.2.118.
- [28] Y. Huang, H.C.A. Ng, X.W. Ng, V. Subbu, Drug-eluting biostable and erodible stents, Journal of Controlled Release. 193 (2014) 188–201. doi:10.1016/j.jconrel.2014.05.011.
- [29] J.R. Weiser, W.M. Saltzman, Controlled release for local delivery of drugs: barriers and models, Journal of Controlled Release. 190 (2014) 664–673. doi:10.1016/j.jconrel.2014.04.048.

- [30] H. Kodama, A scheme for three-dimensional display by automatic fabrication of three-dimensional model, *J. leice*. 64 (1981) 1981–1984.
- [31] H. Kodama, Automatic method for fabricating a three-dimensional plastic model with photo-hardening polymer, *Rev. Sci. Instrum*. 52 (1981) 1770–1773.
- [32] M.A. Alhnan, T.C. Okwuosa, M. Sadia, K.-W. Wan, W. Ahmed, B. Arafat, Emergence of 3D Printed Dosage Forms: Opportunities and Challenges, *Pharm Res*. 33 (2016) 1817–1832.
- [33] K. Sanderson, 3D printing: the future of manufacturing medicine? *The Pharmaceutical Journal*. 294 (2015). doi:10.1211/PJ.2015.20068625.
- [34] A. Goyanes, A.B.M. Buanz, A.W. Basit, S. Gaisford, Fused-filament 3D printing (3DP) for fabrication of tablets, *International Journal of Pharmaceutics*. 476 (2014) 88–92. doi:10.1016/j.ijpharm.2014.09.044.
- [35] J. Skowrya, K. Pietrzak, M.A. Alhnan, Fabrication of extended-release patient-tailored prednisolone tablets via fused deposition modelling (FDM) 3D printing, *Eur J Pharm Sci*. 68 (2015) 11–17. doi:10.1016/j.ejps.2014.11.009.
- [36] K. Pietrzak, A. Isreb, M.A. Alhnan, A flexible-dose dispenser for immediate and extended release 3D printed tablets, *Eur J Pharm Biopharm*. 96 (2015) 380–387. doi:10.1016/j.ejpb.2015.07.027.
- [37] W.E. Katstra, R.D. Palazzolo, C.W. Rowe, B. Giritlioglu, P. Teung, M.J. Cima, Oral dosage forms fabricated by Three Dimensional Printing™, *Journal of Controlled Release*. 66 (2000) 1–9. doi:10.1016/S0168-3659(99)00225-4.
- [38] D.G. Yu, X.-X. Shen, C. Branford-White, L.-M. Zhu, K. White, X.L. Yang, Novel oral fast-disintegrating drug delivery devices with predefined inner structure fabricated by Three-Dimensional Printing, *Journal of Pharmacy and Pharmacology*. 61 (2010) 323–329. doi:10.1211/jpp.61.03.0006.
- [39] D.G. Yu, C. Branford-White, Z.-H. Ma, L.-M. Zhu, X.-Y. Li, X.L. Yang, Novel drug delivery devices for providing linear release profiles fabricated by 3DP, *International Journal of Pharmaceutics*. 370 (2009) 160–166. doi:10.1016/j.ijpharm.2008.12.008.
- [40] Y. Sun, S. Soh, Printing Tablets with Fully Customizable Release Profiles for Personalized Medicine, *Adv. Mater*. 27 (2015) 7847–7853. doi:10.1002/adma.201504122.
- [41] A. Goyanes, J. Wang, A. Buanz, R. Martínez-Pacheco, R. Telford, S. Gaisford, et al., 3D Printing of Medicines: Engineering Novel Oral Devices with Unique Design and Drug Release Characteristics, *Mol. Pharmaceutics*. 12 (2015) 4077–4084. doi:10.1021/acs.molpharmaceut.5b00510.
- [42] S.A. Khaled, J.C. Burley, M.R. Alexander, J. Yang, C.J. Roberts, 3D printing of tablets containing multiple drugs with defined release profiles, *International Journal of Pharmaceutics*. 494 (2015) 643–650. doi:10.1016/j.ijpharm.2015.07.067.

- [43] S.A. Khaled, J.C. Burley, M.R. Alexander, J. Yang, C.J. Roberts, 3D printing of five-in-one dose combination polypill with defined immediate and sustained release profiles, *Journal of Controlled Release*. 217 (2015) 308–314. doi:10.1016/j.jconrel.2015.09.028.
- [44] G. Jonathan, A. Karim, 3D printing in pharmaceuticals: A new tool for designing customized drug delivery systems, *International Journal of Pharmaceutics*. 499 (2016) 376–394. doi:10.1016/j.ijpharm.2015.12.071.
- [45] J.W. Lee, D.-W. Cho, 3D Printing technology over a drug delivery for tissue engineering, *Curr. Pharm. Des.* 21 (2015) 1606–1617.
- [46] L. Zema, A. Melocchi, A. Maroni, A. Gazzaniga, 3D printing of medicinal products and the challenge of personalized therapy, *J. Pharm. Sci.* 106 (2017) 1697–1705. doi:10.1016/j.xphs.2017.03.021.
- [47] I.D. Urgan, L. Chiu, A. Pierce, Three-dimensional drug printing: A structured review, *Journal of the American Pharmacists Association*. 53 (2013) 136–144. doi:10.1331/JAPhA.2013.12217.
- [48] J. Norman, R.D. Madurawe, C.M.V. Moore, M.A. Khan, A. Khairuzzaman, A new chapter in pharmaceutical manufacturing: 3D-printed drug products, *Advanced Drug Delivery Reviews*. 108 (2017) 39–50. doi:10.1016/j.addr.2016.03.001.
- [49] L. Zema, A. Melocchi, A. Maroni, A. Gazzaniga, Three-Dimensional Printing of Medicinal Products and the Challenge of Personalized Therapy, *J. Pharm. Sci.* 106 (2017) 1697–1705. doi:10.1016/j.xphs.2017.03.021.
- [50] I. Gibson, D.W. Rosen, B. Stucker, *Additive Manufacturing Technologies*, Springer Science & Business Media, Boston, MA, 2009. doi:10.1007/978-1-4419-1120-9.
- [51] A. Goyanes, F. Fina, A. Martorana, D. Sedough, S. Gaisford, A.W. Basit, Development of modified release 3D printed tablets (printlets) with pharmaceutical excipients using additive manufacturing, *International Journal of Pharmaceutics*. 527 (2017) 21–30. doi:10.1016/j.ijpharm.2017.05.021.
- [52] A. Melocchi, F. Parietti, A. Maroni, A. Foppoli, A. Gazzaniga, L. Zema, Hot-melt extruded filaments based on pharmaceutical grade polymers for 3D printing by fused deposition modeling, *International Journal of Pharmaceutics*. 509 (2016) 255–263. doi:10.1016/j.ijpharm.2016.05.036.
- [53] J. Wang, A. Goyanes, S. Gaisford, A.W. Basit, Stereolithographic (SLA) 3D Printing of Oral Modified-Release Dosage Forms, *International Journal of Pharmaceutics*. 503 (2016) 1–21. doi:10.1016/j.ijpharm.2016.03.016.
- [54] A. Goyanes, M. Scarpa, M. Kamlow, S. Gaisford, A.W. Basit, M. Orlu, Patient acceptability of 3D printed medicines, *International Journal of Pharmaceutics*. 530 (2017) 71–78. doi:10.1016/j.ijpharm.2017.07.064.

- [55] B.C. Gross, J.L. Erkal, S.Y. Lockwood, C. Chen, D.M. Spence, Evaluation of 3D Printing and Its Potential Impact on Biotechnology and the Chemical Sciences, *Anal. Chem.* 86 (2014) 3240–3253. doi:10.1021/ac403397r.
- [56] J. Malda, J. Visser, F.P. Melchels, T. Jüngst, W.E. Hennink, W.J.A. Dhert, et al., 25th Anniversary Article: Engineering Hydrogels for Biofabrication, *Adv. Mater.* 25 (2013) 5011–5028. doi:10.1002/adma.201302042.
- [57] M. Hospodiuk, K.K. Moncal, M. Dey, I.T. Ozbolat, Extrusion-Based Biofabrication in Tissue Engineering and Regenerative Medicine, *3D Print Biofabrication*. (2016). doi:10.1007/978-3-319-40498-1_10-1.
- [58] J. Sun, Z. Peng, W. Zhou, J.Y.H. Fuh, G.S. Hong, A. Chiu, A Review on 3D Printing for Customized Food Fabrication, 43rd North American Manufacturing Research Conference, NAMRC 43, 8-12 June 2015, UNC Charlotte, North Carolina, United States. 1 IS - (2015) 308–319.
- [59] S.A. Khaled, J.C. Burley, M.R. Alexander, C.J. Roberts, Desktop 3D printing of controlled release pharmaceutical bilayer tablets, *International Journal of Pharmaceutics*. 461 (2014) 105–111. doi:10.1016/j.ijpharm.2013.11.021.
- [60] L. Gordon, Rapid prototyping for orthopedics, medicaldesign.com/prototyping/rapid-Prototyping-Orthopedics.
- [61] W. Wu, Q. Zheng, X. Guo, J. Sun, Y. Liu, A programmed release multi-drug implant fabricated by three-dimensional printing technology for bone tuberculosis therapy, *Biomed Mater.* 4 (2009) 065005. doi:10.1088/1748-6041/4/6/065005.
- [62] D.G. Yu, X.L. Yang, W.D. Huang, J. Liu, Y.G. Wang, H. Xu, Tablets With Material Gradients Fabricated by Three-Dimensional Printing, *J. Pharm. Sci.* 96 (n.d.) 2446–2456.
- [63] R. Daly, T.S. Harrington, G.D. Martin, I.M. Hutchings, Inkjet printing for pharmaceuticals – A review of research and manufacturing, *International Journal of Pharmaceutics*. 494 (2015) 554–567. doi:10.1016/j.ijpharm.2015.03.017.
- [64] N. Scoutaris, M.R. Alexander, P.R. Gellert, C.J. Roberts, Inkjet printing as a novel medicine formulation technique, *Journal of Controlled Release*. 156 (2011) 179–185. doi:10.1016/j.jconrel.2011.07.033.
- [65] D. Rajada, N. Genina, D. Fors, E. Wisaeus, J. Peltonen, J. Rantanen, et al., A Step Toward Development of Printable Dosage Forms for Poorly Soluble Drugs, *J. Pharm. Sci.* 102 (2013) 3694–3704. doi:10.1002/jps.23678.
- [66] M. Kyobula, A. Adedeji, M.R. Alexander, E. Saleh, R. Wildman, I. Ashcroft, et al., 3D inkjet printing of tablets exploiting bespoke complex geometries for controlled and tuneable drug release, *Journal of Controlled Release*. 261 (2017) 207–215. doi:10.1016/j.jconrel.2017.06.025.

- [67] J.-W. Choi, R. Wicker, S.-H. Lee, K.-H. Choi, C.-S. Ha, I. Chung, Fabrication of 3D biocompatible/biodegradable micro-scaffolds using dynamic mask projection microstereolithography, *Journal of Materials Processing Technology*. 209 (2009) 5494–5503. doi:10.1016/j.jmatprotec.2009.05.004.
- [68] R.F. Pereira, P.J. Bártolo, 3D Photo-Fabrication for Tissue Engineering and Drug Delivery, *Engineering*. 1 (2015) 090–112. doi:10.15302/J-ENG-2015015.
- [69] F.P.W. Melchels, J. Feijen, D.W. Grijpma, A review on stereolithography and its applications in biomedical engineering, *Biomaterials*. 31 (2010) 6121–6130. doi:10.1016/j.biomaterials.2010.04.050.
- [70] A. Goyanes, U. Det-Amornrat, J. Wang, A.W. Basit, S. Gaisford, 3D scanning and 3D printing as innovative technologies for fabricating personalized topical drug delivery systems, *Journal of Controlled Release*. 234 (2016) 41–48. doi:10.1016/j.jconrel.2016.05.034.
- [71] M. Vehse, S. Petersen, K. Sternberg, K.-P. Schmitz, H. Seitz, Drug Delivery From Poly(ethylene glycol) Diacrylate Scaffolds Produced by DLC Based Micro-Stereolithography, *Macromol. Symp.* 346 (2014) 43–47. doi:10.1002/masy.201400060.
- [72] J.R. Tumbleston, D. Shirvanyants, N. Ermoshkin, R. Januszewicz, A.R. Johnson, D. Kelly, et al., Continuous liquid interface production of 3D objects, *Science*. 347 (2015) 1349–1352. doi:10.1126/science.aaa2397.
- [73] T.Y. Lee, C.A. Guymon, E.S. Jönsson, C.E. Hoyle, The effect of monomer structure on oxygen inhibition of (meth)acrylates photopolymerization, *Polymer*. 45 (2004) 6155–6162. doi:10.1016/j.polymer.2004.06.060.
- [74] J.P. Rolland, Functional Materials for 3D Manufacturing using Carbon's CLIP Technology, *Journal of Photopolymer Science and Technology*. (2016).
- [75] X. Gu, J.P. Rolland, Cyclic ester dual cure resins for additive manufacturing, *US 20170174827 A1*, 2016.
- [76] R. Januszewicz, J.R. Tumbleston, A.L. Quintanilla, S.J. Mecham, J.M. DeSimone, Layerless fabrication with continuous liquid interface production, *Proc Natl Acad Sci USA*. 113 (2016) 11703–11708. doi:10.1073/pnas.1605271113.
- [77] A.R. Johnson, C.L. Caudill, J.R. Tumbleston, C.J. Bloomquist, K.A. Moga, A. Ermoshkin, et al., Single-Step Fabrication of Computationally Designed Microneedles by Continuous Liquid Interface Production, *PLoS ONE*. 11 (2016) e0162518. doi:10.1371/journal.pone.0162518.
- [78] R. van Lith, E. Baker, H. Ware, J. Yang, A.C. Farsheed, C. Sun, et al., 3D-Printing Strong High-Resolution Antioxidant Bioresorbable Vascular Stents, *Adv. Mater. Technol.* 1 (2016) 1600138–7. doi:10.1002/admt.201600138.
- [79] Food and Drug Administration, Technical Considerations for Additive Manufactured Devices Draft Guidance for Industry and Food and Drug Administration Staff, 2016.

- [80] C.L. Ventola, Medical Applications for 3D Printing: Current and Projected Uses, *P T.* 39 (2014) 704–711.
- [81] F. Rengier, A. Mehndiratta, H. von Tengg-Kobligh, C.M. Zechmann, R. Unterhinninghofen, H.U. Kauczor, et al., 3D printing based on imaging data: review of medical applications, *Int J CARS.* 5 (2010) 335–341. doi:10.1007/s11548-010-0476-x.
- [82] R.J. Morrison, S.J. Hollister, M.F. Niedner, M.G. Mahani, A.H. Park, D.K. Mehta, et al., Mitigation of tracheobronchomalacia with 3D-printed personalized medical devices in pediatric patients, *Sci Transl Med.* 7 (2015) 285ra64–285ra64. doi:10.1126/scitranslmed.3010825.
- [83] S.J. Hollister, C.L. Flanagan, R.J. Morrison, J.J. Patel, M.B. Wheeler, S.P. Edwards, et al., Integrating Image-Based Design and 3D Biomaterial Printing To Create Patient Specific Devices within a Design Control Framework for Clinical Translation, *ACS Biomater. Sci. Eng.* 2 (2016) 1827–1836. doi:10.1021/acsbiomaterials.6b00332.
- [84] S.G. Ju, M.K. Kim, C.-S. Hong, J.S. Kim, Y. Han, D.H. Choi, et al., New technique for developing a proton range compensator with use of a 3-dimensional printer, *Int. J. Radiat. Oncol. Biol. Phys.* 88 (2014) 453–458. doi:10.1016/j.ijrobp.2013.10.024.
- [85] M.P. Chae, W.M. Rozen, P.G. McMenamin, M.W. Findlay, R.T. Spychal, D.J. Hunter-Smith, Emerging Applications of Bedside 3D Printing in Plastic Surgery, *Frontiers in Surgery.* 2 (2015) 25. doi:10.3389/fsurg.2015.00025.
- [86] A. Hornung, M. Kumpf, W. Baden, I. Tsiflikas, M. Hofbeck, L. Sieverding, Realistic 3D-Printed Tracheobronchial Tree Model from a 1-Year-Old Girl for Pediatric Bronchoscopy Training, *Respiration.* (2017) 1–3. doi:10.1159/000459631.
- [87] P.A. Anderson, Clinical Applications of 3D Printing, *Spine.* 42 (2017) S30–S31. doi:10.1097/BRS.0000000000002039.
- [88] H.N. Chia, B.M. Wu, Recent advances in 3D printing of biomaterials, *J Biol Eng.* 9 (2015) 4. doi:10.1186/s13036-015-0001-4.
- [89] F. Cruz, Fabrication of HA/PLLA Composite scaffolds for bone tissue engineering using additive manufacturing technologies, *Biopolymers.* (2012).
- [90] J.-F. Xing, M.-L. Zheng, X.-M. Duan, Two-photon polymerization microfabrication of hydrogels: an advanced 3D printing technology for tissue engineering and drug delivery, *Chem Soc Rev.* 44 (2015) 5031–5039. doi:10.1039/C5CS00278H.
- [91] J. Torgersen, X.-H. Qin, Z. Li, A. Ovsianikov, R. Liska, J. Stampfl, Hydrogels for Two-Photon Polymerization: A Toolbox for Mimicking the Extracellular Matrix, *Adv. Funct. Mater.* 23 (2013) 4542–4554. doi:10.1002/adfm.201203880.
- [92] M.N. Collins, C. Birkinshaw, Hyaluronic acid based scaffolds for tissue engineering—A review, *Carbohydrate Polymers.* 92 (2013) 1262–1279. doi:10.1016/j.carbpol.2012.10.028.

- [93] T.J. Hinton, A. Lee, A.W. Feinberg, 3D bioprinting from the micrometer to millimeter length scales: Size does matter, *Current Opinion in Biomedical Engineering*. 1 (2017) 31–37. doi:10.1016/j.cobme.2017.02.004.
- [94] A. Youssef, S.J. Hollister, P.D. Dalton, Additive manufacturing of polymer melts for implantable medical devices and scaffolds, *Biofabrication*. 9 (2017) 012002–30. doi:10.1088/1758-5090/aa5766.
- [95] R. Chang, K. Emami, H. Wu, W. Sun, Biofabrication of a three-dimensional liver micro-organ as an in vitro drug metabolism model, *Biofabrication*. (2010). doi:10.1088/1758-5090/8/1/015002.
- [96] Y. Zhao, R. Yao, L. Ouyang, H. Ding, T. Zhang, K. Zhang, et al., Three-dimensional printing of Hela cells for cervical tumor model in vitro, *Biofabrication*. 6 (2014) 035001. doi:10.1088/1758-5082/6/3/035001.
- [97] C. Wang, Z. Tang, Y. Zhao, R. Yao, L. Li, W. Sun, Three-dimensional in vitro cancer models: a short review, *Biofabrication*. 6 (2014) 022001. doi:10.1088/1758-5082/6/2/022001.
- [98] F. Marga, K. Jakab, C. Khatiwala, B. Shepherd, S. Dorfman, B. Hubbard, et al., Toward engineering functional organ modules by additive manufacturing, *Biofabrication*. 4 (2012) 022001. doi:10.1088/1758-5082/4/2/022001.
- [99] S.V. Murphy, A. Atala, 3D bioprinting of tissues and organs, *Nature Biotechnology*. 32 (2014) 773–785. doi:10.1038/nbt.2958.
- [100] D.B. Kolesky, R.L. Truby, A.S. Gladman, T.A. Busbee, K.A. Homan, J.A. Lewis, 3D Bioprinting of Vascularized, Heterogeneous Cell-Laden Tissue Constructs, *Adv. Mater.* 26 (2014) 3124–3130. doi:10.1002/adma.201305506.
- [101] M.S. Mannoer, Z. Jiang, T. James, Y.L. Kong, K.A. Malatesta, W.O. Soboyejo, et al., 3D Printed Bionic Ears, *Nano Lett.* 13 (2013) 2634–2639. doi:10.1021/nl4007744.
- [102] S.-Z. Guo, K. Qiu, F. Meng, S.H. Park, M.C. McAlpine, 3D Printed Stretchable Tactile Sensors, *Adv. Mater.* 29 (2017) 1701218–8. doi:10.1002/adma.201701218.
- [103] G. Ratheesh, J.R. Venugopal, A. Chinappan, H. Ezhilarasu, A. Sadiq, S. Ramakrishna, 3D Fabrication of Polymeric Scaffolds for Regenerative Therapy, *ACS Biomater. Sci. Eng.* 3 (2017) 1175–1194. doi:10.1021/acsbiomaterials.6b00370.
- [104] Y. Lu, G. Mapili, G. Suhali, S. Chen, K. Roy, A digital micro-mirror device-based system for the microfabrication of complex, spatially patterned tissue engineering scaffolds, *J Biomed Mater Res A*. 77 (2006) 396–405. doi:10.1002/jbm.a.30601.
- [105] H. Lin, D. Zhang, P.G. Alexander, G. Yang, J. Tan, A.W.-M. Cheng, et al., Application of visible light-based projection stereolithography for live cell-scaffold fabrication with designed architecture, *Biomaterials*. 34 (2013) 331–339. doi:10.1016/j.biomaterials.2012.09.048.

- [106] P.S. Mathieu, E.G. Loba, Cytoskeletal and Focal Adhesion Influences on Mesenchymal Stem Cell Shape, Mechanical Properties, and Differentiation Down Osteogenic, Adipogenic, and Chondrogenic Pathways, *Tissue Engineering Part B: Reviews*. 18 (2012) 436–444. doi:10.1089/ten.teb.2012.0014.

CHAPTER 2: SYNTHESIS AND CHARACTERIZATION OF PHOTOPOLYMERS FOR BIOMEDICAL APPLICATIONS

Chapter goals

This following chapter introduces the basic concepts of radical photopolymerizations. The current use of photopolymers for biomedical applications with an emphasis on additive manufacturing platforms is presented. Experimental work demonstrating the synthesis and characterization of two photopolymerizable polyesters based on polycaprolactone oligomers is presented. Additionally, preliminary results using CLIP to print with the biologically derived hyaluronic acid are discussed.

2.1 Introduction

2.1.1 Radical photopolymerization

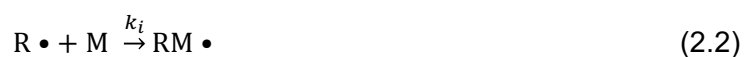
As discussed in Chapter 1, CLIP relies on photopolymerization to form the solid part during the fabrication process. Specifically, CLIP uses UV light (385 nm) wavelength to initiate a radical chain polymerization. Typically radical photopolymer systems are based on monomers containing unsaturated groups, such as acrylate, methacrylate, vinyl ethers and fumarate functional groups. Radical polymerization occurs in three steps: initiation, propagation, and termination [1]

Initiation is a series of two reactions. The first reaction is the generation of free radicals, which is achieved through initiator systems (though examples have been demonstrated without the need for separate initiators [2,3]). The most commonly used initiator type is a single component system, or type I photoinitiator. Alternatively, type II initiators generate free radicals through a bimolecular mechanism such as co-initiating or photosensitizing systems. Type I

systems will be discussed here, as the initiators used in this work and relevant literature utilize type I photoinitiators. In a type I initiating systems, a single UV-absorbing molecule can be excited by a specific wavelength of light and undergo homolytic cleavage, forming two free radicals (not necessarily identical or equally reactive, however) (Eqn. 2.1).

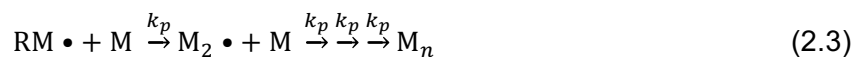


Where k_d is the rate constant for the dissociation of the initiator. The second reaction of the initiation step is the addition of the radical to the monomer molecule (Eqn. 2.2).



Where M represents a monomer molecule, k_i is the rate constant of the initiation step, $RM \bullet$ represents the polymer chain initiating species.

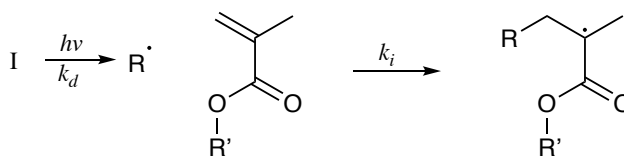
The propagation step of radical polymerization proceeds through successive addition of monomer molecules to the chain initiating species (Eqn. 2.3).



Where k_p is the propagation rate constant. The propagation of the chain occurs very rapidly with rate constants in the range of 10^2 - 10^4 L mol⁻¹ s⁻¹ for most monomers [1].

The initiation and propagation for a methacrylate functional group is illustrated in figure 2.1. Upon irradiation with UV light, the radical of the initiator attacks the methacrylate and forms a bond by combining with one electron of the unsaturated bond. The other electron returns to the tertiary carbon, which can now continue to react with additional monomers to facilitate propagation.

Initiation:



Propagation

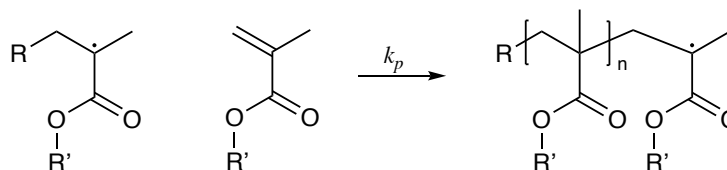
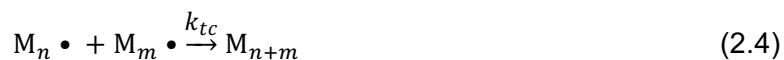


Figure 2.1 Initiation and propagation steps in free radical photopolymerization of a monomethacrylate monomer.

Finally, the termination step can be described generally as the formation of a dead polymer, which occurs potentially through two different mechanisms: chain transfer (to a monomer, solvent, initiator, or additive) and bimolecular termination. Bimolecular termination is the loss of two reactive centers and can proceed through re-combination (Eqn. 2.4) or disproportionation, in which a proton is transferred from one reactive species to another (Eqn. 2.5).



Where k_{tc} and k_{td} represent the termination rate constant through a re-combination and disproportionation mechanism, respectively. These two rate constants can be combined to a constant k_t to describe all forms of termination regardless of mechanism. The termination step for a methacrylate polymerization can be seen in figure 2.2.

Termination

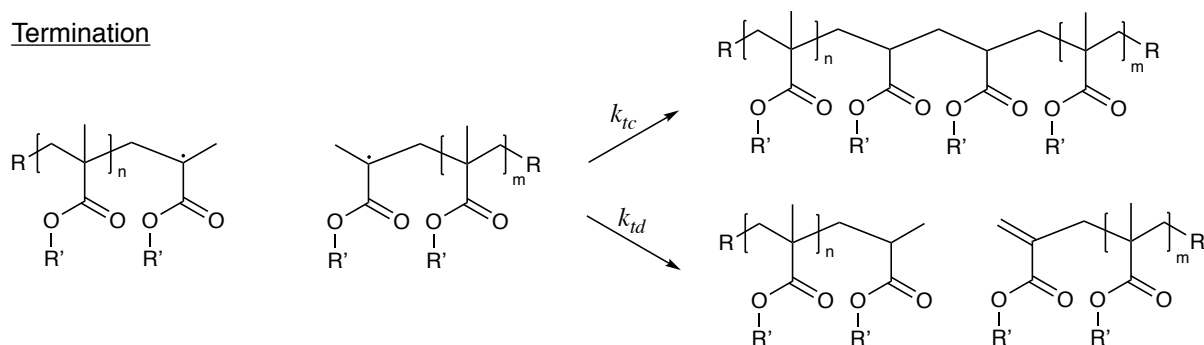


Figure 2.2 Bimolecular termination of propagating methacrylate radicals occurs through combination (top path) or disproportionation (bottom path).

Rate equations for each step can be combined to give an equation for the polymerization rate, R_p (Eqn 2.6) [1].

$$R_p = k_p[M] \left(\frac{R_i}{2k_t} \right)^{\frac{1}{2}} \quad (2.6)$$

Where R_i is the rate of initiation. This equation can be expressed as that shown in equation 2.7 when being applied to photochemical initiation.

$$R_p = k_p[M] \left(\frac{\phi I_a}{k_t} \right)^{\frac{1}{2}} \quad (2.7)$$

Where I_a represents the absorbed light intensity, and is a function of the extinction coefficient, initiator concentration, and layer thickness. It is important to note that equations 2.6 and 2.7 are derived assuming steady state and bimolecular termination. However, radical termination is a diffusion controlled process, and thus the observed k_t will depend on the properties of the polymer network. Because the network properties will change as the polymerization proceeds, k_t is actually regarded as a termination rate coefficient rather than a rate constant and is a function of the kinetic chain length [4]. The most notable effect of diffusion controlled termination is the gel effect or autoacceleration period of polymerization, in which the increased chain lengths of propagating polymers decreases diffusivity and thus termination, leading to an accelerating rate of polymerization. Further, when the monomers have more than one unsaturated group (e.g. another methacrylate group at the end of R' in Fig. 2.1), many other factors have to be

considered including intramolecular cyclization and microgelation, which have been discussed at length elsewhere [4,5].

2.1.2 Current state of biomaterials based on photopolymers

Photopolymers and methacrylate/acrylate-based materials have many uses beyond additive manufacturing techniques. In clinical practice, these chemistries are commonly found in bone cements [6,7], dental resins [8,9], and surgical adhesives [10]. Further, clinical and preclinical research has been focused on using photochemically-initiated polymerization and crosslinking of hydrogels based on synthetic and natural materials for the development of specialized scaffolds for tissue engineering and drug delivery applications [11-14]. Common materials for synthetic hydrogels include methacrylate-functionalized poly(ethylene glycol) (PEG) crosslinkers blended with monomeric materials such as 2-hydroxyethyl methacrylate (HEMA) and 2-(dimethylamino)ethyl methacrylate (DMAEMA). Synthetic hydrogels have been demonstrated as a tunable approach to the release of macromolecules by controlling the concentration and length of crosslinker [15]. Natural hydrogels including gelatin [16,17], hyaluronic acid [18,19], collagen and other extra cellular matrix components [14] have been used for applications including improved cell culture approaches to modeling disease, tissue regeneration, and drug delivery materials for in situ gelation.

Due to the nature of the materials, initiators, and UV light used there are associated cytotoxicities with radical photopolymer systems. Recent work to mitigate these toxicities include the use of novel initiating systems such as using free-radical generators naturally found in biological systems. Nguyen *et. al.* used riboflavin, or vitamin B12, as a free radical generator in a two photon polymerization to generate scaffolds from PEG-diacrylate [20]. Others have focused on using photosynthesizers to allow the use of the less damaging blue light instead of UV light for the initiation of the polymerization [21-23].

Many of these materials and approaches have been applied to additive manufacturing and 3D printing platforms. Certain criteria must be met for a material to be suitable for use with photopolymer-based 3D printing techniques such as CLIP and SLA. The resin, which is the mixtures of the photopolymer starting materials including monomers and initiators, is typically required to be a liquid, fast reacting, and result in a solid polymer that has suitable structural integrity to withstand forces of the printing process. Specific requirements will vary depending on application, including desired mechanical properties, biocompatibility, and biodegradability.

Common materials used for biomedical applications in SLA and CLIP include PEG-based oligomers, small molecule monomers, poly(propylene fumarate) (PPF), and composite materials [24]. PEG-based materials that are functionalized to contain more than one reactive group (each unsaturated functional group is $f=2$) are capable of being a stand-alone monomer material if the molecular weight is less than $\sim 800 \text{ g mol}^{-1}$, as these are amorphous and liquid at room temperature with reasonably low viscosity [25]. PPF is commonly used as a starting material for development of biodegradable networks [26,27]. However, it requires the addition of a non-degradable reactive diluent to achieve appropriate viscosities.

Development of biodegradable photoreactive materials based on functionalized polyesters has been an area of interest over the past decade. Most of these are based on polyesters such as poly(d,l-lactic acid) (PLA) [28], Poly(caprolactone) (PCL) [29], poly(trimethylene carbonate) (PTMC) [30], which have been well characterized and studied for use in biomedical applications [31]. A common approach to synthesize these is through ring opening polymerization, using a poly-ol as an initiator, to generate a polyester with multiple terminal hydroxyl groups. The hydroxyl groups can subsequently be functionalized with methacryloyl chloride, methacrylic anhydrides, or glycidyl methacrylate.

This chapter will outline a few of the approaches to synthesize and characterize photopolymerizable biomaterials including a low molecular weight methacrylate-functionalized PCL. Characteristics of PCL, including the slow degradation kinetics and ability to dissolve

hydrophobic drugs, make it an attractive candidate for use in developing medical devices for prolonged drug delivery towards the applications discussed throughout this dissertation. Additionally, the oligomers of PCL are liquid at room temperature, affording simple resin formulation and handling with no heating required. Additionally, proof-of-concept studies demonstrating the use of CLIP to fabricate structured hydrogels using a naturally derived material, hyaluronic acid, are presented.

2.2 Materials and Methods

2.2.1 Materials

Anhydrous dichloromethane (DCM), triethylamine (TEA), magnesium sulfate, sodium chloride (NaCl), dimethylformamide (DMF) were purchased from Fisher Scientific. Glycidyl methacrylate (GMA), sodium bicarbonate, diphenyl(2,4,6-trimethylbenzoyl)phosphine oxide (TPO), methacryloyl chloride (Fluka, $\geq 97\%$) were purchased from Sigma Aldrich. Lithium phenyl(2,4,6-trimethyl benzoyl) phosphinate (LAP) was purchased from TCI America. Hyaluronic acids (5K, 10K, 40K, 500K, 1M) were purchased from Lifecore Biomedical.

Polycaprolactone-triol ($M_n 900 \text{ g mol}^{-1}$) and polycaprolactone diol ($M_n 530 \text{ g mol}^{-1}$) were purchased from Sigma-Aldrich and vacuum dried overnight prior to use. All other materials were used as received and store as recommended by distributor.

2.2.2 Synthesis of methacrylate-functionalized polycaprolactone

2.2.2.1 Synthesis of PCL₁₁₀₀-TMA

A representative procedure for the synthesis of polycaprolactone-trimethacrylate $M_n = 1100 \text{ g mol}^{-1}$ (PCL₁₁₀₀-TMA) was as follows. Poly- ϵ -caprolactone (PCL) triol (50g, 0.0556 mol, 0.1668 mol –OH) was charged to a 500 mL round bottom flask and stored under reduced pressure in a vacuum oven overnight. The flask was then fitted with a magnetic stir bar and

addition funnel, and was placed under nitrogen flow. DCM (200 mL) was added via cannula and TEA (0.2757 mol) was added via syringe. The solution was placed under stirring in an ice bath. Methacryloyl chloride (0.2757 mol) was transferred to the addition funnel using a syringe and then added dropwise to the reaction solution over the course of one hour. The reaction was allowed to proceed overnight, after which the triethylamine hydrochloride (TEA•HCl) was removed by filtration. The remaining solution was washed with saturated sodium bicarbonate (1x), 10 % NaCl solution (3x), and water (3x). The organic layer was recollected, dried over magnesium sulfate, and the solvent was removed under reduced pressure in a rotary evaporation and vacuum oven.

2.2.2.2 Synthesis of PCL₇₀₀-DMA

A representative procedure for the synthesis of polycaprolactone-dimethacrylate $M_n = 700 \text{ g mol}^{-1}$ (PCL₇₀₀-DMA) was as follows. Poly- ϵ -caprolactone (PCL) diol (102 g, 192.5 mmol) was added to a 2-neck round bottom flask and dried in a vacuum oven. The reaction flask was equipped with an addition funnel, sealed with rubber septa, and placed under magnetic stirring and a N₂ purge. Anhydrous dichloromethane (DCM, 310 mL) and TEA (445 mmol) was added and the flask was placed in an ice bath. A 10 % molar excess of methacryloyl chloride (420 mmol) in 200 mL DCM was added dropwise from the addition funnel over the course of 1.5 hours and the reaction was allowed to proceed for an additional 3 hours. The formed TEA•HCl salt was removed by filtration and the filtrate was diluted 3-fold with DCM, washed three times with NaCl solution and three times with deionized water. The organic layer was collected, dried over magnesium sulfate and filtered. The bulk of the DCM was removed under reduced pressure on a rotary evaporator and the remaining DCM was removed in a vacuum oven at 35 °C. Reaction progress was monitored by ¹H NMR (Bruker, 300 MHz, CDCl₃) and quantitative ¹³C NMR (Bruker, 600 MHz, CDCl₃) was used to confirm degree of functionalization and molecular weight. For quantitative ¹³C NMR, scan conditions were determined by increasing the

relaxation time until relative peak integrations remained constant. A relaxation time of 75 s was used for the final spectrum that is presented here.

2.2.3 Photocalorimetry

Photopolymerization of methacrylated PCL resins was analyzed with photocalorimetry using a Discovery DSC fitted with the PCA accessory, equipped with a Onicure S-2000 mercury UV light source with a 365 nm external filter (TA instruments, New Castle, DE). Both PCL resins contained TPO at 1 wt % as a photoinitiator.

To determine the onset of curing, a drop of resin was added to an aluminum DSC sample pan without a lid and placed in the DSC cell, which was held at a constant temperature of 25 °C under a 50 mL/min nitrogen flow. After an initial isothermal step (3 minutes for PCL₁₁₀₀-TMA, 7 min for PCL₇₀₀-DMA) samples were exposed to UV light for at least 10 minutes at 5 mW cm⁻².

To observe the effect of different light intensities on the double bond conversion (DBC) and rate of polymerization (R_p) during a long UV exposure, 5 -7 mg of resin was added to an aluminum DSC sample pan without a lid and placed in the DSC cell, which was held at a constant temperature of 25 °C under a 50 mL/min nitrogen flow. After a 2-minute dark isothermal step, samples were exposed for 25 minutes to UV light with an intensity of 5, 9.5, or 20 mW cm⁻². The light was then turned off for 5 minutes, after which samples were exposed to another 5-minute cure to ensure the polymerization had completed, and for a baseline value for heat from the light alone. Each sample was run in triplicate.

For pulsed experiments, samples were prepared the same way. Following a 2-minute dark isothermal step, samples were exposed to 1.8 second pulses (of the same intensities as above) followed by a 5-minute dark isothermal step. This was repeated one additional time for a total of two pulses. Following another 5-minute dark step, samples were subjected to a 15-

minute exposure to complete the cure and identify the baseline heat value with the light on.

Each sample was run in triplicate.

Heat was normalized with a horizontal baseline from the heat flow value at the end of the final cure step to account for the heat generated from the light alone. Rate of polymerization was calculated using equation 2.8:

$$R_p = \frac{|Q|}{\Delta H_{max}} \quad (2.8)$$

where Q is heat flow in mW and ΔH_{max} is the theoretical heat evolved if all methacrylate groups in the sample are reacted. For these experiments, ΔH_{max} was calculated as the product of moles of methacrylate in the sample and ΔH for conversion of a methacrylate (60 kJ mol^{-1}) [32]. Bond conversion was calculated by integrating equation 2.8.

2.2.4 Differential Scanning Calorimetry

DSC measurements were carried out on a Discovery series DSC (TA Instruments). For PCL₇₀₀-DMA, a fraction of a disk fabricated with CLIP (~5 mg) was massed into an aluminum pan and sealed with a T-Zero hermetic lid. For PCL₁₁₀₀-TMA, the aluminum pan containing the bulk cured sample (~10 mg) from the photo-DSC analysis was sealed with a hermetic lid. Samples underwent a heat-cool-heat cycle by heating from 30 °C to 100 °C, cooling to -90 °C, and subsequently heating to 100 °C at a rate of 10 °C/min, under nitrogen atmosphere. Trios software (TA Instruments) was used for analysis of glass transition temperatures (T_g) at the midpoint of the transition of the second heat.

2.2.5 Synthesis of HA-GMA

Methacrylation of hyaluronic acid (HA-GMA) ($M_w = 5K, 10K, 40K, 500K, 1M$) was carried out according to the method present by Bencherif *et. al.* [19]. Briefly, HA (2.6 mmol repeat units) was dissolved at 0.5 % in a 1:1 mixture of 1X PBS and DMF in a glass bottle. GMA (132 mmol) and TEA (145 mmol) were added at a molar excess to HA repeat units. Bottles were covered with aluminum foil and placed under magnetic stirring for 10 days at room temperature. HA-

GMA was then precipitated into acetone and separated with filtration, and subsequently dried at 40 °C under reduced pressure in a vacuum oven. HA-GMA were stored at -20 °C. Analysis was carried out using ^1H NMR in deuterated water (Bruker, 300 MHz).

2.2.6 Photo-rheology of HA-GMA

HA-40K-GMA, HA-500K-GMA, and HA-1M-GMA were dissolved in DI water at 2 % (w/v) and the photoinitiator Lithium phenyl(2,4,6-trimethyl benzoyl) phosphinate (LAP) dissolved at 0.2 % (w/v). Solutions were tested for gelation using a TA discovery series photo-rheometer equipped with a 385 nm LED light source (TA Instruments). Samples were placed under constant frequency and exposed to UV light following 120 seconds to equilibrate.

2.2.7 Continuous Liquid Interface Production of a HA-GMA hydrogel

A square pyramidal structure (7x7 mm base) was fabricated using a CLIP S1 prototype printer (Carbon, Redwood City, CA) from the HA-1M-GMA (2 %) and LAP (0.2 %) solution. The part was printed with a light intensity of 20 mW cm⁻², with a base exposure of 10 seconds, and continuous speed of 21 mm hr⁻¹.

2.3 Results and Discussion

2.3.1 Synthesis of methacrylate-functionalized polycaprolactone

The NMR results of the methacrylated PCL oligomeric starting monomers can be seen in figures 2.3-2.5. Three-armed PCL₁₁₀₀-TMA was synthesized through the methacryloyl chloride functionalization of a PCL-triol with a molecular weight of 900 g mol⁻¹. The successful functionalization is confirmed by the presence of the ^1H NMR peaks at 5.54-5.58, and 6.09 ppm, which correspond to the alkene protons, and the peak at 1.94 ppm, which correspond to the three methyl protons of the methacrylate functionality (Fig. 2.3). Comparing the integrations of

these peaks to that of the primary methyl of the initiator (0.9 ppm) indicates a functionalization of 87 %.

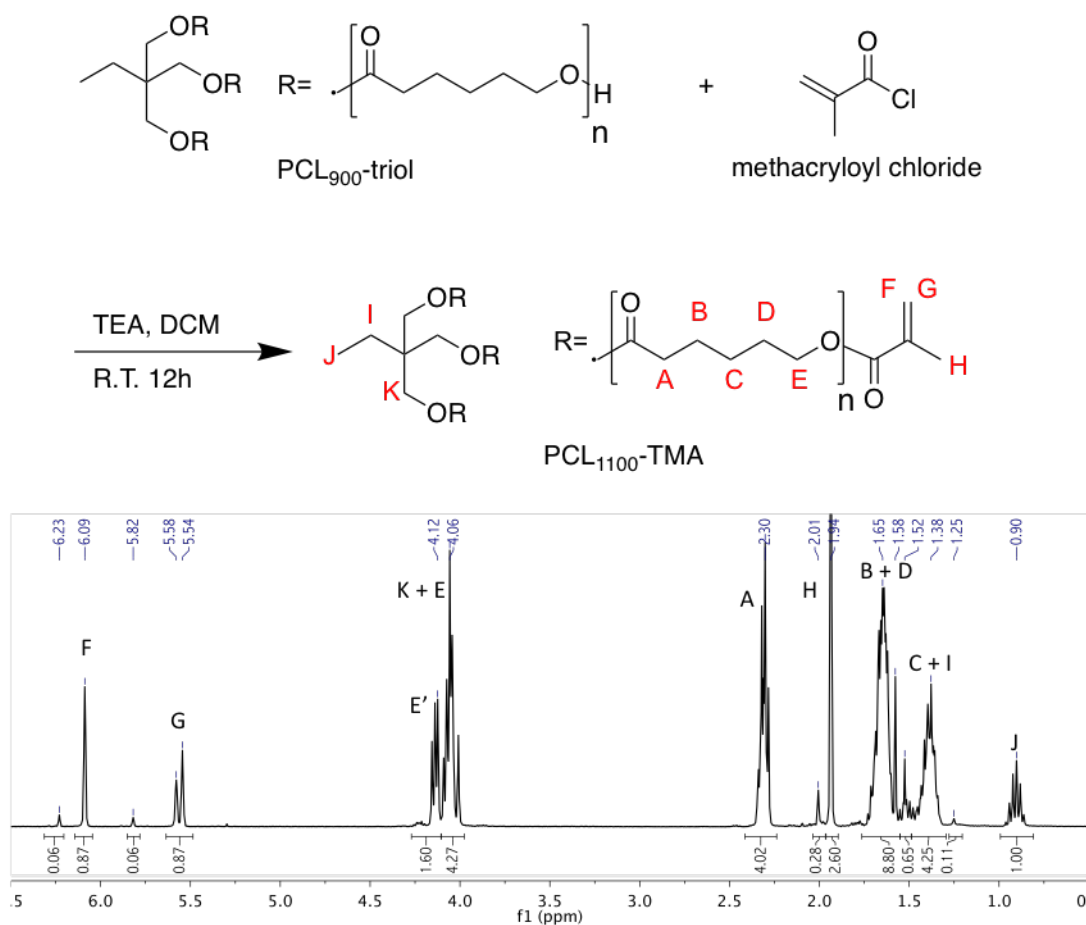
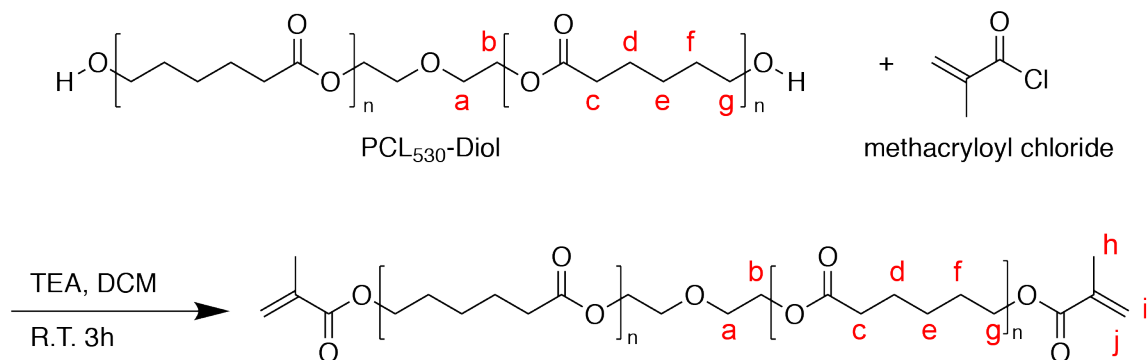


Figure 2.3 Synthesis of PCL₁₁₀₀-TMA. PCL-diol was functionalized with methacrylate groups through reacting the terminal hydroxyl groups with methacryloyl chloride. The ¹H NMR peaks at 1.94, 5.56, and 6.09 represent the protons of the methacrylate groups and indicate a functionalization of 87 % through comparison to the primary methyl group of the backbone.

Successful functionalization of PCL₅₃₀-diol with methacryloyl chloride was evidenced by the appearance of the methacrylate peaks at 1.03, 5.55, and 6.09 ppm (Fig. 2.4). Quantitative ¹³C NMR was carried out to confirm the molecular weight and extent of functionalization (Fig. 2.5). Comparing the integration of peaks for the alpha carbon in the ethylene glycol backbone (K, 68.9 ppm) to the peak for the methylene carbon of the vinyl group (A, 125.2 ppm) indicate a high extent of functionalization (~99 %). Comparison to carbons of the caprolactone repeat unit

(F, 28.2 ppm; G, 25.4 ppm; H, 24.5 ppm) supports the presence of 2 repeat units per methacrylate group (4 per diethylene glycol initiator), indicating a final $M_n = 699 \text{ g mol}^{-1}$.

A



B

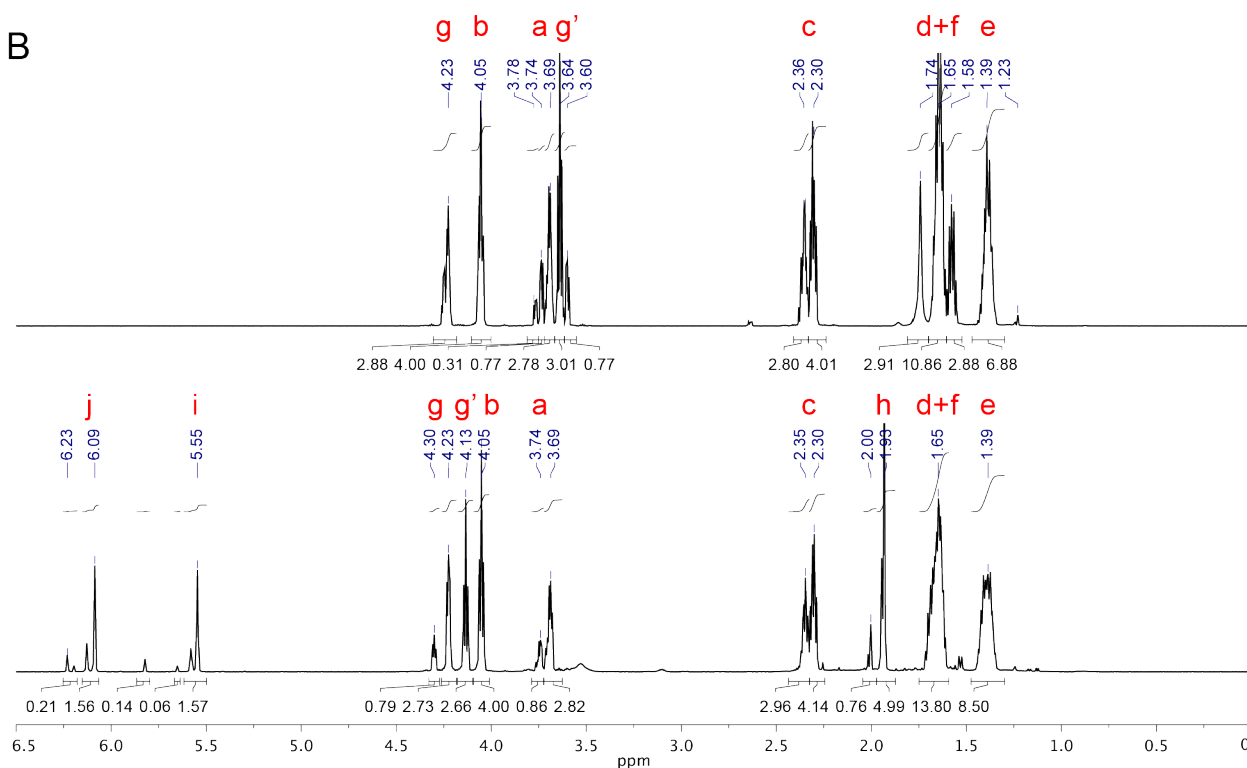


Figure 2.4 Synthesis of PCL₇₀₀-DMA. (A) Functionalization of PCL-diol was achieved through reaction of the terminal hydroxyl groups with a methacryloyl chloride. (B) Successful functionalization is evidenced by comparison ^1H NMR spectra of PCL-diol (top) and the reaction product (bottom). The appearance of peaks at 1.93, 5.55, and 6.09 ppm, indicative of the protons of the methacrylate group.

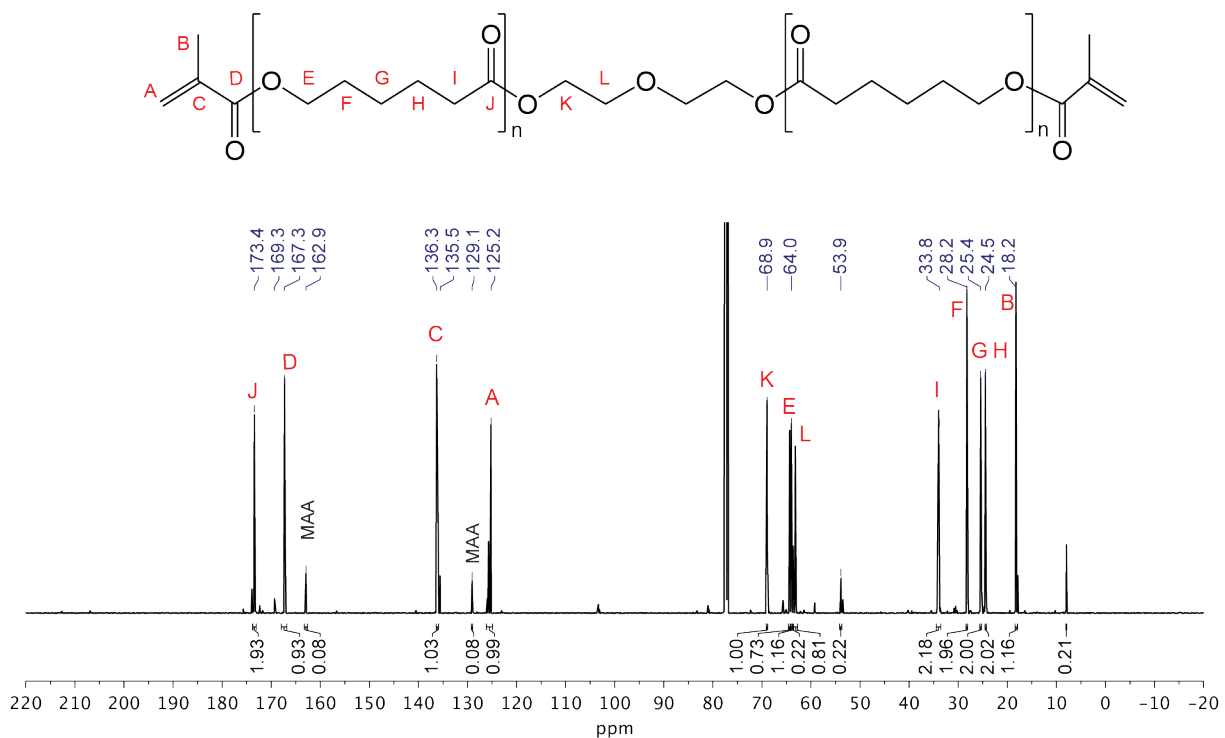


Figure 2.5 Quantitative ¹³C NMR of PCL₇₀₀-DMA was carried out using a Bruker 600 MHz NMR and a relaxation time of 75 s per scan.

2.3.2 Characterization of methacrylate-functionalized polycaprolactone

2.3.2.1 Photokinetics

Differential scanning photocalorimetry (photo-DSC), is a technique used to monitor the reaction progress and kinetics of UV polymerization. Photo-DSC uses the sample cell and platforms of a traditional DSC instrument, while a custom adaptor allows light guides connected to a UV light source to expose the samples during the experiment (Fig. 2.6). The heat evolved from a photopolymer resin held isothermally upon exposure to UV light can be translated to a rate of polymerization and extent of cure using known values for heat of conversion for the reactive functional group.

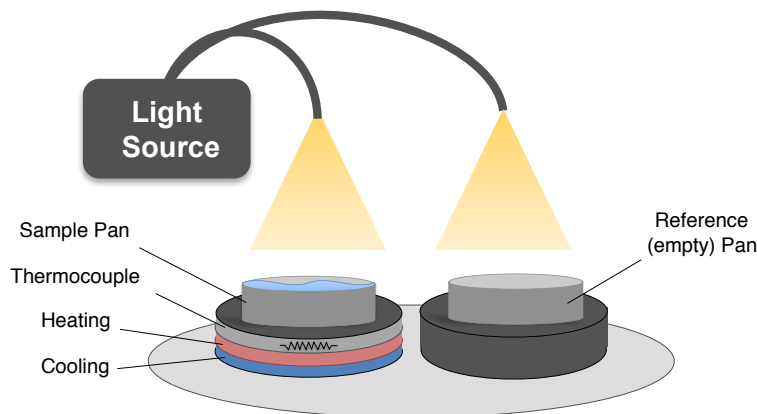


Figure 2.6 Schematic of photo-DSC apparatus.

When PCL₁₁₀₀-TMA and PCL₉₀₀-DMA were analyzed with photo-DSC, a rapid onset of the autoacceleration phase is observed in less than 2 seconds following exposure for each monomer (Fig. 2.7). This is consistent with multi-methacrylated monomers and is also indicative of minimal intramolecular cyclization among the monomer materials [4]. These thermograms of photopolymerization are representative of the rapid polymerization kinetics required for use in CLIP and other photopolymer-based 3D printing techniques.

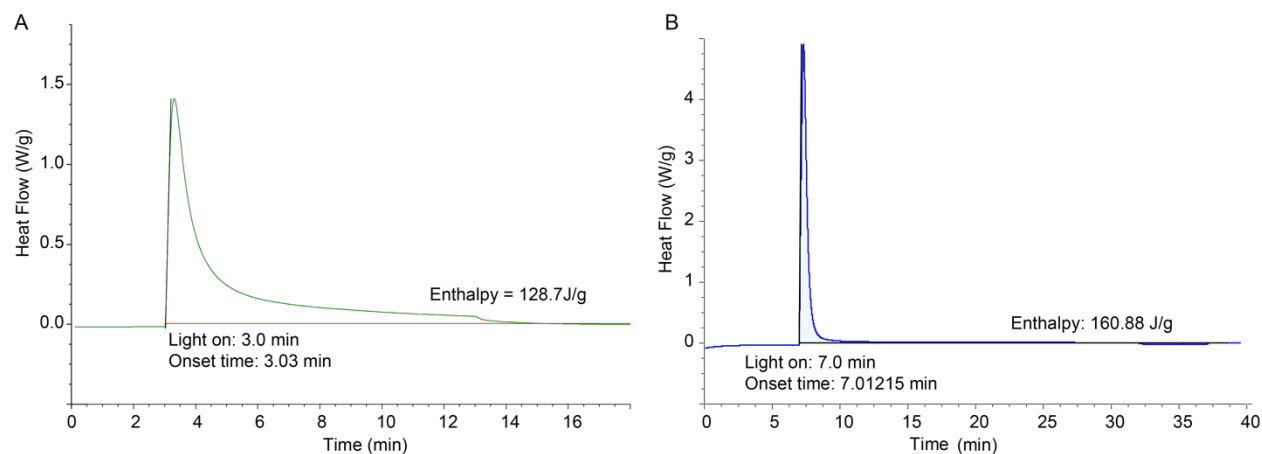


Figure 2.7 Photocalorimetry thermograms for (A) PCL₁₁₀₀-TMA and (B) PCL₇₀₀-DMA.

The effect of light intensity used during photopolymerization on the resulting polymer network was explored with photo-DSC. The differences in the cure kinetics of PCL₁₁₀₀-TMA when exposed to three different light intensities can be seen in figure 2.8 A. The time to max R_p

and total DBC was significantly different for all three intensities (2-way ANOVA with Tukey's multiple comparisons test, $p < 0.005$) (Table 2.1).

Table 2.1 Photokinetic parameters of PCL₁₁₀₀-TMA upon exposure with a range of light intensities for 15 minutes. (n=3, error is given as \pm standard deviations).

Light Intensity (mW cm ⁻²)	Max Rp (s ⁻¹)	DBC @ Max Rp (%)	t _{max} (s)	Total DBC (%)
5	0.0137 \pm 0.0008	19.19 \pm 0.38	25.7 \pm 2.1	81.9 \pm 1.7
9.5	0.0349 \pm 0.0032	19.97 \pm 0.30	10.4 \pm 1.0	87.6 \pm 1.6
20	0.0596 \pm 0.0040	18.58 \pm 0.68	5.8 \pm 0.4	93.8 \pm 4.2

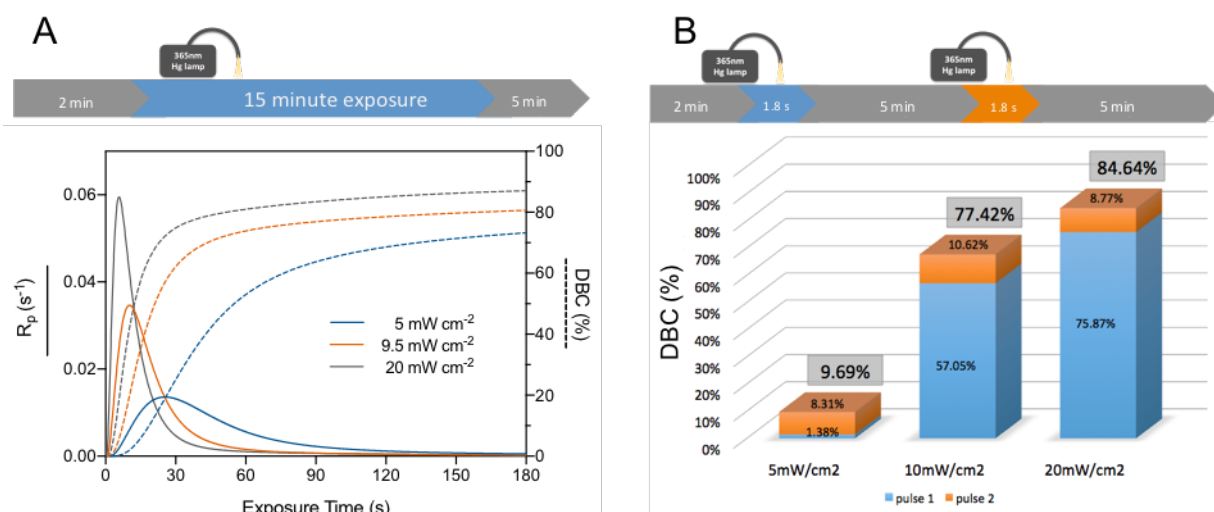


Figure 2.8 Effects of light intensity on the extent of polymerization of PCL₁₁₀₀-TMA. (A) Rate of polymerization, R_p , and total double bond conversion during a 15 minute cure is dependent on the light intensity used to cure the resin. The first three minutes of the cure is shown here, values for the DBC of the complete 15 min cure can be seen in Table 2.1. (B) The effect of light intensity on the DBC when exposed to 1.8s pulses of light of different intensities. The DBC achieved in pulse 1 and 2 are displayed in blue and orange, respectively.

Further, when exposed to short pulses of light, the effect of light intensity on the resulting polymer network is even more apparent (Fig. 2.8 B). A short exposure of light was used to better represent the rapid nature of the CLIP process. During the CLIP process, the speed and/or light intensity can be varied to achieve different overall light exposures. The data presented here indicates that manipulation of total light exposure can result in appreciable differences in the DBC, and thus the crosslink density of the resulting network. This may have

important implications on the resulting parts' release kinetics and mechanical properties. Using light intensity to modify drug release is discussed further in Chapter 5.

2.3.2.2 Thermal properties

The thermal properties were measured to determine the T_g of the cured methacrylated PCL materials. Both PCL₁₁₀₀-TMA and PCL₅₃₀-DMA indicate a low T_g after curing (Fig. 2.9). This agrees with the expected low T_g of PCL polymers. Further discussion of the effects of reactive diluents on the thermal properties of cured PCL materials is discussed in Chapters 3 and 4.

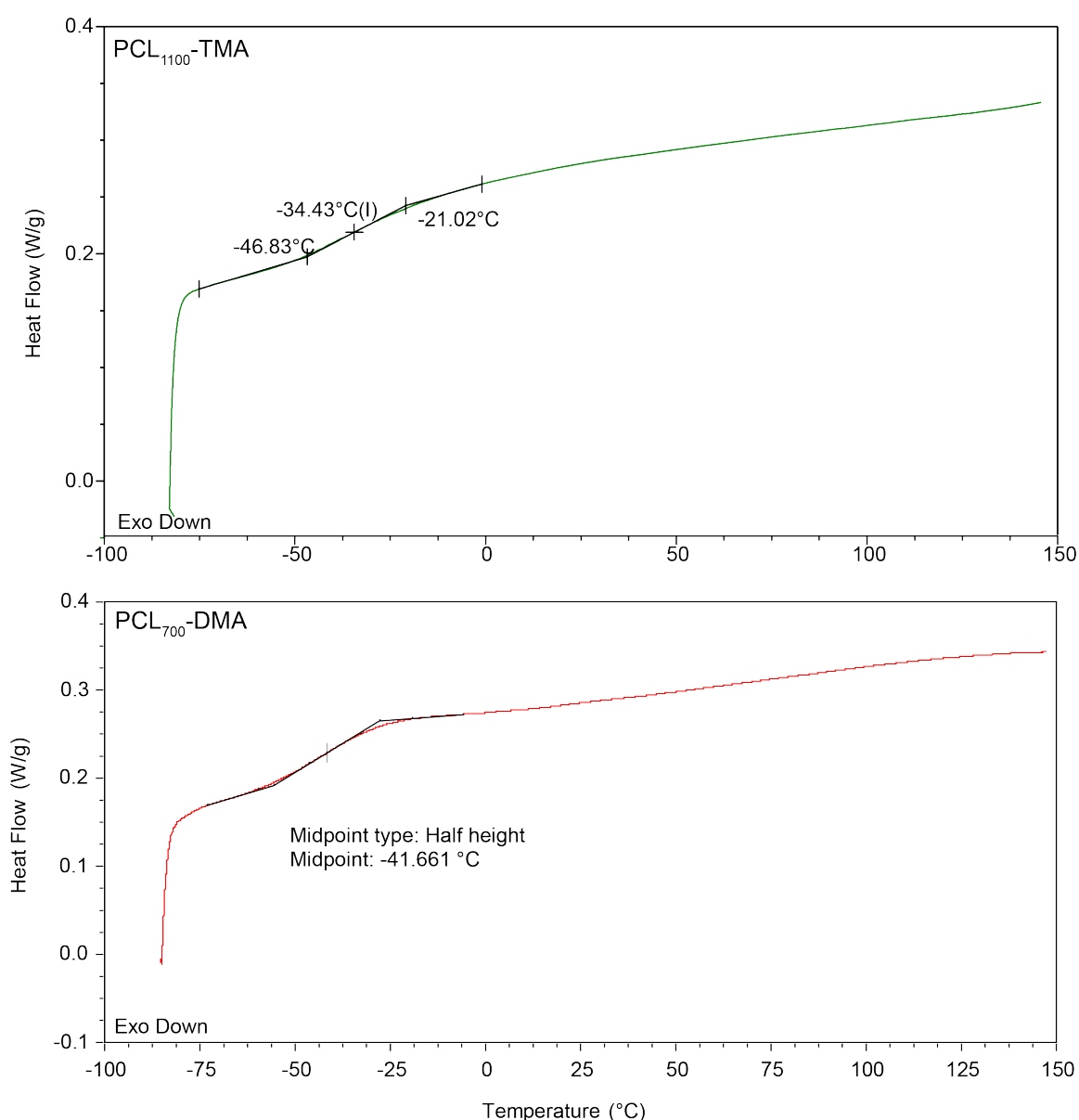


Figure 2.9 Thermal analysis of methacrylated PCL monomers.

2.3.3 Synthesis of HA-GMA

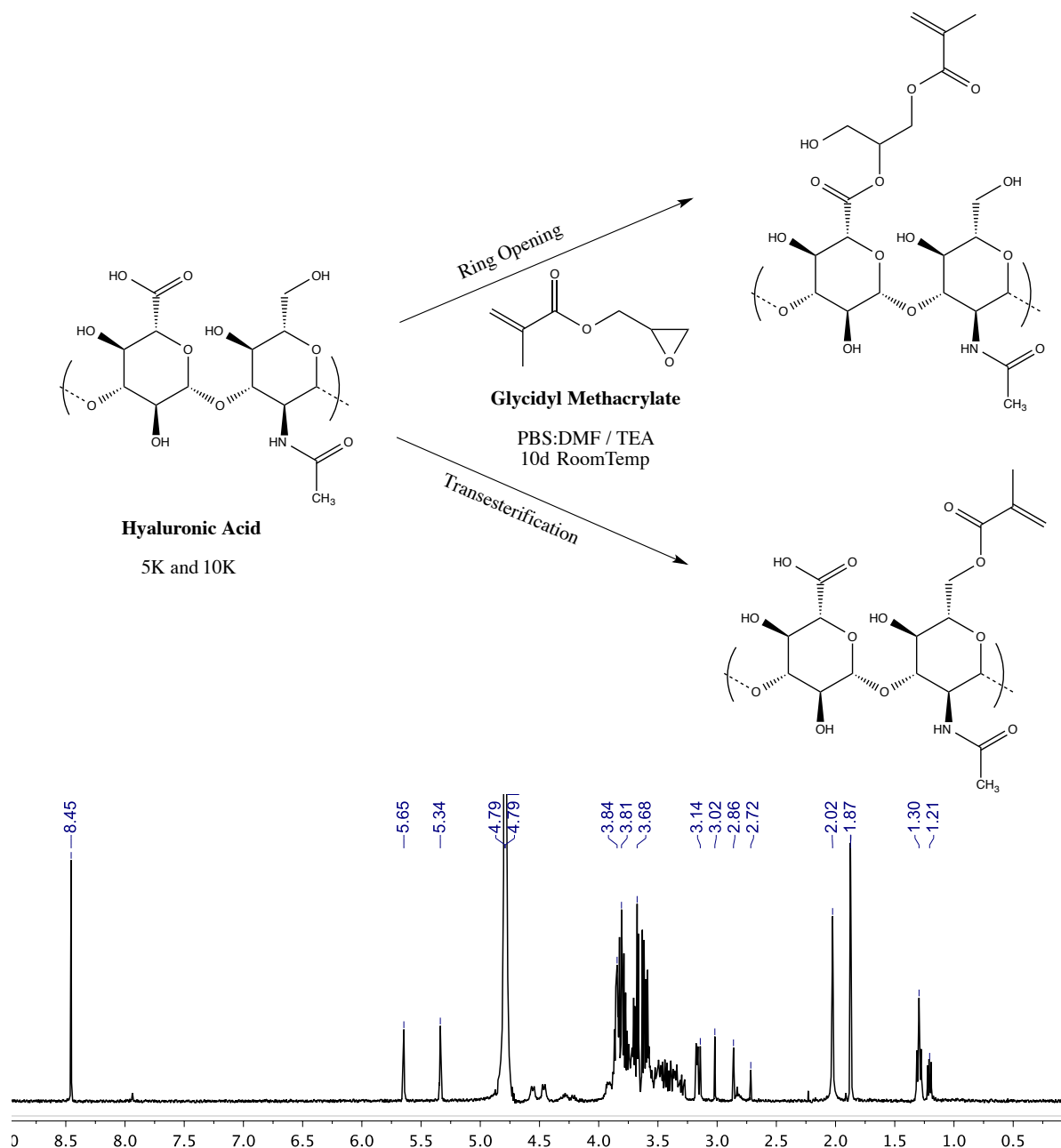


Figure 2.10 Synthesis of HA-GMA. HA-GMA was synthesized by functionalizing hyaluronic acid with glycidyl methacrylate. The reaction was carried out for 10 days to allow for functionalization to occur via both the ring opening and transesterification routes [19]. ¹H NMR spectroscopy indicated successful functionalization of HA by the appearance of peaks at 5.65 and 5.34, representing the methacrylate functional groups. HA-10K is shown as a representative spectrum of a successfully functionalized HA material.

Successful functionalization of HA with methacrylate groups was evidenced by the appearance of peaks at 5.65 and 5.34 ppm (Fig. 2.10). The three largest molecular weight HA-GMA's (1M, 500K, and 40K) were formulated into a photocurable resin by dissolving in water to 2 % (w/v) along with the photoinitiator, LAP, at a concentration of 0.2 % (w/v). When exposed to UV light on a photo-rheometer, all HA-GMA solutions were observed to solidify into a hydrogel within 5 seconds of light exposure (Fig. 2.11 A-C). Additionally, the cure times were seen to be inversely related to the HA molecular weight. Finally, a square pyramidal structure (7 x 7 mm base) was fabricated using CLIP to form a hydrogel using the HA-1M-GMA solution (Fig. 2.11 D).

These results, while preliminary, are important. The photoinitiator used, LAP, has been shown to be cytocompatible, which makes this hydrogel approach a potential method of using photo-based 3D printing to fabricate using cell-laden resins [33]. Further, to the author's knowledge there have been no reported uses of HA as the only monomer to form a hydrogel using UV projection- or laser-based 3D printing techniques. Though there are examples of using interpenetrating networks [34] and lower resolution techniques such as bioplotting [35]. The lack of publications in fabrication of HA-based hydrogels using SLA, despite HA-methacrylates being widely developed [18,36-38], is likely a result of the harsh physical strains of the SLA approach compared to CLIP.

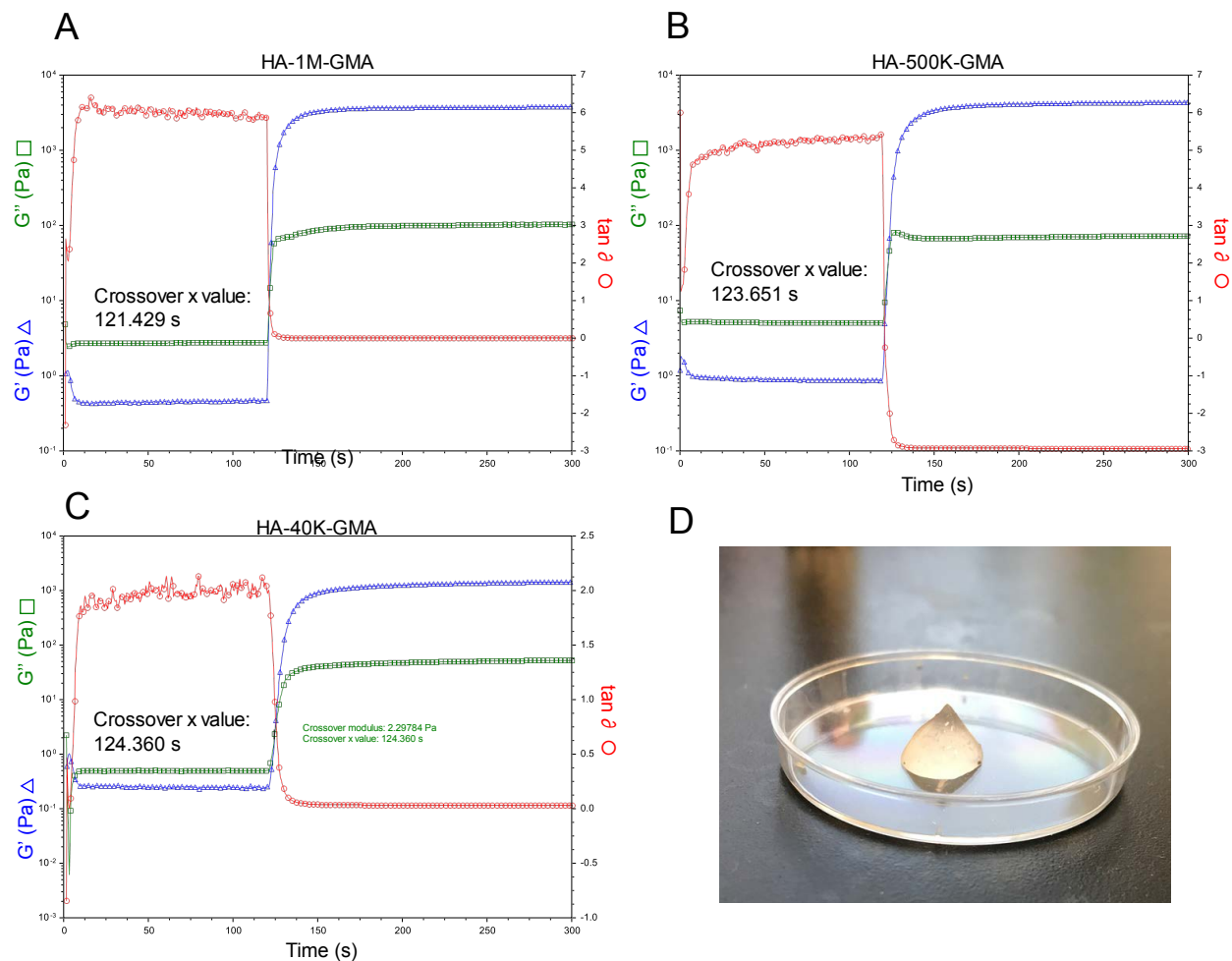


Figure 2.11 Photo-rheology and CLIP of HA-GMA hydrogels. Gelation of HA-GMA was observed in a solution of water using photo-rheology. Under a constant frequency, HA-GMA gels were exposed to UV light after 120 seconds. The crossover between G' (storage modulus) and G'' (loss modulus) indicates rapid gelation upon exposure. (A) HA-1M-GMA, (B) HA-500K-GMA, (C) HA-40K-GMA. (D) Square pyramidal hydrogel part fabricated from 2 % (w/v) HA-1M-GMA resin using CLIP.

2.4 Conclusions

Most of the reported work using photopolymerizable polyesters for 3D printing are designed for applications in tissue engineering, and are typically made using non-reactive diluents in order to meet printing requirements. These non-reactive diluents require a post-print washing step that would not be suitable if a drug was directly dissolved in the resin, due to removal of drug during the non-reactive diluent removal steps. The low molecular weight PCL-based materials presented in this chapter are characterized by being a liquid at room temperature, and fast reaction kinetics. These characteristics afford direct printing with material without requiring the use of diluents. The following chapters will present the use of liquid PCL₇₀₀-DMA along with other commercially available resins to fabricate drug-loaded devices with CLIP from resins with drug dissolved directly into resin during the CLIP process. The use of PCL₁₁₀₀-TMA were reported recently by Johnson *et. al.* [25].

Additionally, the synthesis and CLIP fabrication of a hydrogel from an HA-based resin with a cytocompatible initiator is a promising avenue for potential incorporation of living cells during the CLIP process. Future work would need to include optimization of formulations, fabrication parameters and cytocompatibility testing.

REFERENCES

- [1] G. Odian, Radical Chain Polymerization, in: Principles of Polymerization, 2003: pp. 198–349.
- [2] H. Wang, H.R. Brown, Self-Initiated Photopolymerization and Photografting of Acrylic Monomers, *Macromol. Rapid Commun.* 25 (2004) 1095–1099. doi:10.1002/marc.200400010.
- [3] M. Panagiotopoulou, S. Beyazit, S. Nestora, K. Haupt, B.T.S. Bui, Initiator-free synthesis of molecularly imprinted polymers by polymerization of self-initiated monomers, *Polymer*. 66 (2015) 43–51. doi:10.1016/j.polymer.2015.04.012.
- [4] E. Andrzejewska, Photopolymerization kinetics of multifunctional monomers, *Progress in Polymer Science*. 26 (2001) 605–665. doi:10.1016/S0079-6700(01)00004-1.
- [5] R. Scott, J.H. Ward, N.A. Peppas, Development of acrylate and methacrylate polymer networks for controlled release by photopolymerization technology, in: *Handbook of Pharmaceutical Controlled Release Technology*, CRC Press, 2000.
- [6] S.M. Kenny, M. Buggy, Bone cements and fillers: A review | SpringerLink, *J Mater Sci: Mater Med.* 14 (2003) 923–938. doi:10.1023/A:1026394530192.
- [7] G. Lewis, Properties of nanofiller-loaded poly (methyl methacrylate) bone cement composites for orthopedic applications: a review, *J. Biomed. Mater. Res.* 105 (2017) 1260–1284. doi:10.1002/jbm.b.33643.
- [8] L.G. Lovell, S.M. Newman, M.M. Donaldson, C.N. Bowman, The effect of light intensity on double bond conversion and flexural strength of a model, unfilled dental resin, *Dent Mater.* 19 (2003) 458–465.
- [9] R. Labella, K. Davy, P. Lambrechts, Monomethacrylate co-monomers for dental resins, *European Journal of ...* (1998). doi:10.1046/j.0909-8836.1998.eos106308.x/abstract.
- [10] A.P. Duarte, J.F. Coelho, J.C. Bordado, M.T. Cidade, M.H. Gil, Surgical adhesives: Systematic review of the main types and development forecast, *Progress in Polymer Science*. 37 (2012) 1031–1050. doi:10.1016/j.progpolymsci.2011.12.003.
- [11] M.T. Wolf, C.L. Dearth, S.B. Sonnenberg, E.G. Lobo, S.F. Badylak, Naturally derived and synthetic scaffolds for skeletal muscle reconstruction, *Advanced Drug Delivery Reviews*. 84 (2014) 1–14. doi:10.1016/j.addr.2014.08.011.
- [12] A.S. Hoffman, Hydrogels for biomedical applications, *Advanced Drug Delivery Reviews*. 64 (2012) 18–23. doi:10.1016/j.addr.2012.09.010.
- [13] B.V. Slaughter, S.S. Khurshid, O.Z. Fisher, A. Khademhosseini, N.A. Peppas, Hydrogels in Regenerative Medicine, *Adv. Mater.* 21 (2009) 3307–3329. doi:10.1002/adma.200802106.

- [14] J. Visser, P.A. Levett, N.C.R. te Moller, J. Besems, K.W.M. Boere, M.H.P. van Rijen, et al., Crosslinkable hydrogels derived from cartilage, meniscus, and tendon tissue, *Tissue Eng Part A*. 21 (2015) 1195–1206. doi:10.1089/ten.TEA.2014.0362.
- [15] L.M. Weber, C.G. Lopez, K.S. Anseth, Effects of PEG hydrogel crosslinking density on protein diffusion and encapsulated islet survival and function, *J Biomed Mater Res A*. 90A (2009) 720–729. doi:10.1002/jbm.a.32134.
- [16] M. Schuster, C. Turecek, G. Weigel, R. Saf, J. Stampfl, F. Varga, et al., Gelatin-based photopolymers for bone replacement materials, *Journal of Polymer Science Part a: Polymer Chemistry*. 47 (2009) 7078–7089. doi:10.1002/pola.23747.
- [17] E. Kaemmerer, F. Melchels, B.M. Holzapfel, T. Meckel, Gelatine methacrylamide-based hydrogels—an alternative 3D cancer cell culture system, *Acta Biomaterialia*. 10 (2014) 2551–2562. doi:10.1016/j.actbio.2014.02.035.
- [18] M.N. Collins, C. Birkinshaw, Hyaluronic acid based scaffolds for tissue engineering—A review, *Carbohydrate Polymers*. 92 (2013) 1262–1279. doi:10.1016/j.carbpol.2012.10.028.
- [19] S.A. Bencherif, A. Srinivasan, F. Horkay, J.O. Hollinger, K. Matyjaszewski, N.R. Washburn, Influence of the degree of methacrylation on hyaluronic acid hydrogels properties, *Biomaterials*. 29 (2008) 1739–1749. doi:10.1016/j.biomaterials.2007.11.047.
- [20] A.K. Nguyen, S.D. Gittard, A. Koroleva, S. Schlie, A. Gaidukeviciute, B.N. Chichkov, et al., Two-photon polymerization of polyethylene glycol diacrylate scaffolds with riboflavin and triethanolamine used as a water-soluble photoinitiator, *Regenerative Medicine*. 8 (2013) 725–738. doi:10.2217/rme.13.60.
- [21] S.J. Bryant, C.R. Nuttelman, K.S. Anseth, Cytocompatibility of UV and visible light photoinitiating systems on cultured NIH/3T3 fibroblasts in vitro, *J Biomater Sci Polym Ed*. 11 (2000) 439–457.
- [22] H. Lin, D. Zhang, P.G. Alexander, G. Yang, J. Tan, A.W.-M. Cheng, et al., Application of visible light-based projection stereolithography for live cell-scaffold fabrication with designed architecture, *Biomaterials*. 34 (2013) 331–339. doi:10.1016/j.biomaterials.2012.09.048.
- [23] J. Hu, Y. Hou, H. Park, B. Choi, S. Hou, A. Chung, et al., Visible light crosslinkable chitosan hydrogels for tissue engineering, *Acta Biomaterialia*. 8 (2012) 1730–1738. doi:10.1016/j.actbio.2012.01.029.
- [24] F.P.W. Melchels, J. Feijen, D.W. Grijpma, A review on stereolithography and its applications in biomedical engineering, *Biomaterials*. 31 (2010) 6121–6130. doi:10.1016/j.biomaterials.2010.04.050.
- [25] A.R. Johnson, C.L. Caudill, J.R. Tumbleston, C.J. Bloomquist, K.A. Moga, A. Ermoshkin, et al., Single-Step Fabrication of Computationally Designed Microneedles by Continuous Liquid Interface Production, *PLoS ONE*. 11 (2016) e0162518. doi:10.1371/journal.pone.0162518.

- [26] J.W. Lee, P.X. Lan, B. Kim, G. Lim, D.-W. Cho, 3D scaffold fabrication with PPF/DEF using micro-stereolithography, *Microelectronic Engineering*. 84 (2007) 1702–1705. doi:10.1016/j.mee.2007.01.267.
- [27] Y. Luo, C.K. Dolder, J.M. Walker, R. Mishra, D. Dean, M.L. Becker, Synthesis and Biological Evaluation of Well-Defined Poly(propylene fumarate) Oligomers and Their Use in 3D Printed Scaffolds, *Biomacromolecules*. 17 (2016) 690–697. doi:10.1021/acs.biomac.6b00014.
- [28] F.P.W. Melchels, J. Feijen, D.W. Grijpma, A poly(d,l-lactide) resin for the preparation of tissue engineering scaffolds by stereolithography, *Biomaterials*. 30 (2009) 3801–3809. doi:10.1016/j.biomaterials.2009.03.055.
- [29] L. Elomaa, S. Teixeira, R. Hakala, H. Korhonen, D.W. Grijpma, J.V. Seppälä, Preparation of poly(ϵ -caprolactone)-based tissue engineering scaffolds by stereolithography, *Acta Biomaterialia*. 7 (2011) 3850–3856. doi:10.1016/j.actbio.2011.06.039.
- [30] M.A. Przeradzka, B. Bochove, T.C. Bor, D.W. Grijpma, Phase-separated mixed-macromer hydrogel networks and scaffolds prepared by stereolithography, *Polymers for Advanced Technologies*. 28 (2017) 1212–1218. doi:10.1002/pat.3916.
- [31] L.S. Nair, C.T. Laurencin, Biodegradable polymers as biomaterials, *Progress in Polymer Science*. 32 (2007) 762–798. doi:10.1016/j.progpolymsci.2007.05.017.
- [32] J. Brandrup, E.H. Immergut, E.A. Grulke, *Polymer handbook*, vol. II, New York: Wiley, 1999.
- [33] B.D. Fairbanks, M.P. Schwartz, C.N. Bowman, K.S. Anseth, Photoinitiated polymerization of PEG-diacrylate with lithium phenyl-2,4,6-trimethylbenzoylphosphine: polymerization rate and cytocompatibility, *Biomaterials*. 30 (2009) 6702–6707. doi:10.1016/j.biomaterials.2009.08.055.
- [34] A.X. Sun, H. Lin, A.M. Beck, E.J. Kilroy, R.S. Tuan, Projection Stereolithographic Fabrication of Human Adipose Stem Cell-Incorporated Biodegradable Scaffolds for Cartilage Tissue Engineering, *Front. Bioeng. Biotechnol.* 3 (2015) 6805–9. doi:10.3389/fbioe.2015.00115.
- [35] M.T. Poldervaart, B. Goversen, M. de Ruijter, A. Abbadessa, F.P.W. Melchels, F.C. Öner, et al., 3D bioprinting of methacrylated hyaluronic acid (MeHA) hydrogel with intrinsic osteogenicity, *PLoS ONE*. 12 (2017) e0177628–15. doi:10.1371/journal.pone.0177628.
- [36] S. Ibrahim, C.R. Kothapalli, Q.K. Kang, A. Ramamurthi, Characterization of glycidyl methacrylate “Crosslinked hyaluronan hydrogel scaffolds incorporating elastogenic hyaluronan oligomers, *Acta Biomaterialia*. 7 (2011) 653–665. doi:10.1016/j.actbio.2010.08.006.
- [37] S.S. Prado, J.M. Weaver, B.J. Love, Gelation of photopolymerized hyaluronic acid grafted with glycidyl methacrylate, *Materials Science & Engineering C*. 31 (2011) 1767–1771. doi:10.1016/j.msec.2011.08.008.

- [38] C.E. Schantz, G. Zuber, C. Herlin, T.F. Vandamme, Chemical modifications of hyaluronic acid for the synthesis of derivatives for a broad range of biomedical applications, *Carbohydrate Polymers*. 85 (2011) 469–489.
doi:10.1016/j.carbpol.2011.03.019.

CHAPTER 3: CONTROLLING THE RELEASE OF A SMALL MOLECULE DRUG SURROGATE FROM DEVICES FABRICATED WITH CLIP

3.1 Introduction

Implantable drug delivery systems provide an opportunity for local and sustained delivery of drug molecules to a target site while reducing exposure to healthy tissue, thus afford many benefits over traditional systemic dosage forms [1-3]. In addition to reduced adverse side effects, these devices eliminate the need for patients to take a pill or injection at specified time intervals and/or dosages thereby improving patient compliance and quality of life. Relevant commercial implantable drug delivery devices have been implemented for a range of applications including contraception, cardiovascular disease [4], ocular delivery [5], and opioid addiction [6].

While there are many benefits of localized drug delivery implants, the economics of commercial manufacturing methods such as molding or extrusion, necessitate a mass-produced product of standard sizes. However, the introduction of additive manufacturing, or 3D printing, techniques towards producing drug delivery systems and medical devices provides the opportunity for customization and personalization of devices based on medical imaging and data [7]. 3D printing provides a small footprint, software-driven manufacturing platform, enabling fabrication that could be carried out by healthcare providers in the clinical setting. Further, 3D printing is a versatile platform, requiring no lead time or tooling, with the capability to fabricate a unique device or multiple devices with each print. Though implementation in the clinic is still in its infancy and faces various logistical and regulatory hurdles, there are already examples of 3D printed medical devices implanted in humans. For example, 3D printed pediatric tracheal stents made via fused deposition modeling (FDM) were used to treat airway obstructions carried out by

surgeons at the University of Michigan hospital [8]. Oxford Performance Materials received Food and Drug Administration (FDA) approval for their 3D printed cranial implants in 2013 followed by successful implantation that same year [9]. In 2015 Aprelia Pharmaceuticals received the first FDA approval for an additively manufactured drug formulation with the approval of the anti-epileptic therapy, Spritam [10]. In addition, there are many examples of preclinical development of various 3D printing techniques applied to drug delivery devices [11-15].

Recently the introduction of the 3D printing technique CLIP has been shown to improve speed and resolution, and has the ability to manufacture devices in a delicate manner [15,16]. CLIP utilizes a photoactive resin to reconstruct a 3D computer aided design (CAD) file that has been sliced into two-dimensional layers. A dynamic light projecting (DLP) chip is used to progressively project an ultraviolet (UV) light pattern of each slice through an oxygen-permeable and UV-transparent window beneath a bath of photoactive liquid resin. When exposed to UV light, a photoinitiator in the resin generates free radicals and initiates photopolymerization. Because its reactivity results in the rapid formation of stable, low energy peroxide radicals, permeated oxygen at the interface of the resin and window acts as a radical scavenger and creates a “dead zone” layer in the bath, within which no solidification occurs. At increasing distance into the resin from the window, the concentration of oxygen is depleted until the reaction kinetics favor polymerization over oxygen inhibition and solidification occurs in the UV-exposed regions. Unique to CLIP, the oxygen-inhibited dead zone enables uninterrupted progression of the build, eliminating repeated mechanical delamination and coating steps necessary in layer-by-layer 3D printing techniques, such as stereolithography (SLA). The continuous nature of CLIP results in a delicate process that can produce monolithic parts in a rapid manner [17], and presents a 3D printing platform that is well suited for the fabrication of complex and functional devices in a clinical setting.

Multiple strategies can be employed to incorporate an API into a CLIP-produced medical device for drug delivery. Select examples of potential methods for API loading of CLIP-produced devices are illustrated in Fig. 3.1. These methodologies can be categorized by whether the API is present during the CLIP process or introduced after the production of the device. In the latter case, post-loading avoids subjecting the API to potential sources of degradation and can be achieved through traditional drug loading techniques. These include absorbing drug into the polymer network by swelling the part in a concentrated drug solution, or adsorbing the drug to the surface of the part through dip or spray coating. Further, one could utilize CLIP to fabricate unique devices that can serve as a means of simplifying or improving administration of drug dosage forms. For example, drug administration through a multichannel scala tympani electrode of a cochlear implant has been shown in preclinical models to overcome the difficulty of delivering drugs to the inner ear [18,19]. This theoretical combination product would benefit from personalization to the patient's ear anatomy as well as the design complexity afforded by 3D printing.

Alternative to post-loading, the API can also be directly incorporated into the photoactive liquid resin used to produce the device with CLIP. Soluble drugs, for example, can be dissolved directly into the liquid resin with a controllable and known concentration. The API can also be dispersed in the resin via a secondary phase, such as insoluble drug particulates, drug-loaded nano- or microparticles, or potentially as an emulsion. Before using a drug-loaded resin, additional testing is necessary to ensure that the drug is stable in the resin, is not susceptible to photolysis, and is not reactive towards the free radicals present during the polymerization process. Post processing parameters also need to be taken into account to ensure consistent drug loading. Despite these additional concerns, several potential benefits are provided when the API is incorporated directly in CLIP resins. From a drug release standpoint, complete dissolution of the drug into the resin results in a monolithic distribution in the polymer matrix of the final part. In the case of drug dispersions, the choice of secondary phase may provide

additional control over drug release. Further, direct incorporation of the drug into the resin creates an “ink” that can be used to produce a drug-loaded device directly without the equipment or specific protocols required for traditional post-loading techniques. The use of pre-formulated drug “inks” may provide a level of quality control in implementing 3D printing as a means for producing personalized drug devices in a clinical setting.

Here we explore the potential for the application of CLIP towards the design and fabrication of drug-loaded devices and demonstrate methodologies for tuning release of small molecule drugs from devices produced from drug-loaded liquid resins. We assessed device factors, including device geometry, crosslink density, and polymer network composition, that control the release rate of a surrogate drug molecule, rhodamine-B base (RhB), from 3D printed devices.

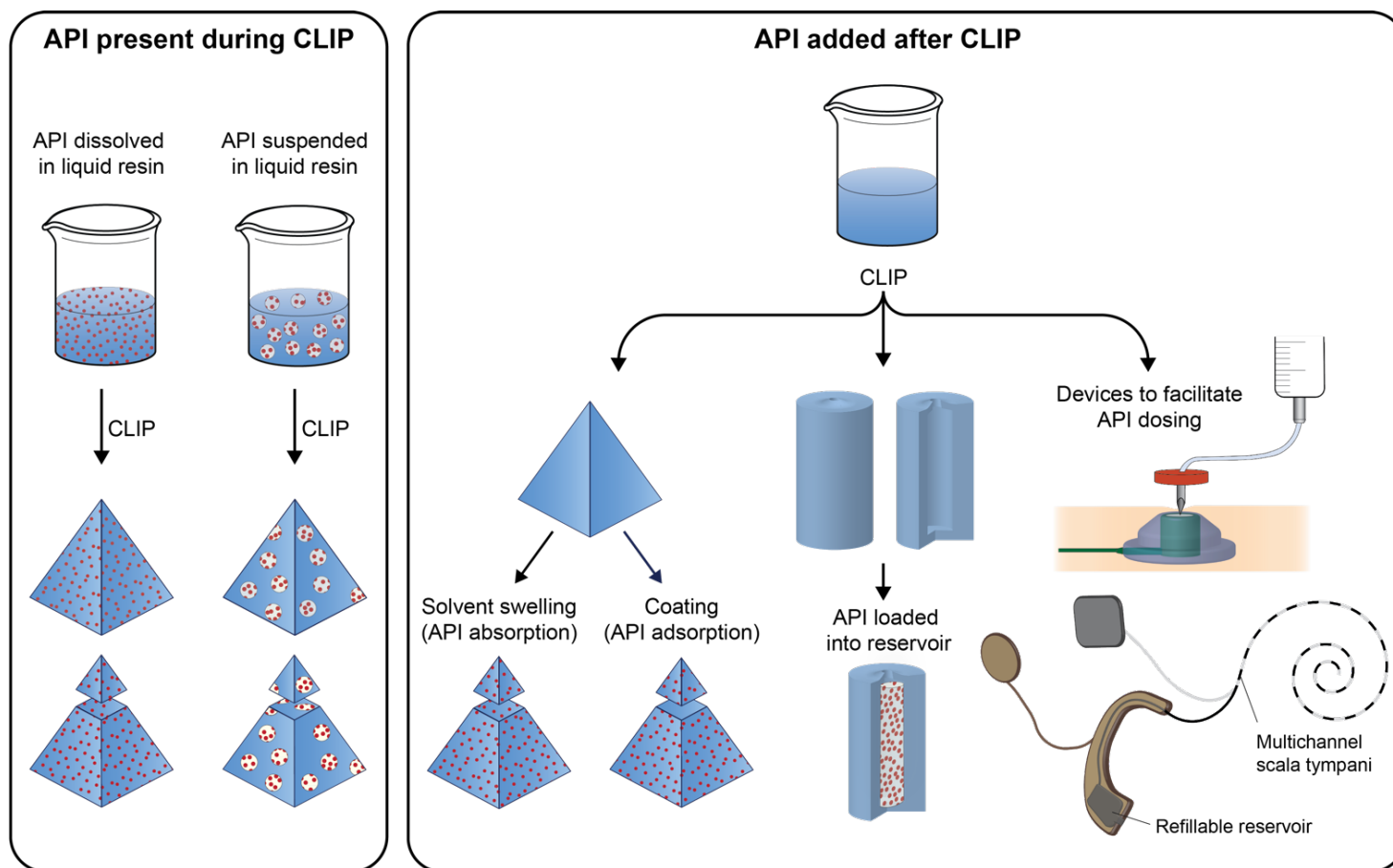


Figure 3.1 Potential approaches for producing drug-loaded devices. API can be dissolved or dispersed directly in the liquid resin prior to the CLIP process. Alternatively, CLIP can be used to fabricate a device without drug. Following complete processing of the CLIP device, API can be loaded through absorption, adsorption, or filling a reservoir. Additionally, CLIP may be utilized to fabricate devices that facilitate drug administration such as subcutaneous infusion ports or cochlear implants with refillable drug reservoirs.

3.2 Materials and Methods

3.2.1 Materials

Monomers poly(ethylene glycol) dimethacrylate $M_n = 750 \text{ g mol}^{-1}$ (PEG₇₅₀-DMA), Poly(ethylene glycol) dimethacrylate $M_n = 550 \text{ g mol}^{-1}$ (PEG₅₅₀-DMA), poly(ethylene glycol) methyl ether methacrylate $M_n = 500 \text{ g mol}^{-1}$ (mPEG₅₀₀-MA), poly(ethylene glycol) methacrylate $M_n = 500 \text{ g mol}^{-1}$ (PEG₅₀₀-MA), poly(ethylene glycol) methacrylate $M_n = 360 \text{ g mol}^{-1}$ (PEG₃₆₀-MA), di(ethylene glycol) methyl ether methacrylate (MP₂MA), 2-hydroxyethyl methacrylate (HEMA), n-propyl methacrylate (PMA), UV radical initiator diphenyl(2,4,6-trimethylbenzoyl)phosphine oxide (TPO), UV-absorber 2-*tert*-Butyl-6-(5-chloro-2*H*-benzotriazol-2-yl)-4-methylphenol (BLS 1326) were purchased from Sigma Aldrich. Rhodamine B-base (RhB) was purchased from Acros Organics. Ethyl (2,4,6-trimethylbenzoyl) phenylphosphinate, sometimes referred to as lucirin TPO (LTPO), was purchased from Combi-Blocks.

Phosphate buffered saline (PBS), 2-propanol, acetonitrile, water, and chloroform were purchased from Fisher Scientific. Solvents were HPLC grade purity or higher. All materials were stored as directed by the supplier and used as received.

Polycaprolactone-dimethacrylate $M_n = 700 \text{ g mol}^{-1}$ (PCL₇₀₀-DMA) was synthesized as described previously in chapter 2.

3.2.2 Continuous Liquid Interface Production

CLIP was utilized to print RhB-loaded devices to study how three design and formulation factors affect drug release kinetics: device geometry, crosslink density, and polymer network composition. For all experiments, a base resin containing no cargo was first formulated at the given ratios. Base resins are formulated as neat solutions with known amounts of photoinitiator, UV-absorber, and reactive diluents dissolved directly into the liquid oligomeric monomers at different ratios. In all cases, mol % is relative to moles of methacrylate. Since all resin components were soluble at the ratios used, resins were formulated by combining the

components in an amber glass bottle and mixing with magnetic stirring overnight at room temperature. For drug surrogate-loaded resins, once the base resin was formulated, the drug or surrogate was added at the given weight percent (wt %) and allowed to dissolve with magnetic stirring overnight at room temperature.

All devices presented were fabricated using a S1 CLIP prototype printer (Carbon) equipped with a 385 nm LED UV light source. STL files were sliced at 5µm using the Carbon printing software. The appropriate build rate and light intensity were based on the device design and resin formulation for each experiment.

3.2.3 CLIP fabrication of geometrically complex devices

3.2.3.1 Varying unit cell geometry with a constant unit cell size

To study the effect of varying geometries, four unique CAD models were generated that had the same overall dimensions, but varying internal geometries (Fig. 3.2). The models were generated using Magics Structures (Materialise) to array three different unit cells to fill a cylinder (5mm diameter, 10 mm height). The dimensions of the unit cells were kept constant at 1.5 x 1.5 x 1.5 mm. The theoretical values of surface area and volume was generated in the software platform.

The base resin was formulated with PEG₅₅₀-DMA with 1 wt % TPO initiator and 0.5 wt % BLS absorber. RhB was then added to a concentration of 0.5 wt %. Parts were arranged on the build platform using the Carbon software interface. All four parts were printed at a speed of 15 mm hr⁻¹ and a light intensity of 4 mW cm⁻². Speed was determined based on the appropriate speed to print the solid cylinder without defects due to resin renewal.

Parts were quickly dipped into isopropyl alcohol, removed from the build platform, and placed into a microcentrifuge filter insert with no membrane and spun at 4500 rpm for 10 minutes at 4 °C. Following the centrifugation, one set of devices was set aside without receiving a postcure and the remaining devices were subjected to a 2 minute postcure in the Hg UV oven.


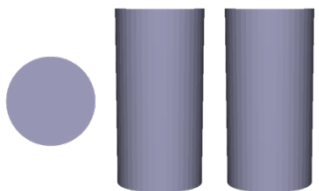
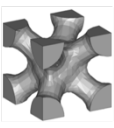
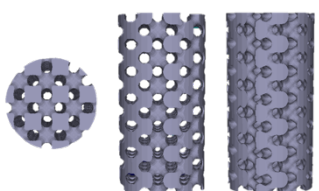
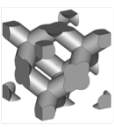
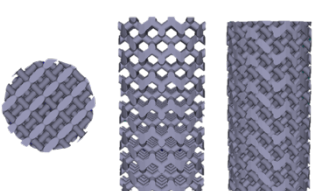
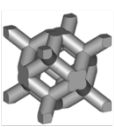
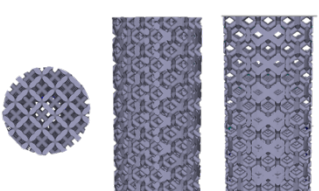
Unit Cell	CAD Model		Surface Area / Volume
Solid			1.00 mm ⁻¹
Node			6.45 mm ⁻¹
Diamond			9.36 mm ⁻¹
Rhombic			12.44 mm ⁻¹

Figure 3.2 Geometrically complex CAD models of varying unit cells. Three different unit cells of a constant size (1.5 mm) were arrayed to fill a cylinder (5 mm diameter, 10 mm height).

3.2.3.2 Varying unit cell size with a constant unit cell geometry and print parameters

To generate structures with similar volumes and a range of surface areas, three different sizes of the same geometric unit cell (0.5, 1, and 2 mm in all dimensions) was arrayed to fill a cylinder (5 mm diameter, 10 mm height). A fourth model was generated by stacking a 3 mm long section of the 1 mm unit cell cylinder between 2 mm long sections of the 0.5 mm and 2 mm unit cell cylinders (Fig. 3.3) of each model. Devices were printed using the same resin formulation as in section 3.2.3.1. Parts were printed at 15 mm hr⁻¹ and 4 mW cm⁻². Parts were processed using microcentrifuge tubes like above, but due to the smaller pore sizes, parts were centrifuged at 2500 rcf for 5 hours at 40 °C. Parts were then exposed to a UV postcure in a Hg oven for 2 minutes.

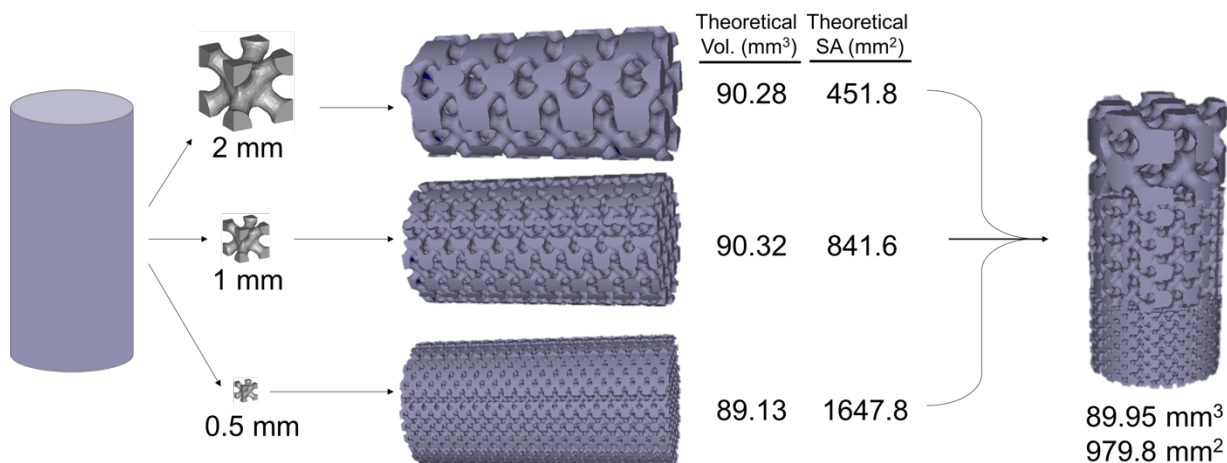


Figure 3.3 Schematic of CAD generation for geometrically complex devices. A single unit cell of varying sizes (0.5, 1, 2 mm) was arrayed to fill a cylinder (5 mm diameter, 10 mm height) to generate the final structures. A device filled with all three unit cell sizes was also made.

3.2.3.3 Constant unit cell geometry, theoretical volume, optimized print parameters

To study the effects of device surface area on the release of a model drug, a single resin was formulated and used to print three model devices with the same volume and various surface areas. The base resin contained 48.5 wt % PEG₅₅₀-DMA, 48.5 wt % HEMA, 0.5 wt % BLS, and 2.5 wt % LTPO. RhB was then added to the base resin at 0.2 wt % to serve as a drug surrogate. Geometrically complex STL models were generated using the CAD software Magics Structures (Materialise) by arraying a nodal unit cell to fill a cylinder (6mm diameter, 6mm height). While holding the dimensional proportions constant, three different sizes of the unit cell (1, 2, and 3 mm) were used to generate scaffolds with similar volumes and a range of surface areas (Fig. 3.4). Theoretical values of volume (V) and surface areas (SA) were generated in Magics and used in calculations of SA/V ratios.

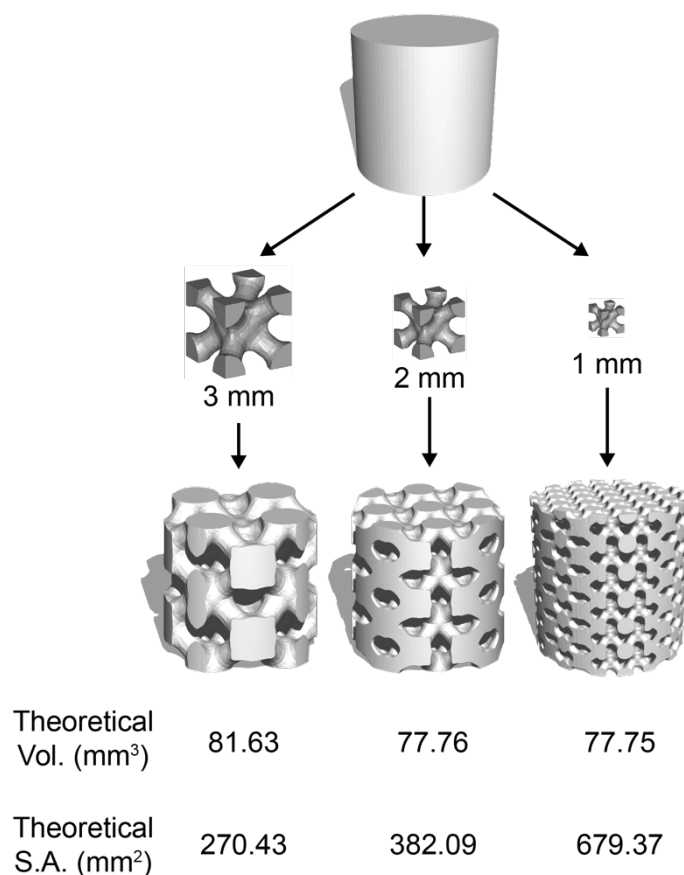


Figure 3.4 Generation of CAD files for model devices containing various surface areas and a constant volume. A nodal unit cell of either 1, 2, or 3 mm in length and height was arrayed to fill a cylinder with a 6 mm diameter and 6 mm height, generating three devices with similar theoretical volumes (Vol.) and different theoretical surface areas (S.A.).

Different print parameters for each unit cell size were optimized so that the mass of the fabricated parts was uniform between all three models, regardless of the size of the unit cell that was arrayed. To optimize the print parameters, each model was printed at a constant speed of 15 mm hr⁻¹ and the light intensity was varied from 5 to 17 mW cm⁻². Final print parameters for each model were decided by choosing the light intensity that resulted in parts with similar average mass across all unit cells sizes.

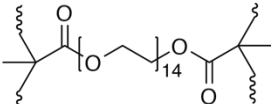
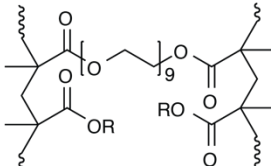
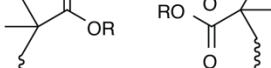
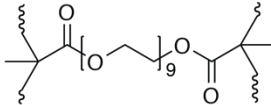
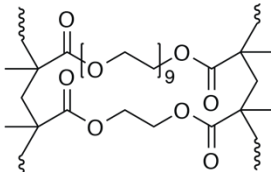
For the release study, devices filled with 1, 2, and 3 mm unit cells were printed at a light intensity of 7, 15, and 17 mW cm⁻², respectively. To avoid extraction of encapsulated RhB by solvent washes, residual resin was removed through centrifugation. Parts were removed from the build platform and placed directly into a microcentrifuge filter insert with no membrane

(Corning) and spun at 2000 rpm for 40 minutes at 30 °C. Devices were then post cured for 5 minutes (2.5 minutes on each side) in an UV oven fitted with an LED area cure unit (Phoseon Technology) with a narrow peak emission at 365 nm and a light intensity of 90 mW cm⁻² at the height of the devices.

3.2.4 CLIP fabrication of devices with varying crosslink density

To evaluate the effect of crosslink density, resins were formulated using PEG₇₅₀-DMA, PEG₅₅₀-DMA, and mixtures of PEG₅₅₀-DMA and the reactive diluents HEMA, MP₂MA, and EGDMA at 25 and 50 wt %. This provides a range of theoretical molecular weight between crosslinks (\bar{M}_C) as well as formulations that provide similar \bar{M}_C with a different pendant endgroup functionality (Fig. 3.5).

Table 3.1 Formulations and \bar{M}_C values for resins used in crosslink density experiment

A	B	Wt% B	M _c (g mol ⁻¹)	Schematic	
PEG ₇₅₀ -DMA (f = 4)	--	--	396		
	HEMA (f = 2)	25%	310		R = CH ₂ CH ₂ OH
		50%	339		
	MP ₂ MA (f = 2)	25%	306		R = (CH ₂ CH ₂ O) ₂ CH ₃
		50%	325		
PEG ₅₅₀ -DMA (f = 4)	--	--	296		
	EGDMA (f = 4)	25%	211		
		50%	166		

\bar{M}_C was defined according to equation (3.1).

$$\bar{M}_C = \frac{\bar{M}_{n,x} + M_r(1 + X)}{2} \quad (3.1)$$

where $\bar{M}_{n,x}$ is the average molecular weight of the crosslinking components ($f > 2$) and M_r is the molecular weight of the polymethacrylate backbone repeat unit not including any pendant groups. X is the crosslinking ratio and is defined as the molar ratio of methacrylates from chain-extending monomers ($f = 2$) to methacrylates from crosslinking agents ($f > 2$). A pictorial representation can be seen in Fig. 3.5.

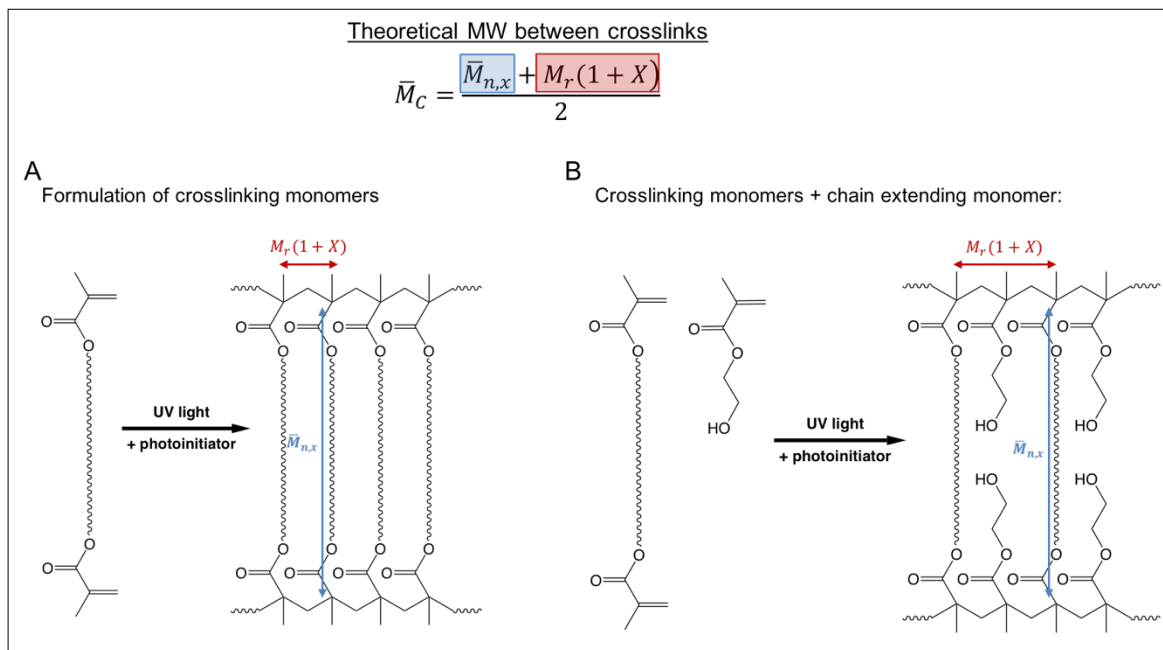


Figure 3.5 Schematic of \bar{M}_c calculation for a network made up entirely of crosslinking monomers (A) and one that contains chain-extending monomers (B). The molecular weight of crosslinking agents, $\bar{M}_{n,x}$, is defined as the average molecular weight of any multimethacrylate ($f > 2$) in the network and is illustrated with the blue arrow and text. The average molecular weight of the polymethacrylate backbone between crosslinking regions and is illustrated with a red arrow and text.

Example calculations for resins formulated with a single crosslinking monomer, two different crosslinking monomers, and a monomethacrylate reactive diluent added to the crosslinking monomer are given below.

For the network composed entirely of PEG₅₅₀-DMA ($M_n = 550 \text{ g mol}^{-1}$):

$$\bar{M}_c = \frac{550 + 41(1 + \frac{0}{1})}{2} = \frac{550 + 41}{2} = 296$$

For the network composed of 75 wt % PEG₅₅₀-DMA (52 mol %, $f = 4$, $M_n = 550 \text{ g mol}^{-1}$), and 25 wt % EGDMA (48 mol %, $f = 4$, $MW = 198.22 \text{ g mol}^{-1}$):

$$\bar{M}_{n,x} = (550)(0.52) + (198.2)(0.48) = 381.1$$

$$\bar{M}_C = \frac{381.1 + 41(1 + \frac{0}{1})}{2} = \frac{381.1 + 41}{2} = 211$$

For a network composed of 75 wt % PEG₅₅₀-DMA (59 mol %, $f = 4$, $M_n = 550 \text{ g mol}^{-1}$), and 25 wt % HEMA (41 mol %, $f = 2$):

$$\bar{M}_C = \frac{550 + 41(1 + \frac{0.41}{0.59})}{2} = 310$$

All resins contained TPO photoinitiator at 1 mol %. RhB was then dissolved into each resin at 0.5 wt %. A solid disk with a thickness of 1mm and a diameter of 5mm was designed in SolidWorks (Dassault Systèmes) to serve as a model device. Disks were arrayed in a 3x3 pattern on the build platform and printed with CLIP at a continuous speed of 15 mm hr^{-1} and a light intensity of 3 mW cm^{-2} . Upon completion of the print, the remaining uncured material on the surface of the part was removed by gently blotting the surface with a wipe. The part was then subjected to a 2 minute postcure under a mercury UV flood lamp (ELC-4001 equipped with UVA lamp, Electro-Lite Corporation, 365 nm peak wavelength, 43.3 mW cm^{-2}).

3.2.5 CLIP fabrication of devices with varying polymer network composition

To evaluate the effect of chemical structure and resin formulation, RhB-loaded solid disks were fabricated from PCL₇₀₀-DMA, with the addition of the monofunctional reactive diluents: mPEG₅₀₀-MA, PEG₅₀₀-MA, PMA, and HEMA at 15, 40 and 65 mol % and photoinitiator TPO at 1 mol % (Fig. 3.7). RhB was then dissolved into each resin at 0.5 wt %. Disks were printed with the same fabrication parameters as those in the crosslink density study.

Table 3.2 Formulations and \bar{M}_c calculations for resins used in the experiments to test the effect polymer network composition.

A	B	Mol% B	Wt% B	\bar{M}_c (g mol ⁻¹)	Schematic
PCL-DMA (f = 4)	--	--	--	371	
	PEG ₅₀₀ -MA (f = 2)	20%	26%	376	
		40%	49%	384	
		65%	73%	409	
	mPEG ₅₀₀ -MA (f = 2)	20%	26%	376	
		40%	49%	384	
		65%	73%	409	
	HEMA (f = 2)	20%	9%	376	
		40%	20%	384	
		65%	41%	409	
	PMA (f = 2)	20%	8%	376	
		40%	20%	384	
		65%	40%	409	

3.2.6 Characterization of CLIP devices

3.2.6.1 Swelling and gel fractions

To determine swelling in PBS, dry disks were first weighed (M_0) and subsequently incubated in 10 mL pH 7.4 PBS at 37 °C under constant oscillation (150 rpm) in an incubating shaker (VWR). After one week, the disks were removed and carefully blotted with a lab wipe, and the swollen mass was recorded (M_s). The disks were then washed with water to remove salts and dried under vacuum at 80 °C overnight and another 24h at room temperature. The final dry mass was recorded (M_d) and degree of swelling was calculated using equation (3.2).

$$\text{Degree of Swelling (\%)} = \frac{M_s - M_d}{M_d} \times 100 \quad (3.2)$$

Swelling and extraction of soluble components of geometrically complex devices was carried out in chloroform to confirm that monomer incorporation and crosslink density are not affected by the print parameters or model design. Scaffolds were swollen in 10 mL chloroform for 6 days at 37 °C under constant oscillation ($n = 3$). In the case of these geometrically complex shapes, the typical method of simply removing the surface liquid with a lab wipe was not sufficient due to their tendency to retain solvent in the small pores of the scaffold structure. Thus, after the device was removed from chloroform, the surface solvent was removed by exposing the device to a compressed air stream for 5 seconds. The swollen device was then transferred to a tared and capped vial to obtain the M_s . The parts were then dried under vacuum at room temperature overnight and the M_d was recorded. The gel fraction of printed parts was determined according to equation (3.3).

$$\text{Gel Fraction (\%)} = \frac{M_d}{M_0} \times 100 \quad (3.3)$$

3.2.6.2 Scanning electron microscopy

Parts were imaged by scanning electron microscope (SEM) with a Hitachi S-4700 SEM. Prior to imaging, parts were coated with 2 nm of a palladium-gold alloy using a Cressington 108 sputter coater.

3.2.6.3 Thermal analysis of printed parts

DSC measurements were carried out on a Discovery series DSC (TA Instruments). Disk fractions (~5 mg) were massed into an aluminum pan and sealed with a T-Zero hermetic lid. Samples underwent a heat-cool-heat cycle by heating from 30 °C to 100 °C, cooling to -90 °C, and subsequently heating to 100 °C at a rate of 10 °C/min, under nitrogen atmosphere. Trios software (TA Instruments) was used for analysis of glass transition temperatures (T_g) at the midpoint of the transition.

3.2.6.3 RhB extraction

RhB was extracted from the geometrically complex devices from section 3.2.3.1. To improve the extraction efficiency, RhB was extracted in parts that had not undergone a UV postcure. Devices were placed in 10 mL of methanol in a 15 mL conical tube and placed under shaking for 5 days at room temperature. The devices were then moved to 10 mL of fresh methanol and allowed to shake for another 30 days at 37 °C. The concentration of RhB in both extraction solutions was determined using a plate reader (BioRad Laboratories) to compare sample fluorescence (ex. 544 nm, em. 590 nm) to a standard curve in methanol.

3.2.6.3 In vitro RhB release

For geometrically complex devices, parts were placed into 20 mL of pH 7.4 PBS in a glass scintillation vial and placed in an opaque box to protect from light. For RhB-loaded disks, parts were added to 10 mL of pH 7.4 PBS in an opaque 15 mL polypropylene conical centrifuge tube containing a glass capillary support. The capillary tube was placed so as to maintain the

disk in a vertical position and avoid forming a plug in the bottom of the tube, creating different concentration gradients on either side of the disk.

The samples were placed in an incubating shaker (VWR) at 37 °C under constant oscillation at 150 rpm. At given timepoints, 1 mL of PBS release medium was removed and replaced with 1 mL of fresh PBS immediately. The concentration of RhB in the solution was determined with a plate reader by comparing sample fluorescence to that of a standard curve of fresh RhB in PBS. Curves were fit to the release data using the DDSolver plug-in for Excel (Weibull model) [20].

3.3 Results and Discussion

3.3.1 Effect of Geometry

One of the most notable benefits of using 3D printing is the freedom to fabricate objects with high geometric complexity, which would not be possible through traditional manufacturing methods such as extrusion or injection molding. Techniques like salt leaching and polymer foaming have been used for decades to generate porous structures with high surface areas [21]. However, these methods result in heterogeneous distribution of pore sizes and lack the control that is capable through 3D printing techniques (Fig. 3.6). Janusiewicz *et al* demonstrated the utility of CLIP to generate porous scaffolds based on CAD models [25]. They were also able to fabricate geometries beyond the capabilities of computer modeling by co-opting the continuous nature of CLIP to introduce gradients in pore sizes, which are not possible to model outside of the limited number of geometries defined by triply periodic functions. This control has important implications in the design and production of controlled release scaffolds. To characterize and demonstrate the application of complex geometries towards the design of controlled release drug delivery systems, models were design by arraying various unit cells to fill

a macro-shape (cylinders). Three approaches were taken: 1) holding the unit cell size constant while varying the unit cell geometry; 2) holding the unit cell geometry constant while varying the unit cell size, using the same print parameters for all; and 3) holding unit cell geometry constant while varying the unit cell size, using optimized print parameters resulting in constant resulting part volumes.

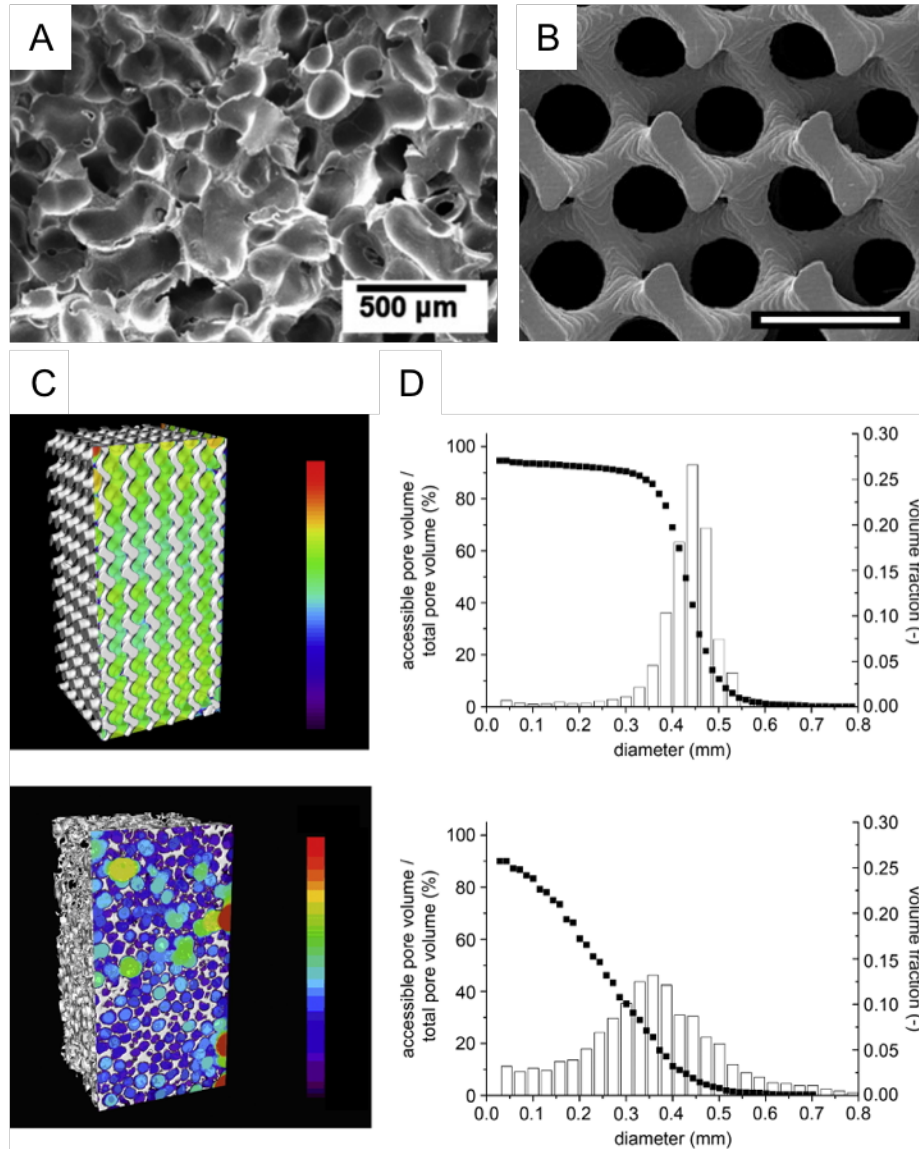


Figure 3.6 Comparison of 3D printed and polymer foam scaffolds. (A) SEM image of hydroxyapatite scaffold. Image reused from [22]. (B) SEM image of PDLLA network scaffold with a gyroid structure fabricated by SLA. Scale bar represents 500 μm. Reproduced with permission from [23]. (C) Pore size maps of μCT analysis and (D) distributions and accessibility curves of built PDLLA gyroid structures and salt-leached scaffolds. Reproduced with permission from [24].

3.3.1.1 Varying unit cell geometry with a constant unit cell size

By arraying various unit cells of the same dimensions into a macro geometry, different models were generated to contain different surface area to volume ratios. Model scaffolds were printed containing 0.5 wt % RhB as a small molecule drug surrogate and were imaged with SEM (Fig. 3.7 A) and a digital camera equipped with a macro (10X) lens (Fig. 3.7 B). Under higher SEM magnification, a patterned texture can be observed in certain regions of the devices (Fig. 3.7 C). These patterns appear on the side of the device facing away from the window and light source, towards the build platform. These appear to be a result of the pixels, and digital measurement reveals that they are approximately 20 μm wide, which is the size of the projected pixel in the S1 printer used. This texture will likely not have an observable effect on devices of this size, but may become important when trying to fabricate parts at a smaller scale.

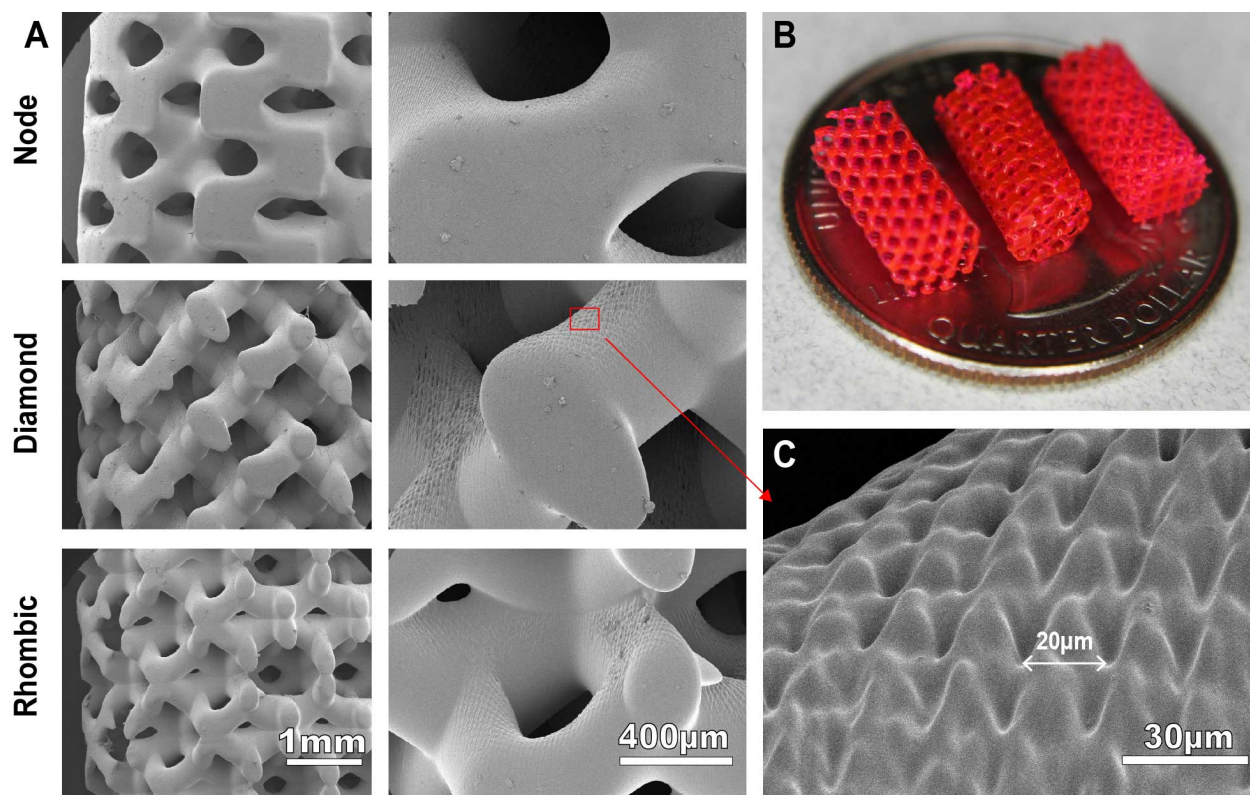


Figure 3.7 Geometrically complex model devices made from three unique unit cell geometries with constant unit cell size. (A) SEM images devices 1.5 mm node, diamond, and rhombic unit cells. (B) Visible light image of devices on a US quarter for scale. (C) High magnification SEM image showing the device surface texture due to pixel effects.

If the approach of using geometry to modify drug release is to be implemented in a clinical setting, it is necessary to ensure that the device geometry is independent of polymer network of the resultant part at the molecular level. To probe the monomer incorporation and crosslink density of the resulting parts, the gel content and solvent uptake were observed in ethanol. Results in Fig. 3.8 indicate that the post processing parameters are important to the uniformity of the resulting polymer network. Devices of different geometries that did not undergo the 2 minute postcure in the Hg UV oven indicate a significant difference among the various geometries in both ethanol uptake and the gel fraction of the part. However, devices subjected to the postcure process appear to have a crosslink density and monomer incorporation that is independent of device design and geometry. Statistical analysis indicated no significant difference between the various shapes, with the exception of solvent uptake in the solid cylinder compared to the diamond unit cell.

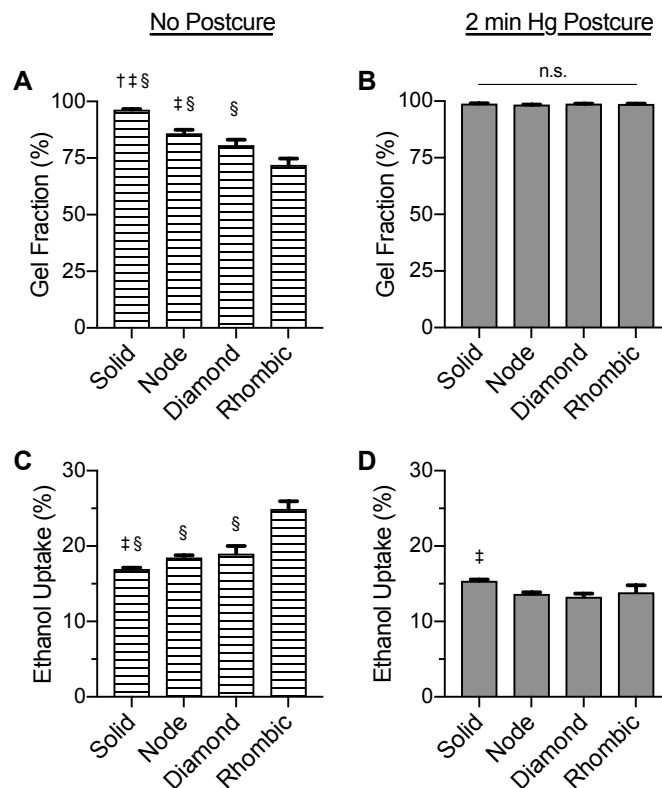


Figure 3.8 Solvent uptake and gel fraction of geometrically complex devices generated by arraying different unit cell geometries. Characterization of the gel fraction (A and B) and solvent uptake (C and D) of devices that received no postcure (left) and those that were subjected to a 2 minute postcure in a Hg UV oven. Statistics were performed using one way ANOVA using Sidek's multiple comparison test. † indicates significance versus Node, ‡ indicates significance versus Diamond, and § indicates significance versus Rhombic.

Further, when the gel fraction is plotted against the theoretical SA/V ratio (Fig. 3.9), parts that were not postcured show a significant correlation between the gel fraction and SA/V ($P = 0.0047$). In postcured samples, correlation is not significantly non-zero ($P = 0.8324$) indicating that there is no correlation between the gel fraction and part geometry following the 2 minute postcure.

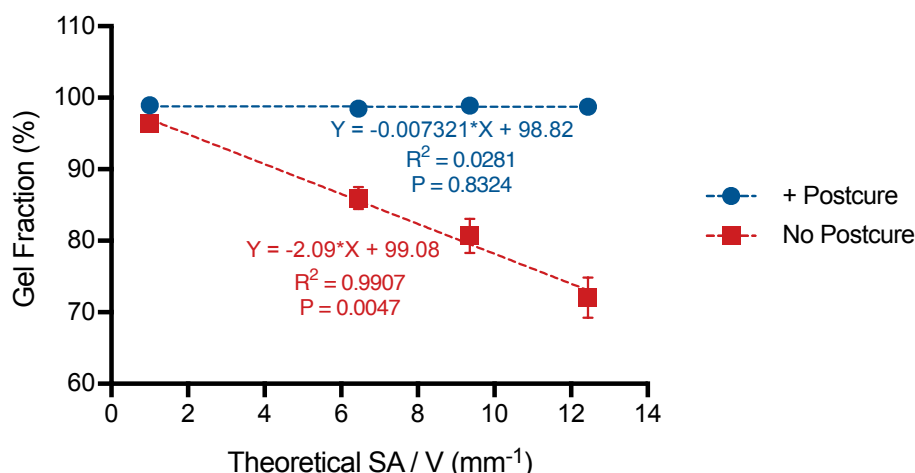


Figure 3.9 Linear correlation between the theoretical surface area to volume ratio and gel fraction.

The mass and RhB loading characterization of the devices can be seen in Fig. 3.10. The difference in device mass can be attributed to the different part volumes that result from arraying unit cells with different geometries to fill the same macro geometry (cylinder with 5 mm diameter, 10 mm height) (Fig. 3.10 A). Because all devices were fabricated from the same resin formulation (0.5 wt % RhB), the mass of RhB loaded in the device also varies depending on the device design (Fig. 3.10 B). Further, the drug loading trends with the device mass, which is expected for monolithic solution, or “one-block” systems, in which the drug mass is directly dependent on device volume. Drug loading was calculated by dividing the mass of RhB that was extracted from device by total part volume prior to extraction (Fig. 3.10 C). The RhB loading was similar for all device geometries with an average of 0.45 ± 0.04 wt %.

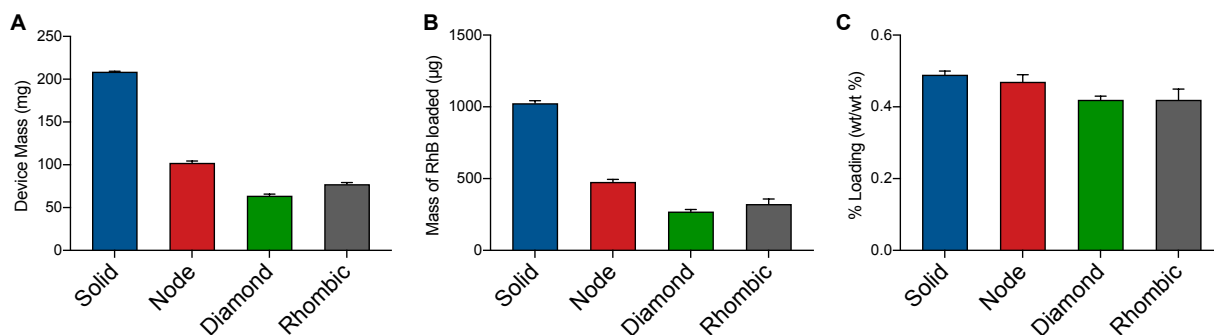


Figure 3.10 Mass and RhB loading in geometrically complex devices with constant unit cell size. (A) Device mass (n=3) (B) Mass of RhB extracted from devices (n=3) and (C) percent loading by weight.

In vitro results indicate that the rate at which RhB is released increases with the increasing SA/V ratio over the first 48 hours (Fig. 3.11 A). Being a highly crosslinked, non-degradable network, the drug release is expected to be through a diffusion mechanism. When the SA/V ratio is increased, the average diffusion distance of the RhB will decrease. Thus, these results are in agreement with the expected outcome. The fraction of RhB released from devices filled with node and diamond unit cells were not statistically significant at any time point analyzed (multiple T-tests with Holm-Sidek method). By 28 days RhB release from all three geometrically complex devices plateaued, while the solid device was still releasing RhB (Fig. 3.11 B).

The difference between the release rates for the devices with different unit cells is a clear indicator of the control the geometry can provide in modifying the release of a drug. However, when plotted as total mass of RhB released, the results demonstrate a possible drawback of this approach. While the solid device has a slower release with approximately 28 % of loaded cargo released compared to 68 % from the high SA/V rhombic device, a total of 296 μg RhB diffused from the solid device compared to 280 μg released from the device arrayed with rhombic unit cells (Fig. 3.11 C). This would present a challenge for implementing this as a technique to modify release to the specific needs of individual patients, because tuning the release rate would also result in a different overall dose.

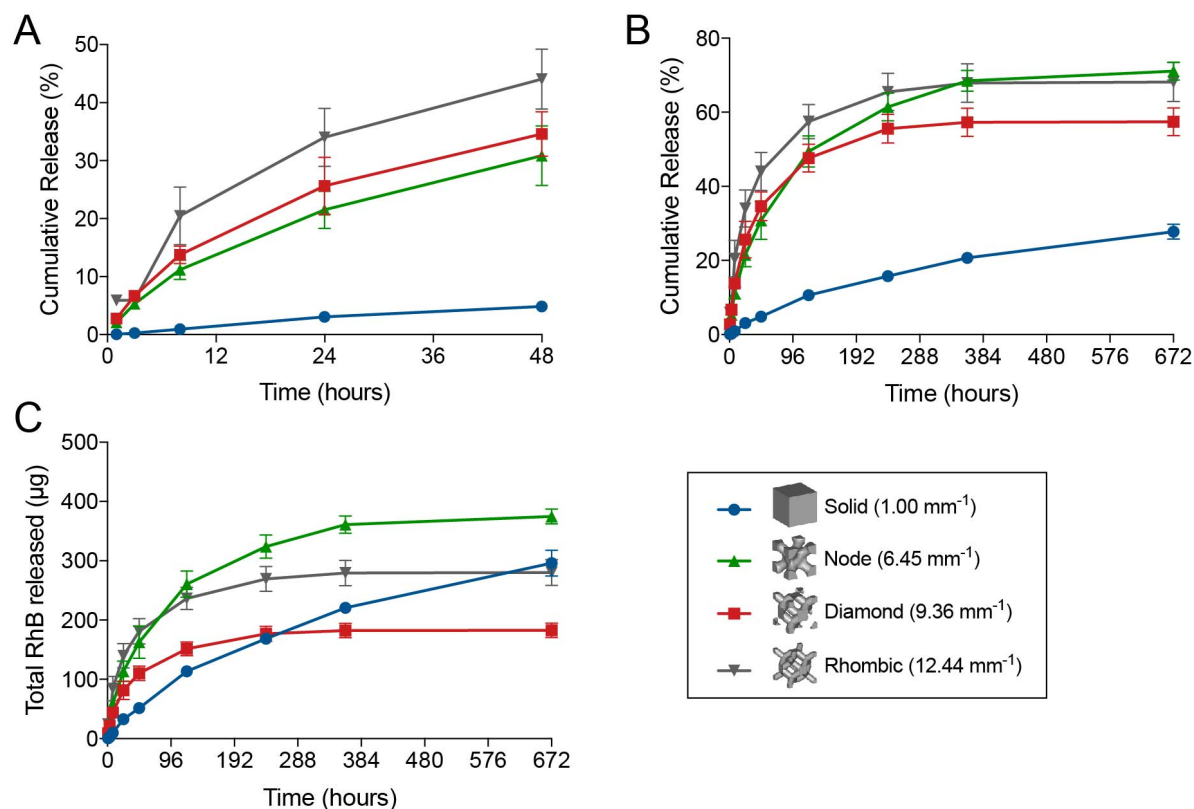


Figure 3.11 *In vitro* RhB release from geometrically complex devices with uniform unit cell size. RhB release was calculated relative to the theoretical RhB loading over 48 hours (A) and 28 days (B). RhB release presented as total mass (in µg) released over 28 days (C).

3.3.1.2 Varying unit cell size while holding unit cell geometry and print parameters constant

An alternative approach to achieve different SA/V ratios within the same macro-geometry is to vary the unit cell size while holding the unit cell geometry constant (Fig. 3.12). This generates CAD models with similar theoretical volumes and thus drug loading, while varying the theoretical surface areas. Four different CAD models were generated for this experiment by arraying a diagonal node unit cell to fill the same 5 x 10 mm cylinder as used in section 3.3.1.1. Three models were generated by uniformly filling the same 5 x 10 mm cylinder as used in section 3.3.1.1 with diagonal node unit cells of 0.5, 1, or 2 mm dimensions. Additionally, a fourth model was generated by filling the cylinder with portions of all three sizes to demonstrate the ability to mix geometries to combine release characteristics to engineer a device with optimal release kinetics.

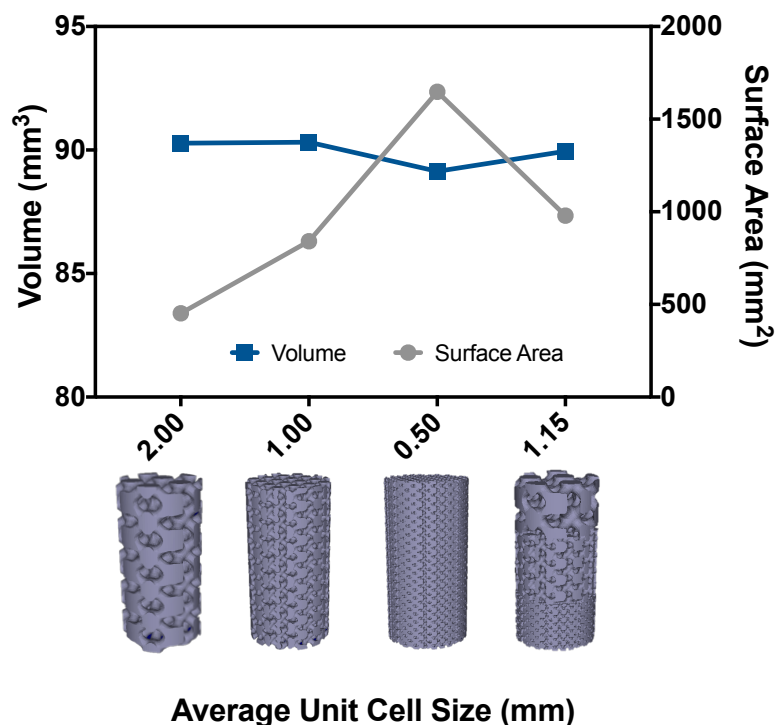


Figure 3.12 Effect of unit cell size on theoretical part volume and surface area. When using the same unit cell geometry, different unit cell dimensions will generate structures with similar volumes and differing surface areas.

Images of the devices containing varying sizes of the same unit cell, fabricated with identical parameters (15 mm hr^{-1} , 4 mW cm^{-2}) can be seen in Fig. 3.13. Because the RhB release from this fully crosslinked system is diffusion-based, it would be expected that release rate would trend inversely with the unit cell size. As the size of the unit cell decrease, the surface area and drug release rate would increase.

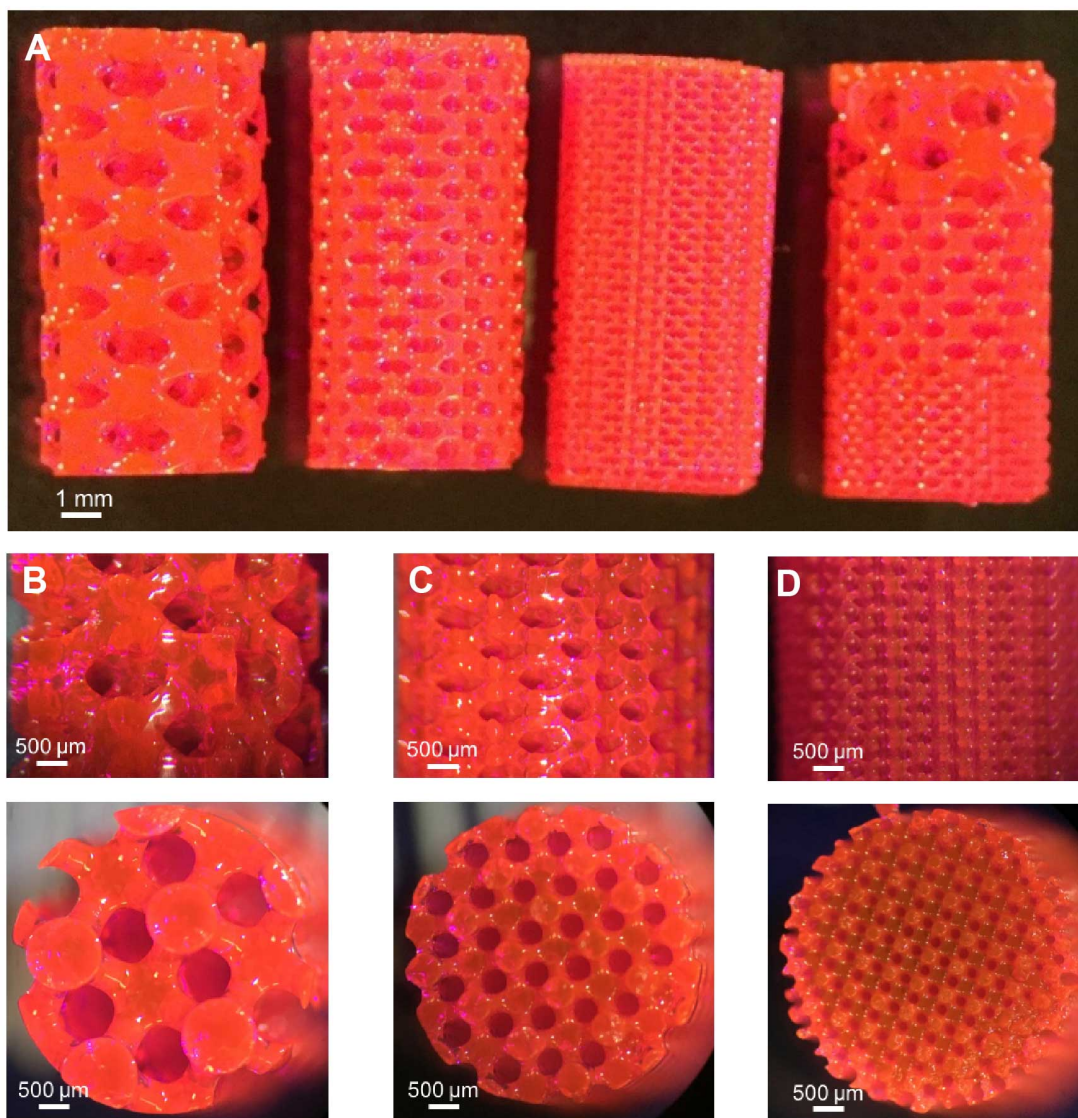


Figure 3.13 Visible light photograph of devices with constant print parameters, constant unit cell geometry, and various unit cell dimensions. (A) Image of three devices printed with uniform unit cell dimensions with decreasing in size from left to right, and a device made with a combination of all three unit cell dimensions in the farthest right device. Zoomed image of devices with uniform 2 mm (B), 1 mm (C), and 0.5 mm (D) unit cells.

Results of the *in vitro* release study (Fig. 3.14 A) support this hypothesis for devices with 1 and 2 mm unit cells. Surprisingly however, the device fabricated with the smallest unit cell (0.5 mm) showed the slowest release despite having the highest theoretical SA/V ratio. This does not align with the expectation for a device with a lower theoretical diffusion distance. When comparing the theoretical volume to the experimental part mass (Fig. 3.14 B), it appears that the cause is inaccuracies in the print. This is likely due to cure-through in the z-plane. Because all

devices were fabricated using the same light intensity, speed, and resin, the light penetration depth light will remain the same for every model. As the unit cell size decreases, the depth of the cure-through becomes larger relative to the desired void volume. Thus, the overall part mass trends inversely with the unit cell size. It is important to note that release from devices fabricated with the combination of all three unit cells still falls right in the middle of the three, demonstrating that the effects of geometry can be combined. This also supports the hypothesis that the change in part mass is a result of the printing process rather than any effects of incomplete resin removal during prost processing. This is promising for future work that may include generating models of the effects of device geometry to facilitate algorithm-based dosage design for personalized devices

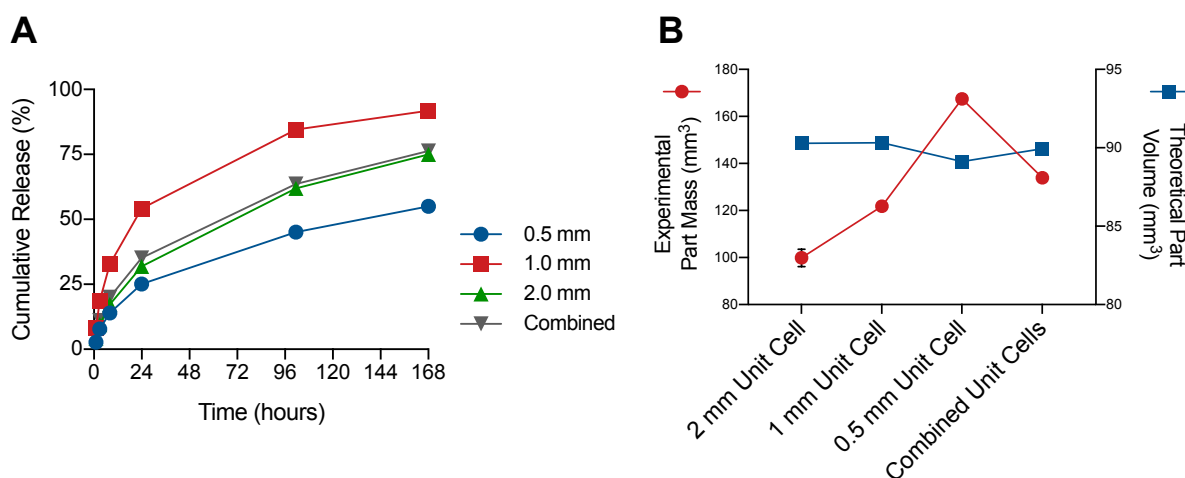


Figure 3.14 *In vitro* RhB release and fabricated part mass. (A) Release rate of RhB in pH 7.4 PBS shows a dependence on the unit cell size of the CAD model. (B) Although the models have similar theoretical volumes, the resulting part mass appears dependent on the unit cell size.

3.3.1.3 Constant unit cell geometry, theoretical volume, optimized print parameters

As with the previous experiment, parts were designed by arraying the same macro geometry with node unit cells of differing sizes. By using the same unit cell geometry, parts are expected to have similar part volumes while surface area is inversely correlated with unit cell size. To address the issue of cure-through discussed in section 3.3.1.2, print parameters were optimized for each device by varying the light intensity with a constant print speed of 15 mm hr⁻¹.

The resulting mass of the devices was used as an indicator of their volume. The mass of devices printed with light intensities between 5 and 17 mW cm⁻² indicated that similar device mass can be achieved for cylinders with node unit cells of 1, 2, and 3 mm by using a light intensity of 7, 15, and 17 mW cm⁻², respectively (Fig. 3.15 A). Average masses of 16 devices printed for each model were not significantly different (Fig. 3.15 B). Of note, there did appear to be an association between part mass and its location on the build platform, with the effect seemingly magnified with the smaller unit cell (Fig. 3.15 C-F).

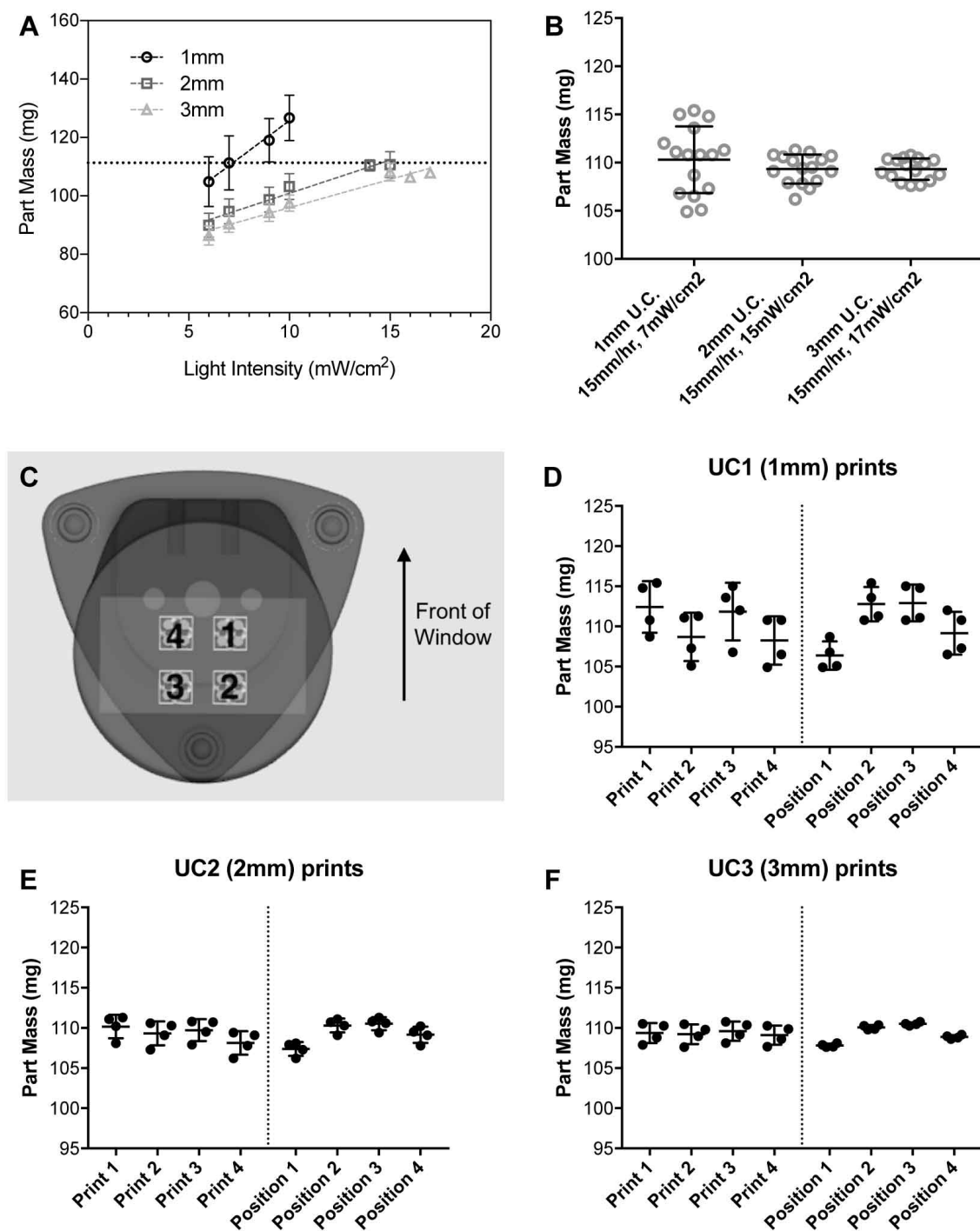
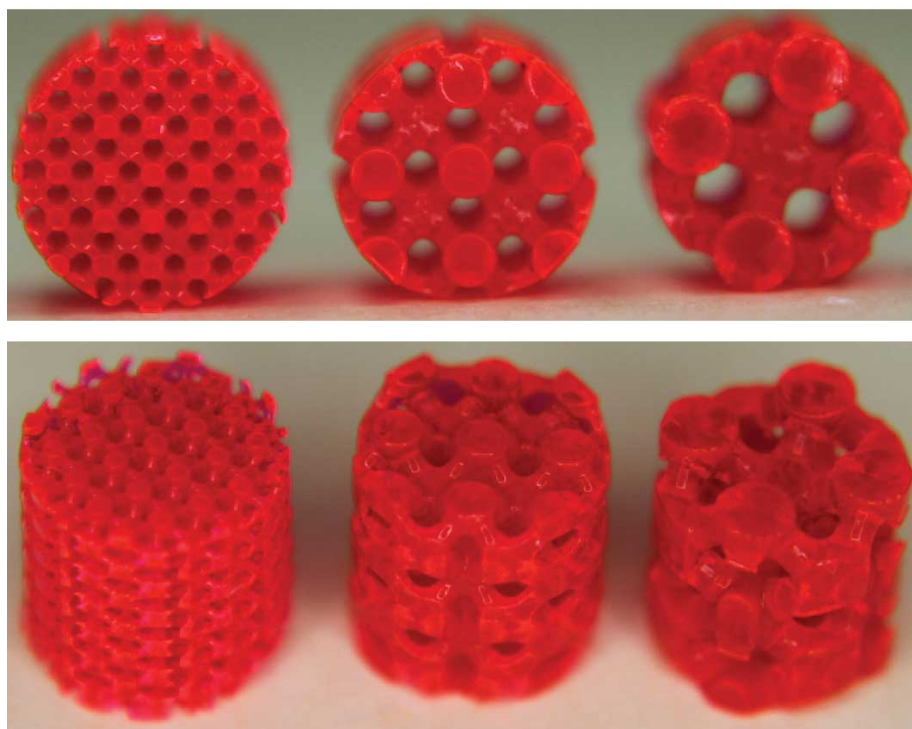


Figure 3.15 Optimization of print parameters to achieve similar device mass. (A) Dependence of part mass on light intensity used to print devices generated using different sizes of the same unit cell printed using a constant build rate (15 mm hr^{-1}). (B) Part mass of devices printed for *in vitro* release studies ($n=16$). (C) Position labels for parts relative to the build platform. Masses of printed devices grouped by print number and their position on the build platform for device built from 1 mm (D), 2 mm (E), and 3 mm (F) unit cells.

Model cylindrical scaffolds fabricated to contain 0.2 wt % RhB as a surrogate small molecule therapeutic (Fig. 3.16) were printed at similar part mass, and thus RhB loading (Fig. 3.18 B). The gel content and solvent uptake characteristics of the devices were used as indicators of the monomer incorporation and crosslink density of the polymer networks. Acetone, ethanol, and chloroform were screened to determine the best solvent to swell the devices in, which was found to be chloroform (Fig. 3.17).

A



B

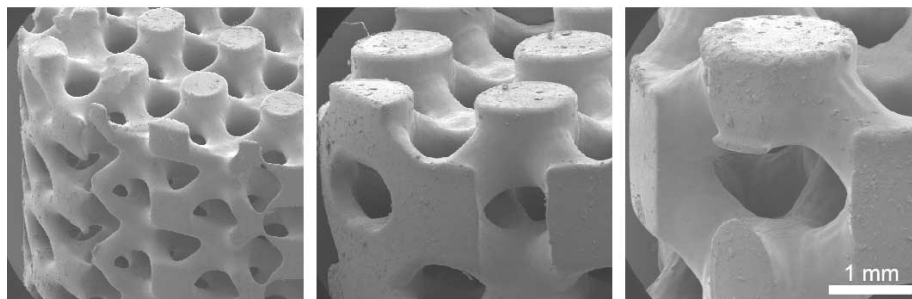


Figure 3.16 Geometrically complex model devices loaded with RhB as a surrogate drug. Visible light photograph (A) and SEM image (B) of 1, 2, and 3mm unit cells arrayed to fill a 6 mm x 6mm (diameter x height) cylinder, from left to right.

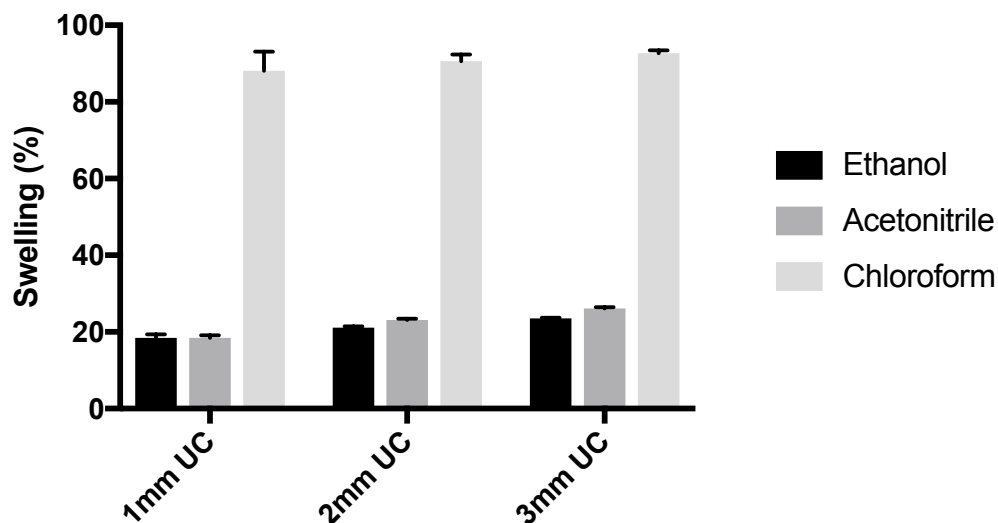


Figure 3.17 Solvent swelling of geometrically complex devices generated by arraying node unit cells of 1, 2, and 3 mm fabricated with optimized parameters to control for part mass.

Devices printed with three different geometries show a gel content over 91 % and similar chloroform uptake at approximately 92 % by weight (Fig. 3.18 A). The similarities in swelling and gel content between devices with different geometries supports the assumption that the polymer networks are identical on a molecular level, regardless of feature size. Consequently, the observed difference in RhB release *in vitro* can be attributed to the device geometry (Fig. 3.18 C). The cylindrical device based on the smallest unit cell, and hence the highest surface area, shows a rapid release, with the majority of the RhB released within the first 3 days. The cylinder with the largest unit cell (lowest surface area) shows a slower gradual release over the course of 28 days. These results are in accordance with the principles of diffusion-controlled drug release systems [26-29]. Decreasing the unit cell size reduces the average diffusion distance for a small molecule drug to move through the polymer network to reach the aqueous tissue phase. An important characteristic of the design scheme presented here is the ability to design drug-loaded devices with numerous possible drug release profiles all with the same total delivered drug dose. This method of design-dictated release benefits from the reproducible precision in architecture fabrication afforded by 3D printing and CLIP, which is not possible with traditional methods of scaffold fabrication such as salt leaching or electrospinning. The reproducible nature

of this method of fabricating complex devices will be beneficial to 3D printing technology when it is evaluated from a regulatory standpoint.

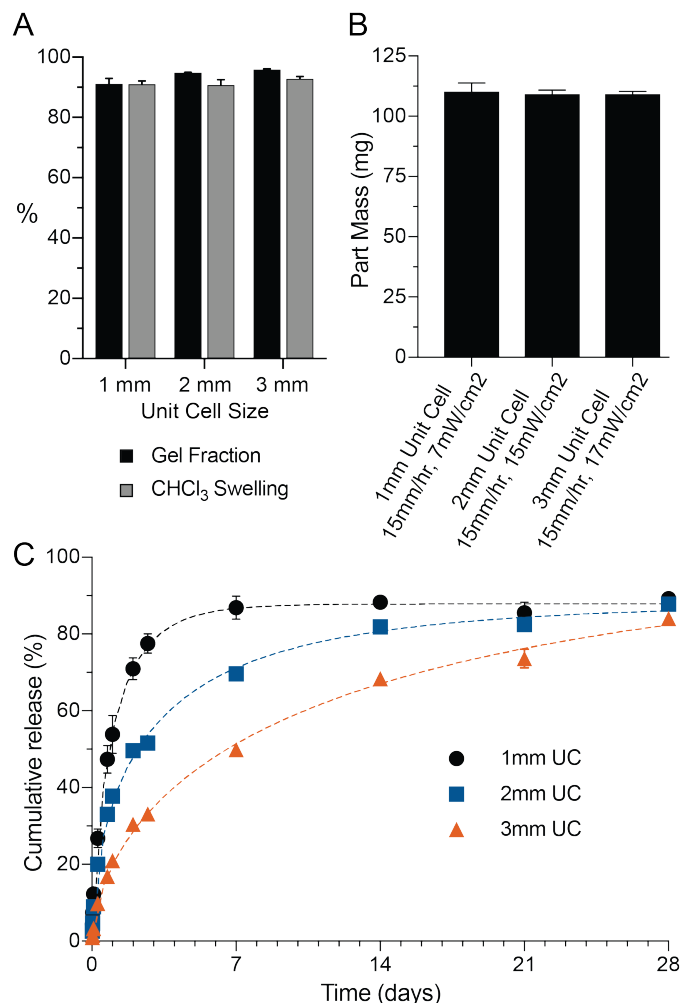


Figure 3.18 Characterization of geometrically complex model devices. (A) Chloroform uptake and gel fraction ($n = 3$). (B) Average mass of parts printed at the indicated print parameters ($n = 16$). (C) Cumulative RhB release *in vitro*. Cumulative release data was fit to the Weibull_3 mathematical model using the DDSolver plug-in in Excel.

3.3.2 Effect of crosslink density

CLIP and other photopolymer-based additive manufacturing techniques utilize UV light to initiate radical polymerization of unsaturated moieties, such as methacrylate groups. Primarily, the formation of the solid part relies on covalent crosslinks in the network, which are introduced by monomers or low molecular weight oligomeric macromers with at least two

photopolymerizable groups. The concentration of the crosslinking agent can be modulated to control the rate of diffusion and release of a small molecule drug that has been incorporated into the resin. To demonstrate and characterize the ability to control the release of small molecule drugs by controlling the crosslink density, PEG-based CLIP resins were formulated to vary the average molecular weight between crosslinks (\bar{M}_C). RhB was dissolved into all resins to serve as a surrogate for a small molecule drug. We varied the theoretical \bar{M}_C of the polymer network in two ways: by changing the molecular weight of the dimethacrylate crosslinker in fully crosslinked systems (PEG₇₅₀-DMA, PEG₅₅₀-DMA, PEG₅₅₀-DMA/EGDMA), and through the addition of chain-extending monomethacrylate diluents to the crosslinking oligomer, PEG₅₅₀-DMA (PEG₅₅₀-DMA/HEMA and PEG₅₅₀-DMA/MP₂MA). The first method, in which the polymer network is formulated entirely of crosslinking oligomers/monomers ($f = 4$), uses the length of the PEG oligomer between the terminal methacrylate functional groups to dictate the molecular weight between the crosslinks, assuming 100 % conversion of methacrylate groups (Fig. 3.5). In the second case, the length of the oligomer between methacrylate groups is constant, but chain-extending monomers are introduced ($f = 2$). Incorporation of these monomethacrylate monomers statistically increases the distance between crosslinks in the network (Fig. 3.5). If we consider \bar{M}_C to be the average of the molecular weight of crosslinking oligomer and the molecular weight of the chain-extended backbone between the crosslinking agents it is possible to compare theoretical \bar{M}_C assuming the ideal and complete reactions (Fig. 3.5).

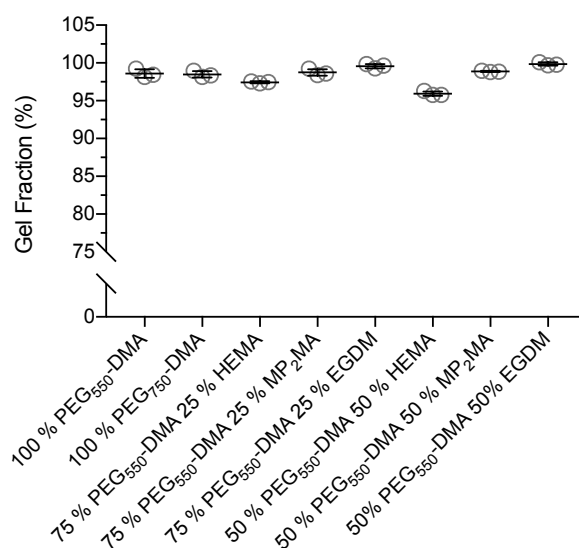


Figure 3.19 Gel fractions of RhB-loaded disks with different crosslink densities.

Regardless of the formulation used, all printed parts produced a high gel fraction of at least 95 % (Fig. 3.19). DSC analysis of the printed disks indicated a higher glass transition temperature (T_g) of -17.8 °C for PEG₅₅₀-DMA compared -39.3 °C for PEG₇₅₀-DMA. Further, the T_g was increased with the addition of HEMA, while slightly decreasing with the addition of MP₂MA (Fig. 3.20 A). The T_g effects are a function of both chemical make-up and crosslink density. As expected due to the increased theoretical \bar{M}_C , PBS swelling trends upward with increasing PEG molecular weight and with the addition of monomethacrylate chain-extenders. Conversely, disks containing the low molecular weight crosslinker EGDMA show minimal uptake of PBS. The effect of crosslink density is evidenced by overlaying the theoretical \bar{M}_C with the PBS swelling (Fig. 3.20 B).

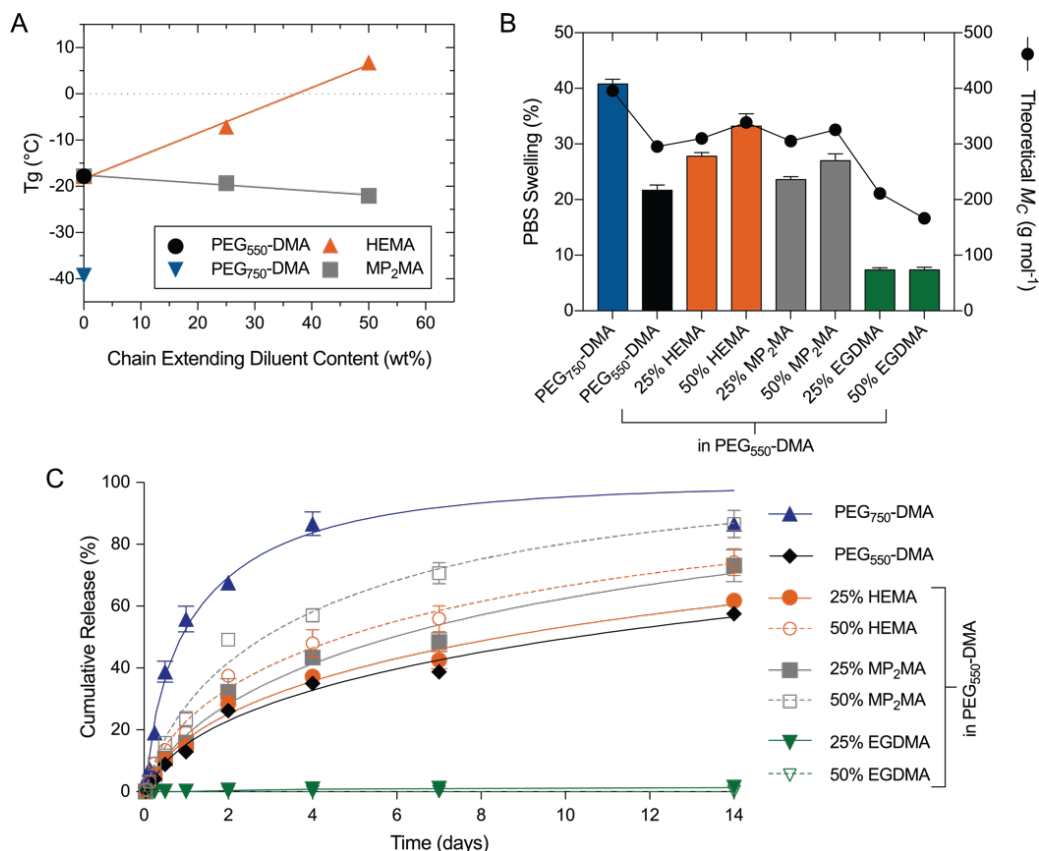


Figure 3.20 Characterization of RhB-loaded model devices with different crosslink density. (A) Dependence of the T_g of the printed part on the amount of chain-extending diluent. (B) Theoretical \bar{M}_c overlaid with the disks swelling in PBS. (C) Cumulative RhB release *in vitro*. Cumulative release was fit to the Weibull_1 mathematical model using the DDSolver plug-in in Excel.

As the primary mechanism of drug release from non-degradable, highly crosslinked networks is diffusion, swelling is expected to be directly correlated with release kinetics. Results of the *in vitro* release study (Fig. 3.20 C) show that disks fabricated with 100 % PEG₇₅₀-DMA, which has the highest swelling in PBS and highest \bar{M}_c , release RhB the fastest with approximately 60 % of the model drug being released in the first 24 hours and 80 % by 4 days. Interestingly, while the addition of HEMA to PEG₅₅₀-DMA increases the swelling in PBS compared to the addition of MP₂MA, parts fabricated from blends of PEG₅₅₀-DMA and MP₂MA showed a higher release rate. This exemplifies the importance of the pendant group on the chain-extending diluent. The slower release from disks containing HEMA is likely a result of hydrogen bonding between the hydroxyl group of HEMA and the RhB molecule, leading to a tighter association between the model drug and the network.

3.3.3 Effect of polymer network composition

Along with the crosslink density, the chemical structure and properties of the polymers will dictate the rate at which the drug molecule is able to diffuse out of the network. To study the effect of resin formulation and the resulting polymer network on drug release, we analyzed RhB release from devices fabricated using five different resins based on polycaprolactone-dimethacrylate: PCL₇₀₀-DMA, PCL₇₀₀-DMA/PEG₅₀₀-MA, PCL₇₀₀-DMA/mPEG₅₀₀-MA, PCL₇₀₀-DMA/HEMA, and PCL₇₀₀-DMA/PMA (Fig. 3.7).

These blends were chosen to study the effect of the addition of hydrophilic PEG groups into the hydrophobic PCL network. The resins were formulated so that the ratios of methacrylates from the crosslinking PCL₇₀₀-DMA to those of the chain-extending diluents were held constant at 80:20, 60:40, and 35:65. Thus, assuming ideal and complete reactions, we can directly compare formulations with the same theoretical \bar{M}_c , with or without the presence of PEG. Further, the effect of pendant functional groups was observed through the comparison of methoxy-terminated PEG to hydroxy-terminated PEG, and HEMA to PMA.

Disks were successfully printed with each formulation, apart from the resin with the highest concentration of PMA, which resulted in a very brittle disk with cracks. The swelling and DSC results demonstrated that addition of hydrophilic PEG greatly increases the uptake of PBS (Fig. 3.21 A) and decreases the T_g of the network (Fig. 3.21 B). Networks containing increasing amounts of HEMA and PMA, which have the same theoretical molecular weight between crosslinks, show an increase in T_g (Fig. 3.21 B) and minimal differences in PBS uptake (Fig. 3.21 A).

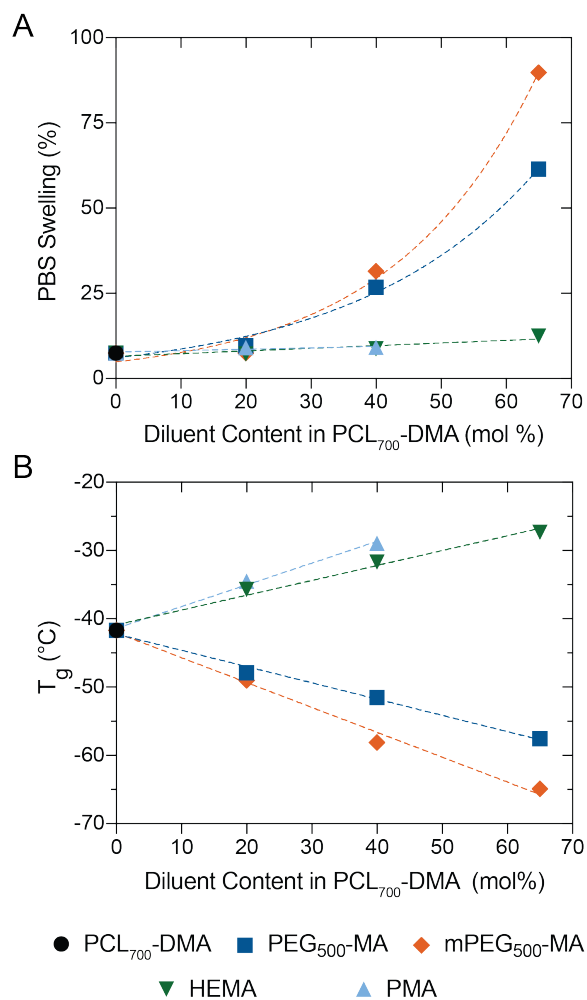


Figure 3.21 Dependence of the PBS uptake (A) and T_g (B) of model devices on diluent content in PCL₇₀₀-DMA.

In the *in vitro* release study, an increased release of RhB was observed with addition of monomethacrylate PEG compared to fully crosslinked PCL₇₀₀-DMA (Fig. 3.22 A). Interestingly however, addition of small molecule chain-extenders, PMA and HEMA, resulted in a decreased RhB release (Fig. 3.22 A and B). This is contrary to purely PEG-based hydrophilic networks where the increased \bar{M}_c from addition of small chain-extending monomers, like HEMA, is correlated with increased swelling and RhB release. This indicates that in primarily hydrophobic networks, like PCL, it is not the crosslink density, but rather the material composition that is the more important variable in controlling the RhB release and part swelling. Also, the end group of the chain-extending diluent appears to play an important role in RhB release in these networks,

as the addition of PMA shows a slower release compared to networks containing the same amount of HEMA (Fig. 3.22 B).

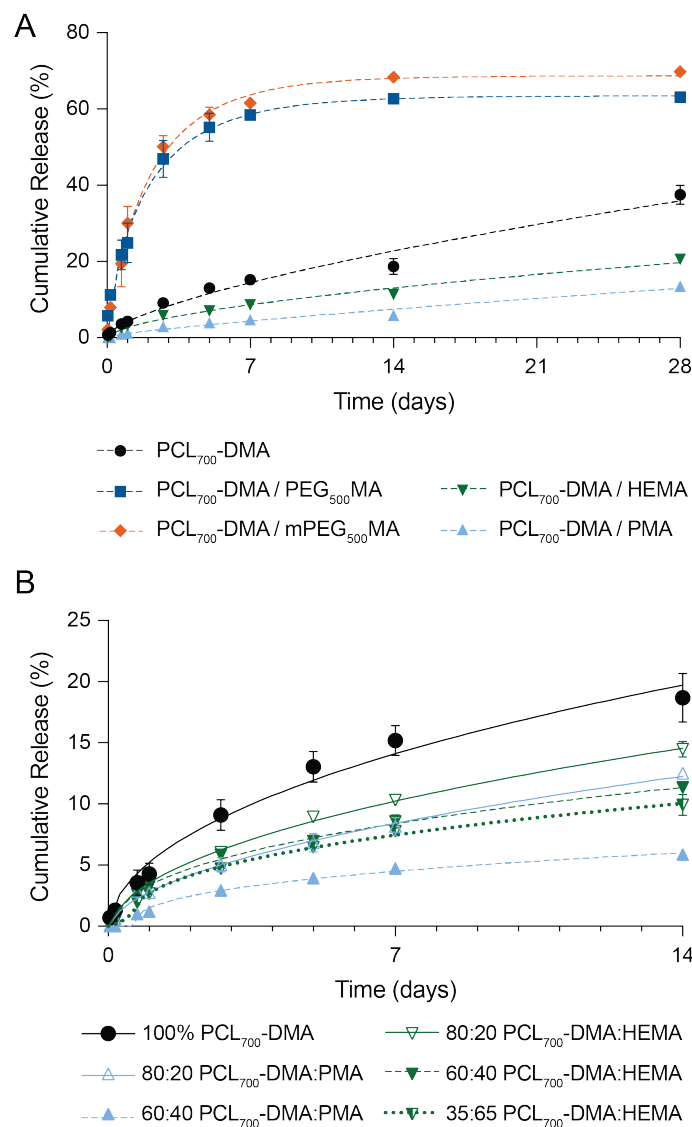


Figure 3.22 Effect of polymer network composition on *in vitro* RhB release from PCL₇₀₀-DMA based formulations with the addition of 50 mol % reactive diluent (A) and PCL₇₀₀-DMA with the addition of increasing amounts of small molecular weight chain-extending monomer (B). Data was fit to the Weibull_3 mathematical model for resins containing mPEG₅₀₀MA or PEG₅₀₀MA; all others fit to Weibull_1 mathematical model using the DDSolver plug-in for Excel.

3.4. Conclusions

3D printing has the potential to play a major role in an anticipated shift towards patient-tailored medicine with the ability to manufacture personalized medical devices and pharmaceutical dosage forms [10,11,30]. Here we demonstrated the feasibility and potential advantages of utilizing CLIP to formulate and fabricate encapsulated drug-loaded devices for controlled and prolonged release applications. *In vitro* drug diffusion studies showed that release of a drug surrogate, RhB, can be tuned with device geometry while holding drug loading constant by changing the size of the unit cell used to create scaffolds. Crosslink density and polymer network composition were also both shown to be additional means to tune the release of RhB. Crosslink density had different impacts on PEG- and PCL-based networks, with PBS swelling and drug release increasing in hydrophilic PEG-based network and decreasing in hydrophobic PCL-based networks, with the addition of chain-extending monomers.

In conclusion, CLIP provides an interesting and promising 3D printing platform for the fabrication of personalized devices for controlled release applications. Moving forward, *in vivo* drug release data will be an important step towards the use of this approach for applications such as implantable drug delivery devices. It may be interesting to try to apply existing models or create new models to characterize the effects of device geometry and formulation on drug release [31,32]. It will also eventually be necessary to develop algorithms and computer programs that apply these models to patients' imaging and medical data. A physician would then be able to enter patient data and generate devices that can have both a personalized shape and release characteristics dependent on that patient's needs.

REFERENCES

- [1] K.E. Uhrich, S.M. Cannizzaro, R.S. Langer, K.M. Shakesheff, Polymeric Systems for Controlled Drug Release, *Chem. Rev.* 99 (1999) 3181–3198. doi:10.1021/cr940351u.
- [2] J.R. Weiser, W.M. Saltzman, Controlled release for local delivery of drugs: barriers and models, *Journal of Controlled Release*. 190 (2014) 664–673. doi:10.1016/j.jconrel.2014.04.048.
- [3] J.C. Wright, D.J. Burgess, Long Acting Injections and Implants, Springer Science & Business Media, 2012.
- [4] G. Acharya, K. Park, Mechanisms of controlled drug release from drug-eluting stents, *Advanced Drug Delivery Reviews*. 58 (2006) 387–401. doi:10.1016/j.addr.2006.01.016.
- [5] J.-H. Lee, R.M. Pidaparti, G.M. Atkinson, R.S. Moorthy, Design of an implantable device for ocular drug delivery, *J Drug Deliv.* 2012 (2012) 527516. doi:10.1155/2012/527516.
- [6] S.C. Sigmon, G.E. Bigelow, Food and Drug Administration approval of sustained-release buprenorphine for treatment of opioid dependence: realizing its potential, *Addiction*. 112 (2017) 386–387. doi:10.1111/add.13539.
- [7] F. Rengier, A. Mehndiratta, H. von Tengg-Kobligk, C.M. Zechmann, R. Unterhinninghofen, H.U. Kauczor, et al., 3D printing based on imaging data: review of medical applications, *Int J CARS*. 5 (2010) 335–341. doi:10.1007/s11548-010-0476-x.
- [8] R.J. Morrison, S.J. Hollister, M.F. Niedner, M.G. Mahani, A.H. Park, D.K. Mehta, et al., Mitigation of tracheobronchomalacia with 3D-printed personalized medical devices in pediatric patients, *Sci Transl Med*. 7 (2015) 285ra64–285ra64. doi:10.1126/scitranslmed.3010825.
- [9] C.L. Ventola, Medical Applications for 3D Printing: Current and Projected Uses, *P T*. 39 (2014) 704–711.
- [10] M.A. Alhnan, T.C. Okwuosa, M. Sadia, K.-W. Wan, W. Ahmed, B. Arafat, Emergence of 3D Printed Dosage Forms: Opportunities and Challenges, *Pharm Res*. 33 (2016) 1817–1832.
- [11] A. Youssef, S.J. Hollister, P.D. Dalton, Additive manufacturing of polymer melts for implantable medical devices and scaffolds, *Biofabrication*. 9 (2017) 012002–30. doi:10.1088/1758-5090/aa5766.
- [12] H.-G. Yi, Y.-J. Choi, K.S. Kang, J.M. Hong, R.G. Pati, M.N. Park, et al., A 3D-printed local drug delivery patch for pancreatic cancer growth suppression, *Journal of Controlled Release*. 238 (2016) 231–241. doi:10.1016/j.jconrel.2016.06.015.
- [13] A. Goyanes, U. Det-Amornrat, J. Wang, A.W. Basit, S. Gaisford, 3D scanning and 3D printing as innovative technologies for fabricating personalized topical drug delivery systems, *Journal of Controlled Release*. 234 (2016) 41–48. doi:10.1016/j.jconrel.2016.05.034.

- [14] L.K. Prasad, H. Smyth, 3D Printing technologies for drug delivery: a review, *Drug Development and Industrial Pharmacy*. 42 (2015) 1019–1031. doi:10.3109/03639045.2015.1120743.
- [15] A.R. Johnson, C.L. Caudill, J.R. Tumbleston, C.J. Bloomquist, K.A. Moga, A. Ermoshkin, et al., Single-Step Fabrication of Computationally Designed Microneedles by Continuous Liquid Interface Production, *PLoS ONE*. 11 (2016) e0162518. doi:10.1371/journal.pone.0162518.
- [16] J.R. Tumbleston, D. Shirvanyants, N. Ermoshkin, R. Janusiewicz, A.R. Johnson, D. Kelly, et al., Continuous liquid interface production of 3D objects, *Science*. 347 (2015) 1349–1352. doi:10.1126/science.aaa2397.
- [17] R. Janusiewicz, J.R. Tumbleston, A.L. Quintanilla, S.J. Mecham, J.M. DeSimone, Layerless fabrication with continuous liquid interface production, *Proc Natl Acad Sci USA*. 113 (2016) 11703–11708. doi:10.1073/pnas.1605271113.
- [18] G. Götze, T. Rahne, A. Liebau, Intracochlear drug delivery in combination with cochlear implants, *Hno*. 65 (2017) 1–10. doi:10.1007/s00106-016-0285-9.
- [19] R.K. Shepherd, J. Xu, A multichannel scala tympani electrode array incorporating a drug delivery system for chronic intracochlear infusion, *Hear. Res*. 172 (2002) 92–98.
- [20] Y. Zhang, M. Huo, J. Zhou, A. Zou, W. Li, C. Yao, et al., DDSolver: an add-in program for modeling and comparison of drug dissolution profiles, *Aaps J*. 12 (2010) 263–271. doi:10.1208/s12248-010-9185-1.
- [21] H. Lo, M.S. Ponticello, K.W. Leong, Fabrication of controlled release biodegradable foams by phase separation, *Tissue Engineering*. 1 (1995) 15–28. doi:10.1089/ten.1995.1.15.
- [22] H. Lee, T.-S. Jang, J. Song, H.-E. Kim, H.-D. Jung, The Production of Porous Hydroxyapatite Scaffolds with Graded Porosity by Sequential Freeze-Casting, *Materials (Basel)*. 10 (2017) 367. doi:10.3390/ma10040367.
- [23] F.P.W. Melchels, J. Feijen, D.W. Grijpma, A poly(D,L-lactide) resin for the preparation of tissue engineering scaffolds by stereolithography, *Biomaterials*. 30 (2009) 3801–3809. doi:10.1016/j.biomaterials.2009.03.055.
- [24] F.P.W. Melchels, K. Bertoldi, R. Gabbrielli, A.H. Velders, J. Feijen, D.W. Grijpma, Mathematically defined tissue engineering scaffold architectures prepared by stereolithography, *Biomaterials*. 31 (2010) 6909–6916. doi:10.1016/j.biomaterials.2010.05.068.
- [25] R. Janusiewicz, C.J. Bloomquist, J.C. Luft, S.J. Mecham, J.M. DeSimone, Fabrication of functionally graded microlattices with continuous liquid interface production (CLIP), *Manuscript Submitted for Publication*. (n.d.).
- [26] A. Goyanes, P. Robles Martinez, A. Buanz, A.W. Basit, S. Gaisford, Effect of geometry on drug release from 3D printed tablets, *International Journal of Pharmaceutics*. 494 (2015) 657–663. doi:10.1016/j.ijpharm.2015.04.069.

- [27] D. Klose, F. Siepmann, K. Elkharraz, J. Siepmann, PLGA-based drug delivery systems: importance of the type of drug and device geometry, *International Journal of Pharmaceutics*. 354 (2008) 95–103. doi:10.1016/j.ijpharm.2007.10.030.
- [28] P.L. Ritger, N.A. Peppas, A simple equation for description of solute release II. Fickian and anomalous release from swellable devices, *Journal of Controlled Release*. 5 (1987) 37–42.
- [29] P. Colombo, P.L. Catellani, N.A. Peppas, L. Maggi, U. Conte, Swelling characteristics of hydrophilic matrices for controlled release New dimensionless number to describe the swelling and release behavior, *International Journal of Pharmaceutics*. 88 (1992) 99–109. doi:10.1016/0378-5173(92)90307-N.
- [30] G. Jonathan, A. Karim, 3D printing in pharmaceuticals: A new tool for designing customized drug delivery systems, *International Journal of Pharmaceutics*. 499 (2016) 376–394. doi:10.1016/j.ijpharm.2015.12.071.
- [31] J. Siepmann, F. Siepmann, Mathematical modeling of drug delivery, *International Journal of Pharmaceutics*. 364 (2008) 328–343. doi:10.1016/j.ijpharm.2008.09.004.
- [32] P.L. Ritger, N.A. Peppas, A simple equation for description of solute release I. Fickian and non-Fickian release from non-swellable devices in the form of slabs, spheres, cylinders or discs, *Journal of Controlled Release*. (1987).

CHAPTER 4: PRE-CLINICAL EVALUATION OF CLIP FOR THE FABRICATION OF PHARMACEUTICAL AND MEDICAL DEVICES

4.1 Introduction

As discussed in the introductory chapter of this dissertation, 3D printing has garnered a great deal of interest for biomedical applications both in pre-clinical development and clinical implementation. 3D printing in the biomedical field has the potential to dramatically change the way physicians treat and interact with patients, but important feasibility and regulatory concerns will need to be addressed. Notably, the exciting aspects of point-of-care manufacturing for personalized devices raises important quality questions. Future regulations and guidances will need to focus on issues specific to 3D printing, such as quality of the raw materials used, technical aspects of the production method, and guidances for post-production quality assurance.

One of the earliest examples of personalized medical device manufacturing is the production is the 3D printing of tracheal splints designed for the individual anatomy of three infants [1]. Further, the interdisciplinary team of physicians and biomedical engineers published a review that presents their experience navigating the current regulatory requirements and a perspective on what areas will be important focal points as 3D printing ushers in an era of customization in the medical field [2]. For personalization of medical devices to be achieved on a large scale, 3D printing methods will require extensive studies to understand all parameters that affect the condition and performance of the final product. If each part were unique and produced in different settings then the risks of inconsistency and failure would be too high to manage. For example, the anisotropic nature of traditional 3D printing means that a simple change in the orientation during fabrication can significantly affect the resulting physical properties of the final part. Thus, novel approaches to quality control will be needed, such as

regulation to ensure consistent source materials combined with well characterized and regulated software that ensure consistent performance of parts regardless of the design being produced.

In the case of using 3D printing to produce customized dosage forms, these controls become even more vital to the success of the technology. Development and validation of process analytical technology (PAT) will be an important aspect of quality control when manufacturing moves beyond the assembly line [3-6]. Additional development and regulatory considerations will have to be made to ensure that the active pharmaceutical ingredient (API) is stable to the process used and that an accurate and stable dosage form is reproducibly generated. Previous review articles present a more thorough discussion of regulatory considerations for 3D printed products for drug administration [6] and implantable medical devices [2].

In this chapter, experiments are presented to demonstrate the potential use of CLIP for biomedical and drug delivery applications. We screened a panel of 12 clinically relevant small molecule drugs for radical and UV stability. Docetaxel (DTXL) and dexamethasone-acetate (DexAc) were dissolved into 5 different CLIP resins with a range of crosslink densities and hydrophobicity. The effect the addition of an API had on the photokinetics of the resins was characterized using photocalorimetry. DTXL and DexAc-loaded resins were used to fabricate model devices which were analyzed for drug loading and release kinetics for comparison to outcomes observed in chapter 3. Devices without API were analyzed for toxicity *in vitro* according to ISO 10993, a widely used standard for validation of medical devices.

4.2 Materials and Methods

4.2.1 Materials

Poly(ethylene glycol) dimethacrylate $M_n = 750 \text{ g mol}^{-1}$ (PEG₇₅₀-DMA), poly(ethylene glycol) methacrylate $M_n = 360 \text{ g mol}^{-1}$ (PEG₃₆₀-MA), poly(ethylene glycol) dimethacrylate $M_n = 550 \text{ g mol}^{-1}$ (PEG₅₅₀-DMA), poly(ethylene glycol) dimethacrylate $M_n = 350 \text{ g mol}^{-1}$ (PEG₃₅₀-DMA), 2-hydroxyethyl methacrylate (HEMA), 2-hydroxyethyl acrylate (HEA), ethylene glycol dimethacrylate (EGDMA), acrylic acid (AA), diphenyl(2,4,6-trimethylbenzoyl)phosphine oxide (TPO), poly(ethylene glycol) dimethyl ether $M_n = 250 \text{ g mol}^{-1}$, poly(ethylene glycol) $M_n = 10,000 \text{ g mol}^{-1}$ (PEG), polycaprolactone-diol $M_n = 530 \text{ g mol}^{-1}$ (PCL-diol) and Tween80 were purchased from Sigma Aldrich. Poly(ethylene glycol) $M_n = 200 \text{ g mol}^{-1}$ was purchased from Acros Organics.

Phosphate buffered saline (PBS), 2-propanol, acetonitrile, and water were purchased from Fisher Scientific. Solvents were HPLC grade purity or higher. The therapeutic drugs progesterone, hydrocortisone, dexamethasone-21-Acetate (DexAc), paclitaxel, bicalutamide, acetaminophen, ibuprofen, acetylsalicylic acid, and salicylic acid were purchased from Sigma-Aldrich; docetaxel (DTXL) and gemcitabine were purchased from LC Labs; and 5-fluorouracil (5FU) was purchased from Acros Organics. All materials were stored as directed by the supplier and used as received.

Polycaprolactone-dimethacrylate $M_n = 700 \text{ g mol}^{-1}$ (PCL₇₀₀-DMA) was synthesized as described in Chapter 2.

4.2.2 Drug screen for UV and radical stability

The UV-stability was tested for a panel of small molecule drugs including: progesterone, hydrocortisone, DexAc, DTXL, paclitaxel, gemcitabine, bicalutamide, 5FU, acetaminophen, acetylsalicylic acid, salicylic acid, and ibuprofen. UV-stability was assessed in UV-inert resins

formulated by dissolving each drug at 2 % (w/w) into either PEG-diol or PEG-dimethyl ether (mPEG) alone or in the presence of photoinitiator, TPO at 1 wt %.

A drop (10-20 μL) of the drug-loaded UV-inert resins was added to the bottom of a clear glass vial and irradiated in a nitrogen purged UV oven with either a mercury light source with peak emission at 365 nm (ELC-4001 equipped with UVA lamp, Electro-lite Corporation) or an LED light source with narrow emission centered at 365 nm (FireJet FJ800, Phoseon Technology) for 2.5, 5, 7.5, and 10 minutes. The UV intensity of the ovens was measured using a pass-through radiometer (DISKURE 365) to be 43.3 mW cm^{-2} and 180 mW cm^{-2} for the Hg and LED lamps, respectively. DTXL was also tested with a 10 minutes exposure in an oxygen atmosphere, with all other conditions remaining the same. Following UV exposure, samples were dissolved in 1 mL of acetonitrile, filtered through a $0.45 \mu\text{m}$ PVDF filter, and analyzed with HPLC. UV stability was calculated as the ratio of the integrated peak area, normalized by sample mass, of the UV-irradiated samples to that of an unexposed sample.

Additional tests were carried out to irradiate three formulations (DTXL, DexAc, and progesterone) with light from an LED light source with a wavelength of 385 nm. This was carried out in the photocalorimetry apparatus (see section 4.2.5 for further details). Samples (10-20 μL) were irradiated in an aluminum DSC pan. The resin was then dissolved by placing the entire pan into a glass vial containing 1 mL of acetonitrile. After vortexing for 10 minutes, solutions were filtered and analyzed with HPLC.

Four HPLC methods were used to analyze the panel of drugs screened for UV and radical stability. An Agilent 1260 series HPLC equipped with a Zorbax Eclipse C-18 reverse phase column (Agilent) at 40°C and a constant flow rate of 1 mL/min was used for all methods. Samples were run on a gradient method composed of solvents A and B. Method details for each method are presented in Table 4.1. The composition of the mobile phase was changed as a linear gradient between the steps.

Table 4.1 Details of HPLC methods used in UV and radical stability screen

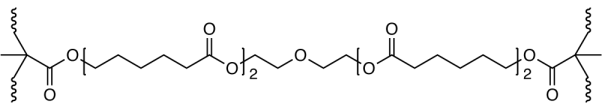
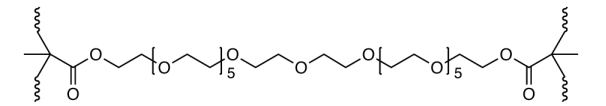
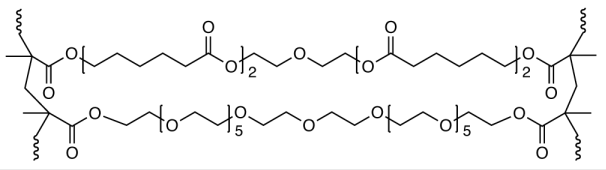
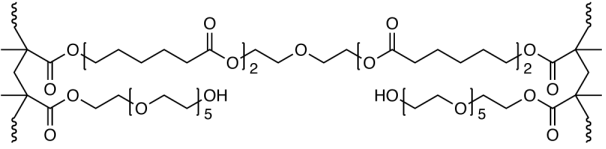
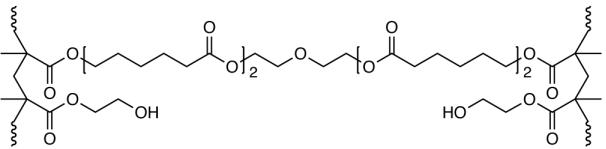
Method ID	Solvent		Method		Drug (detection wavelength, nm)
	A	B	% B	Time	
1	Water	Acetonitrile	50%	0 min	Docetaxel (227)
			85%	7 min	Paclitaxel (227)
			100%	7.1 min	Bicalutamide (280)
			100%	15 min	Gemcitabine (280)
			50%	15.1min	Progesterone (254)
			50%	19 min	Dexamethasone-Acetate (254)
2	Water	Acetonitrile	0%	0 min	Hydrocortisone (254)
			100%	10 min	
			100%	12 min	
			0%	12.1 min	
			0%	15 min	
3	Water + 0.1% TFA	Acetonitrile + 0.1% TFA	30%	0 min	Salicylic Acid (227)
			30%	7 min	Acetylsalicylic Acid (227)
					Acetaminophen (254)
					5-Fluorouracil (280)
4	Water + 0.1% TFA	Acetonitrile + 0.1% TFA	30%	0 min	Ibuprofen (227)
			100%	10 min	
			100%	15 min	
			30%	15.1 min	
			30%	20 min	

4.2.3 Formulation of docetaxel and dexamethasone-acetate resins

For each formulation presented, 3 versions were prepared: blank, DTXL-loaded, and DexAc-loaded. Five base resins containing no cargo were first formulated from neat PCL₇₀₀-DMA and PEG₇₅₀-DMA, as well as blends of PCL₇₀₀-DMA with PEG₇₅₀-DMA, PEG₃₆₀-MA, and HEMA at 50 mol % (table 4.2). TPO photoinitiator was added at 1 mol % by mixing under magnetic stirring at room temperature overnight to complete the blank resin formulation. To prepare the DTXL- and DexAc-loaded resins, DTXL and DexAc were added to the blank resin at 2 wt % and allowed to stir for an additional night at room temperature. Mol % is defined by the ratio of moles of methacrylates of the component to the total moles of methacrylate in the

formulation multiplied by 100. Wt % is defined as the ratio of the component mass to the total mass multiplied by 100.

Table 4.2 Formulations and \bar{M}_c values for resins used to fabricate DTXL- and DexAc-loaded disks and disks used in degradation and cytotoxicity studies.

A	B	Mol % B	Wt % B	\bar{M}_c (g mol ⁻¹)	Wt % PEG	Schematic
PEG ₇₅₀ -DMA (<i>f</i> = 4)	--	--	--	396	82 %	
	--	--	--	371	0 %	
PCL ₇₀₀ -DMA (<i>f</i> = 4)	PEG ₇₅₀ -DMA (<i>f</i> = 4)	50 %	52 %	383	42 %	
	PEG ₃₆₀ -MA (<i>f</i> = 2)	50 %	50 %	391	41 %	
	HEMA (<i>f</i> = 2)	50 %	28 %	391	0 %	

4.2.4 Polymerization kinetics of resins

Photopolymerization kinetics of blank and drug-loaded resins were characterized with photocalorimetry using a Discovery DSC (TA instruments, New Castle, DE) equipped with an AccuCure LED light source with emission at 385 nm (Digital Light Lab, Knoxville, TN). 5-7 mg of resin was added to an aluminum DSC sample pan without a lid and placed in the DSC cell, which was held at a constant temperature of 25 °C under a 50 mL/min nitrogen flow. After a 3-minute isothermal step, samples were exposed to UV light for 5 minutes at 6 mW cm⁻². The light was then turned off for 3 minutes followed by another 3 minute UV exposure to ensure the

reaction was complete. Heat was normalized with a horizontal baseline from the heat flow value at 298 seconds of the UV exposure step. Rate of polymerization (R_p) was calculated using (4.1).

$$R_p = \frac{|Q|}{\Delta H_{max}} \quad (4.1)$$

where Q is heat flow in mW and ΔH_{max} is the theoretical heat evolved if all methacrylate groups in the sample are reacted. For these experiments, ΔH_{max} was calculated as the product of moles of methacrylate in the sample and ΔH for conversion of a methacrylate (60 kJ mol^{-1}) [7]. Bond conversion was calculated by integrating equation 5.

4.2.5 Continuous Liquid Interface Production

Drug-loaded and blank disks (1mm x 5mm) were fabricated on a S1 CLIP prototype printer (Carbon) equipped with a 385 nm LED UV light source. Disks were printed at a continuous speed of 25 mm hr^{-1} and light intensity of 3 mW cm^{-2} for fully crosslinked systems (PCL₇₀₀-DMA, PEG₇₅₀-DMA, PCL₇₀₀-DMA/PEG₇₅₀-DMA) and 25 mm hr^{-1} and 5 mW cm^{-2} for chain-extended systems (PCL₇₀₀-DMA/PEG₃₆₀-MA, PCL₇₀₀-DMA/HEMA). Unreacted resin on the surface of the disks was removed by dabbing with a lab wipe. The devices were then postcured for 5 minutes (2.5 minutes on each side) in a LED UV oven (365 nm , 90 mW cm^{-2}) under a nitrogen atmosphere.

4.2.6 Drug loading and *in vitro* release from DTXL- and DexAc-loaded devices

To determine drug-loading, drug was extracted from the disks in 1 mL of a 1:1 (v/v) solution of acetonitrile and 2-propanol at 37°C while shaking at 150 rpm. After at least 24 hours, the concentration of the drug in the extraction solution was determined by removing 400 μL for HPLC analysis. To ensure complete extraction, 400 μL of fresh acetonitrile/2-propanol solution was added and the extraction was allowed to continue. This process was replicated for a total of 4 total samples over the course of 2 weeks. It was determined that 48 hours was sufficient for complete drug extraction from sample disks.

The concentration of drug in the extract solutions was determined using an Agilent 1260 series HPLC equipped with a Zorbax Eclipse C-18 reverse phase column (Agilent) at 40 °C and a constant flow rate of 1 mL/min. Samples were run on a gradient method composed of solvents A (pure water) and B (pure acetonitrile). The mobile phase was changed from 50 % to 85 % B over 7 minutes, washed with a 3-minute isocratic hold of 100 % B, and followed by 5 minutes at 50 % B to equilibrate the column prior to the next sample. Absorbance was measured at 227 nm for DTXL and 254 nm for DexAc, and concentrations of the extraction solution were calculated by comparing peak integrations to a standard curve of known concentrations.

To test *in vitro* drug release, DTXL- and DexAc-loaded disks were individually added to a scintillation vial containing 15 mL of pH 7.4 PBS with 0.1 % (v/v) Tween 80 to maintain sink conditions. Samples were placed in an incubating shaker at 37 °C and 150 rpm. Drug release was calculated by determining the amount of drug remaining in the disk after a given amount of time in the release medium. At given timepoints, disks were removed from the release medium ($n = 3$ for each timepoint) and the remaining drug was extracted and analyzed. Fraction of drug (F) released was calculated according to (4.2):

$$F = \frac{D_0 - D_t}{D_0} \times 100 \quad (4.2)$$

where D_0 is the mass of drug extracted from disks that have not been exposed to release conditions (initial loading) and D_t is the mass of drug extracted from disks after the given amount of time in the release solution.

4.2.7 Coating devices with DTXL and DexAc

A coating solution was made by dissolving DTXL and DexAc at a concentration of 30 mg/mL in a mixture of 75 % acetonitrile and 25 % 2-propanol by volume. PEG ($M_w = 10,000$ g mol^{-1}) was then dissolved in the drug solutions to a concentration of 330 mg/mL. Blank disks made from PCL₇₀₀-DMA, PEG₇₅₀-DMA, and blends of PCL₇₀₀-DMA/PEG₇₅₀-DMA, PCL₇₀₀-DMA/PEG₃₆₀-MA, and PCL₇₀₀-DMA/HEMA at 50 mol % were dipped into the drug/polymer

solution for 1-2 seconds. Disks were then lifted out of the solution so that the 1 mm thickness of the disk was in a vertical orientation. The disk was allowed to air dry for around 15 seconds, placed on wax paper and allowed to dry under reduced pressure in a vacuum oven at room temperature overnight. Coating mass was calculated by recording the mass of each disk prior to coating and following overnight drying.

In vitro release was carried out by adding disks to 15 mL pH 7.4 PBS with 0.1 % Tween80 and placing under constant oscillation of 150 rpm at 37 °C in the incubated shaker (n = 3). At given timepoints, 5 mL of release solution was removed and replaced with fresh PBS/Tween80. Following the 25 hour timepoint, all of the release medium was removed and replaced with 75 % acetonitrile 25 % 2-propanol and allowed to extract the remaining drug at 37 °C for 3 days. The drug concentration in the release and final extraction solutions was analyzed using HPLC.

4.2.8 *In vitro* cytocompatibility

4.2.8.1 Cell culture

HUVEC human umbilical vein endothelial cells and HeLa human epithelial adenocarcinoma cells were originally obtained from American Type Culture Collection (ATCC). 344SQ cells were a gift from the University of Texas M.D. Anderson Cancer Center (Jon Kurie Lab). HUVEC cells were cultured in HuMEC complete medium containing HuMEC supplement and bovine pituitary extract. HeLa cells were cultured in MEM containing Earle's salts. 344SQ cells were cultured in RPMI medium. Both media were supplemented with 10 % fetal bovine serum. All cells were maintained in a humidified atmosphere of 5 % CO₂ at 37 °C.

4.2.8.2 Cytotoxicity of monomers

Small molecule and oligomeric monomers were screened for cytotoxicity using murine small cell lung cancer cells, 344SQ cells. Cells were seeded in 200 µL of media in a 96 well plate (5000 cells/well) and allowed to adhere overnight. Resins were dissolved or well dispersed

in fresh medium at concentrations between 10 and 1.28×10^{-6} % (w/v) and dosed to cells for 72 hours. After the incubation period, cell viability was assessed using a luminescence-based assay. All media was removed by aspiration and 100 μ L fresh medium was added back to the cells. 100 μ L of CeLLTiter-Glo® Luminescent Cell Viability Assay reagent (Promega) was added and the plate was placed on a microplate shaker for 2min, followed by 10 minutes at room temperature in the dark. The luminescence signal was then recorded using a SpectraMax M5 plate reader (Molecular Dynamics). Cell viability was expressed as a percentage of the viability of cells treated with fresh PBS only.

4.2.8.3 Cytocompatibility of leachables and degradation products

Cytotoxicity of any leachable or degradation product was observed in accordance to ISO 10993-5. Blank disks made from PCL₇₀₀-DMA, PEG₇₅₀-DMA, and blends of PCL₇₀₀-DMA/PEG₇₅₀-DMA, PCL₇₀₀-DMA/PEG₃₆₀-MA, and PCL₇₀₀-DMA/HEMA at 50 mol % were first sterilized by soaking in 70 % ethanol for 20 minutes followed by two rinses with PBS. Disks were then transferred to a sterile screw cap microcentrifuge tube containing 1.5 mL pH 7.4 PBS under aseptic conditions and placed in an incubated shaker at 37 °C under oscillation at 150 rpm. At given timepoints, disks were removed (n=3) and mass loss due to degradation and dissolution of leachables was determined. The soluble fraction was defined as the mass loss when disks were incubated with 2 mL of acetone for 24 hours. Mass loss was calculated according to (4.3).

$$\text{Mass Loss (\%)} = \left[1 - \frac{M_d}{M_0} \right] \times 100 \quad (4.3)$$

PBS swelling of blank disks was measured using the 10 day timepoint of the degradation studies (section 4.2.8.2). Swelling was determined using the method presented previously in chapter 3 (section 3.2.6.1).

To test for potential cytotoxicity of the leachable and degradation products, HUVEC and HeLa cells were seeded in 200 μ L of media in a 96-well plate with 5000 cells per well. After

allowing 24 hours for cells to adhere, media was aspirated off, and 50 μ L of the PBS extraction solution diluted with 150 μ L of fresh medium was added to the well in triplicate for 72 hours. PBS kept at identical conditions to that of the extractions was used to ensure that no potential cytotoxic effect was due to the experimental set up. Fresh PBS was used as a negative control, and paclitaxel was used as positive control. Viability was assessed using the luminescence assay as presented in section 4.2.8.2.

4.3 Results and Discussion

4.3.1 Drug screen for UV and radical stability

A primary concern when formulating pharmaceutical products is the stability of the API, and with respect to CLIP, exposure to UV light and reactive radicals can pose a threat to this stability. However, due to the potential for prolonged release kinetics achieved with encapsulation compared to that of drug-coated devices, it was of interest to explore the potential to incorporate drugs directly into the resins and thereby encapsulate them during the CLIP fabrication process. To determine whether small molecule, clinically relevant drugs could be encapsulated directly during the printing of a personalized device, we tested the UV stability of a panel of 12 small molecule drugs dissolved in photo-inert PEG resins. The formulation of photo-inert resins was chosen to mimic the conditions experienced by an API dissolved in a CLIP formulation, such as drug concentration, viscosity, and radical presence, without facilitating crosslinking upon UV exposure. Thus, the liquid resin can be easily solubilized following UV exposure for analysis of the drug stability.

All drugs presented were completely dissolved to make a transparent solution in the photo-inert resin. Stability was evaluated by comparing HPLC chromatographs (normalized by sample mass) of irradiated samples to samples that received no UV exposure. Representative

chromatographs for a UV stable and UV labile drugs are shown in Fig. 4.1 A and B, respectively. Further, when TPO radical initiator is included in the resin, peaks for both the photoinitiator and drug can be observed prior to UV exposure (Fig. 4.1 C and D). The disappearance of the peak for radical initiator upon UV exposure is evidence of the homolytic cleavage and generation of radicals. In resins containing stable drugs, only the drug is detectable following exposure, indicating stability towards the UV light and radical presence (Fig. 4.1 C). Resins with unstable drugs have significantly reduced or no resolvable peak areas at the respective elution time following UV exposure (Fig. 4.1 D).

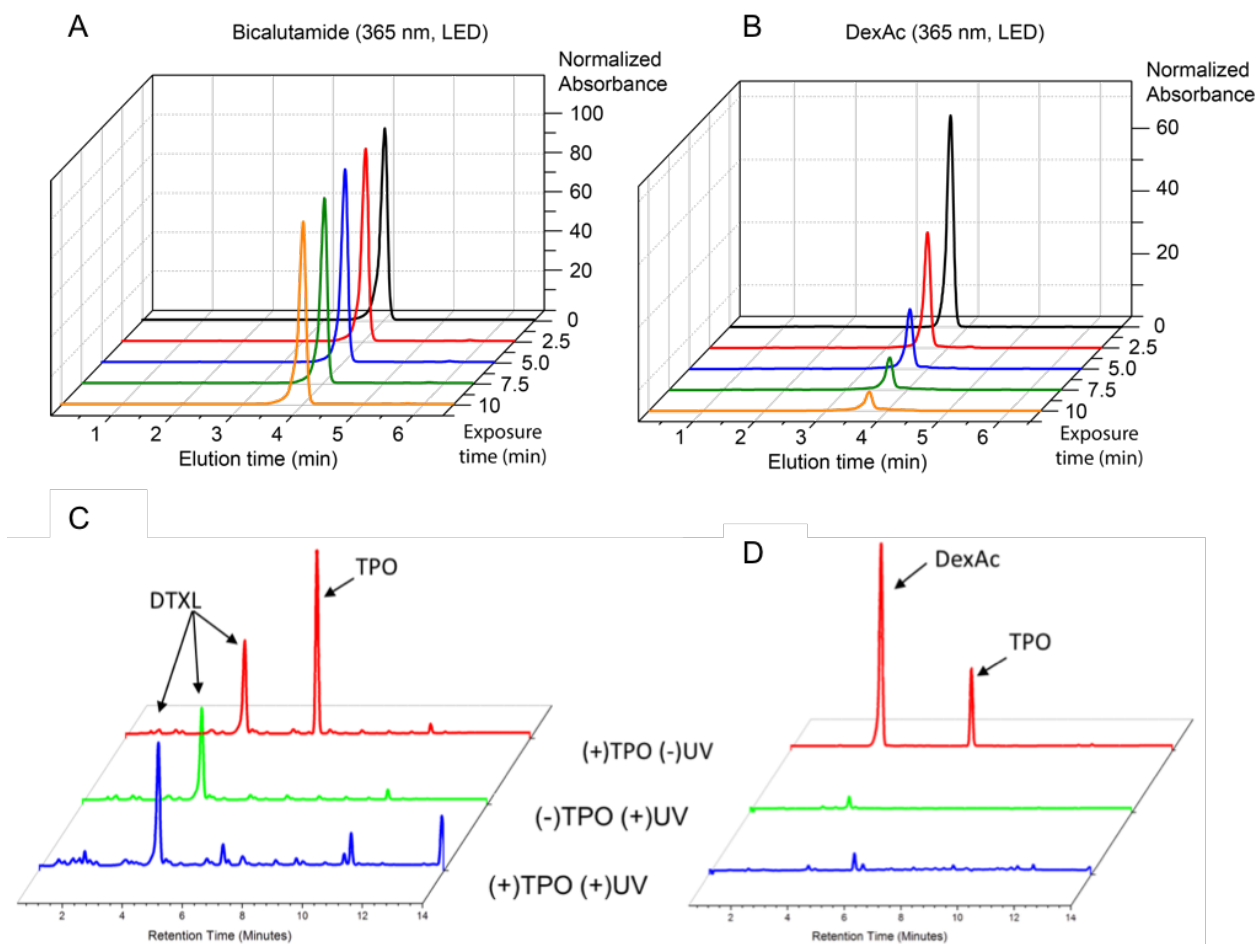


Figure 4.1 Representative HPLC chromatographs for drugs that are UV stable and UV labile. Representative chromatograms of (A) UV stable drugs (Bicalutamide shown) and (B) the photo-induced degradation of UV-labile drugs (DexAc shown) demonstrating a relationship between extent of degradation and exposure time. HPLC chromatograms for DTXL (C) and DexAc (D) are shown as representative chromatograms for UV and radical stable and labile drugs, respectively. (+) and (-) indicate the presence or absence of TPO photoinitiator and UV exposure in an LED oven.

The results of the full stability screen can be seen in figure 4.2. Comparison of HPLC peak areas, normalized by sample mass, reveals a relative stability to the 365 nm LED light and radical initiator in all drugs tested except for the corticosteroids: hydrocortisone, progesterone, and dexamethasone-acetate (Fig. 4.2). The likely mechanism of degradation for these drug compounds is the rearrangement of the conjugated ketone group, which occurs upon irradiation with 365 nm light [8].

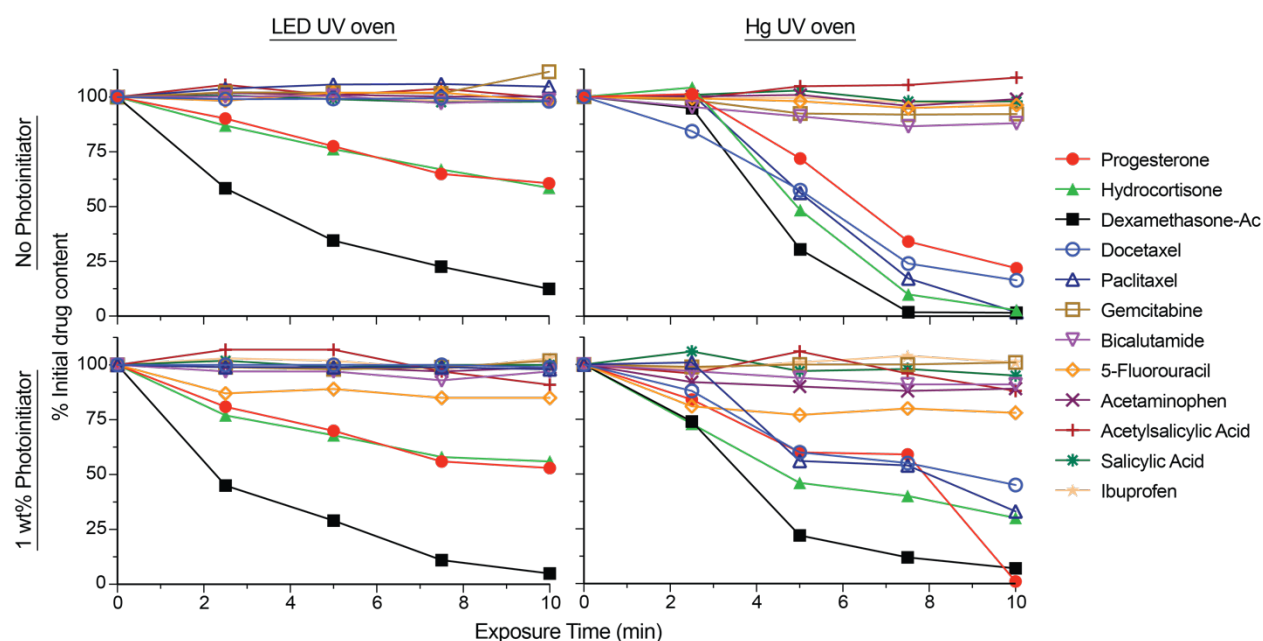


Figure 4.2 Stability of a panel of clinically-relevant drugs to UV exposure and radical presence. Drugs were dissolved at 2 wt % in PEG-based UV-inert resins alone (top row) or with the presence of radical photoinitiator TPO (1 wt %) (bottom row) and exposed to UV light from a LED light source (left column) or mercury light source (right column).

When the UV-inert resins were exposed to the broad wavelength of the mercury arc lamp, docetaxel and paclitaxel also showed an instability, which appears independent of radical initiator presence. This is likely a result of an instability when exposed to the higher energy and shorter wavelengths of the mercury lamp spectrum, demonstrating the potential positive impact of utilizing the narrow emission of LED-based UV light sources for printing and post-cure. Further, an application requiring the encapsulation of a steroid could still be potentially

developed by identifying and using an LED light source of a compatible wavelength and a complementary radical photoinitiator.

Other factors that were tested included the presence of oxygen, as UV exposure is known to generate the highly reactive singlet state oxygen [9]. For resins containing DTXL, no difference in drug concentration between samples in an oxygen or nitrogen atmosphere was observed following UV irradiation (Fig. 4.3 A). Additionally, comparison between resins formulated from PEG-diol (PEG) and PEG-dimethyl ether (mPEG) indicates no effect of the terminal group of oligomeric resin component. An important note, however, is that these resins did not contain radical initiator, which would likely lead to a higher concentration of singlet state oxygen.

Drug resins were also irradiated for 10 minutes with a light source of 385 nm, the same wavelength used in the CLIP printer (Fig. 4.3 B). Results indicated less degradation in the steroids, DexAc and progesterone, compared to exposure from the 365 nm LED light or the broad wavelength of the Hg light source. Which supports the theory of ketone rearrangement, which occurs with exposure to 365 nm light, being the degradation pathway. However, these results should not be compared directly to those of the 365 nm exposure due to the 6-fold higher light intensity used in the 365 nm LED experiment (30 mW cm^{-2} and 180 mW cm^{-2}). The goal of this experiment, rather, was to simulate the exposure and wavelength experienced during the CLIP process; whereas the high intensity light of the 365 nm LED is more representative of the postcure process.

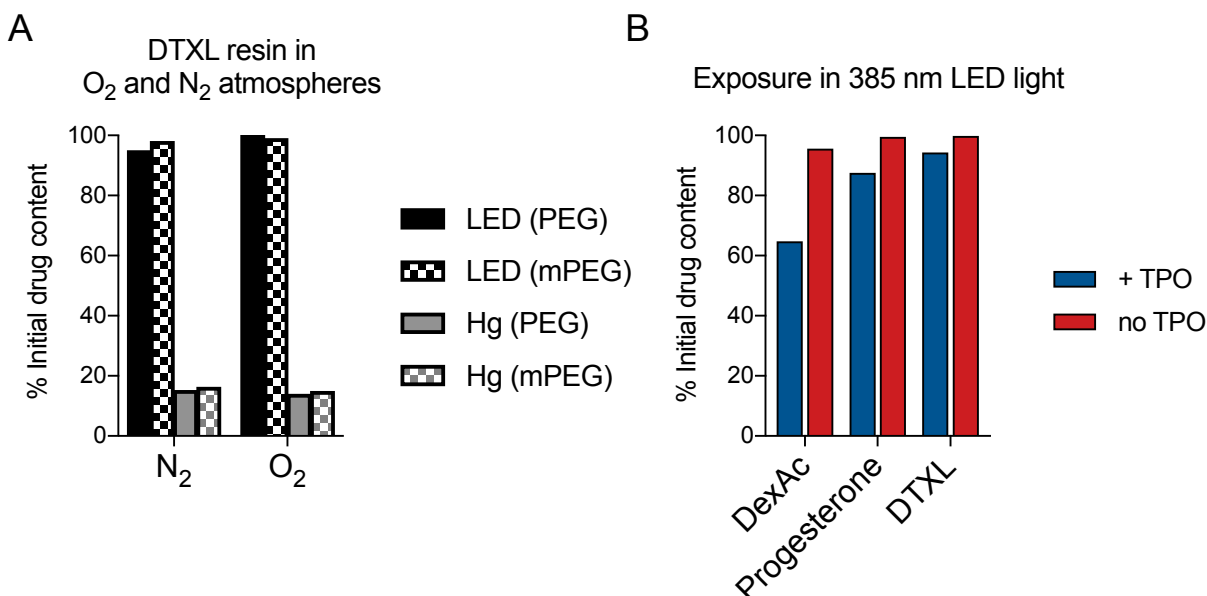


Figure 4.3 Stability testing in additional conditions. (A) Stability of DTXL in UV-inert resins upon exposure to UV light in an oxygen and nitrogen environment. (B) Fraction of initial drug content of DexAc, Progesterone, and DTXL resins following irradiation with 385 nm LED light (30 mW cm^{-2}) for 10 minutes

4.3.2 Formulation and photokinetics of drug-loaded resins

Five resin formulations were chosen to confirm the patterns observed for the release of RhB using clinically relevant drugs (DTXL and DexAc). Resins were formulated to observe the effect of material composition and crosslink density in PCL₇₀₀-DMA based resins. PCL₇₀₀-DMA was compared to PEG₇₅₀-DMA of a similar molecular weight, as well as blends of PCL₇₀₀-DMA with PEG₇₅₀-DMA, PEG₃₆₀-MA, and HEMA at 50 mol %. Although DexAc showed degradation during the UV stability screen, preliminary data indicated stability of DexAc in CLIP devices. Therefore, we sought to encapsulate DexAc using the entire CLIP process to further investigate potential stability compared to the panel screen.

DTXL and DexAc both dissolved easily into each resin formulation containing photoinitiator to make a clear solution. Photocalorimetry was used to observe the effect of the addition of dissolved drugs on the extent and rate of polymerization in the CLIP resins. Max polymerization rate (R_p), time to reach max R_p (t_{max}), double bond conversion (DBC) at t_{max} , and

total DBC for each formulation can be seen in table 1. All five resins analyzed resulted in high total bond conversion of over 95 %. More highly crosslinked systems reached max R_p faster than those containing chain-extending diluents (PEG₃₆₀-MA and HEMA), which is consistent with the differences in polymerization kinetics of monomethacrylate and dimethacrylate systems previously observed [10,11]. Overlaying the curves of the DTXL and DexAc-loaded resin with that of the base resin for each material indicates that the addition of drug did not appear to influence the rate or extent of polymerization (Fig. 4.4).

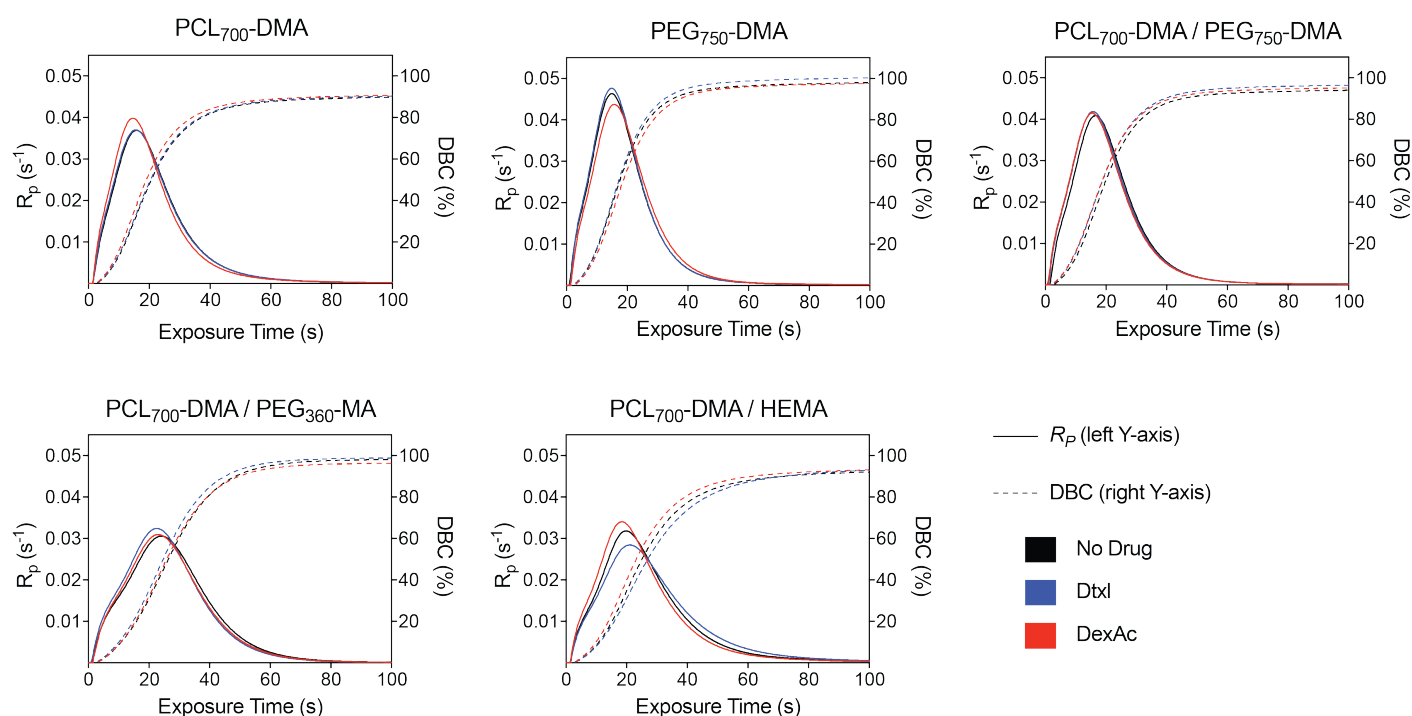


Figure 4.4 Photocalorimetry thermal traces of blank and DTXL- and DexAc-loaded resins.

Table 4.3 Photocalorimetry results of blank and drug-loaded resins.

Formulation	Max Rp (s ⁻¹)			t _{max} (s)			DBC at t _{max} (%)			Total DBC (%)		
	No	2 wt%	2 wt%	No	2 wt%	2 wt%	No	2 wt%	2 wt%	No	2 wt%	2 wt%
	Drug	DTXL	DexAc	Drug	DTXL	DexAc	Drug	DTXL	DexAc	Drug	DTXL	DexAc
PCL ₇₀₀ -DMA	0.037	0.037	0.040	15.8	15.5	14.6	32.7%	32.7%	33.0%	91.2%	91.6%	92.1%
PEG ₇₅₀ -DMA	0.046	0.048	0.044	14.9	14.9	15.8	38.6%	39.8%	38.3%	99.3%	101.8%	99.0%
PCL ₇₀₀ -DMA / PEG ₇₅₀ -DMA	0.041	0.042	0.042	16.6	15.8	15.5	37.0%	37.8%	37.2%	95.4%	97.9%	96.6%
PCL ₇₀₀ -DMA / PEG ₃₆₀ -MA	0.031	0.032	0.031	24.1	22.7	23.1	42.9%	43.5%	41.6%	99.0%	99.8%	97.2%
PCL ₇₀₀ -DMA / HEMA	0.032	0.029	0.034	19.8	21.1	27.7	33.9%	34.0%	34.7%	93.9%	95.4%	94.8%

These results indicate that the addition of DTXL or DexAc to a CLIP resin will not affect fabrication requirements, affording a plug-and-play approach in which the design and CLIP parameters for a device can be optimized without the use of drug, thus limiting the consumption of expensive therapeutics and reducing costs due to the handling and disposal of hazardous material. However, incorporation of higher concentrations of drug or different drugs that absorb at the wavelengths used in CLIP may require some fabrication parameter optimization.

4.3.3 Encapsulation, extraction and release of docetaxel and dexamethasone-acetate from CLIP devices

Drug-loaded disks were printed with API-loaded resins using the same parameters used for non-loaded resins. The encapsulated drug was then extracted using an acetonitrile/2-propanol solution. All formulations of DTXL-loaded devices resulted in an actual drug loading close to the 2 wt % theoretical loading (Fig. 4.5 A). Despite the relative UV instability of DexAc observed during the stability study, the CLIP devices still contain close to 2 wt % of the active drug, although the loading shows variability between formulations (Fig. 4.5 A). This is likely due to the lower total irradiation experienced by the drug during the CLIP printing process compared

to what the drug experiences in the UV oven. During the printing process, devices printed at 3 and 5 mW cm⁻² are only exposed to a theoretical total of 432 and 720 mJ cm⁻², respectively. After printing, the solid polymeric network of the device may provide added protection from the irradiation dose of 27,000 mJ/cm⁻² applied in the UV oven during the postcure process.

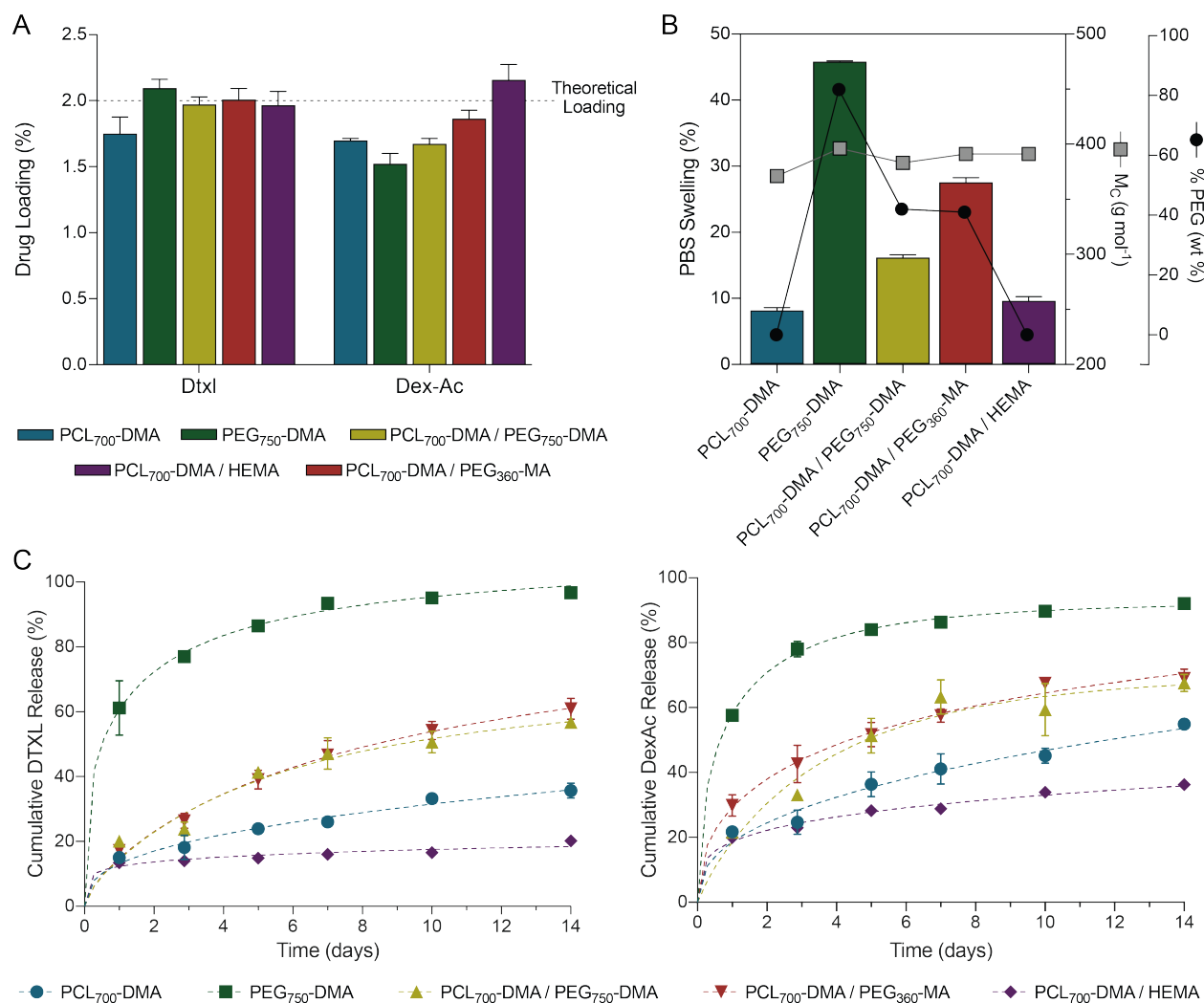


Figure 4.5 Characterization of DTXL- and DexAc-loaded model devices. (A) Drug loading of devices as determined by extractions and HPLC analysis. (B) Theoretical M_C and PEG content overlaid with PBS uptake for devices without drug. (C) Characterization of DTXL and DexAc release *in vitro*.

Although the calculated \bar{M}_C values are similar for all formulations, when disks were incubated in pH 7.4 PBS the swelling was considerably greater in disks containing PEG-based monomers (Fig. 4.5 B). Comparison of disks formulated with PCL₇₀₀-DMA/HEMA to PCL₇₀₀-DMA/PEG₃₆₀-MA, both with identical molar ratios of crosslinking monomers to chain-extending

monomer and thus identical \bar{M}_C (as calculated in Chapter 3), exemplifies the importance of the role that pendant PEG moieties play in defining the characteristics of the polymer network.

Release of DTXL and DexAc *in vitro* both follow the same trends observed in the release of RhB (Fig. 4.5 C). Devices fabricated with 100 % PEG₇₅₀-DMA resulted in the fastest release of both drugs. As seen in the RhB release, the addition of HEMA to PCL₇₀₀-DMA slowed the release of the therapeutics compared to the more highly crosslinked 100 % PCL₇₀₀-DMA networks. Also, blends of PCL₇₀₀-DMA with PEG₇₅₀-DMA to PEG₃₆₀-MA indicate a similar release profile. This is interesting because PEG₃₆₀-MA has a functionality of 2 (non-crosslinking) and PEG₇₅₀-DMA has a functionality of 4 (crosslinking), leading to half of the number of theoretical crosslinks in the network containing PEG₃₆₀-MA. However, both formulations contain the same amount of hydrophilic PEG by weight, indicating that the solute release is at least as dependent on the hydrophilicity of the network as the crosslink density.

Complete extraction of the drug remaining in the release samples was confirmed for each timepoint by carrying out the extraction for 2 weeks. The extraction solution was monitored by HPLC to determine the amount of drug remaining. It was observed that approximately 48 hours was adequate for complete extraction of drug from the devices. (Fig. 4.6).

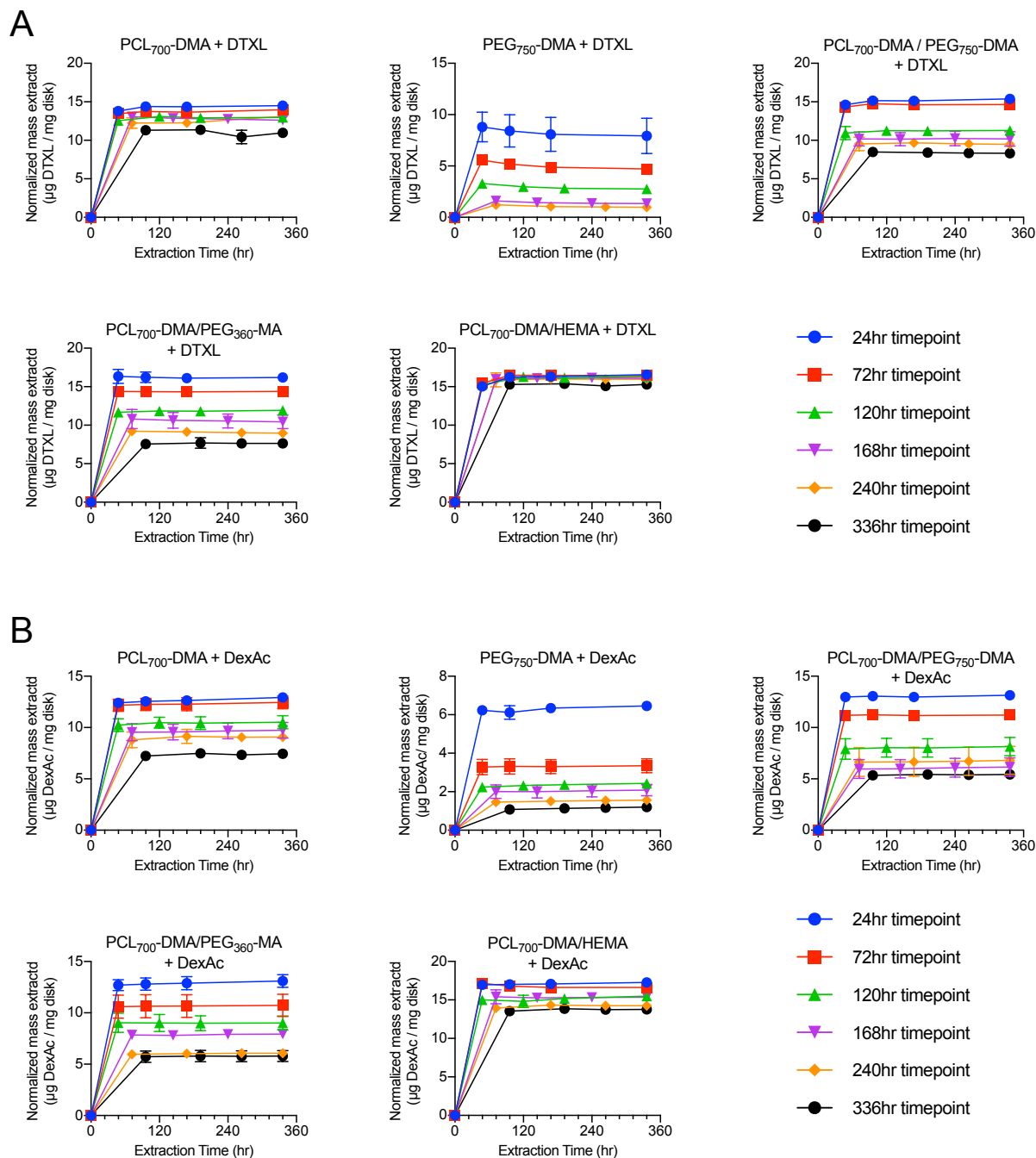


Figure 4.6 Analysis of progress of drug extraction from release study samples. Cumulative mass of DTXL (A) or DexAc (B) extracted from release disks at each timepoint plotted against extraction time. Extractions were carried out in 1:1 (v/v) acetonitrile/2-propanol solution at 37 °C and 150 rpm. At each time point, 400 µL was removed for HPLC analysis and replaced with fresh extraction solution.

4.3.4 Coating as a method for API incorporation

Certain applications may require alternative methods for loading of an API. For example, post-loading may be desirable when an API is instable to the CLIP process or is reactive with a component of the resin. Additionally, methods like coating devices with drug can facilitate a rapid release effect of the API, which may be desirable for some applications. To demonstrate the ability to post-load CLIP devices, blank devices were coated with DTXL and DexAc. The drugs were dissolved in a PEG solution, into which the devices were dipped before drying in a vacuum oven. The inconsistent coating mass (Fig. 4.7 A) and drug loading (Fig. 4.7 B) is likely a result of the manual coating process. This proof of concept experiment could be improved through automated dipping, allowing more precise control of speed and duration, or a spray coating technique. Methods of coating devices using a molten liquid of a lower MW PEG were also attempted with a greater inconsistency in coating thickness (data not shown).

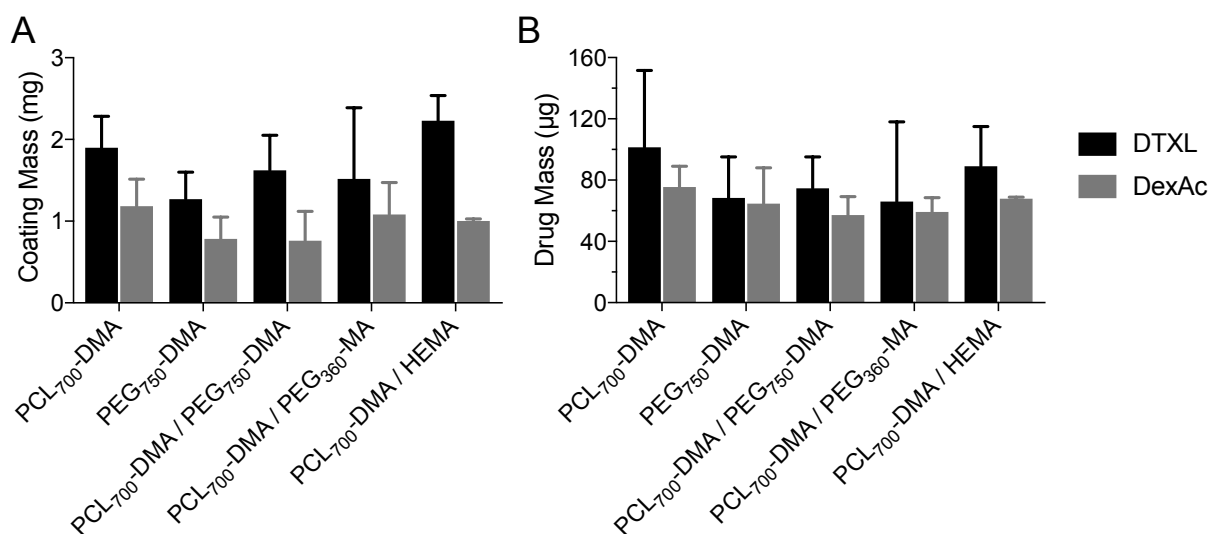


Figure 4.7 Drug loading of coated disks (1mm thick, 5mm diameter). Coating mass (A) was calculated as the difference in mass before and after the PEG coating dried. Drug mass (B) was defined as the sum of the total mass released during dissolution studies and the subsequent acetonitrile / 2-propanol extraction.

Dissolution results of the coated parts can be seen in figure 4.8. For both DTXL and DexAc coated devices, most of the drug was released within 24 hours, for all fully crosslinked systems. The ability to achieve similar release rates for devices regardless of the polymer

network is important if it is desirable to be able to modulate mechanical or thermal properties of a device while maintaining uniform release kinetics of a coated API.

The resins with monomethacrylate reactive diluents (PEG360-MA and HEMA) only released approximately 50-70 % of the total loaded API. This is likely due to a higher level of swelling of the polymer network in the coating solution, leading to drug penetration into the device. If the desired outcome is to achieve adsorption on the outside only, this could likely be corrected by choosing a solvent for formulating the coating solution in which the device material will not swell.

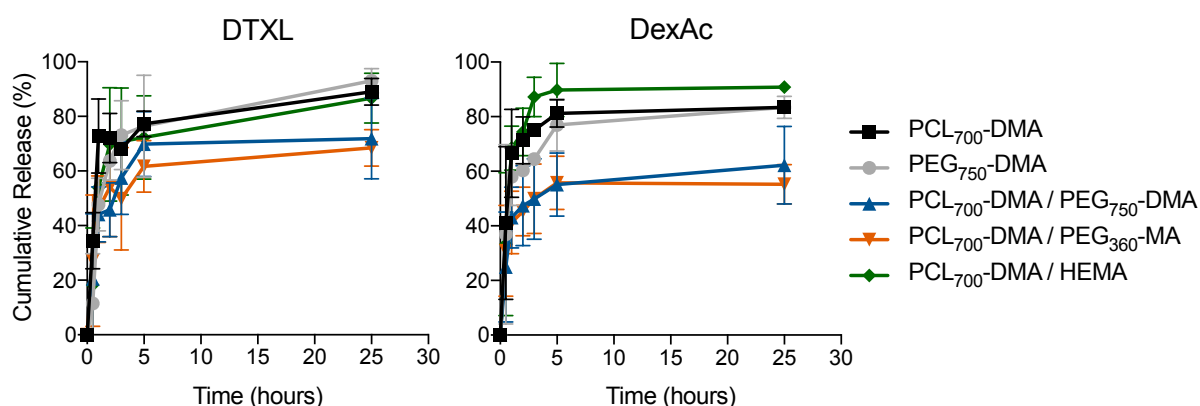


Figure 4.8 Dissolution of DTXL and DexAc from drug-coated model disks.

4.3.5 *In vitro* biocompatibility of CLIP materials

Photopolymerizable and acrylate-based materials have been used in biomedical applications widely, including use as surgical glues, dental resins, and bone cements. However, these types of materials are also well known to have associated toxicities [12]. Many of the materials presented throughout this dissertation are derived from materials that are generally regarded as safe (GRAS) by the FDA. While GRAS materials have been extensively tested for medical and food use, modification of these materials to contain methacrylic and acrylic functional groups necessitates further characterization and toxicity testing.

4.3.5.1 Cytotoxicity screen of CLIP monomers

During the CLIP process, monomers undergo polymerization, resulting in materials with a much lower toxicity compared to the starting materials [13]. However, a major concern with photopolymerization as a method of synthesizing biomaterials is the residual monomer that can leach out. Thus, it is important to characterize the toxicity of monomers.

The results of a cytotoxicity screen of methacrylate and acrylate functionalized materials used to produce our drug loaded devices is shown in Fig. 4.9. Also presented is the toxicity of PCL₅₃₀-diol, the starting material in the synthesis of PCL₇₀₀-DMA. IC₅₀ values for these materials are presented in table 4.4. Toxicity was the highest in AA, with an observed toxicity for all concentrations studied. All oligomeric dimethacrylate materials showed a similar toxicity, which was comparably lower than the low molecular weight dimethacrylate, EGDMA. However, when comparing relative to the molar concentration of methacrylate groups (Fig. 4.8 B), the difference is not as substantial. The mono-acrylate, HEA, showed a higher toxicity relative to all methacrylate materials. This agrees with previous observations of increased toxicity in acrylic monomers compared to methacrylic counterparts [12,14-16]. Comparison of the viability of cells treated with PCL₅₃₀-diol and PCL₇₀₀-DMA illustrates the effect of functionalizing a material with methacrylate groups.

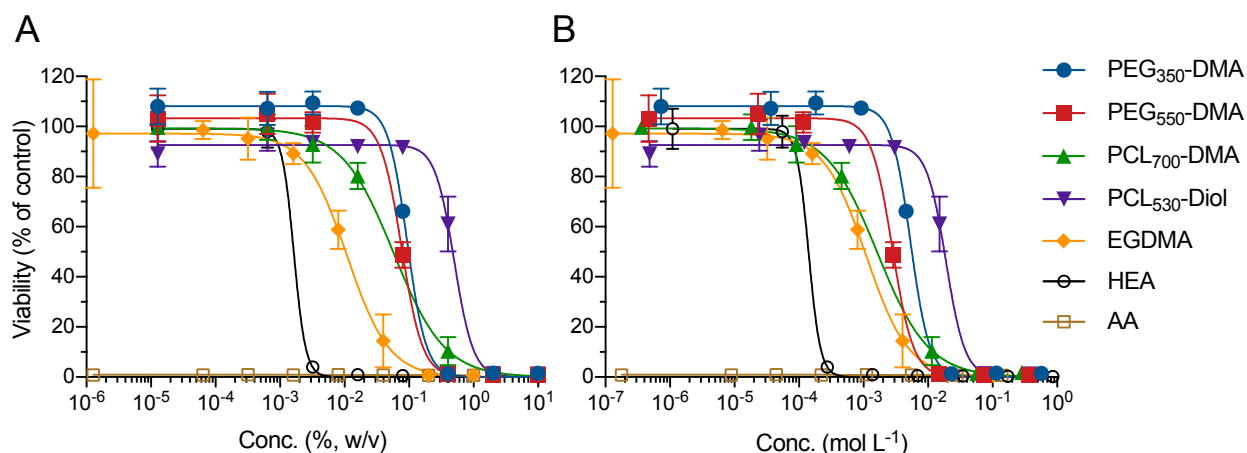


Figure 4.9 Biocompatibility of monomers on 344SQ cells. Cell viability is presented as a fraction of the control and is plotted against (A) weight percent monomer (w/v) and (B) a molar concentration of the functional group (acrylate, methacrylate, or hydroxyl groups).

Table 4.4 IC_{50} values for resin components in 344SQ cells. IC_{50} values were generated by fitting a nonlinear regression model with a variable slope using GraphPad PRISM 7. Error is given in standard error (SE).

Material	# (type) of functional groups	MW per func. group ($g\ mol^{-1}$)	$IC_{50} \pm SE$ (wt%)	$IC_{50} \pm SE$ ($mmol\ L^{-1}$)
PEG ₃₅₀ -DMA	2 (methacrylate)	175	0.093 ± 0.005	5.3 ± 0.3
PEG ₅₅₀ -DMA	2 (methacrylate)	275	0.077 ± 0.004	2.8 ± 0.1
PCL ₇₀₀ -DMA	2 (methacrylate)	350	0.057 ± 0.008	1.6 ± 0.2
PCL ₅₃₀ -diol	2 (hydroxyl)	265	0.50 ± 0.05	18.9 ± 1.8
EGDMA	2 (methacrylate)	99.1	0.011 ± 0.002	1.1 ± 0.2
HEA	1 (acrylate)	116.2	0.0016 ± 0.0004	0.14 ± 0.03
AA	1 (acrylate)	72.1	$< 1.28 \times 10^{-6}$	$< 1.8 \times 10^{-7}$

4.3.5.2 Degradation and cytotoxicity of CLIP devices

When designing a long-acting, implantable drug release device, it is desirable to have that device be biodegradable and bioabsorbable, so as to eliminate the need for a follow up procedure for device removal. Numerous devices have been developed and FDA approved using linear aliphatic polyesters such as PLA, PGA, PLGA, PCL, and their copolymers [17]. These polyesters are hydrolytically- and enzymatically-labile and can display a wide range of degradation and release kinetics depending on parameters such as molecular weight, crystallinity and monomer ratios [18]. Here, we synthesized a photopolymerizable PCL oligomer to be used to form a network with degradable crosslinks. The PCL₇₀₀-DMA used here is a free-flowing liquid at room temperature and can be directly utilized as a resin without the addition of reactive or non-reactive diluents.

Results of the degradation of a series of printed disks in pH7.4 PBS at 37 °C (Fig. 4.10 A) indicate a slow degradation of devices containing PCL₇₀₀-DMA. The degradation in PBS is expected to be slow, as PCL is a hydrophobic polymer and is known to exhibit a slow degradation profile [19,20]. The devices in this study are expected to degrade even slower due to the tight crosslinking further inhibiting water infiltration and erosion. Over the course of 6 months the 100 % PCL₇₀₀-DMA network showed a degradation weight loss of 15 % and the PCL₇₀₀-DMA/HEMA disks lost 7.5 % by mass. The disks fabricated from 100 % PEG₇₅₀-DMA showed no increased mass loss over the initial soluble fraction of the network, as expected with PEG₇₅₀-DMA forming a non-degradable network. Disks formulated with PCL₇₀₀-DMA blended with PEG₃₆₀-MA or PEG₇₅₀-DMA both show very slight mass loss over the initial release of the soluble fraction. The high soluble fraction in parts containing PEG₃₆₀-MA is believed to be caused by the presence of unfunctionalized PEG in the starting material.

A concern in the design and development of medical devices, especially implantables, is the cytotoxicity of leachables and degradation products. To test for this, solutions of pH7.4 PBS, which contain any leachable or degradation product released by the device during the

incubation time, were screened for cytotoxicity against an epithelial cell line (HeLa) and an endothelial cell line (HuVEC). Regardless of formulation or incubation time, no samples displayed cytotoxicity greater than 25 % *in vitro* (Fig. 4.10 B and C).

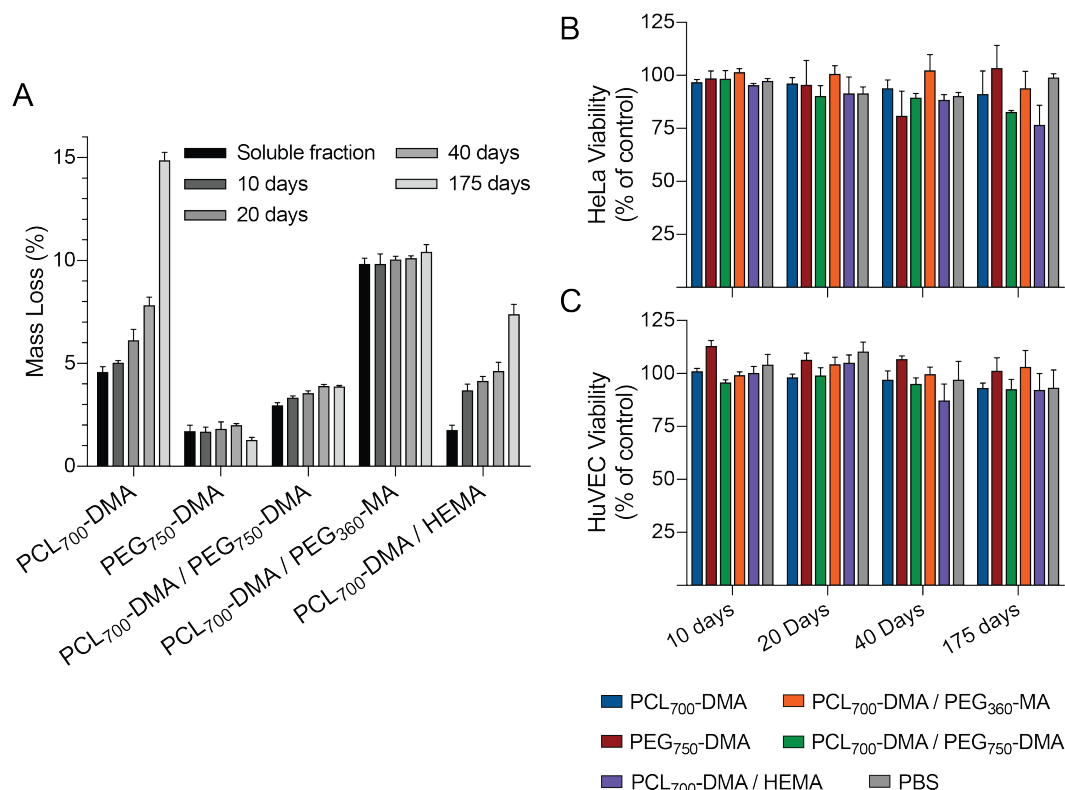


Figure 4.10 (A) Mass loss from blank disks due to degradation and extraction of soluble content. Cytotoxicity of degradation products and extractables on (B) HeLa cells and (C) HUVEC cells.

4.4 Conclusion and Future Work

The work presented in this chapter outlines the investigations of the potential utility of CLIP in a clinical setting. A relatively simple screening method for small drug molecules to determine the potential stability towards the CLIP process was demonstrated. However, the use of DexAc as an example also indicated that drugs that show instability during the initial screen may in fact be able to be formulated into a device with a majority of the API intact. Further optimization of this screening method will be required to improve the accuracy of the ability to

predict drugs that will or will not be suitable for formulation directly into the liquid photopolymer resins.

Further enhancements of this screening method may include implementation of high throughput techniques such as using microwell plates used in biomolecule purification for rapid sample prep, testing, filtration, and HPLC analysis. Optimization of a pre-screening technique may significantly reduce the effort and time required to find appropriate therapeutics to be applied with this CLIP technique. One area this approach may benefit is for the screening of proteins, of which a large portion would be expected to be instable to the UV light and radical chemistry of CLIP. Thus, a high throughput screen would reduce the time and cost necessary to identify a suitable candidate for an application.

A goal of this chapter was to apply the principles established in Chapter 3 for controlling drug release formulation parameters using therapeutically relevant drugs. We successfully loaded 5 resins of varying crosslink density and polymer network compositions. We used CLIP to print model devices that with accurate loading and release kinetics that paralleled those observed for the release of RhB. Further, devices were loaded with drugs through coating with a PEG solution as an alternative method of loading, which was characterized by a rapid drug release.

A logical next step in this development would be to pursue the loading of multiple drugs through the combination of the two loading methods discussed in this chapter. For example, a device can be fabricated to contain two drugs, drug A and drug B. Said device can be fabricated using a resin containing drug A dissolved, to achieve a prolonged release that will be dependent on the formulation of the network. Drug B can then be coated onto the device following fabrication, affording a rapid release of drug B independent of the device material and release kinetics of drug A.

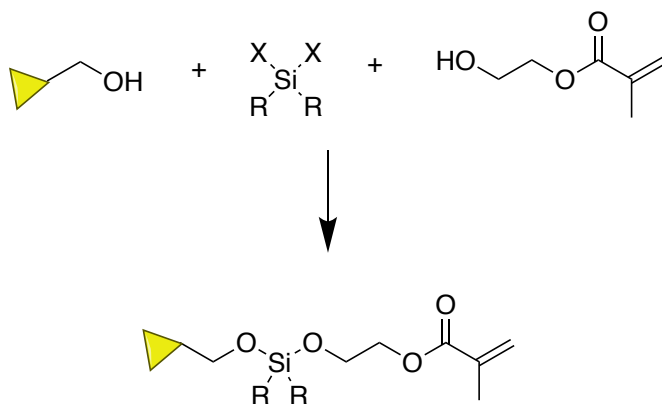
Future directions for drug loading in CLIP devices should include further exploration of drug loading methods, both traditional and novel. More sophisticated coating schemes would

afford added control over the release kinetics of post-loaded drugs, including multilayered coatings for tuned release or sequential release of multiple drugs [21]. Incorporating multiple phases into the network through emulsions or particulate suspensions would provide another method of controlling drug release. Further, if the drug and the radical initiator are in separate phases, this approach may serve as a strategy to further protect the API from potential degradation.

In addition to applying well-established methods of controlling drug release, methods such as conjugating the drugs into the network through cleavable linkers may serve as an interesting approach. For example, the use of asymmetric bifunctional silyl-ether (ABS) prodrug chemistry has been shown to be a viable method of controlling drug release in hydrogel nanoparticles (Fig. 4.11 A) [22]. Conjugation of the drug into the network would also allow for thorough washing steps to remove any unreacted monomers without the worry of extracting the loaded drug. Another interesting approach would be to conjugate the drug into the network during the washing procedure. One potential method of achieving this would be to use Click chemistry to react an azide-functionalized prodrug into a network containing pendant alkyne groups (Fig. 4.11 B) [23].

Lastly, this chapter presented initial *in vitro* cytocompatibility towards any degradation product or leachable material through 175 days. Further work to demonstrate biocompatibility will require *in vivo* characterization of tolerability. Preliminary *in vivo* experiments are presented in Chapter 5. Collectively, this work serves as the foundational evidence for biocompatibility of CLIP devices and the suitability of the platform as a technique to fabricate drug loaded devices.

A



B

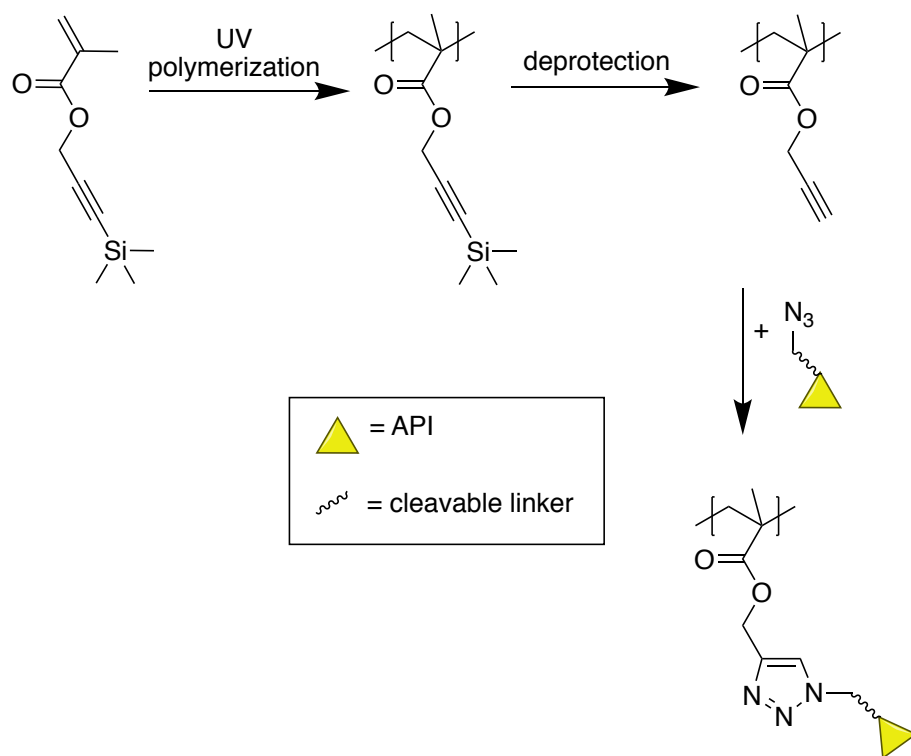


Figure 4.11 Theoretical approaches to functionalize drug into network using (A) asymmetric bifunctional silyl-ether prodrug strategy to incorporate API into the network during fabrication and (B) click chemistry as a method to conjugate the API into the network following fabrication., either following or as a step of the post-processing wash procedures.

REFERENCES

- [1] R.J. Morrison, S.J. Hollister, M.F. Niedner, M.G. Mahani, A.H. Park, D.K. Mehta, et al., Mitigation of tracheobronchomalacia with 3D-printed personalized medical devices in pediatric patients, *Sci Transl Med.* 7 (2015) 285ra64–285ra64. doi:10.1126/scitranslmed.3010825.
- [2] R.J. Morrison, K.N. Kashlan, C.L. Flanagan, J.K. Wright, G.E. Green, S.J. Hollister, et al., Regulatory Considerations in the Design and Manufacturing of Implantable 3D-Printed Medical Devices, *Clin Transl Sci.* 8 (2015) 594–600. doi:10.1111/cts.12315.
- [3] Food and Drug Administration, PAT—Framework for Innovative-Pharmaceutical Development, Manufacturing, and Quality Assurance., 2004.
- [4] H. Vakili, R. Kolakovic, N. Genina, M. Marmion, H. Salo, P. Ihalainen, et al., Hyperspectral imaging in quality control of inkjet printed personalised dosage forms, *International Journal of Pharmaceutics.* 483 (2015) 244–249. doi:10.1016/j.ijpharm.2014.12.034.
- [5] N. Sandler, I. Kassamakov, H. Ehlers, N. Genina, T. Ylitalo, E. Haeggstrom, Rapid interferometric imaging of printed drug laden multilayer structures, *Sci Rep.* 4 (2014) 4020. doi:10.1038/srep04020.
- [6] J. Norman, R.D. Madurawe, C.M.V. Moore, M.A. Khan, A. Khairuzzaman, A new chapter in pharmaceutical manufacturing: 3D-printed drug products, *Advanced Drug Delivery Reviews.* 108 (2017) 39–50. doi:10.1016/j.addr.2016.03.001.
- [7] J. Brandrup, E.H. Immergut, E.A. Grulke, *Polymer handbook*, vol. II, New York: Wiley, 1999.
- [8] E. Fasani, A. Albini, Photostability Stress Testing, in: S.W. Baertschi, K.M. Alsante, R.A. Reed (Eds.), *Pharmaceutical Stress Testing*, 2nd ed., 2016: pp. 192–217.
- [9] M.C. DeRosa, R.J. Crutchley, Photosensitized singlet oxygen and its applications, *Coordination Chemistry Reviews.* (2002).
- [10] E. Andrzejewska, Photopolymerization kinetics of multifunctional monomers, *Progress in Polymer Science.* 26 (2001) 605–665. doi:10.1016/S0079-6700(01)00004-1.
- [11] T.F. Scott, W.D. Cook, J.S. Forsythe, Photo-DSC cure kinetics of vinyl ester resins II: influence of diluent concentration, *Polymer.* 44 (2003) 671–680. doi:10.1016/S0032-3861(02)00788-7.
- [12] E. Yoshii, Cytotoxic effects of acrylates and methacrylates: relationships of monomer structures and cytotoxicity, *J. Biomed. Mater. Res.* 37 (1997) 517–524.
- [13] B.V. Slaughter, S.S. Khurshid, O.Z. Fisher, A. Khademhosseini, N.A. Peppas, *Hydrogels in Regenerative Medicine*, *Adv. Mater.* 21 (2009) 3307–3329. doi:10.1002/adma.200802106.

- [14] J. Autian, Structure-toxicity relationships of acrylic monomers, *Environ. Health Perspect.* 11 (1975) 141–152.
- [15] W.H. Lawrence, G.E. Bass, W.P. Purcell, J. Autian, Use of mathematical models in the study of structure-toxicity relationships of dental compounds. I. Esters of acrylic and methacrylic acids, *J. Dent. Res.* 51 (1972) 526–535. doi:10.1177/00220345720510024701.
- [16] H. Tanii, K. Hashimoto, Structure-toxicity relationship of acrylates and methacrylates, *Toxicol. Lett.* 11 (1982) 125–129.
- [17] B.D. Ulery, L.S. Nair, C.T. Laurencin, Biomedical Applications of Biodegradable Polymers, *Journal of Polymer Science Part B: Polymer Physics.* 49 (2011) 832–864. doi:10.1002/polb.22259.
- [18] F. Alexis, Factors affecting the degradation and drug-release mechanism of poly(lactic acid) and poly[(lactic acid)-co-(glycolic acid)], *Polym. Int.* 54 (2004) 36–46. doi:10.1002/pi.1697.
- [19] L. Yang, J. Li, Y. Jin, M. Li, Z. Gu, In vitro enzymatic degradation of the cross-linked poly(ϵ -caprolactone) implants, *Polymer Degradation and Stability.* 112 (2015) 10–19. doi:10.1016/j.polymdegradstab.2014.12.008.
- [20] H. Sun, L. Mei, C. Song, X. Cui, P. Wang, The in vivo degradation, absorption and excretion of PCL-based implant, *Biomaterials.* 27 (2006) 1735–1740. doi:10.1016/j.biomaterials.2005.09.019.
- [21] W. Wu, Q. Zheng, X. Guo, J. Sun, Y. Liu, A programmed release multi-drug implant fabricated by three-dimensional printing technology for bone tuberculosis therapy, *Biomed Mater.* 4 (2009) 065005. doi:10.1088/1748-6041/4/6/065005.
- [22] M.C. Parrott, M. Finniss, J.C. Luft, A. Pandya, A. Gullapalli, M.E. Napier, et al., Incorporation and Controlled Release of Silyl Ether Prodrugs from PRINT Nanoparticles, *J. Am. Chem. Soc.* 134 (2012) 7978–7982. doi:10.1021/ja301710z.
- [23] D. Quemener, D. Quemener, M.L. Hellaye, M.L. Hellaye, C. Bissett, C. Bissett, Graft block copolymers of propargyl methacrylate and vinyl acetate via a combination of RAFT/MADIX and click chemistry: Reaction analysis, *Journal of Polymer* 46 (2008) 155–173. doi:10.1002/pola.22367.

CHAPTER 5: PRECLINICAL EVALUATION OF CLIP MEDICAL DEVICES

Chapter goals

This chapter presents preclinical characterization of two implantable devices fabricated with CLIP for the treatment of cancer. The first device is an intraoperative implant, which is a chemotherapeutic-eluting patch, which can be placed in a resection cavity during a surgical procedure to reduce tumor recurrence. The devices are characterized for *in vitro* drug release and *in vivo* efficacy in a mouse model for lung cancer recurrence. Due to the singularity of each tumor, no single resection cavity will be identical. Thus, this device is an example of a potential clinical application that would benefit from the ability of a surgeon to modify a design specifically for the patient's anatomy.

The second application is using CLIP to fabricate drug-loaded spacers to supplement brachytherapy, which is the placement of radioactive seeds locally into the tumor site for the treatment of prostate cancer. Preliminary *in vivo* efficacy studies are presented. Additionally, proof of concept studies demonstrating the potential of applying methods to modify drug release (as introduced in Chapter 3) to small devices like brachytherapy spacers is discussed.

5.1 Introduction

5.1.1 Lung cancer recurrence following surgical resection

Lung cancer is the leading cause of cancer deaths in the world. In the United States alone, approximately 220,000 new cases of lung cancer are expected to be diagnosed in 2017, and an estimated 160,000 deaths will be caused by the disease [1-3]. In cases of non-small cell lung cancers (NSCLC), which makes up around 85 % of lung cancer diagnoses, surgical resection has been shown to provide the best possibility of cure and chance for survival [2,3]. However, post-resection recurrence remains a large challenge for treating NSCLC, with

between 30 and 70 % of patients, depending on the disease stage, suffering a recurrent tumor either locally or at a metastatic site [4]. In a study monitoring 1073 patients that underwent complete resections, 445 patients developed recurrent tumors with a 11.5 month median time between resection and recurrence and 8.1 month median survival following recurrence.

One reason for this poor prognosis, even with early stage cancers, is due to the inability of many patients to undergo a local excision with wide negative margins. Surgical techniques that limit the resection area, such as wedge and segmentectomy, have been shown to have a worse survival outcome compared to more invasive lobectomy [5,6]. The use of multimodal approaches to treat NSCLC, such as combining resection with adjuvant chemotherapy or postoperative radiotherapy, have been shown to be beneficial in the reduction of tumor recurrence for stage II and some stage IB tumors [7]. However, with cisplatin-based doublet regimens serving as the standard of care for adjuvant chemotherapy, nephrotoxic and neurotoxic side effects can lead to lower quality of life for patients [8]. Further, the use of chemotherapy adjuvant is not indicated for patients with stage IA disease [7].

Local delivery of chemotherapeutics has been shown to limit systemic side effects, allowing for a higher exposure of the disease tissue to the active drug. Many forms of local delivery for cancer recurrence are being developed including films, particulate systems, and gels [9-14]. Due to the heterogeneous nature of each operation and resulting resection cavity, the use of a universal drug delivery device could be disadvantageous. The ability of 3D printing to fabricate a unique part would afford the production of customized drug delivery vehicles designed based on the anatomy of the individual patient. Within this chapter, we aim to demonstrate the potential of implementing the CLIP technology to fabricate drug-eluting patches to prevent the lung cancer recurrence following resection. Parameter optimization and ability to print with paclitaxel and a cisplatin prodrug directly incorporated into the liquid resin are presented. The presented device was characterized for *in vitro* drug release and *in vivo* efficacy for reducing tumor recurrence in a non-small cell lung adenocarcinoma resection model.

5.1.2 Brachytherapy background

Prostate cancer (PCa) is the most common non-skin cancer in men in the United States with over 180,000 new cases expected to be diagnosed in 2017 [1]. Fortunately, approximately 90 % of PCa patients present with localized and curable disease where the main curative treatments are radiotherapy and surgery [15]. One of the key radiotherapy treatment approach is low dose rate (LDR) interstitial brachytherapy, where iodine-125 seeds are placed directly into the prostate. Localization of the radiation source limits exposure to surrounding healthy tissue and increases the dose to the primary tumor (Fig. 5.1).

In several large studies, brachytherapy has been shown to be effective for the treatment of low to intermediate-risk PCa with disease-free survival rates comparable to that of surgery and external beam radiotherapy [16,17]. Further, results of the recent ASCENDE-RT trial [18] indicated that LDR brachytherapy plus external beam is the most effective treatment for high-risk PCa with 9-year disease free rates of 83 %, unmatched by any other treatment regimens [19]. Despite the favorable characteristics of brachytherapy, it has several significant limitations. First, brachytherapy can cause significant urinary side effects, including dysuria, urinary frequency, urgency, and, in some cases, urinary obstruction [19]. These urinary side effects are caused by the post-procedural edema and limit brachytherapy from use in patients with prostate weights greater than 60 grams or less than 20 grams [20]. Such size restrictions have kept many patients from pursuing brachytherapy. In addition, brachytherapy has been shown to be less effective as a sole treatment against intermediate- and high-risk PCa [21] [22]. Additional treatments may negate the simplicity of the single outpatient procedure of brachytherapy. Given the importance of brachytherapy, there is a high interest in the development of novel strategies to further improve its therapeutic index.

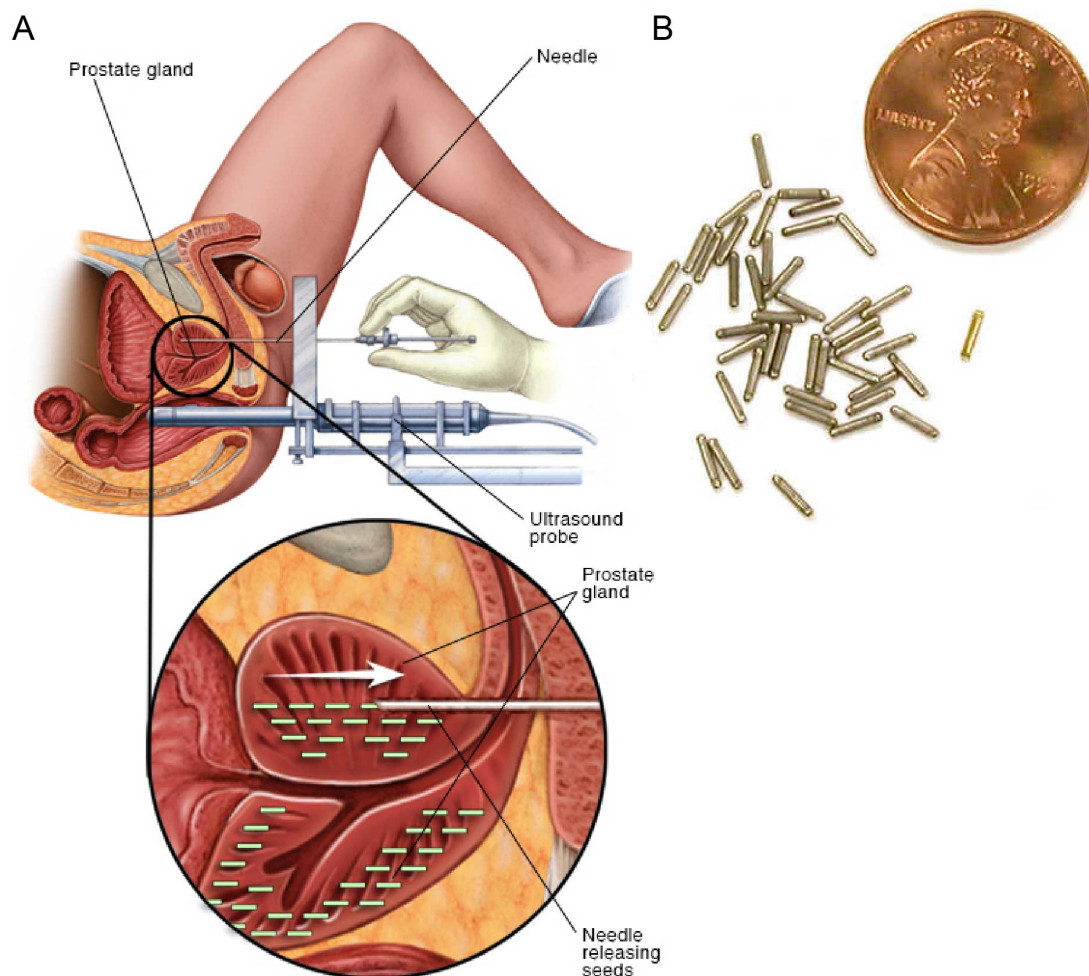


Figure 5.1 Brachytherapy schematic. Brachytherapy is a treatment is the placement (A) of radioactive seeds placed directly inside of the prostate gland. Spacers are devices that are placed between the seeds (B) to achieve the desired radiation dose and dosimetry. Figure (A) was used with permission of Mayo Foundation for Medical Education and Research. All rights reserved. Photo (B) was courtesy of Nuclear Regulatory Council.

One approach to improving brachytherapy is the addition of several therapeutics that have shown potential in either minimizing the side effects of brachytherapy or improving its efficacy. Dexamethasone (DEX), a corticosteroid, has been evaluated extensively in brachytherapy for mitigating urinary side effects by reducing edema [23]. However, systemic effects limit the prolonged use of DEX after brachytherapy and its use has not been widely adopted. Docetaxel (DTXL) is another therapeutic that has been shown to act synergistically with radiotherapy in treating high-risk PCa [24]. Clinical evaluation of concurrent administration

of DTXL with external beam radiotherapy for high-risk and locally advanced PCa have shown promising results [24-26]. Unfortunately, DTXL's systemic side effect profile has been prohibitive to its incorporation into brachytherapy.

A strategy to overcome the systemic side effects of the above-mentioned medications is to deliver these drugs locally in the prostate. Local drug delivery can minimize systemic side effects while achieving the desired therapeutic effect. To attain both sustained reduction in side effects and improvement in efficacy, an ideal release would occur in a controlled and prolonged fashion over the course of 2 months, which is equivalent to the half-life of iodine-125 decay. Currently, brachytherapy seeds are implanted into tissue along with biologically inert spacers, which simply serve as a mechanism to separate radioactive seeds. Thus, we sought to incorporate therapeutics into spacers. This chapter will present preliminary studies on the use of CLIP to engineer drug-eluting brachytherapy spacers with controlled release properties. We sought to implement geometric design strategies demonstrated in Chapter 3 on the scale of brachytherapy spacers (cylinders with 0.75 mm diameter, 5 mm length). We also investigated controlling network crosslink density through manipulation of light intensity and exposure during the print process. Uses of such strategies would provide a platform for production of precisely engineered spacers with tunable drug release kinetics. Such devices would be designed to minimize the urinary side effects as well as improve therapeutic efficacy of brachytherapy and ultimately translate into better quality of life and improved survival.

5.2 Materials and Methods

5.2.1 Materials

Poly(ethylene glycol) dimethacrylate $M_n = 550 \text{ g mol}^{-1}$ (PEG₅₅₀-DMA), 2-hydroxyethyl methacrylate (HEMA), diphenyl(2,4,6-trimethylbenzoyl)phosphine oxide (TPO), and UV-

absorber 2-*tert*-Butyl-6-(5-chloro-2*H*-benzotriazol-2-yl)-4-methylphenol (BLS 1326) were purchased from Sigma Aldrich. Ethyl (2,4,6-trimethylbenzoyl) phenylphosphinate, sometimes referred to as lucirin TPO (LTPO), was purchased from Combi-Blocks. Polycaprolactone-dimethacrylate $M_n = 700 \text{ g mol}^{-1}$ (PCL₇₀₀-DMA) was synthesized as described in Chapter 2.

Phosphate buffered saline (PBS), chloroform, 2-propanol, acetonitrile, dimethyl sulfoxide (DMSO), diethyl ether, and water were purchased from Fisher Scientific. Solvents used for HPLC analysis were all HPLC grade purity or higher. Docetaxel (DTXL) and Paclitaxel (PTX) were purchased from LC Labs. Cisplatin (CDDP) was purchased from sigma and octanoic anhydride was purchased from TCI America. Clinical formulations of DTXL, PTX, and CDDP were purchased from the University of North Carolina Hospital pharmacy. All materials were stored as directed by the supplier and used as received.

CPP was synthesized according to well described methods elsewhere [27-30]. Briefly, CDDP was oxidized to the Pt(IV) complex, $\text{Pt}(\text{NH}_3)_2\text{Cl}_2(\text{OH})_2$ by stirring with a tenfold excess of hydrogen peroxide in water at 50 °C for 1 hour. The suspension was cooled to room temperature and the Pt(IV) complex was recollected via crystallization and washed with DI water (2x), cold ethanol, and cold diethyl ether. The complex was then acetylated with octanoic anhydride in DMSO overnight. An equal volume of water was added to precipitate the prodrug, which was subsequently recollected via filtration. Residual water was removed by dissolving in acetonitrile followed by removal of the water and acetonitrile azeotrope through rotary evaporation.

5.2.2 Cell culture

344SQ cells were a gift from the University of Texas M.D. Anderson Cancer Center (Jon Kurie Lab). LNCaP cells and PC3 cells were purchased from ATCC. 344SQ and LNCaP cells were cultured in RPMI (Gibco) medium and PC3 cells were cultured in F12-DMEM (Gibco).

Both media were supplemented with 10 % fetal bovine serum. All cells were maintained in a humidified atmosphere of 5 % CO₂ at 37 °C.

5.2.3 Experimental Animals

All experiments involving animals were performed in accordance with the National Research Council's Guide to Care and Use of Laboratory Animals (1996), under an animal use protocol approved by the University of North Carolina Institutional Animal Care and Use Committee. All animals used were supplied by the University of North Carolina Animal Studies Core. All mouse procedures were performed with the help of the UNC Animal Studies Core staff.

5.2.4 Methods for Intraoperative needles to reduce cancer recurrence

5.2.4.1 Optimization of CLIP parameters for the fabrication of intraoperative devices

Devices were fabricated using a formulation with and without UV absorber. The resins were formulated with 48.5 parts PEG₅₅₀-DMA, 48.5 parts HEMA, 2.5 parts UV initiator LTPO. 0.5 parts BLS 1326 was added as UV absorber to the UV-absorber resin. Resins were mixed in a planetary centrifugal mixer (Thinky USA, Inc.) for 5 minutes at 2000 rpm to produce a transparent solution. All prints were carried out on a S1 prototype CLIP printer (Carbon). Print parameters were optimized by first finding an appropriate speed to print the backing without major defects due to resin flow. Then with print speed held constant, the light intensity was systematically decreased until the resolution was appropriate for an accurate fabrication or when structural integrity of the part was compromised. The optimal parameters were achieved with the UV absorber containing resin (48.5 parts PEG₅₅₀-DMA, 48.5 parts HEMA, 2.5 parts LTPO, and 0.5 parts BLS 1326). The print parameters were found to be 10 mm hr⁻¹ and 10 mW cm⁻². These parameters were used for fabrication of devices in all subsequent experiments for studying intraoperative devices.

The post-processing protocol was established by visual comparison of implants that had been washed using a custom fabricated apparatus to hold the printed implant in a wash solution that is under constant stirring on a magnetic stir plate. A short wash (5 seconds) in 2-propanol was compared to a longer wash (30 seconds) in DI water. It was found that the water wash followed by quickly dipping the part into acetone removed residual resin. The final post processing protocol was as follows:

1. 30 seconds in DI water (in 100 mL Thinky brand disposable mixing cup, with 2 cm stir bar and Cimarec Barnstead Thermolyne stir plate set to level 8)
2. 1 second dip into acetone
3. Remove surface acetone with compressed air canister
4. 5 minute postcure in UV LED oven

This wash protocol was used for the remainder of the studies for intraoperative devices.

5.2.4.2 Fabrication of drug-loaded intraoperative devices

Drug-loaded resins were formulated by adding either 5 wt % PTX or 4 wt % CPP to the base resin containing UV absorber established in Sect. 5.2.4.1. Drug was mixed into the resins under magnetic stirring in amber vials. PTX was completely soluble and resulted in a transparent solution. CPP was insoluble and resulted in an opaque yellow-white solution. Drug-loaded spacers were fabricated using the optimized parameters and wash protocol described in Sect. 5.2.4.1 above. If devices were to be used in an *in vitro* cell culture or *in vivo* mouse experiment, an extra step of exposing to the germicidal UV light of a biological hood for 10 minutes and handled aseptically for all future procedures. Parts were imaged by scanning electron microscope (SEM) with a Hitachi S-4700 SEM. Prior to imaging, parts were coated with 2 nm of a palladium-gold alloy using a Cressington 108 sputter coater.

5.2.4.3 In vitro drug release studies

Drug release studies were carried out using model devices that were designed to have the same surface area to volume (SA/V) ratio as the intraoperative devices. The model disks

were printed and post-processed using identical parameters to the implants. Drug release was studied by placing a single, pre-weighed disk into microcentrifuge filter units with no filter in place (Corning). Filter units containing the devices were inserted into floating racks and placed into a 15 L bath of pH 7.4 PBS, which was kept under constant stirring at 37 °C using a immersed circulating heating unit. At given time points, devices were removed (n=5) and the remaining drug was extracted in 10 mL of a solution of 1:1 acetonitrile:2-propanol for 3 days under constant oscillation in an incubated shaker at 150 rpm and 37 °C. Mass of the extracted drug was quantified using an Agilent 1260 series HPLC equipped with a Zorbax Eclipse C-18 reverse phase column at 40 °C and a constant flow rate of 1 mL min⁻¹. Both PTX and CPP samples were analyzed using a gradient mobile phase composed of solvents A (water) and B (acetonitrile). The mobile phase was changed from 50 % to 100 % B over 10 minutes, washed with a 5-minute isocratic hold of 100 % B, and followed by 5 minutes of 50 % B to equilibrate the column prior to the next sample. Absorbance was measured at 227 nm and concentration of the extraction solution was determined by comparing peak integrations to a standard curve of known concentrations. PTX elution time was observed at 4.6 minutes and CPP eluted at 6.0 minutes.

5.2.4.4 In vivo tumor recurrence model

Female athymic nude mice between 6-8 weeks of age and weighing between 20-30g were inoculated with luciferase-expressing 344SQ cells into the right flank (10⁶ cells in 100 µL in 50 % v/v complete medium and Matrigel®). When tumors reached 7 mm in the longest dimension, mice were anesthetized by inhalation with 2 % isoflurane and tumors were resected through a small 1 cm incision. Mice were randomized into one of eight treatment groups, which was administered immediately following resection: (1) resection only, (2) blank implant, (3) PTX implant, (4) CPP implant, (5) PTX/ CPP implant, (6) 100 µL I.V. PTX (18 mg/kg), (7) 100 µL I.V. CDDP (5 mg/kg), (8) 100 µL I.V. PTX/CDDP (18 mg/kg, 5 mg/kg). For mice receiving no

additional treatment or I.V. administration, the incision was closed with wound clips and the I.V. treatment was administered via tail vein injection. For mice treated with an implant, the implant was placed in the resection cavity prior to closing the incision with wound clips. Tumor volumes were monitored via physical measurements using calipers. Tumor volume was calculated using: $L \times W^2/2$, where L is longer than W . Bioluminescence was monitored by intraperitoneal injection of luciferin followed by imaging using an IVIS Lumina system (Caliper Inc.) and analyzed using ROI analysis of total radiance (photons/s/cm²/sr) using the Living Image analysis program (Caliper Life Sciences). Tumor measurements were taken every Monday, Wednesday, and Friday. Mice were humanely sacrificed using CO₂ inhalation when tumors reached 2 cm in the largest dimension or if tumors became ulcerated.

5.2.4.5 Clinical chemistry and histopathological analysis

Blood was drawn via submandibular bleeds on the day of tumor resection, 4 days following, and 8 days following resection and treatment. Complete blood counts and a metabolic activity panel including aspartate aminotransferase (AST), alanine aminotransferase (ALT), blood urea nitrogen (BUN), and creatinine (Crea) were carried out by the UNC clinical chemistry core. At the end of the study, tumors were harvested and fixed in 10 % neutral buffered formalin for at least 7 days at room temperature and transferred to the Animal Histopathology Core in the UNC School of Medicine for H&E and Masson's trichrome staining.

5.2.5 Methods for CLIP brachytherapy spacers

5.2.5.1 CLIP brachytherapy spacers for *in vitro* toxicity and *in vivo* efficacy

Brachytherapy spacers with no drug and spacers containing 2 wt % DTXL were tested for cytotoxicity *in vitro* and efficacy *in vivo*. The base resin was formulated by dissolving TPO at a concentration of 1 wt % in PCL₇₀₀-DMA under magnetic stirring at room temperature overnight. Drug-loaded resins were formulated by dissolving DTXL into the base resin at 2 wt % with an additional night stirring at room temperature. Spacers were fabricated using a CLIP7

prototype printer equipped with a 365 nm UV LED light source (Carbon) using a light intensity of 2.35 mW cm^{-2} and a continuous speed of 75 mm hr^{-1} . Spacers were washed by dipping the build platform into a bath of acetonitrile three time for ~ 2 seconds each. Spacers were then dried with compressed air and then further under reduced pressure in a vacuum oven overnight (room temperature). Spacers receiving a post cure were placed in a UV oven equipped with a mercury arc lamp for 3 minutes (ELC-4001 equipped with UVA lamp, Electro-lite Corporation) prior to being placed in the vacuum oven.

5.2.5.2 In vitro cytotoxicity of CLIP brachytherapy spacers

LNCaP prostate cancer cells were plated at a density of $5000 \text{ cells cm}^{-2}$ in a 24-well plate and allowed 24 hours to adhere. Cells were then incubated with fresh culture medium (2 mL) and a transwell insert containing 1, 2, or 4 brachytherapy spacers. Four spacer types were screened: (1) blank spacers without postcure, (2) blank spacers with postcure, (3) DTXL spacers without postcure, and (4) DTXL-spacers with postcure. Spacers were incubated with cells for 72 hours, at which point culture medium was aspirated off and 150 μL of Cell Titer-Glo® reagent (Promega) and 150 μL of fresh medium was added. Cells were then incubated for 2 minutes at 37°C , placed on a shaker for 2 minutes, and stored in the dark at room temperature for 5 minutes to allow the luminescence signal to stabilize. Solution was then transferred to an opaque 96-well plate and the luminescence signal was recorded using a SpectraMax M5 plate reader (Molecular Dynamics). Viability was expressed as a percentage of the signal compared to cells treated with PBS.

5.2.5.3 In vivo efficacy of CLIP brachytherapy spacers

Male athymic nude mice between 20-30 g body weight and 6-8 months of age were inoculated in the subcutaneous region of the right flank with 1×10^6 luciferase expressing PC3 human prostate cancer cells in 100 μL of 50 % v/v Matrigel® (Corning) in FBS-free F12-DMEM medium. Tumors were allowed to grow until they reached $80\text{-}150 \text{ mm}^3$, at which point they were

randomized into four groups (n=8 for each) to be treated by: (1) CLIP DTXL spacers, (2) CLIP blank spacer, (3) I.V. Docetaxel (10 mg/kg), and (4) no treatment. I.V. treatments were administered via tail vein injections. For mice receiving spacers, two spacers were placed directly into the tumor using an 18-gauge needle and a custom fabricated plunger. Spacers were placed into the tumor parallel to each other to cover the most area as possible. Tumor volumes and bioluminescence was monitored as described above in Sect. 5.2.4.4.

5.2.5.4 Solvent uptake in brachytherapy spacers printed with different overall light exposures

Solvent uptake was determined for brachytherapy spacers printed with a range of print speeds at constant light intensity. 25 brachytherapy spacers were arrayed onto a 1mm thick backing in a 5x5 array. A model was also generated of the backing alone. The models were printed on a CLIP7 prototype printer equipped with a 365 nm LED light source (Carbon). A light intensity of 1.75 mW cm^{-2} was used for all prints and three speeds (45, 67.5, and 90mm hr⁻¹) were used. The bases were printed at the same intensity and speed regardless of the speed used for the spacer region of the model.

Parts were dried in the vacuum oven, massed and placed in chloroform for 24 hours. Swollen parts were collected by pouring over a gravity filter, massed, and dried in the vacuum oven. At that point in the experiment, spacer models and the base without spacers was weighed to calculate the mass of the spacers alone according to (5.1).

$$M_{sp} = M_{part} - M_{base} \quad (5.1)$$

Where M_{sp} is the mass of the spacers, M_{part} is the mass of the entire printed part including the base, and M_{base} is the average mass of three bases printed without any spacers arrayed on the model. Solvent uptake was then defined according to (5.2).:

$$\text{Degree of swelling in spacers (\%)} = \frac{M_{s,sp} - M_{0,sp}}{M_{0,sp}} \times 100 \quad (5.2)$$

Where $M_{s,sp}$ is the swollen mass of the spacers only and $M_{0,sp}$ is the initial mass of the spacers only. A relative dosage was calculated for each set of prints using (5.3).

$$D_r = \frac{I}{S} \quad (5.3)$$

Where D_r is relative light dosage (mJ cm^{-3}), I is light intensity (mW cm^{-2}), and S is print speed (cm s^{-1}).

5.2.5.5 DTXL release from brachytherapy spacers printed with different overall light exposures

DTXL-loaded spacers were printed using the CLIP7 prototype printer at a constant speed of 75 mm hr^{-1} and a range of light intensity (7.7, 5.3, and 2.4 mW cm^{-2}). A spacer was also fabricated using a continuous linear gradient of intensity between 7.7 and 2.4 mW cm^{-2} over the course of the print. The post-process was carried out as described in Sect. 5.2.5.1.

In vitro drug release was characterized by placing 45 spacers for each study arm in a 2 mL Slide-A-LyzerTM MINI dialysis cassette with the bottom of the conical tube cut off (Fig. 5.2). The cassettes were then inserted into foam floating racks and placed into 2 L of pH 7.4 PBS, which was under constant stirring on a magnetic stir plate in an incubator set to 37°C . The PBS release medium was changed every 3 days to ensure sink conditions were maintained. At each designated timepoint, 3 spacers were removed and the drug remaining was extracted from the spacers in acetonitrile for 2 weeks at 37°C under constant shaking. The drug concentration in the extraction solution was quantified using HPLC analysis as stated in Sect. 5.2.4.3.

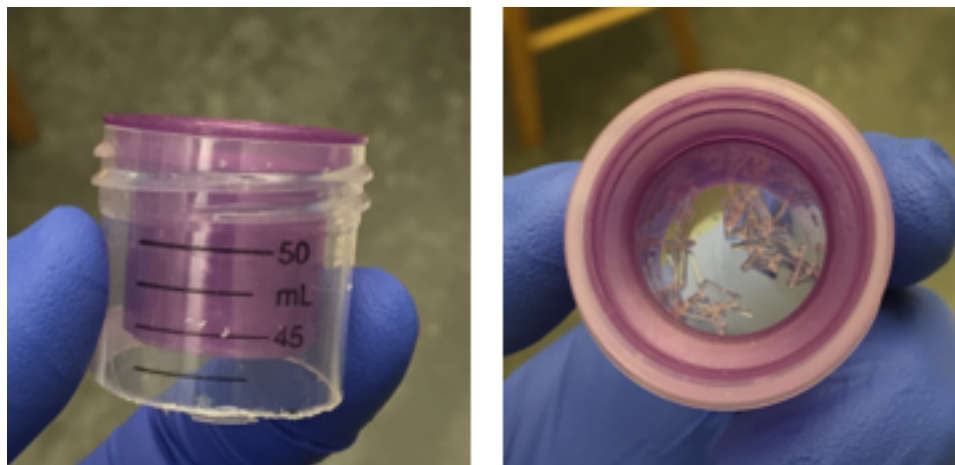


Figure 5.2 Modified Slide-a-lyzers™ MINI dialysis cassettes for *in vitro* release studies. 45 replicates of each type of spacer was added to individual cassettes (one cassette per study arm) and floated in a 2 L bath of pH 7.4 PBS, which was changed regularly to maintain sink conditions.

5.2.5.6 Printing complex geometries on the scale of brachytherapy spacers

The ability to print complex geometries on the scale of brachytherapy spacers was demonstrated using a resin formulated from 1 wt % TPO initiator and 0.05 wt % BLS1326 UV absorber dissolved into PEG₅₅₀-DMA. Models were generated in Magics Structures (Materilise) by arraying rhombic, diamond unit cells (0.75 x 0.75 x 0.375 mm) to fill 1mm tall cylinders (0.75 mm diameter) on a backing slab. A second model was generated by arraying diamond unit cells (0.75 x 0.75 x 0.75 mm) vertically to fill cylinders of 1, 2.5, and 5 mm in length both with and without a solid shell surrounding the cylindrical structure. Parts were fabricated at a speed of 50 mm hr⁻¹ and a light intensity of 3 mW cm⁻² using a CLIP S1 prototype printer equipped with a 385 nm UV LED light source. Parts were subsequently washed with 2-propanol, dried and subjected to a 5 minutes postcure under a mercury UV lamp.

5.3 Results and Discussion

5.3.1 Intraoperative implants to reduce cancer recurrence

5.3.1.1 Optimization of CLIP parameters and processing for fabrication of intraoperative device

A model device was designed to be used in a mouse model of cancer recurrence following surgical resection (Fig. 5.3). Various backing thicknesses were tested, and the optimal thickness was found to be 0.75 mm. Thicker backings were bulky and would likely cause discomfort to the mice, and thinner backings were not structurally suitable to support the needles. A barbed arrowhead design was used to allow insertion, while subsequently resisting the elastic nature of soft tissue to remain embedded following placement

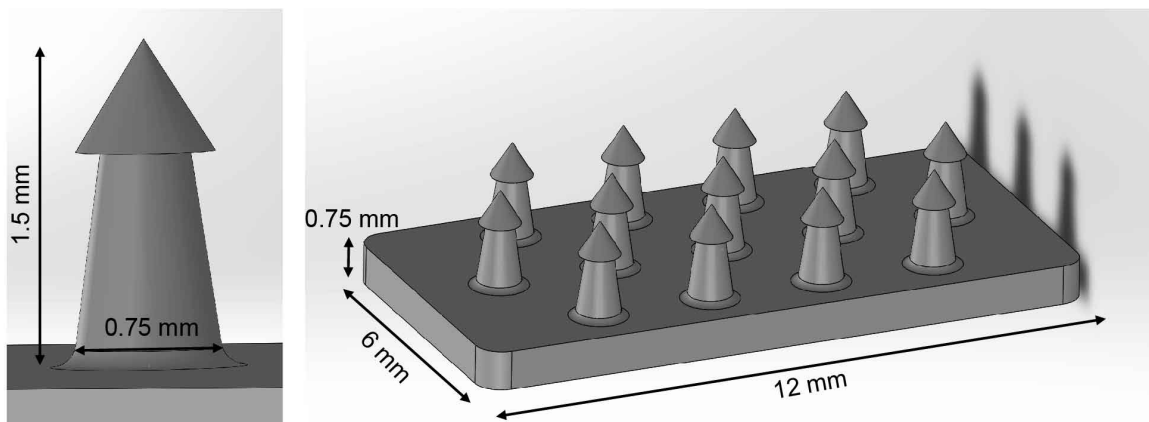


Figure 5.3 Intraoperative implant model

CLIP parameters and processing methods were first established using the base resin alone, with plans to eventually incorporate PTX and CPP. Devices were fabricated using a resin that contained equal parts (by mass) of HEMA and PEG₅₅₀-DMA. This formulation was chosen because of the additional rigidity that the increased T_g provides when HEMA is blended with a low T_g oligomer resins such as PEG₅₅₀-DMA (see Fig. 3.21 in Chapter 3). Further, previous studies indicated that HEMA increased solubility of taxane-based drugs such as PTX (data not shown). LTPO was used as the UV radical initiator (2.5 wt %) and the UV absorber BLS 1326 was added to a concentration of 0.5 wt % to serve to improve resolution during fabrication. The

effect of the addition can be seen in figure 5.4, where the devices fabricated using resins with no additional UV absorber have poor resolution of the undercut arrowhead in the z-dimension. This is the result of increased UV light penetration and a deeper cure depth.

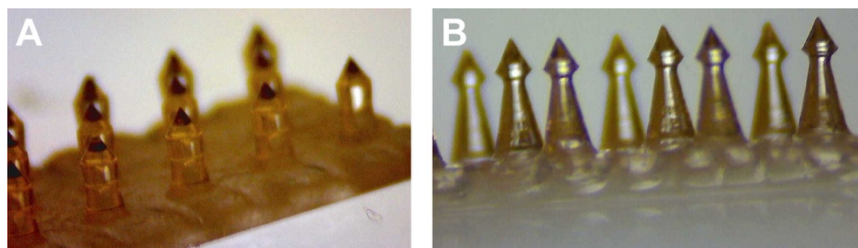


Figure 5.4 Effect of UV absorber on resolution of needle arrowhead resolution. Difference in resolution of barbed arrowhead needle structure fabricated using a resin with no additional absorber (A) and with a resin containing 0.5 wt % UV absorber, BLS 1326 (B)

The depth of cure in photopolymer systems is often described using equations derived from the Beer-Lambert law, and is a function of two factors: the total light dosage and absorption coefficient of the resin [31,32]. Light dosage is a measure of the overall light exposure and is defined as the product of light intensity and exposure time. In CLIP, the light intensity can be modulated through the software interface and the exposure time can be controlled through the print speed, with exposure time being inversely related to print speed. The absorption coefficient of a resin can be manipulated through the addition of UV absorbing molecules, including both photo-reactive initiators and inert UV absorbers.

Without the addition of UV absorber, the minimum exposure values necessary to maintain structural integrity resulted in unresolved arrowheads (Fig. 5.4 A). However, both part integrity and arrowhead resolution was achieved upon the incorporation of BLS 1326 as a UV absorber (Fig 5.4 B). Optimal accuracy was achieved using a light intensity of 10 mW cm^{-2} and printing at a speed of 10 mm hr^{-1} . A relatively slow build rate was required to print the implant base's large surface area without major defects.

A centrifugation process, like that used for the removal of residual resin from the pores of geometrically complex devices (Chapter 3), resulted in sheering of the needle tips, and was

thus unsuitable for use with this design. Residual resin removal can typically be achieved through simple solvent rinses; however, a high level of procedural control needed to be developed to ensure uniformity among devices, sufficient removal of residual resin, and maintain a high and consistent drug loading. To that end, an apparatus was fabricated (using a CLIP M1 printer) to hold the device in a beaker containing a wash solution under constant magnetic stirring. The design featured a hook to hold the apparatus at a uniform depth (Fig. 5.5 A) and a slot with a keyed orientation to ensure identical alignment of the device for each wash (Fig. 5.5 B).

To avoid substantial removal of drug, two wash conditions were tested: a 5 second exposure to 2-propanol and a 30 second exposure to water. The short wash was necessary when using 2-propanol to avoid solubilizing the PTX and CPP, but resulted in incomplete resin removal (Fig. 5.5 C). While the resin is not as soluble in the water, the longer exposure and rapid stirring facilitated mechanical removal of the unpolymerized surface resin (Fig. 5.5 D). Further the low solubility of PTX and CPP in water ensures minimal drug extraction during the wash procedure. Subsequent drying of the water-rinsed parts, however, revealed crystallization of the UV absorber on the surface of the part (Fig. 5.5 E). An additional 1 second dip of the part in acetone eliminated the observed precipitation (Fig. 5.5 F) and further accelerated the drying process for the final devices (Fig. 5.5 G).

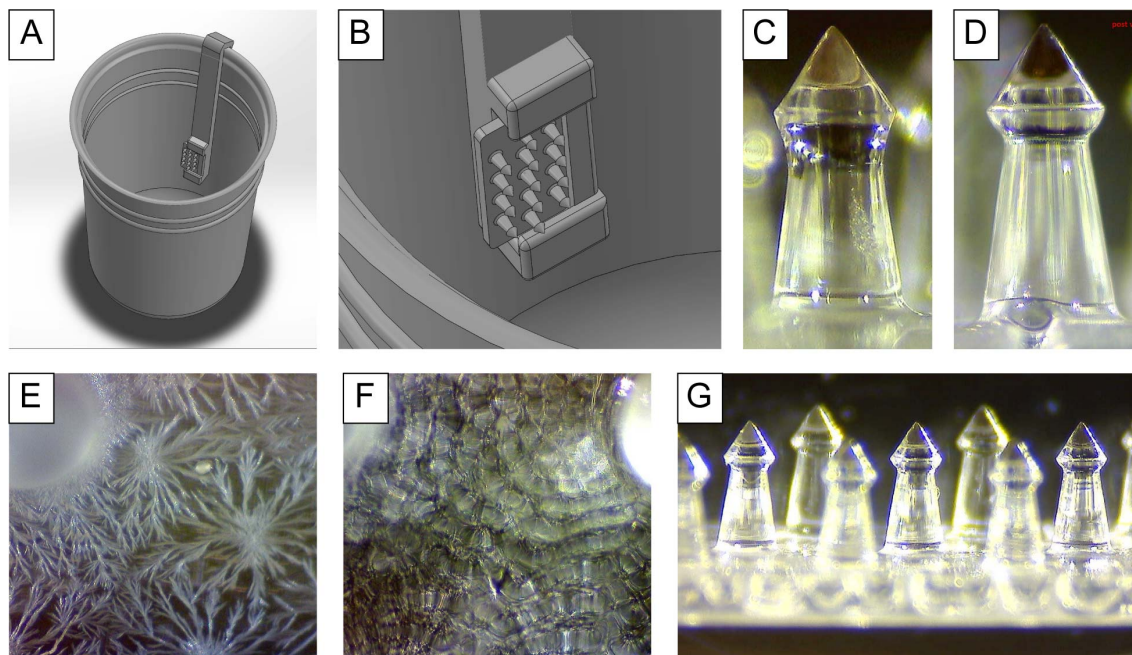


Figure 5.5 Optimization of parameters for the post-processing of intraoperative implants to ensure uniformity of fabricated devices. (A) CAD model of implant washing apparatus in a beaker. (B) Intraoperative implant in place in the wash apparatus demonstrating the only orientation the the device can be relative to the flow of the wash solution. (C) Incomplete removal of residual resin when devices were washed for 5 seconds with 2-propanol. (D) The mechanical removal of residual resin during a 30 second wash using DI water was sufficient to remove unpolymerized resin. (E) crystallization of UV absorber following water wash alone. (F) No precipitate is observed when device is exposed to a one second dip in acetone. (G) Light microscope image of the needle array in drug-free HEMA/PEG₅₅₀-DMA devices.

5.3.1.2 Fabrication and characterization of drug loaded intraoperative devices

Drug-loaded resins were formulated to contain 5 wt % and 4 wt % PTX or CPP, respectively. An additional resin was also formulated to contain both drugs at the same total concentration. PTX was found to be soluble in the resin up to 8 wt %, but 5 wt % was used to avoid any potential saturation concerns. Originally, the acetylated cisplatin prodrug (CPP) was synthesized in hopes of improving the solubility in the resins. Ultimately, the CPP was not soluble in the chosen resin formulation; however, it did show an improvement in stability of the drug suspension. Cisplatin alone was observed to crash out of suspension within minutes, while CPP remained in suspension on the order of weeks to months.

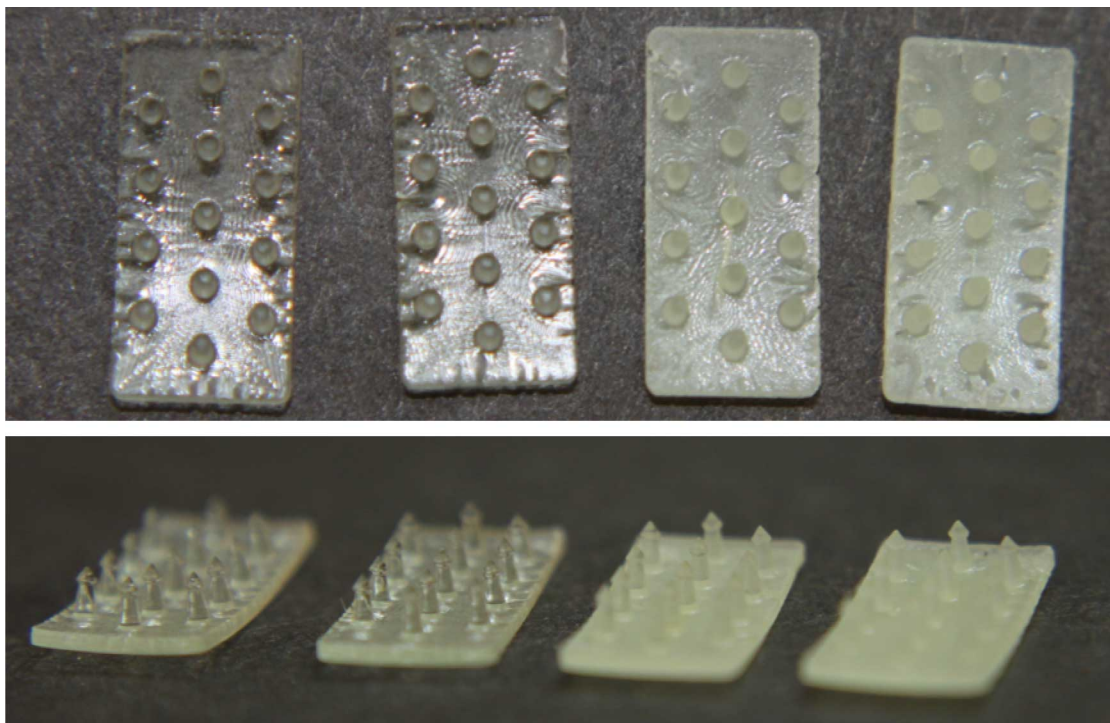


Figure 5.6 Visible light image of blank, PTX, CPP, and PTX/CPP intraoperative implants (left to right).

Blank devices (no drug) and devices with PTX resulted in transparent parts, while the CPP and CPP/PTX resin yielded an opaque device that was the same light-yellow color as the synthesized CPP powder (Fig. 5.6). The effect that the suspended drug has on the surface finish of the final part can be seen when comparing the SEM micrographs of the parts printed with no drug, PTX, and CPP (Fig. 5.7). Devices with soluble drug look similar to those with no drug loaded (Fig. 5.7 A and B), while there is a noticeable texture on the surface of the devices containing CPP in suspension (Fig. 5.7 D).

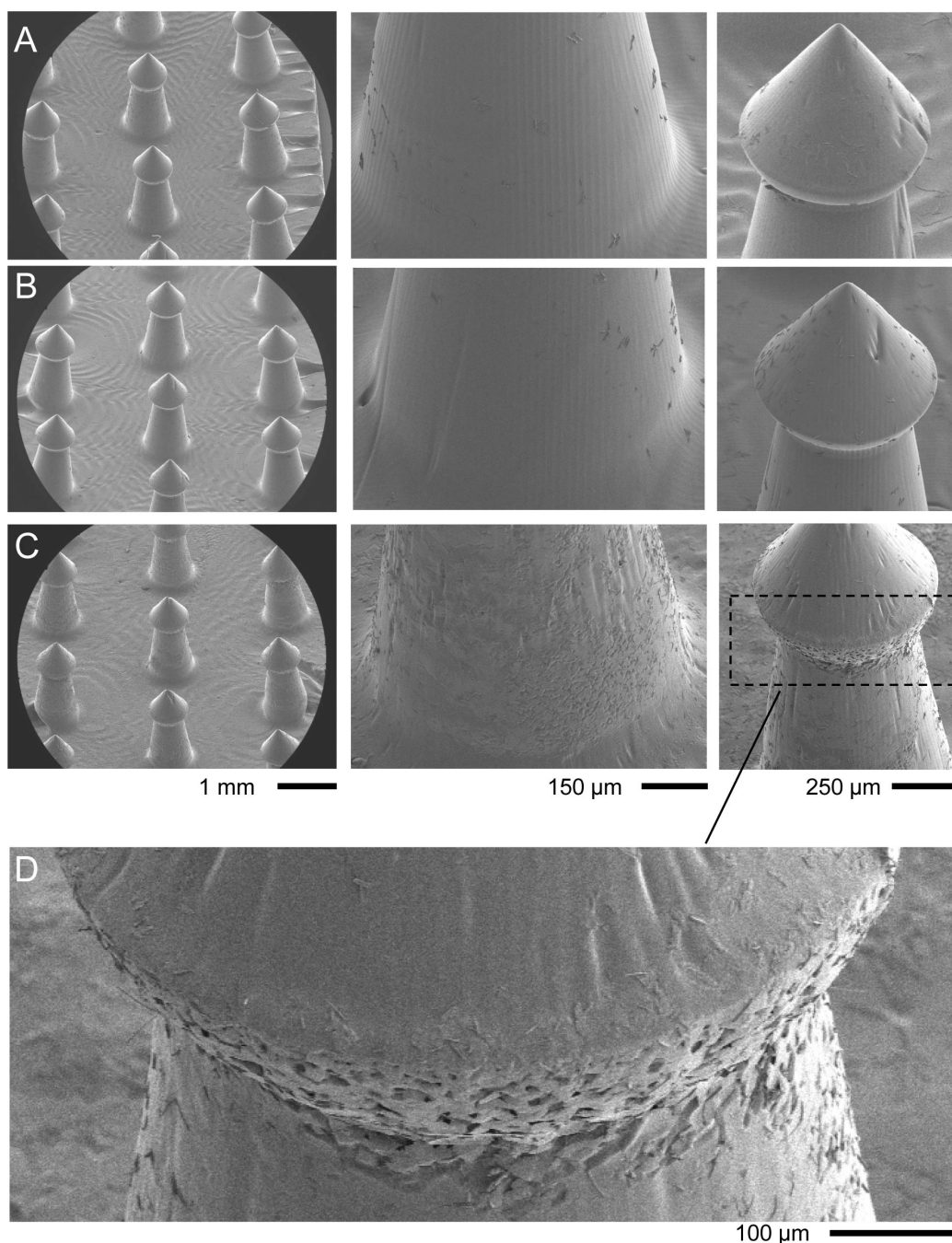


Figure 5.7 SEM imaging of intraoperative devices fabricated to with (A) no drug, (B) PTX, (C) CPP. (D) Expanded view of the texture of the device fabricated with CPP in suspension.

Regardless of the drug content, the backing of the device had patterning that was likely an artifact of the resin flow during the CLIP process. These patterns are notable in the visible

light photographs as well as the SEM images (Fig. 5.8). Further optimization of CLIP fabrication parameters and reduction of resin viscosity would help improve these visible defects.

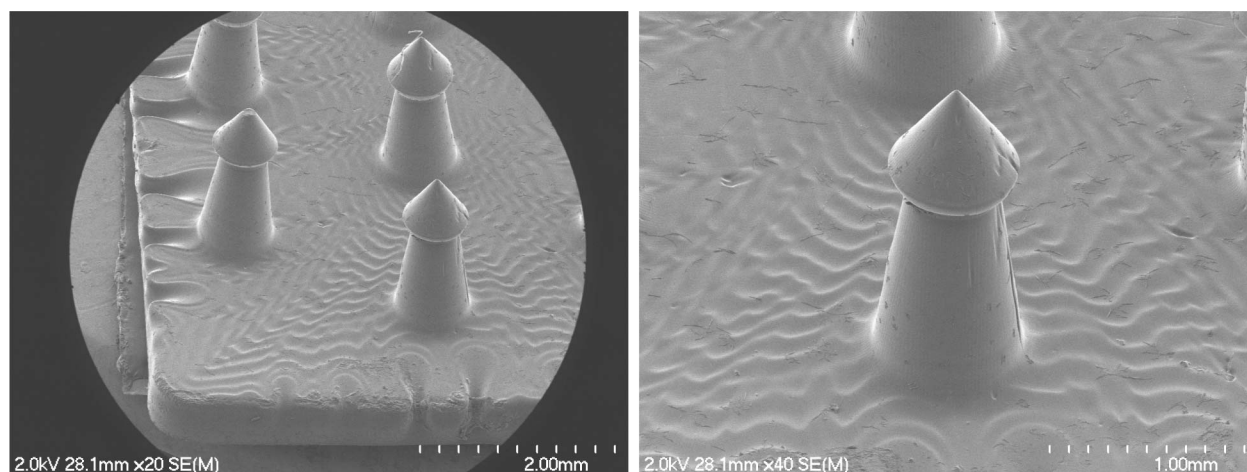


Figure 5.8 SEM micrographs of intraoperative devices (no drug) showing surface texture of implant backings, which is an artifact of resin flow during CLIP.

For the *in vitro* drug release study presented here, the amount of drug released at each time point was determined by analysis of the amount of drug remaining in the device after a given time in a pH 7.4 PBS bath. With a $n=5$ for each timepoint, a full study required upwards of 50 total devices. For that reason, the release study was carried out using model disks with a lower volume to conserve resin and drug. Due to the implications of the surface to volume (SA/V) ratio on drug release kinetics, as discussed in Chapter 3, the model device was designed to have the same SA/V ratio as the intraoperative implants (Fig. 5.9 A). *In vitro* release analysis indicates a very consistent drug release profile of PTX over the course of 28 days (Fig. 5.9 B). Release of CPP was much more variable compared to PTX (Fig. 5.9 C). The mean coefficient of variance for the mass of drug extracted at each timepoint was 6.9 % and 17.4 % for PTX release and CPP release, respectively. The higher variability of drug release is likely a result of the CPP being suspended in the resin in comparison to the isotropic solution of PTX in the resin.

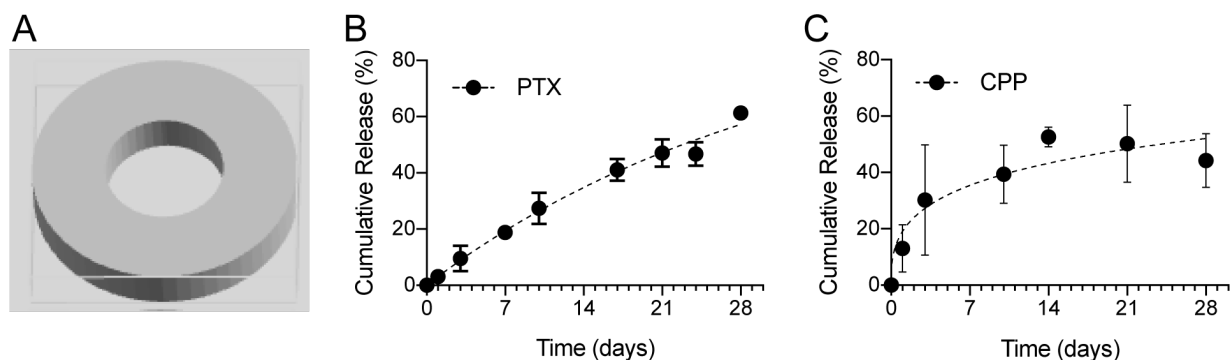


Figure 5.9 *In vitro* release of PTX and CPP from PEG₅₅₀-DMA/HEMA resins. (A) Model disks were designed to have the same surface area to volume ratio as the intraoperative implant (1 mm thick, 5mm outer radius, 1.1 mm inner radius). Release results for of PTX (B) and CPP (C).

5.3.1.3 Preliminary characterization of *in vivo* resection and recurrent tumor models

Preliminary tumor studies were carried out to characterize the resection and recurrence model using a murine lung adenocarcinoma cell line, 344SQ, and a human ovarian cancer cell line, OVCAR5 (Fig. 5.10). Flank subcutaneous tumors were resected when tumors reached 7 mm in the longest dimension, which occurred 7 and 20 days after inoculation for 344SQ and OVCAR5, respectively. 344SQ tumors resulted in recurrence within a few days following resection, while OVCAR5 tumors recurred after approximately 25 days. 2 mice with 344SQ tumors were euthanized early due to ulceration of the recurrent tumor.

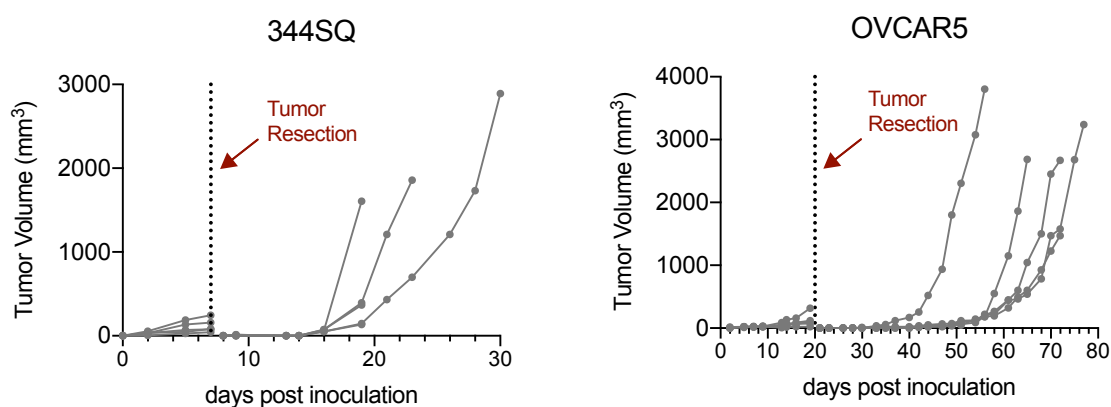


Figure 5.10 Tumor volume curves for preliminary characterization of recurrent tumor model with 344SQ lung cancer and OVCAR5 ovarian cancer flank tumors.

A second preliminary study was carried out to establish the tolerability of the device at the level of drug loading (4 wt % CPP and 5 wt % PTX). After implanting drug-loaded devices into tumor-free mice (Fig. 5.11 A), the devices did not appear to hinder normal movement or cause discomfort in mice. Over the course of 2 weeks, the body weight of mice remained at or above the body weight measured at the time of treatment (Fig. 5.11 B). Following two weeks, devices were removed and the amount of drug remaining in the device was extracted and used as a measure of the amount of drug released over the two week period. Both PTX and CPP implants appeared to release over half of the loaded drug cargo *in vivo* (Fig. 5.11 C).

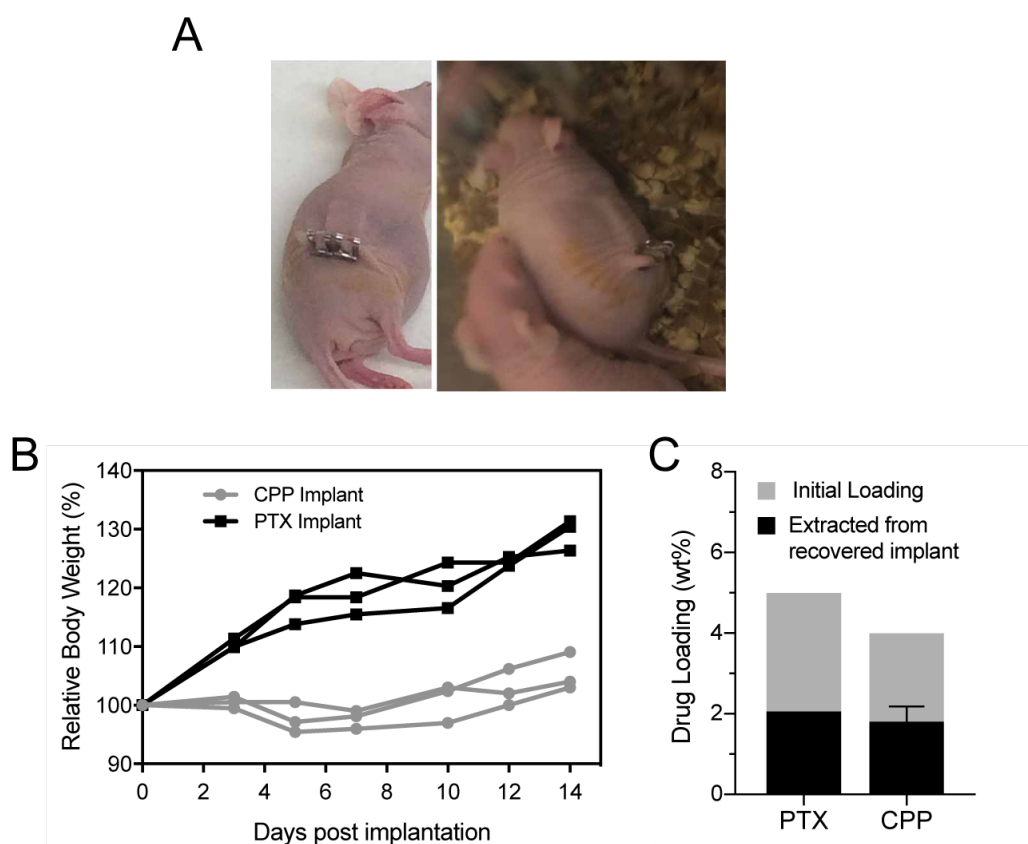


Figure 5.11 Results of preliminary tolerability study. PTX and CPP implants were placed in the subcutaneous region of non-tumor bearing mice (A) and body weight was monitored (B). After termination of the experiment, devices were recollected and the drug remaining was extracted (C).

5.3.1.4 In vivo efficacy of intraoperative devices against tumor recurrence

7 days following inoculation, 344SQ flank subcutaneous tumors were resected and mice were treated with placement of an implant containing PTX, CPP, or a combination PTX/ CPP; a single I.V. treatment of PTX, CDDP, or a combination PTX/CDDP; or no additional treatment. Tumor volume measurements and bioluminescent imaging of luciferase-expressing cells indicate a rapid tumor recurrence in mice receiving I.V. PTX, blank implants or no additional treatment following resection (Fig. 5.12). While the blank implant does appear to delay recurrence in the physical tumor measurements, the rapid increase in bioluminescence signal may indicate that the implant may slightly interfere with the physical measurement of the tumor.

Although placement of PTX and CPP implants was tolerated up to 14 days in non-tumor bearing mice during preliminary experiments, all mice treated with drug-loaded implants in the resection model resulted in skin lesions above the implant. Treatment arms were monitored until 50 % of the initial treatment group was euthanized. Due to the rapid development of skin lesions in mice treated with CPP and PTX/ CPP implants, no usable tumor data was collected. Thus, only PTX related treatment groups are presented. Tumor data is only shown out to 28 days post-inoculation, when >50 % of mice treated with PTX implants had developed skin lesions.

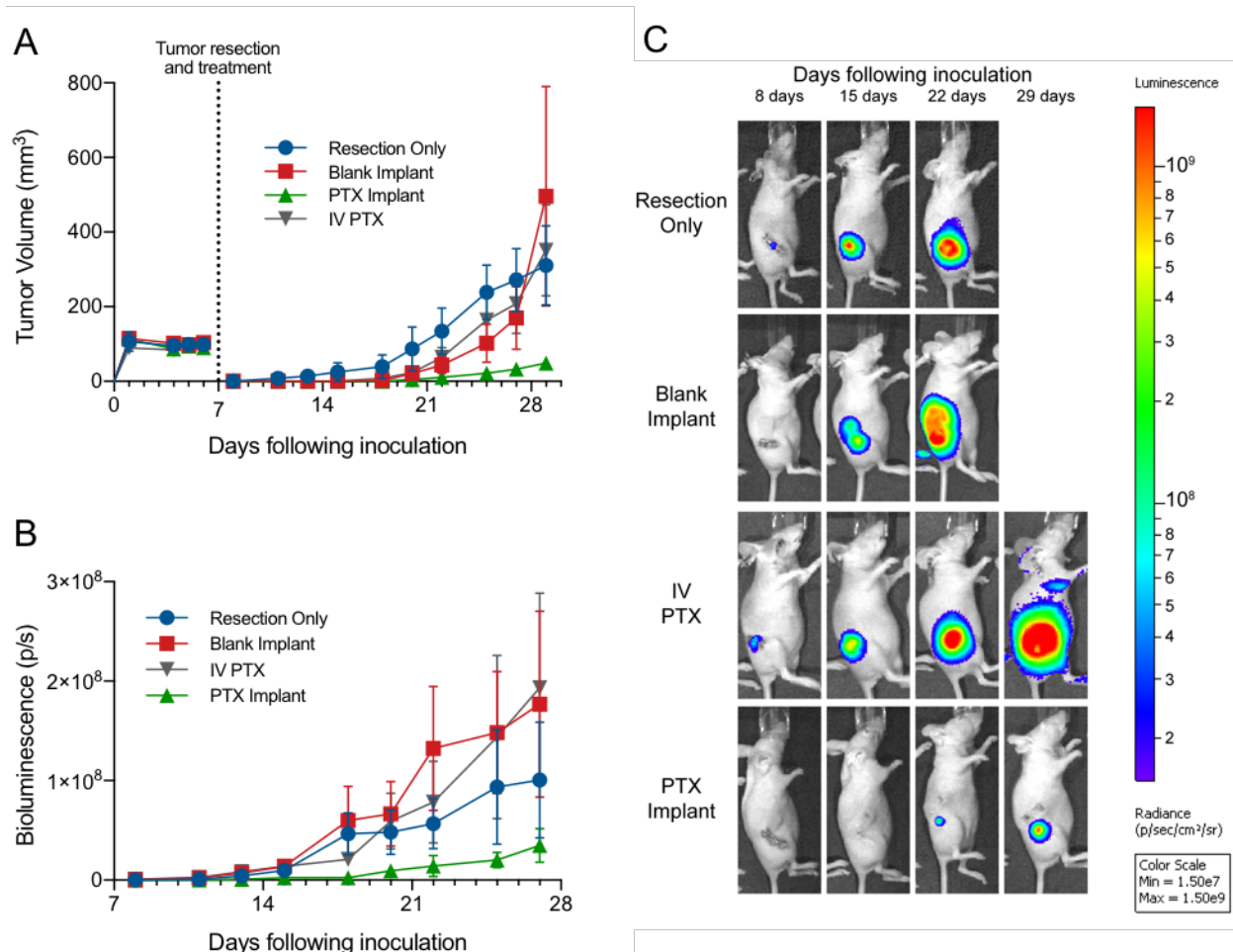


Figure 5.12 Tumor inhibition effects of PTX implants compared to I.V. PTX, blank implants, and resection only. (A) Tumor volume curves. (B) Bioluminescence of tumors. (C) Representative bioluminescence images of mice with recurrent tumors for each treatment group.

Due to the variable nature of resection and recurrence, each treatment group resulted in mice with recurrent tumors and mice in remission. The tumor growth curves for individual mice can be seen in figure 5.13. The symbols at the end of each tumor volume curve corresponds to the reason for euthanasia of that mouse. For mice receiving a resection only ($n=8$), three mice were observed to be in remission and five resulted in recurrent tumors. Of mice that were treated with a blank implant ($n=10$), one was euthanized for abdominal distension prior to recurrence, three were in remission, five had locally recurrent tumors, and one mouse had no recurrence in the primary site but developed a secondary tumor on the ipsilateral shoulder. In

the treatment group receiving a single I.V. PTX dose following tumor resection (n=8) seven mice had recurrent tumors. In mice treated with PTX implants, all mice were euthanized due to development of skin lesions. Some mice began having tumor regrowth while others developed lesions prior to a physically measurable tumor recurring.

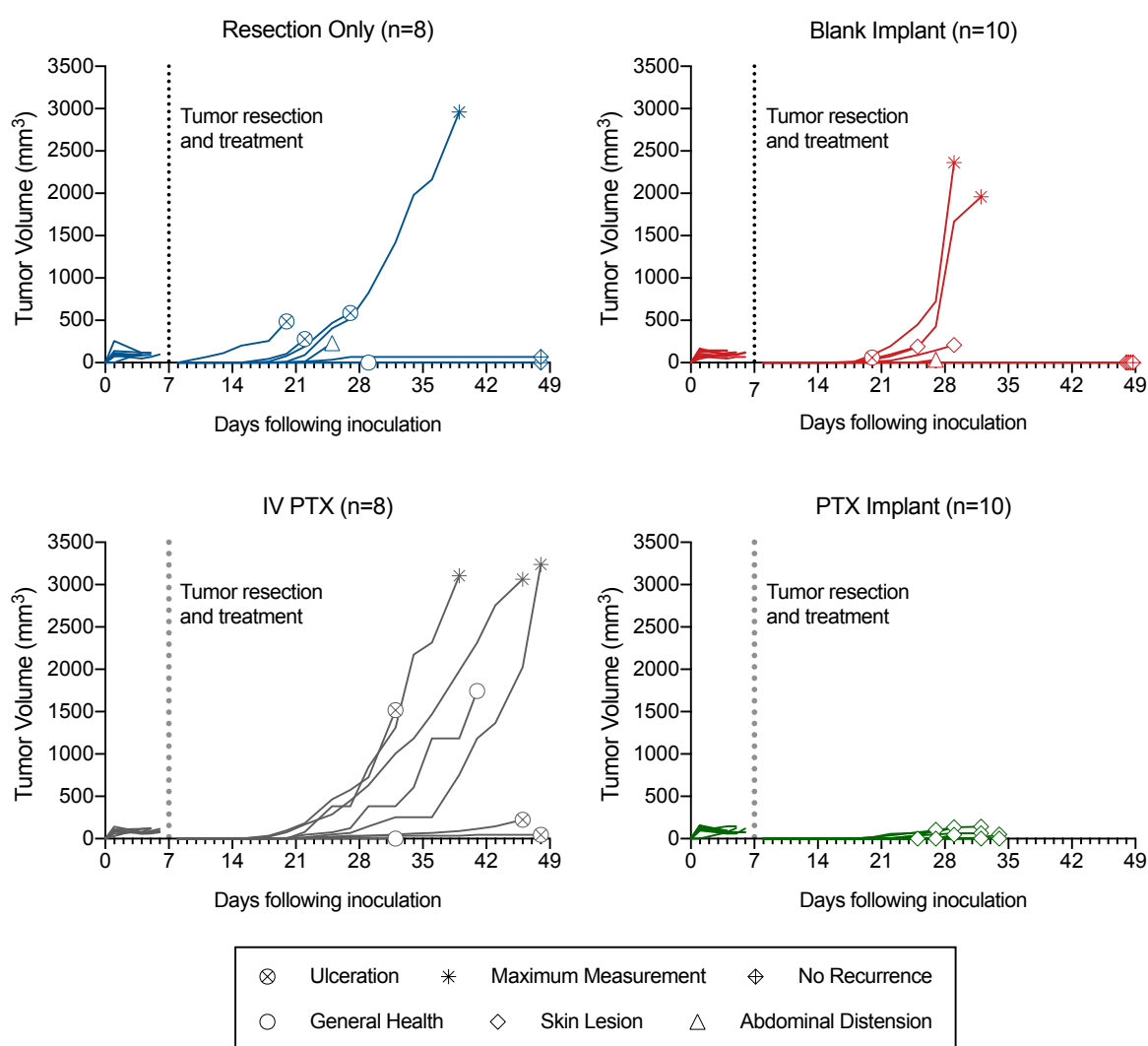


Figure 5.13 Individual tumor volume curves for each treatment arm. The endpoint for each experimental animal is indicated with a symbol, which corresponds to a reason for euthanasia indicated in the legend.

Histological analysis of the site of tumor recurrence in mice receiving resection only and I.V. PTX indicated wide cancer growth and a necrotic core, typical in large tumors (Fig. 5.14 A-B). Cross sections of the implant needle can be seen in the tumor sections taken from mice

treated with intraoperative implants. Blank devices are seen surrounded by cancer tissue, though the immediate surrounding tissue appears necrotic (Fig. 5.14 C). In sections taken from mice treated with PTX implants, no tumor is observed (Fig. 5.14 D). A granuloma is observed the proximity of the implant. Trichrome staining reveals dispersed and seemingly random collagen distribution in the cancer tissue (Fig. 5.14 E). However, the tissue at the interface of the blank device is characterized by an orderly collagen structure, indicating a fibrotic response to the implant (Fig. 5.14 G). Trichrome staining of tissue with a PTX implant shows no fibrosis at the interface of the device and tissue (Fig. 5.14 F). This is in agreeance with the proliferation-inhibiting mechanism of PTX. For this reason, PTX is used clinically in drug-eluting stents and implants to mitigate the fibrotic response [33,34].

A metabolic activity panel and complete blood count did not indicate hematological, hepatic, or renal toxicity at the day of resection and treatment and 4 and 9 days following (Fig. 5.15). There does appear to be a drop in red blood cell counts following the surgical procedure, but never outside of the normal range (as defined in [35]).

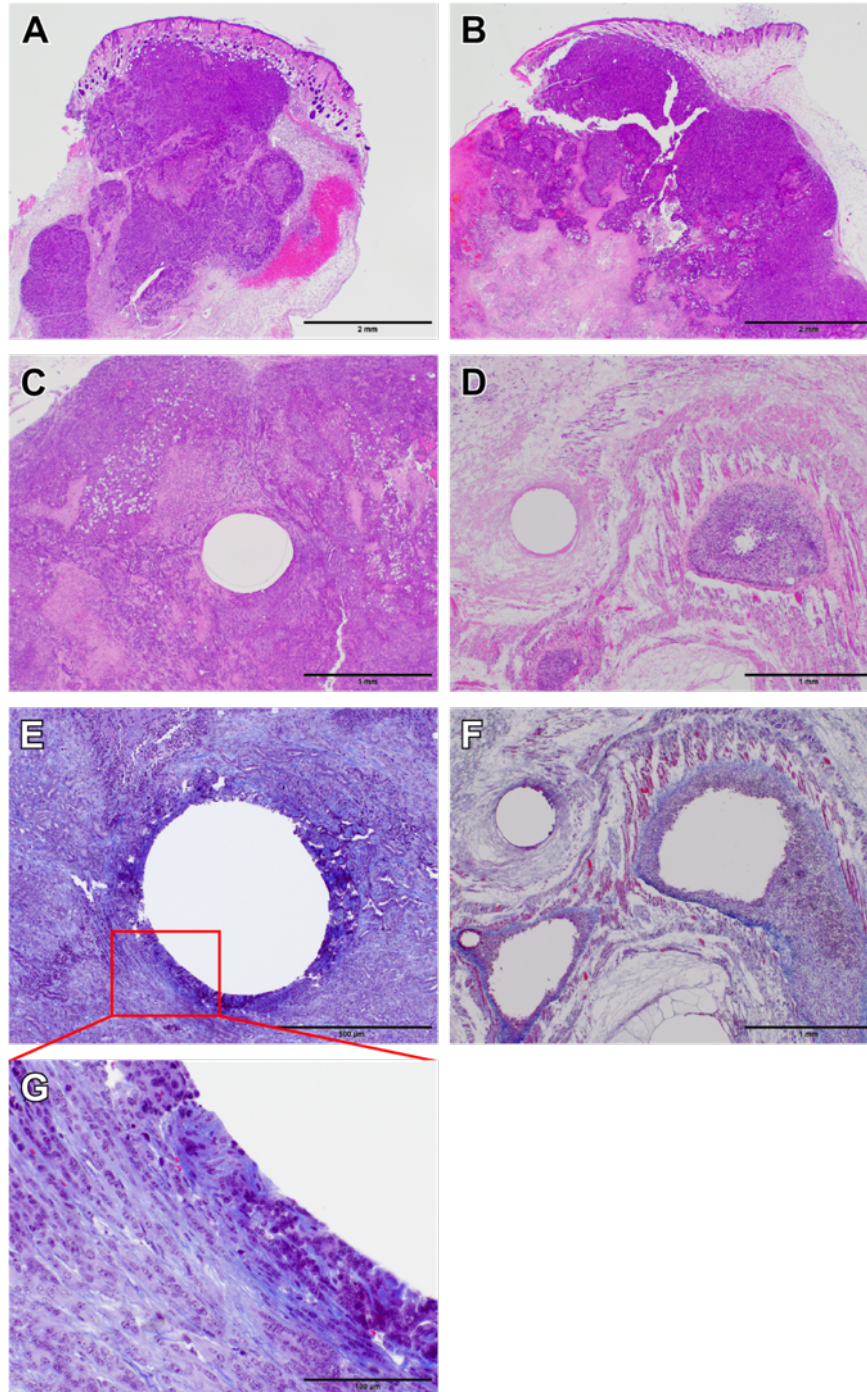


Figure 5.14 Histopathology of tumor tissue. 5 μ m slices were made parallel to the implant backing and perpendicular to the needles. H&E staining was used to observe histopathology of tumor tissue from mice treated with resection only (A), I.V. PTX (B), blank implant (C), and PTX implant (D). White circles are cross-sections of the implant needles, which were fixed in place along with the tumor tissue. Trichrome staining of tumor tissue with (E) blank implant shows dispersed collagen throughout the tumor tissue. (G) The tissue directly surrounding the implant needle has organized collagen structure more indicative of fibrosis. (F) Trichrome staining of PTX implants in the tumor lack collagen. (A,B: 20X, scale = 2 mm; B,C,F: 40X, scale = 1 mm; E: 100X, scale = 500 μ m; G: 400X, scale = 100 μ m)

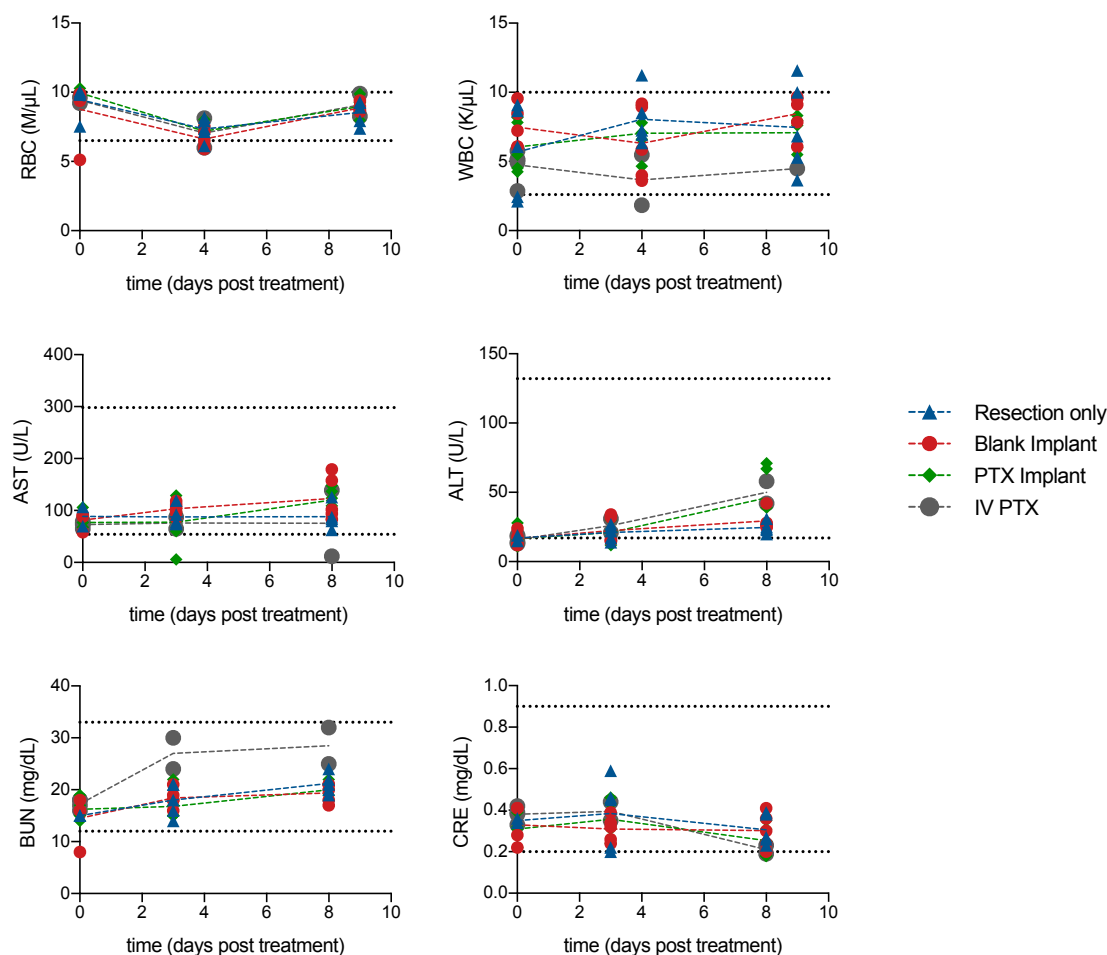


Figure 5.15 Results of complete blood count and serum biochemical analysis of hematological, hepatic, and renal toxicity. Dotted lines represent normal range for nude mice (normal range referenced from [35])

5.3.1.5 Future directions for development of intraoperative implants

While the PTX implants outperformed blank implants, I.V. PTX, and resection only treatment approaches, the toxicity to the skin of mice required termination of the study without the opportunity to observe any potential long-term benefits against tumor recurrence. Future work should focus on selectively loading drug into the device in a way that ensures drug will elute out of the device primarily in the direction of the resection cavity and reduce exposure to the dermis. One approach that we have tried is through fabricating a Janus device, where one resin containing a drug (in this case a drug surrogate, rhodamine) is used for the fabrication of the needles and another for the backing (Fig. 5.16). This spatially-specific loading may also be

achieved through selectively applying a drug-loaded coating to the needle side of the device, leaving the dermal-facing surface of the device free of drug. Additionally, applying a biocompatible drug-free coating to the dermal facing surface, would limit the contact between the chemotherapeutic and the skin. This would allow the production of the device without the need to optimize new parameters for CLIP.

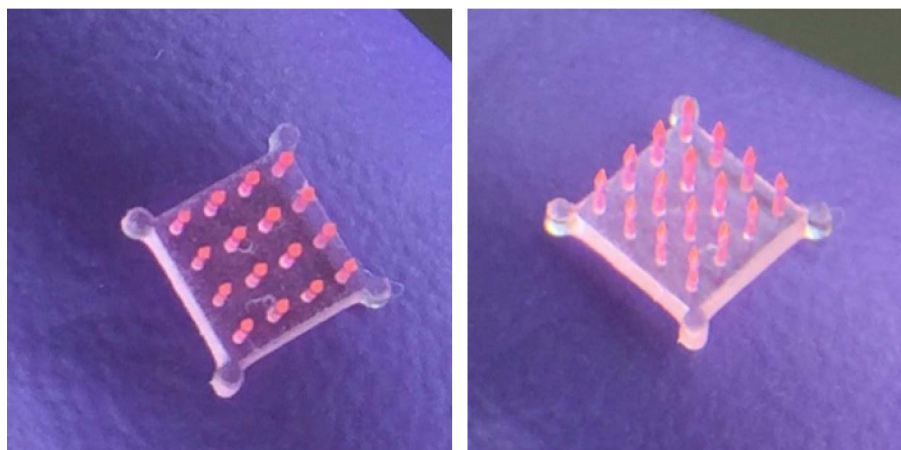


Figure 5.16 Janus-style intraoperative devices can serve as a potential approach to mitigating the dermal toxicity caused by the cytotoxic drug in the device backing.

5.3.2 Brachytherapy spacers

5.3.2.1 *In vitro* cytotoxicity of CLIP brachytherapy spacers

Brachytherapy spacers fabricated with PCL₇₀₀-DMA were tested for *in vitro* cytotoxicity in LNCaP prostate cancer cells (Fig. 5.17). When 1, 2 or 4 postcured, drug-free brachytherapy spacers were incubated in a transwell insert above LNCaP cells, no cytotoxicity is observed. No significant difference in viability was observed between cells incubated with drug-free spacers that were unpostcured. All spacers containing docetaxel were cytotoxic to LNCaP cells.

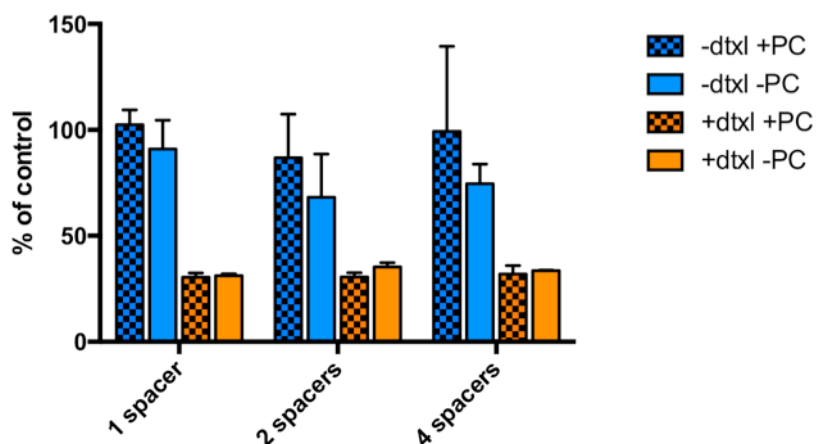


Figure 5.17 *In vitro* cytotoxicity of brachytherapy spacers. Brachytherapy spacers were incubated above a monolayer of LNCaP prostate cancer cells in a transwell insert for 72 hours. Drug-free spacers show a greater cytocompatibility compared to DTXL-loaded spacers, with postcured spacers showing the lowest toxicity.

5.3.2.2 *In vivo* efficacy of DTXL-loaded brachytherapy spacers

Brachytherapy spacers containing 2 wt % DTXL were implanted into flank xenograft tumors using an 18-gauge needle and a custom fabricated plunger. Results of the tumor growth inhibition study can be seen in figure 5.18. I.V. DTXL outperformed the intratumorally implanted brachytherapy spacers. This is thought to be a result of too low of a dose of DTXL being released by the spacer in the appropriate period, which is the result of a combination of insufficient drug loading and too slow of drug release.

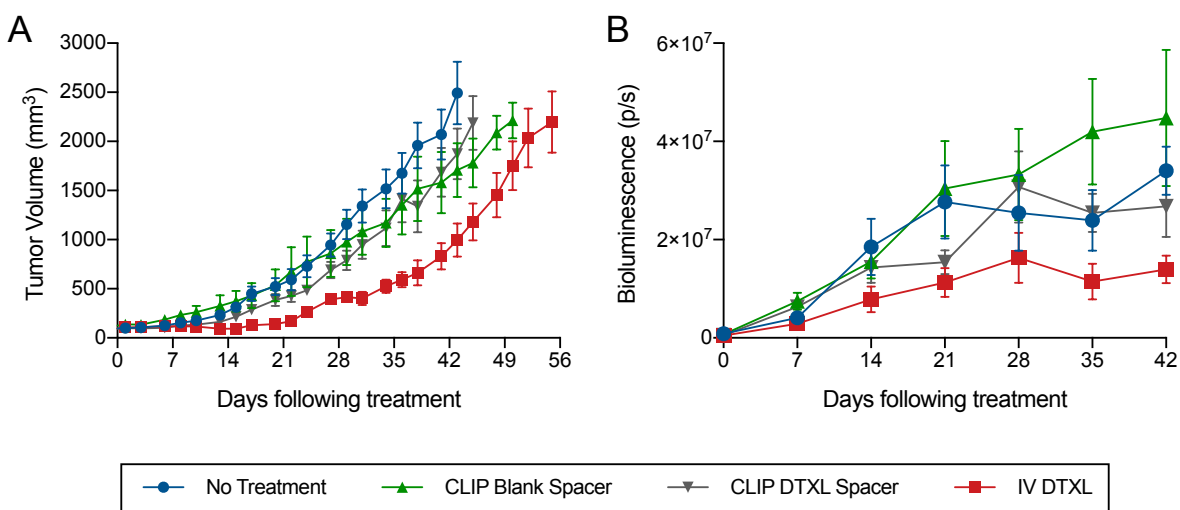


Figure 5.18 *In vivo* efficacy of DTXL-loaded brachytherapy spacers. (A) Tumor volumes and (B) bioluminescence intensity

5.3.2.3 Photopolymerization kinetics as a method to control drug release

In chapter 2, the effect that light intensity can have on the resulting polymer network bond conversion was presented. In Chapter 3 the crosslink density of the polymer network was shown to have important impacts on the release kinetics of dissolved drugs. Thus, we sought to co-opt the effects of the photopolymerization kinetics to try to control the drug release through manipulation of light exposure during the printing process.

First, we sought to demonstrate that the use of different light exposures during the CLIP process results in parts with different network properties. To do this, solvent swelling in chloroform was used as a measure of crosslink density. Spacers were arrayed and printed on a 1mm backing. Printing spacers onto a backing allowed for the solvent uptake study to be carried out on parts with a larger mass, while keeping the part dimensions similar to a brachytherapy spacer. The larger part mass reduces the error associated with weight measurements in the swelling experiment. Three parts printed at a range of speeds resulted in solvent swelling that was inversely related to the relative dosage of the print (Fig. 5.19). The greater solvent uptake in parts printed with a lower relative dosage is indicative of a less dense crosslinked network, which agrees with the observations made during the photocalorimetry experiments presented in Chapter 2.

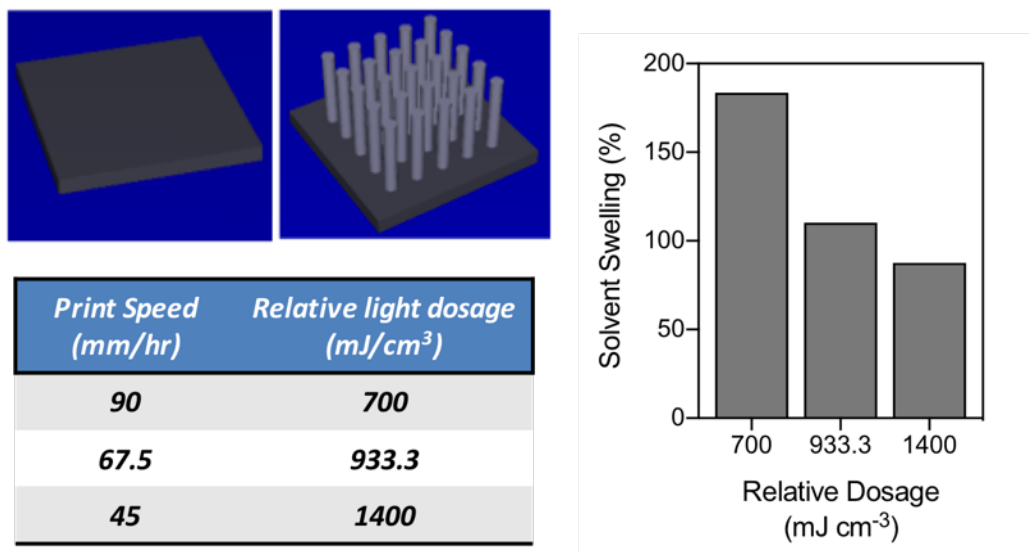


Figure 5.19 Characterization of CLIP brachytherapy spacers fabricated using different overall light exposures.

To observe the effect these changes to the polymer network have on drug release, docetaxel-loaded spacers were fabricated using a range of light intensities. However, the DTXL release does not appear to be greatly affected by the light intensity used during fabrication (Fig. 5.20). This study does reveal, however, the effect that the post processing has on the release kinetics. There was a significant difference in extent of release between spacers receiving a postcure and those that did not.

While changing the light intensity does not appear to be a sufficient method to modify drug release from PCL-based networks, there are useful insights gained from this experiment. Notably, DTXL is released in a prolonged fashion over the course of 70 days, which meets the desired criteria to match the 2 half-lives of the iodine-125 isotopes in the brachytherapy seeds. Further, for many applications the fact that drug release is not affected by changes in CLIP fabrication parameters will be a benefit. For example, when printing various geometries, the overall exposure may need to be manipulated to achieve the desired resolution. In the case of this network and drug, altering the print parameters would not affect the release kinetics.

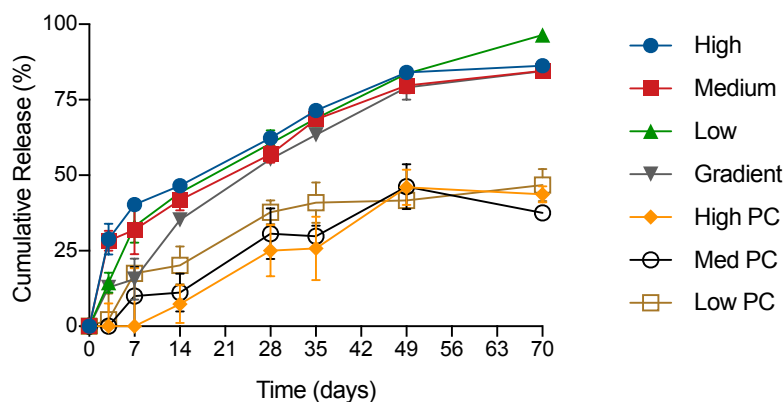
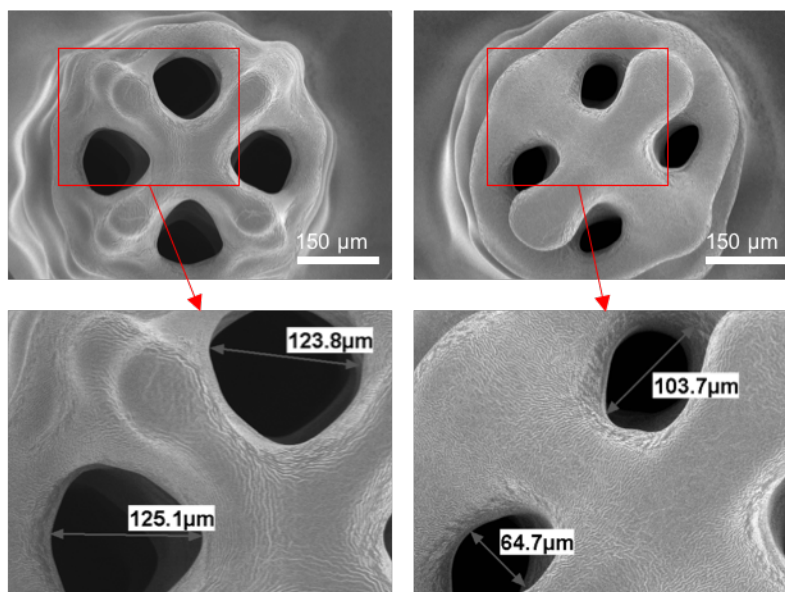


Figure 5.20 *In vitro* DTXL release from spacers printed at different light intensities. All spacers were printed at 75 mm hr^{-1} . High, medium, and low spacers were printed at 7.7 , 5.3 , and 2.4 mW cm^{-2} . Gradient spacers were printed with a continuous linear gradient of intensity between 7.7 and 2.4 mW cm^{-2} over the course of the print. Samples that received a postcure, were postcured under a mercury UV lamp for 3 minutes.

5.3.2.4 Complex geometries on the scale of brachytherapy spacers

The benefit of using complex geometries to control the diffusion distance, and thus the drug release rate, was presented in Chapter 3. Implementation of the same design strategy for devices on the scale of a brachytherapy spacer ($750 \text{ }\mu\text{m}$ diameter) can be challenging. Proof of concept studies were carried out to demonstrate the potential of printing complex geometries on this small scale. As seen in figure 5.21, complex geometries were printed on the scale of brachytherapy spacers. SEM images of complex geometries from above (Fig. 5.21 A) indicate resolution in the x- and y-dimensions of less than $100 \text{ }\mu\text{m}$ for both void volumes and solid features. When printing different lengths of geometrically complex spacers the ability to resolve details in the z-dimension is apparent (Fig. 5.21 B). A potential problem, which is highlighted by tendency for the full-length spacer to bend, is the lack of stability in scaffolds printed with this small of a feature size. This may cause a problem for implementation as brachytherapy spacer, in that they may not provide the rigidity required to serve the purpose of keeping radioactive seeds at the appropriate location in the needle. However, the addition of a solid shell surrounding the complex scaffold did improve the structural integrity of the spacer.

A



B

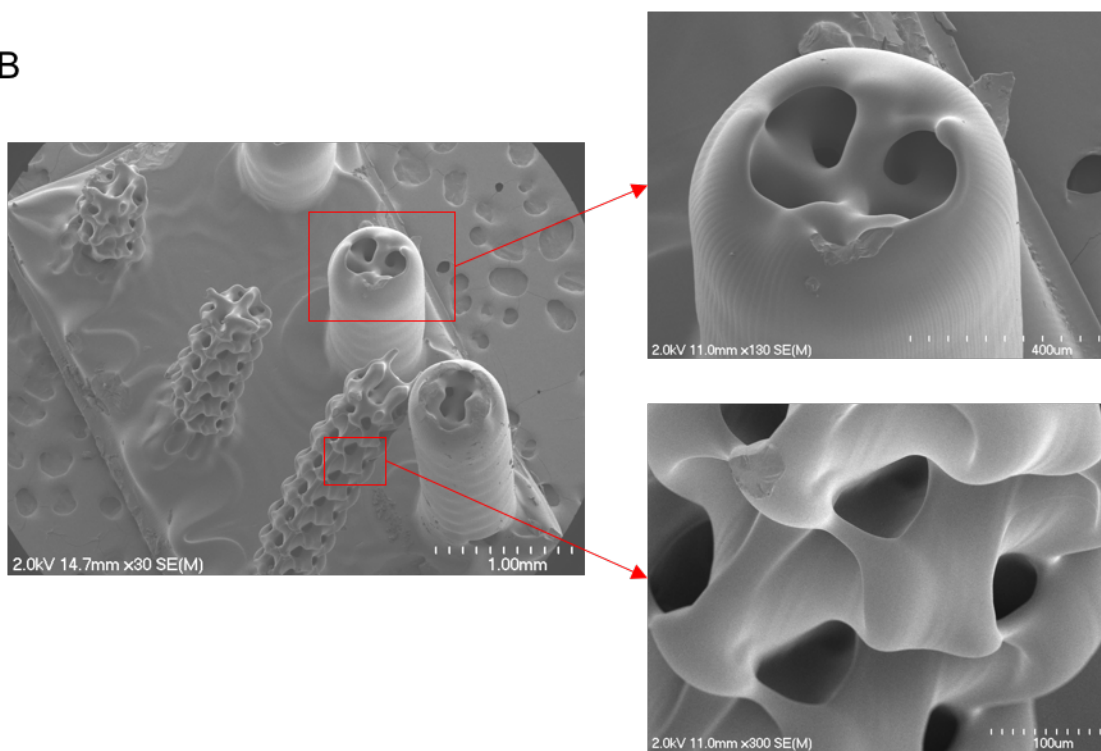


Figure 5.21. Complex geometries printed on the scale of brachytherapy spacers. Spacers were printed with a PEG₅₅₀-DMA resin. Various unit cells were arrayed to demonstrate the ability to resolve features smaller than 100 μm. (A) 1 mm tall cylinders filled with a single diamond and rhombic unit cells (left and right, respectively). (B) 1, 2.5 and 5 mm long cylinders filled with diamond unit cells with and without a shell.

5.4 Conclusions and future directions

The work outlined in this chapter is the first investigation of CLIP-fabricated devices in preclinical *in vivo* animal models. In an *in vivo* mouse model, a CLIP intraoperative implant loaded with paclitaxel was able to lower the extent of recurrence following tumor resection. However, observed dermal toxicities, caused by contact with the backing of the drug-loaded implant, indicate a complication for the evaluation of the efficacy of the device in a preclinical model. This highlights the need for further development of novel approaches to load drugs in a spatially controlled way.

Additionally, further material development to expand the range of usable mechanical and physical properties will be important for continued improvement of these implants. For example, the ability to print with an elastomeric backing and rigid needles will be beneficial for application of this approach to resection from tissues that are flexible, like skin or the gastrointestinal tract. Future work should also include demonstration of the potential for customizing the implant to the resection cavity, whereas the described patch was simply a generic shape for preclinical testing. This should involve all steps that would be necessary in a clinical setting, starting with the scanning of a resection cavity, conversion of the 3D data to a CAD model with a needle surface, and successful CLIP fabrication.

The use of CLIP to produce drug-loaded brachytherapy spacers was also presented. CLIP was used to fabricate a spacer using a methacrylated polycaprolactone that was capable of prolonged release of docetaxel over the course 60 days. This met the criteria for extended release for two half-lives of the iodine-125 used in the radioactive seeds. However, a mouse xenograft model of prostate cancer did not indicate any benefit from the implantation of docetaxel-loaded spacers. Further work for this application should focus on developing biodegradable materials that exhibit a faster release rate for testing on the time scale of the mouse cancer model.

Additional methods of drug incorporation, including methods to independently control release of multiple drugs from the same device would be valuable to the development of devices for numerous applications, including brachytherapy. One strategy could be covalent attachment to the network using cleavable linkers of varying degradation kinetics. This potential approach was further discussed in the conclusion of Chapter 4 (Sect. 4.4). Another approach could be to incorporate a secondary phase like nano- or microparticles containing drug, which would add another level of control to modify release kinetics. Techniques like these will be imperative if 3D printing, and CLIP, is to be used to design and fabricate personalized therapies with bespoke drug release profiles.

REFERENCES

- [1] R.L. Siegel, K.D. Miller, A. Jemal, Cancer statistics, 2017, *CA Cancer J Clin.* 67 (2017) 7–30. doi:10.3322/caac.21387.
- [2] D.E. Midthun, Overview of the initial evaluation, treatment and prognosis of lung cancer, UpToDate, 2017.
- [3] H. Sugimura, F.C. Nichols, P. Yang, M.S. Allen, S.D. Cassivi, C. Deschamps, et al., Survival After Recurrent Nonsmall-Cell Lung Cancer After Complete Pulmonary Resection, *The Annals of Thoracic Surgery.* 83 (2007) 409–418. doi:10.1016/j.athoracsur.2006.08.046.
- [4] N. Hanna, Adjuvant systemic therapy in resectable non-small cell lung cancer, UpToDate, 2017.
- [5] R.R. Veluswamy, N. Ezer, G. Mhango, E. Goodman, M. Bonomi, A.I. Neugut, et al., Limited Resection Versus Lobectomy for Older Patients With Early-Stage Lung Cancer: Impact of Histology, *JCO.* 33 (2015) 3447–3453. doi:10.1200/JCO.2014.60.6624.
- [6] A. El-Sherif, H.C. Fernando, R. Santos, B. Pettiford, J.D. Luketich, J.M. Close, et al., Margin and Local Recurrence After Sublobar Resection of Non-Small Cell Lung Cancer, *Ann Surg Oncol.* 14 (2007) 2400–2405. doi:10.1245/s10434-007-9421-9.
- [7] J.-P. Pignon, H. Tribodet, G.V. Scagliotti, J.-Y. Douillard, F.A. Shepherd, R.J. Stephens, et al., Lung Adjuvant Cisplatin Evaluation: A Pooled Analysis by the LACE Collaborative Group, *JCO.* 26 (2008) 3552–3559. doi:10.1200/JCO.2007.13.9030.
- [8] A. Bezjak, C.W. Lee, K. Ding, M. Brundage, T. Winton, B. Graham, et al., Quality-of-Life Outcomes for Adjuvant Chemotherapy in Early-Stage Non–Small-Cell Lung Cancer: Results From a Randomized Trial, *JBR.10, JCO.* 26 (2008) 5052–5059. doi:10.1200/JCO.2007.12.6094.
- [9] H. Brem, S. Piantadosi, P.C. Burger, M. Walker, R. Selker, N.A. Vick, et al., Placebo-controlled trial of safety and efficacy of intraoperative controlled delivery by biodegradable polymers of chemotherapy for recurrent gliomas. The Polymer-brain Tumor Treatment Group, *Lancet.* 345 (1995) 1008–1012.
- [10] J.B. Wolinsky, Y.L. Colson, M.W. Grinstaff, Local drug delivery strategies for cancer treatment: Gels, nanoparticles, polymeric films, rods, and wafers *Journal of Controlled Release.* 159 (2012) 14–26. doi:10.1016/j.jconrel.2011.11.031.
- [11] J.A. Kaplan, R. Liu, J.D. Freedman, R. Padera, J. Schwartz, Y.L. Colson, et al., Prevention of lung cancer recurrence using cisplatin-loaded superhydrophobic nanofiber meshes, *Biomaterials.* 76 (2016) 273–281. doi:10.1016/j.biomaterials.2015.10.060.
- [12] S.M. Azouz, J. Walpole, S. Amirifeli, K.N. Taylor, M.W. Grinstaff, Y.L. Colson, Prevention of local tumor growth with paclitaxel-loaded microspheres, *The Journal of Thoracic and Cardiovascular Surgery.* 135 (2008) 1014–1021. doi:10.1016/j.jtcvs.2007.12.011.

- [13] R. Liu, J.B. Wolinsky, J. Walpole, E. Southard, L.R. Chirieac, M.W. Grinstaff, et al., Prevention of Local Tumor Recurrence Following Surgery Using Low-Dose Chemotherapeutic Polymer Films, *Ann Surg Oncol.* 17 (2009) 1203–1213. doi:10.1245/s10434-009-0856-z.
- [14] J.B. Wolinsky, R. Liu, J. Walpole, L.R. Chirieac, Y.L. Colson, M.W. Grinstaff, Prevention of in vivo lung tumor growth by prolonged local delivery of hydroxycamptothecin using poly(ester-carbonate)-collagen composites, *Journal of Controlled Release.* 144 (2010) 280–287. doi:10.1016/j.jconrel.2010.02.022.
- [15] T.J. Wilt, R. MacDonald, I. Rutks, T.A. Shamliyan, B.C. Taylor, R.L. Kane, Systematic review: comparative effectiveness and harms of treatments for clinically localized prostate cancer, *Ann. Intern. Med.* 148 (2008) 435–448.
- [16] W.J. Morris, M. Keyes, D. Palma, I. Spadinger, M.R. McKenzie, A. Agranovich, et al., Population-based study of biochemical and survival outcomes after permanent 125I brachytherapy for low- and intermediate-risk prostate cancer, *Urology.* 73 (2009) 860–5– discussion 865–7. doi:10.1016/j.urology.2008.07.064.
- [17] E.Y. Shapiro, S. Rais-Bahrami, C. Morgenstern, B. Napolitano, L. Richstone, L. Potters, Long-Term Outcomes in Younger Men Following Permanent Prostate Brachytherapy, *The Journal of Urology.* 181 (2009) 1665–1671. doi:10.1016/j.juro.2008.11.122.
- [18] W.J. Morris, S. Tyldesley, S. Rodda, R. Halperin, H. Pai, M. McKenzie, et al., Androgen Suppression Combined with Elective Nodal and Dose Escalated Radiation Therapy (the ASCENDE-RT Trial): An Analysis of Survival Endpoints for a Randomized Trial Comparing Low-Dose-Rate Brachytherapy Boost to Dose-Escalated External Beam Boost for High- and Intermediate-risk Prostate Cancer, *Radiation Oncology Biology.* 98 (2017) 275–285. doi:10.1016/j.ijrobp.2016.11.026.
- [19] J.L. Gore, L. Kwan, S.P. Lee, R.E. Reiter, M.S. Litwin, Survivorship Beyond Convalescence: 48-Month Quality-of-Life Outcomes After Treatment for Localized Prostate Cancer, *JNCI Journal of the National Cancer Institute.* 101 (2009) 888–892. doi:10.1093/jnci/djp114.
- [20] J.H. Petit, C. Gluck, W.S. Kiger, D. Laury Henry, C. Karasiewicz, J.A. Talcott, et al., Androgen deprivation-mediated cyto-reduction before interstitial brachytherapy for prostate cancer does not abrogate the elevated risk of urinary morbidity associated with larger initial prostate volume, *Brachytherapy.* 6 (2007) 267–271. doi:10.1016/j.brachy.2007.08.007.
- [21] D.A. Wattson, M.-H. Chen, J.W. Moul, B.J. Moran, D.E. Dosoretz, C.N. Robertson, et al., The number of high-risk factors and the risk of prostate cancer-specific mortality after brachytherapy: implications for treatment selection, *Int. J. Radiat. Oncol. Biol. Phys.* 82 (2012) e773–9. doi:10.1016/j.ijrobp.2011.11.023.
- [22] A.V. D'Amico, R. Whittington, S.B. Malkowicz, D. Schultz, Biochemical outcome after radical prostatectomy, external beam radiation therapy, or interstitial radiation therapy for clinically localized prostate cancer, *Jama.* (1998).

- [23] D.E. Sacco, M. Daller, J.A. Grocela, R.K. Babayan, A.L. Zietman, Corticosteroid use after prostate brachytherapy reduces the risk of acute urinary retention, *BJU International*. 91 (2003) 345–349. doi:10.1046/j.1464-4096.2003.04082.x.
- [24] R.C. Chen, J.G. Rosenman, L.G. Hoffman, W.-K. Chiu, A.Z. Wang, R.S. Pruthi, et al., Phase I study of concurrent weekly docetaxel, high-dose intensity-modulated radiation therapy (IMRT) and androgen-deprivation therapy (ADT) for high-risk prostate cancer, *BJU International*. 110 (2012) E721–E726. doi:10.1111/j.1464-410X.2012.11536.x.
- [25] M. Bolla, J.M. Hannoun-Levi, J.-M. Ferrero, P. Maingon, J. Buffet-Miny, A. Bougnoux, et al., Concurrent and adjuvant docetaxel with three-dimensional conformal radiation therapy plus androgen deprivation for high-risk prostate cancer: preliminary results of a multicentre phase II trial, *Radiother Oncol*. 97 (2010) 312–317. doi:10.1016/j.radonc.2010.08.012.
- [26] M. Perrotti, T. Doyle, P. Kumar, D. McLeod, W. Badger, S. Prater, et al., Phase I/II trial of docetaxel and concurrent radiation therapy in localized high risk prostate cancer (AGUSG 03-10), *Urol. Oncol*. 26 (2008) 276–280. doi:10.1016/j.urolonc.2007.04.003.
- [27] J. Tian, Y. Min, Z. Rodgers, X. Wan, H. Qiu, Y. Mi, et al., Nanoparticle delivery of chemotherapy combination regimen improves the therapeutic efficacy in mouse models of lung cancer, *Nanomedicine*. 13 (2017) 1301–1307. doi:10.1016/j.nano.2016.11.007.
- [28] Y.-R. Zheng, K. Suntharalingam, T.C. Johnstone, H. Yoo, W. Lin, J.G. Brooks, et al., Pt(IV) Prodrugs Designed to Bind Non-Covalently to Human Serum Albumin for Drug Delivery, *J. Am. Chem. Soc*. 136 (2014) 8790–8798. doi:10.1021/ja5038269.
- [29] S. Dhar, F.X. Gu, R. Langer, O.C. Farokhzad, S.J. Lippard, Targeted delivery of cisplatin to prostate cancer cells by aptamer functionalized Pt(IV) prodrug-PLGA-PEG nanoparticles, *Proc. Natl. Acad. Sci. U.S.A.* 105 (2008) 17356–17361. doi:10.1073/pnas.0809154105.
- [30] M.D. Hall, C.T. Dillon, M. Zhang, P. Beale, Z. Cai, B. Lai, et al., The cellular distribution and oxidation state of platinum(II) and platinum(IV) antitumour complexes in cancer cells, *Journal of Biological Inorganic Chemistry*. 8 (2003) 726–732. doi:10.1007/s00775-003-0471-6.
- [31] J.R. Tumbleston, D. Shirvanyants, N. Ermoshkin, R. Janusiewicz, A.R. Johnson, D. Kelly, et al., Continuous liquid interface production of 3D objects, *Science*. 347 (2015) 1349–1352. doi:10.1126/science.aaa2397.
- [32] J.H. Lee, R.K. Prud'Homme, I.A. Aksay, Cure depth in photopolymerization: Experiments and theory, *Journal of Materials Research*. 16 (2001) 3536–3544. doi:10.1557/JMR.2001.0485.
- [33] L. Choritz, J. Grub, M. Wegner, N. Pfeiffer, H. Thieme, Paclitaxel inhibits growth, migration and collagen production of human Tenon's fibroblasts—potential use in drug-eluting glaucoma drainage devices, *Graefes Arch Clin Exp Ophthalmol*. 248 (2009) 197–206. doi:10.1007/s00417-009-1221-4.

- [34] M.R. Bennett, In-stent stenosis: pathology and implications for the development of drug eluting stents, *Heart*. 89 (2003) 218–224.
- [35] L. Miao, S. Guo, J. Zhang, W.Y. Kim, L. Huang, Nanoparticles with Precise Ratiometric Co-Loading and Co-Delivery of Gemcitabine Monophosphate and Cisplatin for Treatment of Bladder Cancer, *Adv. Funct. Mater.* 24 (2014) 6601–6611.
doi:10.1002/adfm.201401076.